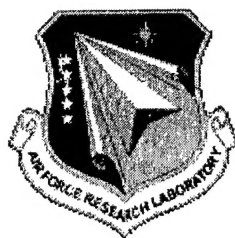AFRL-SN-HS-TR-2005-001

PROCEEDINGS OF THE 2002 ANTENNA APPLICATIONS SYMPOSIUM -

VOLUME II

Mr. Daniel Schaubert
University of Massachusetts
149 Aubinwood Road
Amherst MA 01002

Final Technical Report: 18 September 2002 – 20 September 2002

APPROVED FOR PUBLIC RELEASE DISTRIBUTION UNLIMITED

20041122 062

AIR FORCE RESEARCH LABORATORY
Sensors Directorate
Electromagnetics Technology Division
80 Scott Drive
Hanscom AFB MA 01731-2909

TECHNICAL REPORT

TITLE: PROCEEDINGS OF THE 2002 ANTENNA APPLICATIONS SYMPOSIUM
VOLUME II

APPROVED FOR PUBLIC RELEASE
DISTRIBUTION UNLIMITED

NOTICE

THIS TECHNICAL REPORT HAS BEEN REVIEWED AND IS APPROVED FOR PUBLICATION.

\\SIGNED//

HARVEY E. TOBIN
Antenna Technology Branch
Electromagnetics Technology Division

\\SIGNED\\

LIVIO D. POLES
Chief,Antenna Technology Branch
ElectromagneticsTechnology Division

\\SIGNED\\

ROBERT V. McGAHAN
Technical Advisor
Electromagnetics Technology Division

REPORT DOCUMENTATION PAGE

Form Approved OMB No. 0704-0188

Public reporting burden for this collection of information is estimated to average 1 hour per response, including the time for reviewing instructions, searching existing data sources, gathering and maintaining the data needed, and completing and reviewing this collection of information. Send comments regarding this burden estimate or any other aspect of this collection of information, including suggestions for reducing this burden to Department of Defense, Washington Headquarters Services, Directorate for Information Operations and Reports (0704-0188), 1215 Jefferson Davis Highway, Suite 1204, Arlington, VA 22202-4302. Respondents should be aware that notwithstanding any other provision of law, no person shall be subject to any penalty for failing to comply with a collection of information if it does not display a currently valid OMB control number. **PLEASE DO NOT RETURN YOUR FORM TO THE ABOVE ADDRESS.**

1. REPORT DATE *(DD-MM-YYYY)* 18-03-2003	FINAL REPORT	18-20 September 2002

4. TITLE AND SUBTITLE
Proceedings of the 2002 Antenna Applications Symposium – Volume II

5a. CONTRACT NUMBER
GSA#GS01K99BKM012

5b. GRANT NUMBER

5c. PROGRAM ELEMENT NUMBER

6. AUTHOR(S)
Daniel Schaubert, et al.

5d. PROJECT NUMBER

5e. TASK NUMBER
Task Order #R15701321

5f. WORK UNIT NUMBER

7. PERFORMING ORGANIZATION NAME(S) AND ADDRESS(ES)
Electromagnetics Technology Division

Sensors Directorate
Air Force Research Laboratory
80 Scott Drive
Hanscom AFB MA 01731-2909

8. PERFORMING ORGANIZATION REPORT

9. SPONSORING / MONITORING AGENCY NAME(S) AND ADDRESS(ES)
Electromagnetics Technology Division
Sensors Directorate
Air Force Research Laboratory
80 Scott Drive
Hanscom AFB MA 01731-2909

10. SPONSOR/MONITOR'S ACRONYM(S)
AFRL/SNHA

11. SPONSOR/MONITOR'S REPORT NUMBER(S)

12. DISTRIBUTION / AVAILABILITY STATEMENT
APPROVED FOR PUBLIC RELEASE. DISTRIBUTION UNLIMITED. OTHER REQUESTS FOR THIS DOCUMENT SHALL BE REFERRED TO DTIC-OMI, 8725 JOHN J. KINGMAN RD, FT BELVOIR, VA 22060-6218

13. SUPPLEMENTARY NOTES
Volume I contains pages 1 – 220
Volume II contains pages 221 – 456

14. ABSTRACT
The Proceedings of the 2002 Antenna Applications Symposium is a collection of state-of-the-art papers relating to antenna arrays, millimeter wave antennas, simulation and measurement of antennas, integrated antennas, and antenna bandwidth and radiation improvements.

15. SUBJECT TERMS
Antennas, Phased Arrays, Digital Beamforming, Millimeter Waves, Antenna Measurements

16. SECURITY CLASSIFICATION OF: Unclassified			17. LIMITATION OF ABSTRACT	18. NUMBER OF PAGES	19a. NAME OF RESPONSIBLE PERSON Harvey Tobin
a. REPORT Unclassified	b. ABSTRACT Unclassified	c. THIS PAGE Unclassified	SAR	228	19b. TELEPHONE NUMBER *(include area code)* 781-377-9473

Standard Form 298 (Rev. 8-98)
Prescribed by ANSI Std. Z39.18

i

Volume II

Identifiers for Proceedings of Symposia

The USAF Antenna Research and Development Program

Year	Symp. No.	Identifier
1951	First	_____
1952	Second	C054 520
1953	Third	AD63794
1954	Fourth	AD63139
1955	Fifth	AD90397
1956	Sixth	AD114702
1957	Seventh	AD138500
1958	Eighth	AD301151
1959	Ninth	AD314721
1960	Tenth	AD244388 (Vol. 1)
		AD319613 (Vol. 2)
1961	Eleventh	AD669109 (Vol. 1)
		AD326549 (Vol. 2)
1962	Twelfth	AD287185 (Vol. 1)
		AD334484 (Vol. 2)
1963	Thirteenth	AD421483
1964	Fourteenth	AD609104
1965	Fifteenth	AD474238L
1966	Sixteenth	AD800524L
1967	Seventeenth	AD822894L
1968	Eighteenth	AD846427L
1969	Nineteenth	AD860812L
1970	Twentieth	AD875973L
1971	Twenty-First	AD888641L
1972	Twenty-Second	AD904360L
1973	Twenty-Third	AD914238L

Antenna Applications Symposium

		TR#	ADA#
1977	First	None	955413
1978	Second	None	955416
1979	Third	_____	077167
1980	Fourth	_____	205907
1981	Fifth	_____	205816
1982	Sixth	_____	129356
1983	Seventh	_____	142003; 142754
1984	Eighth	85-14	153257; 153258
1985	Ninth	85-242	166754; 165535
1986	Tenth	87-10	181537; 181536
1987	Eleventh	88-160	206705; 206704
1988	Twelfth	89-121	213815; 211396
1989	Thirteenth	90-42	226022; 226021
1990	Fourteenth	91-156	237056; 237057
1991	Fifteenth	92-42	253681; 253682
1992	Sixteenth	93-119	268167; 266916
1993	Seventeenth	94-20	277202; 277203
1994	Eighteenth	95-47	293258; 293259
1995	Nineteenth	96-100	309715; 309723
1996	Twentieth	97-189	341737
1997	Twenty First	1998-143	355120
1998	Twenty Second	1999-86	364798
1999	Twenty Third	2000-008 (I) (II)	386476; 386477
2000	Twenty Fourth	2002-001 Vol I & II	
2001	Twenty Fifty	2002-002 Vol I & II	

5% for ε_r, while air was with in 10% below 8.92 GHz. The 0.0165 inch thick Teflon sample was not within 10%, but exhibited a trend towards 10% as the frequency increased.

10.0 Conclusion

A method and procedure for calibrating to the coaxial flanged probes, over 2 to 18 GHz, using the full 2-port method has been generated. This method deletes the subjective delay based on wrapping around a point on the Smith chart, known as probe extension, for a short or open. This method is expandable over the entire useable frequency range of the network analyzer used for material measurements. The method does use the modified calibration data set [31].

A method and set of example, readily made coaxial probes have been described and used in the HP 8510C network analyzer testing environment. The developed probe technique uses commercially available off the shelf connectors that can cover the entire frequency measurement range of the network analyzer. The frequency measurement range of the probes is only limited by the operational frequency range of the type of connector installed in the coaxial probe flange.

A limitation, to the only dual coaxial probe analysis, known to date, was discovered. This discovery, impacts the calculation, for the forward problem, where the S-parameters are determined. The limitation was that the material boundary condition, between the flanges was set to infinity, as well as the probes. The practical use for this analysis uses finite flanges that require additional formulation for the discontinuity at the flange edges. This limitation implies that the measured data presented in this dissertation is closer to the theoretical than stated on the comparison data plots.

A finite element model was developed, using the High Frequency Circuit Simulator (HFSS) analytic code. Several problems were discovered in the materials and S-parameter calculations of this analytic code. The model generated worked over the full 2 to 18 GHz frequency range for the air material measurement between the dual coaxial probes. The model aided in the discovery of how the dual coaxial probes should really need to be modeled. The predicted data matched, within 20%, the location of the measured resonances in the measured data.

The comparison between the HFSS and the measured data provided the discovery of how the dual coaxial probe materials measurement technique is actually working. The measurement technique is actually behaving as a lossy resonator. Calculations do show that the material to free space edge acts like a total reflection point and behaves like a metallic wall of a cylindrical cavity. The

Research community to date, has not looked at this materials measurement technique as a cavity resonator.

The determination that the dual coaxial probe technique is actually a cavity resonator was verified with measured field probe data for the 0.25 inch thick air space measurement. The data is provided in the dissertation for the radial electric field from the feed point to the outer edge of the probe flanges. This data shows, with measured data, that the electric field is approximately zero at the outer flange edges. This supports the premise that the electric field is not radiated out of the coaxial flange assembly, but is reflected back into the coaxial assembly. This enables the assembly to act as a lossy cavity resonator with material walls by the impedance mismatch at the flange edges.

The measured data is compared to the TportFor analytic model with results illustrating the adequacy of the measurement technique for use from a minimum of 2 to 12 GHz for various thicknesses of Teflon and Rexolite, that is , low loss materials. The predicted versus measured S-parameters exhibit errors, in this frequency range, of less than 10%. All measured material results show that the measured data closely matches the low frequency end predicted data, suggesting that the analytic model is accurate at the lower frequencies. It also shows that the measured data is accurate at the lower frequencies as compared to TportFor S-parameter data.

A transmission line model was derived for this dual coaxial flanged probe assembly. The assembly approximates a radial line transmission line once it is recognized that only the electric field in the z-direction and the magnetic field in the axial direction exist due to the circumferential symmetry of the problem. The equations derived illustrate the complexity of the problem due to the need for Hankel functions of order 2 with complex arguments. The method follows power conservation, and knowing the input and output power of the probes, the power absorbed in the material can be calculated. This then allows the forward problem to be analyzed for the complex dielectric constant, but not easily.

11.0 References

[1]   A. M. Nicolson and G. F. Ross, "Measurements of the Intrinsic Properties of Materials by Time-Domain Techniques," IEEE Trans. Instrum. Meas., Vol. IM-19, No. 4, pp. 377-382, November, 1970.

[2]   W. B. Weir, "Automatic Measurement of Complex Dielectric Constant and Permeability at Microwave Frequencies," Proc. IEEE, Vol. 62, No. 1, pp. 33-36, January, 1974.

[3] J. Munk and A. Dominek, "Calibration of Automatic Network Analyzers," Report723224-1, ElectroScience Laboratory, The Ohio State University, September,1990.

[4] P. W. Stemp and I. J. Youngs, "Reproducibility, Traceability and Uncertainty of Dielectric Measurements Using Automated Vector Network Analysis," Seventh International Conference on Dielectric Materials, Measurements and Applications, Conf. Pub. No. 430, 23-26 pp. 1-3, September, 1996.

[5] J. Baker-Jarvis, and M. D, Janezic, "Analysis of a Two-Port Flanged Coaxial Holder for Shielding Effectiveness Dielectric Measurements of Thin Films and Thin Materials," IEEE Trans. Elect. Comp, Vol. 38, No. 1, pp. 66-70, February, 1996.

[6] A. Kraszewski, M. A. Stuchly, and S. S. Stuchly, "ANA Calibration Method for Measurements of Dielectric Properties," IEEE Trans. Instrum. Meas., Vol. IM-32, No. 2, pp. 385-387, June, 1983.

[7] T. W. Athey, M. A. Stuchly, and S. S. Stuchly, "Measurement of Radio Frequency Permittivity of Biological Tissues with an Open-Ended Coaxial Line: Part I," IEEE Trans. Microwave Theory Tech., Vol. MTT-30, No. 1, pp. 82-86, January, 1982.

[8] J. R. Mosig, J. E. Besson, M. Gex-Fabry, and F. E. Gardiol, "Reflection of an Open-Ended Coaxial Line and Application to Nondestructive Measurement of Materials," IEEE Trans. Instrum. Meas., Vol. IM-30, No. 1, pp. 46-51, March, 1981.

[9] N. E. Belhadj-Tahar, O. Dubrunfaut, and A. Fourrier-Lamer, "Broad-Band Microwave Characterization of a Tri-Layer Structure Using a Coaxial Discontinuity with Applications for Magnetic Liquids and Films," IEEE Trans. Microwave Theory Tech., Vol. 46, No. 12, pp. 2109-2116, December, 1998.

[10] S. O. Nelson and P. Bartley, Jr., "Open-Ended Coaxial-Line Permittivity Measurements on Pulverized Materials," IEEE Trans. Instrum. Meas., Vol. 47, No. 1, pp. 133-137, February, 1998.

[11] W. R. Humbert and W. R. Scott, "A New Technique for Measuring the Permittivity and Loss Tangent of Cylindrical Dielectric Rods," IEEE Microwave and Guided Wave Letters, Vol. 6, No. 7, pp. 262-264, July, 1996.

[12] Zulkifly Abbas, R. D. Pollard, and R. W. Kelsall, "A Rectangular Dielectric Waveguide Technique for Determination of Permittivity of

Materials at W-Band," IEEE Trans. Microwave Theory Tech., Vol. 46, No. 12, pp. 2011-2015, December, 1998.

[13] M. A. Stuchly, S. S. Stuchly, and G. Kantor, "Diathermy Applicators with Circular Aperture and Corrugated Flange," IEEE Trans. Microwave Theory Tech., Vol. MTT-28, No. 3, pp. 267-271, March, 1980.

[14] J. A. Berrie and A. K. Dominek, "Measurement of Electrical Parameters for Planar Materials," Report 720964-16, ElectroScience Laboratory, The Ohio State University, January, 1992.

[15] G. S. Smith and J. D. Nordgard, "Measurement of the Electrical Constitutive Parameters of Materials Using Antennas," IEEE Trans. Antennas Propagat., Vol. Ap-33, No. 7, pp. 783-792, July, 1985.

[16] L. S. Anderson, G. B. Gajda, and S. S. Stuchly, "Analysis of an Open-Ended Coaxial Line Sensor in Layered Dielectrics," IEEE Trans. Instrum. Meas., Vol. IM-35, No. 1, pp. 13-18, March, 1986.

[17] J. Ayer, "Measurement of Dielectric Constant at RF and Microwave Frequencies," RF Design, pp. 44-47, April, 1987.

[18] C. H. Durney, H. Massoudi, and M. F. Iskander, Radiofrequency Radiation Dosimetry Handbook, Fourth Edition, USAFSAM-TR-85-73, Brooks AirForce Base, October, 1986.

[19] D. Blackham, "Permittivity Measurements Using an Open-Ended Coaxial Probe," AMTA Workshop on Electromagnetic Characterization of Materials, Date, Paper 3-1.

[20] J. Baker-Jarvis, C. Jones, B. Riddle, M. Janezic, R. G. Geyer, J. H. Grosvenor, Jr., and C. M. Weil, "Dielectric and Magnetic Measurements: A Survey of Nondestructive, Quasi-Nondestructive, and Process-Control Techniques," Springer-Verlag, New York, Inc., pp. 117-136, 1995.

[21] D. Misra, M. Chabbra, B. R. Epstein, M. Mirotznik, and K. R. Foster, "Noninvasive Electrical Characterization of Materials at Microwave Frequencies Using an Open-Ended Coaxial Line: Test of an Improved Calibration Technique," IEEE Trans. Microwave Theory Tech., Vol. 38, No. 1, pp. 8-14, January, 1990.

[22] M. A. Stuchly, M. M. Brady, S. S. Stuchly, and G. Gajda, Equivalent Circuit of an Open-Ended Coaxial Line in a Lossy Dielectric," IEEE Trans. Instrum. Meas., Vol. IM-31, No. 2, pp. 116-119, June, 1982.

[23] B. G. Colpitts and J. S. Ployer, "Finite-Difference Time Domain Model of a Coaxial Probe," Symposium on Antenna Technology A. (ANTEM'94), Conf. Proc., Winnipeg, Canada, pp. 357-361, 1994.

[24] C. Gabriel, T. Y. A. Chan, and E. H. Grant, "Admittance Models for Open Ended Coaxial Probes and Their Place in Dielectric Spectroscopy," Phys. in Medicine and Biology, Vol. 39, pp. 2183-2200, 1994.

[25] T. Ando, "Determining Complex Permittivity by Measuring the Scattered Waveform from a Dielectric Circular Cylinder," IEEE Trans. Instrum. Meas., Vol. 38, No. 5, pp. 1012-1014, October, 1989.

[26] R. Afzalzadeh, "Dielectric Constant Measurement of Finite-Size Sheet at Microwave Frequencies by Psuedo-Brewster's Angle Method," IEEE Trans. Microwave Theory Tech., Vol. 46, No. 9, pp. 1307-1309, September, 1998.

[27] J. Baker-Jarvis, M. D. Janezic, P. D. Domich, and R. G. Geyer, "Analysis of an Open-Ended Coaxial Probe with Lift-Off for Nondestructive Testing," IEEE Trans. Instrum. Meas., Vol. 43, No. 5, pp. 711-718, October,.

[28] C. H. Riedel, M. B. Steer, M. R. Kay, J. S. Kasten, M. S. Basel, and R. Pomerleau, "Dielectric Characterization of Printed Circuit Board Substrates," IEEE Trans. Instrum. Meas., Vol. IM-39, No. 2, pp. 437-440, April, !990.

[29] S. Ramo and J. R. Whinnery, Fields and Waves in Communication Electronics, 2nd edition, John Wiley and Sons, NewYork, pp. 395-400, 1984.

[30] R. C. Collin, Field Theory of Guided Waves, 2nd Edition, IEEE Press, Piscataway, New Jersey, 1991.

[31] T. R. Holzheimer, Broadband Nondestructive Materials Measurements Using Readily Made Dual Coaxial Probes, Ph.D. Dissertation, University of Texas at Arlington, May, 2000.

[32] Network Analysis: Specifying Calibration Standards for the HP 8510 Network Analyzer, Product Note 8510-5A, February 1, 1998.

A Broadband Materials Measurements Technique Using the Full Frequency Extent of the Network Analyzer

Tim Holzheimer, Ph.D., P.E.
Raytheon
Legacy C3I, National Systems
Garland, Texas 75042

Abstract

A Technique is presented that allows for broadband nondestructive material electrical parameter measurements. Electrical parameters of materials are not readily available over extremely broad bandwidths (multiple octaves as an example) for input into analytical models for microwave circuits and antennas. These parameters consist of complex permittivity and complex permeability which cause attenuation due to the types and thickness of materials to be used. A Method is required that allows for fast, accurate and low cost measurements of the materials under test.

The technique of using dual coaxial probes provides a solution that can be applied to numerous materials including thin films. It takes advantage of the full frequency extent of the network analyzer. This measurement uses dual coaxial probes, as compared to the implementation of cavity resonators, coaxial lines, waveguides and free space measurements, and performs the measurement in a 2-port calibration procedure. The Coaxial probes are described and can be easily made with available components where the only limitation is the valid component frequency bandwidth. Several materials examples show the expected accuracy versus frequency range of this measurement technique.

1.0 Introduction

Broadband, nondestructive, material electrical parameter measurement techniques include free space, open ended rectangular waveguides, coaxial monopoles, flush coaxial transmission lines, single coaxial probes, embedded single coaxial probes and dual coaxial probes all with and without flanges. Waveguide and coaxial line measurements are considered to be narrowband measurements that are not used over multiple octaves. Additionally the line measurements are considered destructive measurements since the materials must be cut to fit inside the lines, minimizing the gap capacitances, for measurements to occur. The method of calibration for each of these measurements is critical and limits the accuracy and use of these techniques.

Calibration using automatic network analyzers (ANA) has been addressed by Nicholson and others [1-2]. This provided the basic method of backing out the complex permittivity and complex permeability of measured materials. The method was based on a, air to material to air, system in a coaxial waveguide. Using the S_{11} and S_{21} parameters the reflection and transmission coefficients can be extracted and then in turn the appropriate electrical parameters can be derived using the thicknesses of the materials measured. More recently Munk and Dominic evaluated the open, short and load versus the same using a sliding load for calibration accuracy [3-4]. Others have looked at time domain versus frequency domain for the measurements and recommended the frequency domain for obtaining increased accuracy measurements. Another technique uses the port extension of the ANA, but this does not take into account the differences of the probes being used for the measurement [5]. The ANA is recognized as the best means of performing the measurement. The number of data points can be adjusted by changing the delimiting start and stop frequency bandwidths. The random measurement errors can be reduced by using averaging in the ANA. This coupled with the ability to read the data directly into present day personal computer spreadsheets makes the use of ANA measurements extremely desirable.

Present techniques have varying degrees of construction difficulty in implementing the probes to be used for the materials measurements. All have limitations in the accuracy of the broadband measurement based on how they are calibrated. Full 2-port measurements have been reported and generally accepted as the most accurate method of measurement. The best accuracy is obtained with calibration based on the smallest number of known standards that are used [6]. Another technique called Thru-reflection-transmission line is postulated as being even more accurate because it does not rely on a standard load for a constant load impedance. A broadband load for placement on the end of the probes has proven to be the real problem in calibration of the measurements. Others have investigated the use of a liquid with well known dielectric properties for use in

place of the load [7]. Calibration using present day network analyzers such as the Hewlett Packard 8510 provide a fast means of measurement. The key to accurate measurements is in the implementations of the standards required for calibration. A secondary point is that higher order evanescent modes need to be included since they can influence the measurements of the reflection [8].

A coaxial line with a material sample used as a discontinuity has been investigated over the full frequency range of the ANA (45 MHz to 18 GHz) [9]. The higher order modes were accounted for due to the discontinuity. The problem is that the material has been destructively placed inside the coaxial line. This is not feasible with the newer more costly and limited availability materials.

Another method whereby the material is placed at the shorted wall of a rectangular or cylindrical waveguide has been investigated [10]. Again this is a destructive measurement to the materials to be measured and is frequency limited in that multiple waveguides and different sample thicknesses are required in order to obtain electrical parameters over frequency. This can become quite time consuming in obtaining the data.

Cavity resonant techniques could be used, but many cavities and higher order modes would be required in order to make electrical parameter measurements over broad frequency bands. A technique was investigated for the measurement of dielectric rods [11]. This is a resonant technique which takes advantage of a commonly available sample shape providing excellent results for the measurement of low loss tangent materials.

Free space techniques consist of radiating and receiving both in front of the material and in back of the material. When both are in front of the material this yields a reflection measurement. When the receive antenna is behind the material this is a transmission measurement. The distances from the antennas to the material under test are $2D^2/\lambda$. Problems typically occur with the dimensions of the test sample driving the distance for far field to extremely large distances in addition to the test sample having to be large, on the order of multiple wavelengths. This is not possible with some of the newer limited availability and more costly materials. This measurement is typically performed in an anechoic chamber or in a naval research laboratory (NRL) arch.

The open ended waveguides have been investigated both with and without flanges for measurement of electrical parameters of many different material types including anisotropic materials [12]. Others have used circular waveguides with choke flanges in order to prevent energy leakage in the measurement [13]. It was determined that construction was difficult when a flange was added, which is required for collocation in using a dual waveguide measurement. Bandwidth is limited to the size of the particular waveguide used for the probe. Calibration is typically performed as a 1-port using an open and a short where the short is a plate placed across the end of the exposed waveguide end. These type of probes

are not typically used in the dual configuration. The material to be measured is generally backed by free space or a perfect electrical conductor (PEC) or ground plane.

Coaxial monopoles were investigated, but they require the addition of a hole in the material to be measured for insertion of the monopole into a solid [14]. Others used the monopole for measurement of the electrical properties of liquids by comparing the before and after insertion antenna impedance [15]. The height of the monopole must be smaller than the thickness of the material to be measured that can limit its use for measurement of thin films. The technique was investigated for both a single probe for reflection and a dual set of probes for transmission on the same surface. Several materials were investigated as well as thickness limitations on the materials to be measured.

Flush coaxial transmission lines have been investigated by several groups both at room temperature and at extremely high temperatures [16]. These probes are easily made using presently available transmission lines, generally cylindrical, but the capability of dual probes imposes a potential alignment problem when flanges are not included. When flanges are included the probes then become coaxial probes. Bandwidth of the measurement is limited by the transmission line implemented. Problems can occur if the transmission line that is used is not large enough in diameter to allow enough energy to radiate into the material to be measured.

Resonators of specific type have also been investigated which includes open ended coaxial line and shielded open circuit sample holders [17]. The open ended coaxial resonator incorporates a quarter wavelength resonator at its end surface. Complexity of buiding is a potential problem that must be considered. The shielded open circuit sample holders have been investigated both in rectangular and cylindrical configuration. These are typically used for the measurements of powders and liquids.

Another technique is to use coaxial probes and flush coaxial probes embedded in materials. This is typical for measurements of tissue [18]. This method has been looked at both in a 1-port and 2-port method. The use of two probes both on the top and bottom of the material or tissue to be measured has not occurred.

The preferred method uses either single coaxial probes with or without the material backed by a conductive ground plane or dual coaxial probes [19]. The problem encountered is both aperture area exposed to the material and the method of calibration. The limitations on transmission line diameters are reported where the flange diameter must be a minimum of four times the outer diameter of the transmission line. The method employed by some groups calibrates to the end of the coaxial cables and then uses a port extension, phase length addition, adjustment in order to move the reference plane for the measurement to the probe

face. This can cause large errors, due to the differences that are encountered in the quasi-identical probes, which are not accounted for in the calibration whether it is a 1-port or full 2-port measurement. There is disagreement over valid bandwidth for these measurements using this calibration technique [20]. Hewlett Packard advertises their coaxial probe as working up to 26.5 GHz, while others use the probe only up to 3 GHz.

The single and dual coaxial probe techniques use the TEM incident fields of the coaxial feed applied to a axially symmetric infinite parallel plate waveguide which only supports TM modes with higher order TM modes being evanescent. Higher order TM modes must be accounted for in order to maintain accuracy of the measurement technique. Reported findings have not included air gaps in the calculations and measurements for the use of dual coaxial probes. Air gaps have been investigated and reported for single coaxial probes leading to the required solution of transcendental equations [21].

Analytical probe analysis has occurred for all probes using method of moments (MOM) [22]. FDTD modeling of the probes has occurred and limited FEM analysis has also occurred [23]. Hybrid modeling has also occurred using both MOM and FEM combined [24]. Other analysis includes different probe admittance models, scattering methods, spectral domain method, optimization methods, frequency-varying technique, and numerous others.

Numerous other techniques exist for the measurement and determination of material electric and magnetic parameters [25]. These include time domain techniques, optical techniques, modified antennas and probes, propagation calculations, amplitude only calculations, and techniques for measuring multiple layers [26].

The following four charts, shown in figures 1 through 4, summarize the different techniques available at the time of this writing.
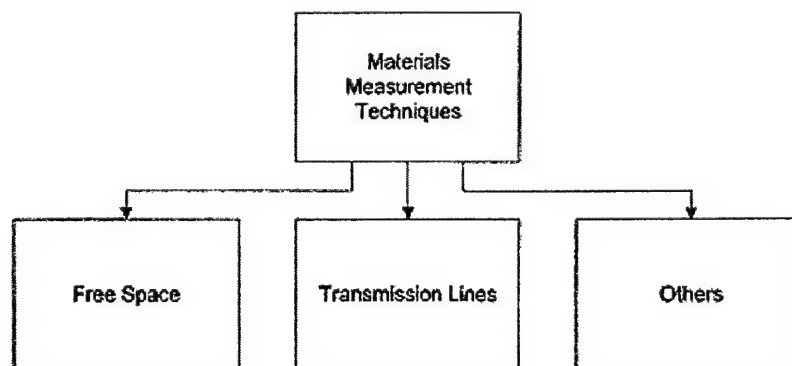
Figure 1. The Main areas of material measurement techniques.
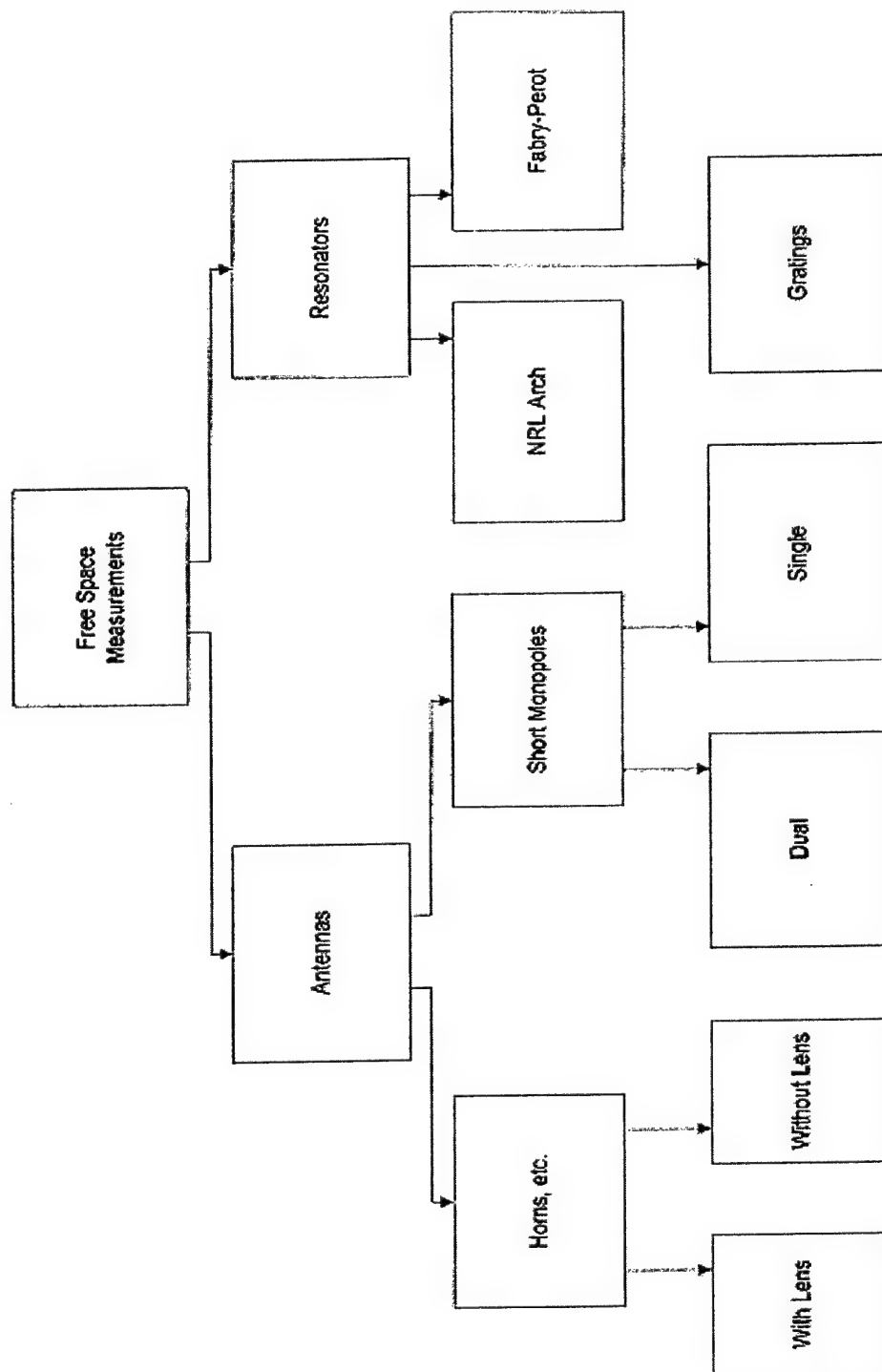
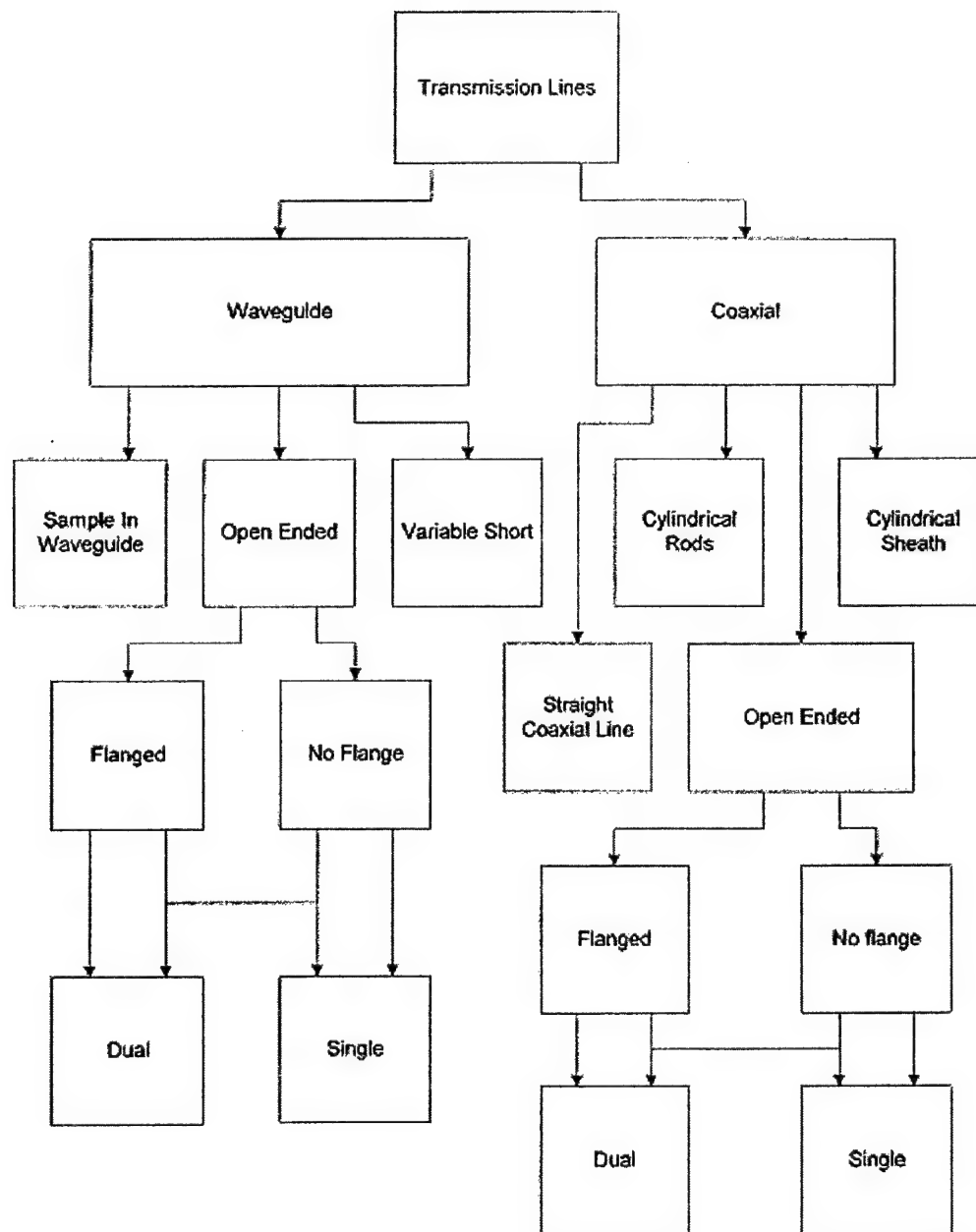Figure 2. The Main areas of free space material measurement techniques.

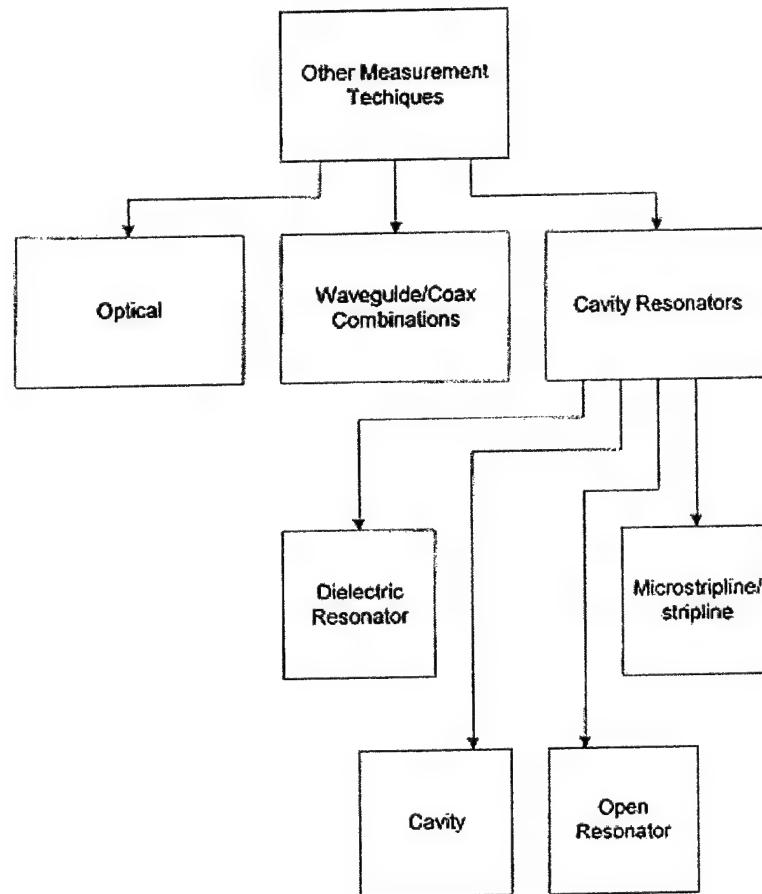Figure 3. The Main areas of transmission line material measurement techniques.

Figure 4. The Main areas of other material
measurement techniques.

1.0 Theory of Coaxial Probes

The theoretical analysis of coaxial probes and in particular dual coaxial
probes is complicated. Dual coaxial probes have been investigated with limited
models using transverse magnetic (TM) modal analysis [27]. Only a few have
looked at this problem as a complete theoretical measurement system. The dual
coaxial probe, is shown in figure 5. It is recognized that the dual coaxial probe
assembly looks like a radial transmission line (radial parallel plate waveguide)

and also like a cavity resonator. As a transmission line (TRL), the assembly can be analyzed with transverse electromagnetic mode (TEM) theory. As a cavity resonator, the assembly can be analyzed as a lossy dielectric filled cavity resonator. The theoretical models must include losses. The desired parameters are the dielectric constant and S-parameters of materials to be measured.

The data that was measured, after controlled calibration, exhibited what looked to be resonances in the S-parameter measurements. This data illustrated a lossy cavity resonator. It is recognized that two problem types are required for solution of the material parameters that are the forward and inverse solutions. The forward solution requires input dielectric constant information and provides results that are the S-parameters of the material being measured. The inverse problem uses the measured S-parameter data taken, on the measured material, and provides the resultant complex dielectric constant for the material

Materials for measurement can span the entire range from solids to liquids. These materials can be dielectric with electric and magnetic properties. The materials can be poor conductors, not perfect, such as high temperature superconductor, that is a dielectric at room temperature and a superconductor at 77°K.
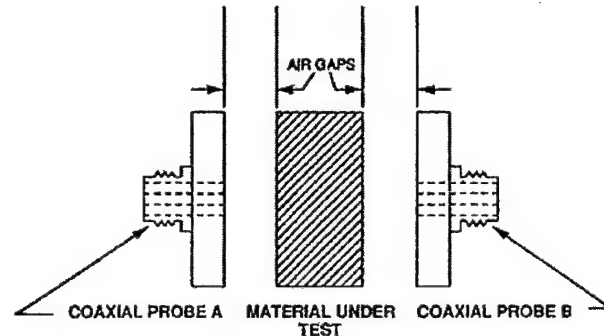
Figure 5. The Dual coaxial probe model used in this research.

The relative complex dielectric constant in terms of electric loss, is the relative permittivity. It is defined as:

$$\varepsilon_r = \varepsilon_r^{'} - j\varepsilon_r^{''} = \varepsilon_r^{'} - j\varepsilon_r^{'}\tan\left(\delta_e\right) \text{ or } = \varepsilon_r^{'} - j\frac{\sigma}{\omega\varepsilon_0} \tag{1}$$

where

$$\tan\left(\delta_e\right) = \left(\frac{\varepsilon_r^{''}}{\varepsilon_r^{'}}\right) \text{ or } = \frac{\sigma}{\omega\varepsilon_0\varepsilon_r} = \frac{\sigma}{\omega\varepsilon} \tag{2}$$

The relative complex dielectric constant in terms of magnetic loss, is relative permeability. It is defined as:

$$\mu = \mu_r^{'} - j\mu_r^{''} = \mu_r^{'}\left(1 - j\tan\left(\delta_m\right)\right) \text{ and } \tan\left(\delta_m\right) = \left(\frac{\mu_r^{''}}{\mu_r^{'}}\right) \tag{3}$$

The literature defines the various tangent functions, electric loss tangent for dielectrics and magnetic loss tangent for magnetic materials. The real part of the complex dielectric constant is equated with energy storage and the imaginary part is equated to energy loss. The complex dielectric constant varies with frequency, typically decreasing with increasing frequency. The comparison of the loss tangent to 1 determines whether or not the material is a good insulator or a good conductor. A good conductor will have loss tangent much less than 1 and the opposite for a good conductor

The component consisting of the radial waveguide or radial transmission line has been derived, for the air case, without loss [28]. Ramo and Whinnery provided a derivation for the radial transmission line with a voltage source applied at the center of the circular (radial) waveguide plates and for a source applied at the edges of the plates [29]. This problem is axially symmetric in the ϕ-direction or circumferentially resulting in only E_z and H_ϕ due to no field components in the r-direction (radial propagation direction). This is where the simplification to the problem is made, as to the mode fields that can be propagated. This limits the problem to propagating only TM modes. It is from this point that the theory of deriving this assembly as a transmission line results. At the same time the TRL or TEM mode theory can be applied to a cavity resonator.

A dual coaxial probe model has been derived using only TM modes [27] and does account for the coaxial feedpin and outer shield discontinuity on each coaxial probe. The problem, that was discovered, is that the boundary conditions, on the inserted material of the model, is assumed to be infinite. This by itself is appropriate, but the flanges are also defined to be infinite. Figure 5, where ρ is the radial direction instead of r illustrates the problem with this model, that must

be modified. This model still provides adequate results at the lower frequencies (less than 2 GHz). The practical flanges have defined edges and are not infinite, requiring an additional boundary condition and a method to handle the edge discontinuity at the edge of the flanges. The model, investigated in this analysis, shown in figure 5, approximates the air gaps to zero.

The measured data, from the HP 8510C network analyzer showed periodic resonances that are characteristic of a cavity resonator. The dual coaxial probe assembly was modeled with HFSS, using equivalent parameters, exhibiting the similar resonance structure. As a potential cavity resonator the fields needed to be probed in order to determine the type of resonator, such as half-wave. This prompted the measurement of the radial fields, in the dual coaxial probe assembly, in order to determine if the fields actually went to zero at the extents of the probe flanges.

The radial power in the z-direction was measured as the probe was moved from the center of the dual coaxial probe assembly to the outer edge. A comparable HFSS prediction verifies the measurement and it also shows the expected double discontinuity at the coaxial feed to flange interface. The peak locations, in the HFSS predicted data, are the exact locations for the center pin and outer shield of the SMA connector that was used in the coaxial probes. These peaks should exist and are due to the coaxial feed discontinuity.

A theoretical calculation, based on TRL theory [30], is made in order to verify this is indeed a lossy resonator system. The resonator is open to free space and therefore the impedance of freespace is the load applied to the radial TRL. The inductance and a capacitance for the radial transmission line is defined to be as follows:

$$L_{line} = \frac{\mu d}{2\pi r} \quad \text{and} \quad C_{line} = \frac{\varepsilon 2\pi r}{d} \tag{4}$$

d = spacing between coaxial probes
r = radial distance from center towards outer edge of coaxial probe flange

The radial field data shows differences in the peak values where the discontinuity, due to the coaxial feed pin is located. This calculation shows that very little energy is coupled into the radial waveguide at the lower frequencies explaining why the peaks at the feed pin are at different levels versus frequency.

The impedance of the radial TRL is calculated in order for the reflection coefficient to be derived at the radial TRL to free space boundary interface. The diameter of the coaxial probe flanges is 2.5 inches and the radius is 1.25 inches. The spacing between the coaxial probes is 0.25 inches. The impedance of the radial transmission line or impedance between the dual coaxial probe plates is 8.48 ohms at the outer edge of the flanges. The Impedance of freespace is 377 ohms, the load in this case, and the reflection coefficient can be determined as follows:

$$\Gamma_{edge} = \frac{Z_{load} - Z_{line}}{Z_{load} + Z_{line}} \tag{5}$$

Substituting the above impedance values into equation 3.9, results in a reflection coefficient of $\Gamma_{edge} = 0.956$, that says almost all of the energy is reflected directly back into the dual coaxial probe assembly or resonator. This matches the radial power measurements that show no energy being radiated from the edges of the dual coaxial probe assembly.

2.0 Transmission Line Analysis

The Transmission line analysis looks at solving the problem as if it were a transverse electromagnetic (TEM) transmission line (TRL) as described by several authors. The basic transmission line equations, which can become the wave equations for both voltage and current, utilize the cylindrical field quantities and loss in order to end up with a method of performing the inverse problem based on the input of measured S-parameters. The transmission line model is used outside of the discontinuity region of the coaxial feed, as compared to TportFor that does use the discontinuity by accounting for at least six of the TM modes. The TRL analysis allows the use of the voltage and current relations and uses the dominant TEM mode for solution. A calculation is derived to show that the approximation by excluding the discontinuity is very small compared to the rest of the calculation for the problem.

The basic transmission line equations are analogous to the electromagnetic field theory equations and for cylindrical geometry and are of the following form:

$$\frac{dV}{dr} + (R + j\omega L)I = 0 \text{ and } \frac{dI}{dr} + (G + j\omega)C = 0 \tag{6}$$

The second derivative of the voltage equation with respect to r and the second derivative of the current equation with respect to r, will result in the wave equations for voltage and current. The probes act as a radial transmission line and this provides axial symmetry. The symmetry provides no field variation circumferentially resulting in only H_ϕ and E_z. The axial symmetry also says that only TM modes will propagate and as a result then $H_z = 0$. The model for the radial transmission line is shown in figure 6.

The Transmission Line model of 6 has r_i = radius at the inner and r_o = radius at the outer position of the flanges. Z_l is the load which is assumed to be purely real 377 ohms to start with. V_g and Z_g are the source voltage and source impedance. We also know that the variation in the z-direction is constant so that $V = E_z s$, where s = spacing between the dual coaxial probe flanges. The current in the radial direction is $I = 2\pi r H_\phi$. The inductance and capacitance along the radial transmission line can be defined as follows:

$$L = \frac{\mu s}{2\pi r} \text{ from } L = \frac{n\phi}{1} \text{ and } C = \frac{2\pi r \varepsilon}{s} \text{ from } C = \frac{\varepsilon \times \text{area}}{s} \tag{7}$$

The radial TRL plates or coaxial probe flanges exhibit radial current flow in opposite directions, on the top versus lower plate, as you would see on a transmission line, with decreasing amplitude from the feedpoint due to the spreading of the radial (or cylindrical) propagated waves. The propagating fields are radial cylindrical waves from inside the dual coaxial probe flange plates making the transmission line model relevant.
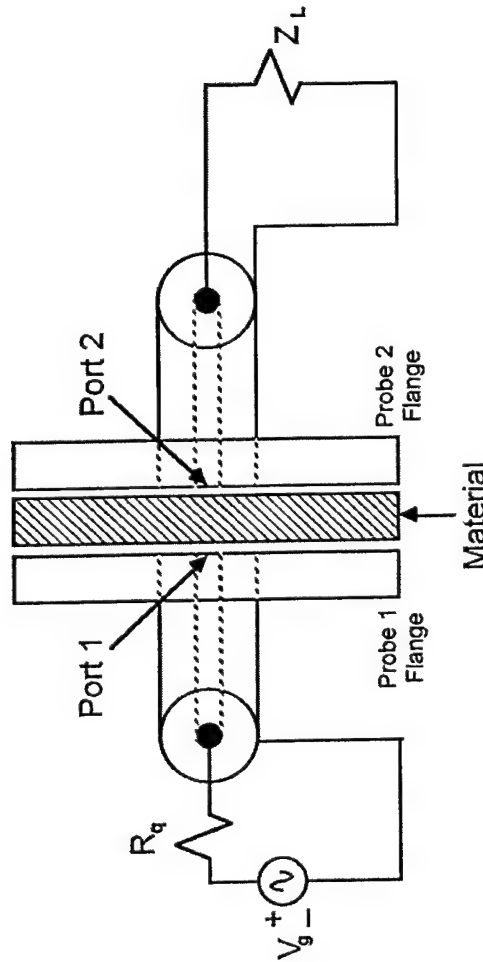
Figure 6. The Transmission line model used in the analysis of the radial line.

The basic transmission line equation can be used with inductance and capacitance, and setting resistance to zero. The resistance is set to zero by assuming that the conductivity of the plates is high. The complex permittivity is still retained through ε. The complex permeability can also be maintained, but for this analysis $\mu_r = 1.0$. The first test will be air.

Implementing the standard TRL procedure of solving for current (I), and then substituting the result allows the solution for the voltage (V). This is now purely a voltage equation in the form of a Bessel equation of zeroth order and argument $\omega^2 \sqrt{\mu_o \varepsilon_o \left(\varepsilon_r' - j\varepsilon_r'' \right)} r$. It is more recognizable when the r is divided through as follows:

$$\frac{d^2V}{dr^2} + \frac{1}{r}\frac{dV}{dr} + \omega^2\mu_o\varepsilon_o\left(\varepsilon_r^{'} - j\varepsilon_r^{''}\right)V = 0 \tag{8}$$

In the assumed solution, Hankel functions are used , since they represent cylindrical traveling waves for the radial transmission line. The solution to this first Bessel equation provides us with voltage on the transmission line. It is as follows:

$$V = AH_0^1\left(\omega\sqrt{\mu_o\varepsilon_o}\sqrt{\varepsilon_r^{'} - j\varepsilon_r^{''}}r\right) + BH_0^2\left(\omega\sqrt{\mu_o\varepsilon_o}\sqrt{\varepsilon_r^{'} - j\varepsilon_r^{''}}r\right) \tag{9}$$

where A and B are constants still to be determined.

The traveling waves can be seen by considering the asymptotic forms of the Hankel functions.

The z-direction is the radial direction in the model and is equivalent to $(\alpha + j\beta)r$ which is attenuation for lossy material. There is a propagating input wave traveling to the load, assumed to be free space, where it is completely reflected and returns to the input with some attenuation. The assumption of no radiated fields out of the flange edges, follows from the radial field measurements where the field was verified as zero at the flange edges. The impedance mismatch makes the material installed in the cavity resonator look like a perfect short or conducting wall between the radial transmission line plates at the flange edges. The radial line data shows that the waves on the transmission line are traveling waves exhibiting the 1/R electric field rolloff. This is seen by the decaying low level ripple where the forward traveling wave moves to the load and then continues back, reflected, and is still falling off, as on the forward traveling wave.

Continuing with the solution for the current, the Bessel equation solution, equation 9 is substituted into the current equation. After taking the derivative with respect to r, the Hankel functions of first order are obtained. The equation is as follows:

$$I = -\frac{1}{j\omega\mu_o\left(\dfrac{s}{2\pi r}\right)}\frac{d}{dr}\left(AH_0^1\left(\omega\sqrt{\mu_o\varepsilon_o}\sqrt{\varepsilon_r'-j\varepsilon_r''}\,r\right)+BH_o^2\left(\omega\sqrt{\mu_o\varepsilon_o}\sqrt{\varepsilon_r'-j\varepsilon_r''}\,r\right)\right)$$

(10)

and

$$I = -j\frac{\sqrt{\varepsilon_r'-j\varepsilon_r''}}{\sqrt{\dfrac{\mu_o}{\varepsilon_o}}\left(\dfrac{s}{2\pi r}\right)}\left(AH_1^1\left(\omega\sqrt{\mu_o\varepsilon_o}\sqrt{\varepsilon_r'-j\varepsilon_r''}\,r\right)+BH_1^2\left(\omega\sqrt{\mu_o\varepsilon_o}\sqrt{\varepsilon_r'-j\varepsilon_r''}\,r\right)\right) \qquad (11)$$

This equation provides the current on the radial transmission line once the constants A and B are determined. The next equation needed is the voltage from the generator on the radial transmission line. It is as follows at the inner radius (r_i):

$$V_g = -j\frac{R_g\sqrt{\varepsilon_r'-j\varepsilon_r''}}{\sqrt{\dfrac{\mu_o}{\varepsilon_o}}\dfrac{s}{2\pi r_i}}\left[AH_1^1\left(\omega\sqrt{\mu_o\varepsilon_o}\sqrt{\varepsilon_r'-j\varepsilon_r''}\,r_i\right)+BH_1^2\left(\omega\sqrt{\mu_o\varepsilon_o}\sqrt{\varepsilon_r'-j\varepsilon_r''}\,r_i\right)\right]$$

$$+\left[AH_0^1\left(\omega\sqrt{\mu_o\varepsilon_o}\sqrt{\varepsilon_r'-j\varepsilon_r''}\,r_i\right)+BH_o^2\left(\omega\sqrt{\mu_o\varepsilon_o}\sqrt{\varepsilon_r'-j\varepsilon_r''}\,r_i\right)\right] \qquad (12)$$

and at the outer radius or flange edge (r_o):

$$AH_0^1\left(\omega\sqrt{\mu_o\varepsilon_o}\sqrt{\varepsilon_r'-j\varepsilon_r''}\,r_0\right)+BH_o^2\left(\omega\sqrt{\mu_o\varepsilon_o}\sqrt{\varepsilon_r'-j\varepsilon_r''}\,r_0\right)=$$

$$-j\frac{Z_1\sqrt{\varepsilon_r'-j\varepsilon_r''}}{\sqrt{\dfrac{\mu_o}{\varepsilon_o}}\dfrac{s}{2\pi r_0}}\left[AH_1^1\left(\omega\sqrt{\mu_o\varepsilon_o}\sqrt{\varepsilon_r'-j\varepsilon_r''}\,r_0\right)+BH_1^2\left(\omega\sqrt{\mu_o\varepsilon_o}\sqrt{\varepsilon_r'-j\varepsilon_r''}\,r_0\right)\right] \qquad (13)$$

The result is two equations with two unknowns, where the argument is complex and the functions are transcendental.

The roots are in the form of the classic solutions. These solutions allow the breaking up of the Hankel function arguments into the form of a + jb, in order for numerical values to be determined for the Hankel functions. The, a and b derived above, equations are exactly like those for the cavity resonator [163]. The A and B constants, are determined, by solving the second voltage equation for A and then substituting its result into the first voltage equation, in order to solve for B. The A and B constants are now determined. The voltage and the current are now known anywhere along the radial transmission line. The result that is desired is a power calculation based on conservation of energy.

$$A = -B \frac{\left[(C) H_1^2 (\arg 1) + H_0^2 (\arg 1) \right]}{H_0^1 (\arg 1) + (C) H_1^1 (\arg 1)} \tag{14}$$

where

$$C = \frac{j Z_1 \sqrt{\varepsilon_r' - j\varepsilon_r''}}{\sqrt{\dfrac{\mu_0 s}{\varepsilon_0 2\pi r_0}}} \quad \text{and} \quad \arg 1 = \omega \sqrt{\mu_0 \varepsilon_0} \sqrt{\varepsilon_r' - j\varepsilon_r''} r_0 \tag{15}$$

$$B = \frac{V_g}{\left[(D) \left[\dfrac{\left[C H_1^2 (\arg) + H_0^2 (\arg) \right]}{H_0^1 (\arg) + H_1^1 (\arg)} \left(H_1^1 (\arg 2) \right) - H_1^2 (\arg 2) \right] + \left\{ H_0^2 (\arg 2) - \dfrac{\left[C H_1^2 (\arg) + H_0^2 (\arg) \right]}{H_0^1 (\arg) + H_1^1 (\arg)} \left(H_0^1 (\arg 2) \right) \right\} \right]} \tag{16}$$

where

$$\arg 2 = \omega \sqrt{\mu_0 \varepsilon_0} \sqrt{\varepsilon_r' - j\varepsilon_r''} r_i \quad \text{and} \quad D = j \frac{R_g \sqrt{\varepsilon_r' - j\varepsilon_r''}}{\sqrt{\dfrac{\mu_0 s}{\varepsilon_0 2\pi r_i}}} \tag{17}$$

$$1 = (D) \left[A_1 H_1^1 (\arg 2) + B_1 H_1^2 (\arg 2) \right] + \left[A_1 H_0^1 (\arg 2) + B_1 H_0^2 (\arg 2) \right] \tag{18}$$

where A_1 and B_1 all have V_g divided out resulting in the complex argument transcendental equation.

The transcendental equation, with Hankel functions of complex argument, results when A and B are substituted into the voltage and current equations. The normal solution to a transcendental equation can occur with minimal effort, but this equation has complex argument and is complicated for arriving at an acceptable solution. The Hankel functions can be replaced with the asymptotic expressions, but the result is again a transcendental equation, but with sinusoids, hyperbolics and exponentials in the overall resultant equations. The above equations can be modeled with appropriate numerical modeling codes such as Mathematica] which will be accomplished in another research effort.

The conservation of energy (power) is now addressed. The input power to the first port must equal the power that comes out of the second port, except for the power that is reflected back to the source, at port one. The difference is the power absorbed by the material being measured. This quantity can then be input into the determined power equation, based on the above derived voltage and current equations, and the complex dielectric constant will result as a solution. The power that is being dealt with here is complex power which has an amplitude and a phase angle.

The S_{11} and S_{21} that are measured with the network analyzer are used in the normalized (to 1.0) complex voltage format. This now allows the calculation of the power absorbed by the material because all of the required information is available in complex form.

$$P_{material} = P_{input} - P_{output} \tag{19}$$

$$P_{material} = \frac{1}{Z}\left\{\left[|V_+|^2\left(1-|S_{11}|^2 + S_{11} - S_{11}^*\right)\right] - S_{21}S_{21}^*\right\} \tag{20}$$

The calculated power in the material allows the use of the derived voltage and current equations. The prevention of blowing up, due to the feed discontinuity, in the equations is accomplished by looking at the volume ratio of the feed point versus the volume left in the radial transmission line. This is as follows:

$$\text{Volume ratio} = \frac{\pi r_{\text{feedpoint}}^2 d}{\pi r_{\text{flange}}^2 d - \pi r_{\text{feedpoint}}^2 d} \tag{21}$$

The volume ratio, for the dual coaxial probes in this research, is 0.004217 or 0.422%. This says that the feedpoint area can be eliminated from the calculations with almost no impact on the calculation of the complex dielectric constant.

3.0 Information for Models

The TportFor code is used in the forward problem solution as a reference for the measured S-parameter values. The reference S-parameter data is shown in figures 7 and 8 [31]. Data illustrates S_{11} and S_{21} for both the real and imaginary parts over the 2 to 18 GHz frequency range. This code solves the forward problem, whereby, complex dielectric constant is the input and the output is the S-parameters.

The formulation for TportFor exhibits the limitation that both the flanges and the material to be measured are infinite. This is approximately true for this measurement system due to the fact that the flanges used are finite. This requires a reformulation that should include the discontinuity of the flange edge and the edge of the material sample not at infinity. However, this analytical model can provide a comparison of the measured S-parameter data with the realization that the errors shown are actually worse than they really are due to the model limitations. This formulation works well at 2 GHz and below and the measured data are very close on all measurements.
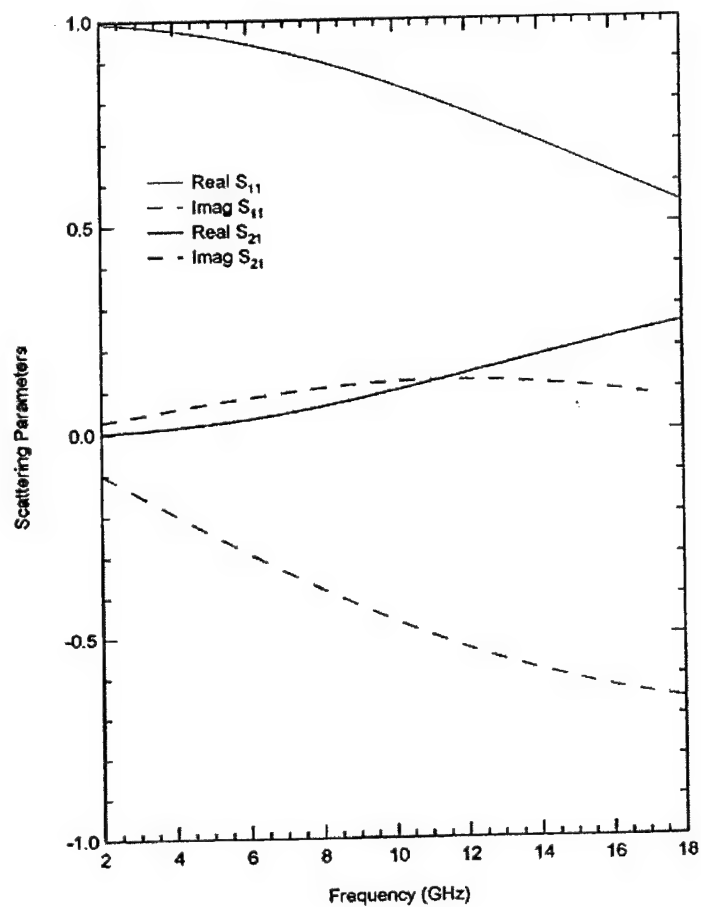
Figure 7. The Theoretical real and imaginary parts of S-parameters for 0.0625 inch thick Rexolite 1422.
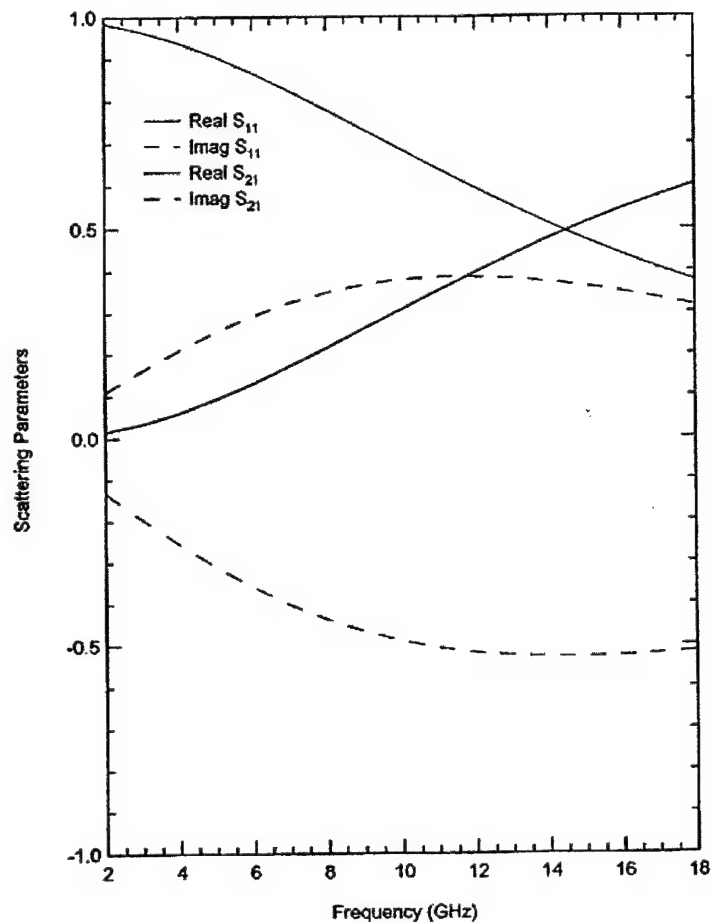
Figure 8. The Theoretical real and imaginary parts of S-parameters for 0.0165 inch thick Teflon.

The HFSS model is a finite element modeling code, where both the structure and the space between the structure and $\frac{1}{4}\lambda$ from the structure are meshed up in tetrahedrons. This calculation uses on the order of 28,000 tetrahedrons. The HFSS model is only used for air where the flange spacing is 0.25 inches. The complex magnitude of the electric field is plotted out. The poynting vector was also investigated and backed up the assumption that no power is radiated out of the dual coaxial probe assembly. Figures 9 and 10 illustrate the finite element models that were generated in order to produce the analytical results of this research.
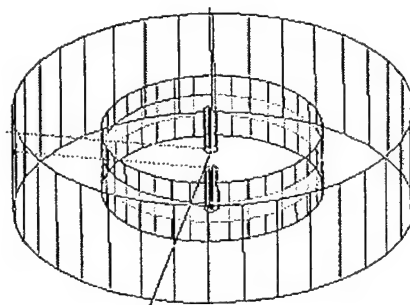
Figure 9. The Finite element model with material between the flanges with absorbing boundary encasing the model.
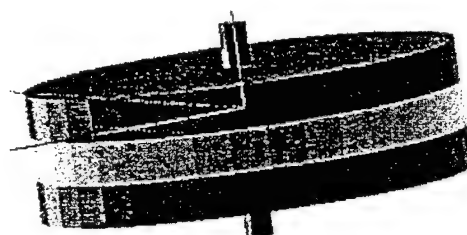
Figure 10. The Rendered finite element model with material between the flanges.

5.0 Full 2-port Measurement of Materials

The measurement technique used to obtain the material electrical parameters is a full 2-port measurement using the HP 8510C network analyzer. The technique uses dual coaxial probes that are calibrated to the probe faces. This necessitated the use of new calibration standards for short, open and load. The short consists of Brass and foil, the open is the probes facing air, and the load is a modified extension with either a sliding load or a broadband load. The sliding load is required for measurements above 2 GHz while the broadband load can be used below 2 GHz. The sliding load is used in all measurements providing the highest accuracy possible. These standards are implemented through a modification of the HP 8510C calibration coefficients [32]. The calibration is performed at the probe faces and the implemented standards required the offset open capacitances and offset short inductances to be set to zero. In standard calibrations using the HP 8510C deliverable calibration kit the capacitance of the open and the inductance of the short are input as functions of capacitance and inductance versus frequency.

The measurement implemented did not assume that the fringing capacitance at the probe face is zero for the open standard. The value used was determined to be zero based on a measurement of the open faced probe using a 1-port measurement. The resultant phase was constant and when the $C_{effective}$ was calculated, the value was approximately zero. The sliding load required a modification due to the short length of line added to insure calibration at the probe face.

The load was adjusted by the length of 0.71 inches which resulted in an additional load offset delay of 0.87173 nanoseconds. The load offset impedance was modified to a value of 48.64 ohms. The load offset loss was maintained at 1.3 gigaohms per second. Figure 11 shows the calibration standards that are implemented in the reported measurements of this research.
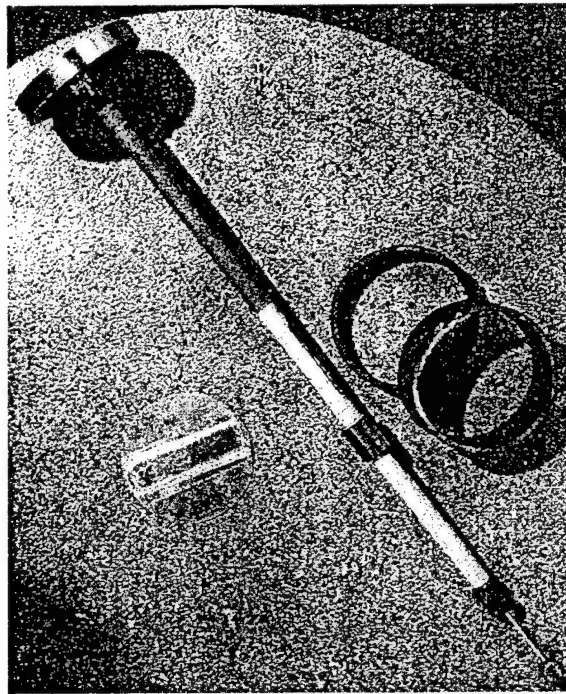
Figure 11. The Calibration standards used in this research.

Others have used port extension in the calibration process whereby the standards from the manufacturer can still be used. In this case, the Smith Chart display is invoked on the HP 8510C and then the delay function is activated. The delay is increased or decreased in order to move all the measurement frequency points to a dot on the real axis of the Smith Chart. In the case for using the sliding

load the focusing point is at the center of the Smith Chart. The open requires focusing of all points on the right side of the real axis while a short would focus on the left side of the real axis of the Smith Chart. The problem that occurs is a subjective decision as to where the points all focus on the real axis. Another researcher may come up with another point that then complicates calibration repeatability.

6.0 Coaxial Probes

The measurements were accomplished with readily constructed coaxial probes. These probes are made using available microwave connectors. The choice of connector depends on the frequency range over which the measurements are to be performed The measurements were performed over the 2 to 18 GHz frequency range and used the SMA connector. The flanges used are stainless steel and are flat to within 0.3 tenths of 1 mil. The probes were all polished in order to achieve this flatness tolerance. The dimensions of the probe used in the 2 to 18 GHz measurements have flange diameter = 2.49 inches, outer transmission line radius = 0.81 inches and Inner transmission line radius = 0.025 inches.

7.0 Calibration to Coaxial Probe Flanges

The measurement is developed as a nondestructive measurement. A method of collocation of the probe face center pins is required and could be, as shown with rings, infinite sheet extensions with co-locating pins on the perimeter. In order to negate air gap problems clamps were used to make sure the coaxial probes were flat against the material to be measured.

The first step that must be taken prior to any measurements is calibration of the system. In this case, the calibration was made at the coaxial probe flange faces where the material to be measured will be placed, as shown in figure 12. This includes any coaxial cable and adapter connections connected to the HP 8510C network analyzer. The calibration coefficients must be modified in order to reflect the newly developed standards. Once the modified calibration has been input into the analyzer then the full 2-port calibration can be started. The full 2-port calibration performs a forward as well as a reverse calibration. This is determined when asked to place open, short and sliding load on each port of the 2-port system. The sliding load is measured a minimum of six times with the load location adjusted to a different location in each load measurement. The short is performed with a brass sheet with pressure sensitive conductive tape in order to insure a complete short across the center pin to the flange on the probe face. This can be verified after the measurement by checking the conductive tape after completion of the short measurement. The open is the probes open to the air.
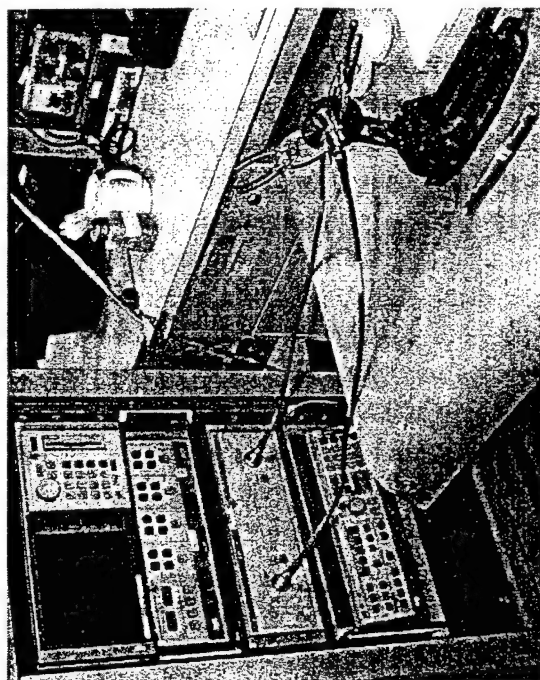
Figure 12. The HP 8510C. dual coaxial flanged probes, materials measurement test setup

The thru measurement is accomplished with the two probe faces pressed against each other. This measurement will show how flat the probes are by looking at the return loss (in dB) seen by each port of the measurement.

8.0 Comparison to Available Data

It was recognized very early in this effort that the practical operator, of this technique, in the field, is going to be looking at the network analyzer and that a lot of information can be gained from knowledge of the materials S-parameters. It was also recognized that typical purchased material is not specified with tolerances, on relative dielectric constant, less than $\pm 5\%$. Error plots in the S-parameters are presented in figures 13 through 15. Each figure plots the delta, in percent, between the measured and predicted values of the NIST TportFor code. This does not mean that the TportFor analytic code is taken as the correct. However, this comparison does provide a mean of bounding the practical use of this technique over thickness of material, frequency range of measurement and types of materials that are to be measured.

The Rexolite 1422 measurement comparison to measured data, shown in figure 13, exhibited $\leq 10\%$ error up to approximately 12 GHz. This is over two and one-half octaves. This material is typically used as a standard and with the extremely low loss tangent this measurement technique is stressed.

The Rexolite 1422 measurement comparison to measured data, shown in figure 14, exhibited $\leq 10\%$ error up to approximately 11.75 GHz. This is also

close to two and one-half octaves of useable measurement frequency range. This measurement did show some differences due to thickness as this material sample was one-quarter inch thick.

The Teflon comparison to measured data, shown in figure 15, exhibited $\leq$ 10% error up to approximately 11 GHz. This is the thinnest piece of Teflon measured, 0.0165 inch, where wild variations do appear above 11 GHz. The real and imaginary parts of S_{11} and S_{21} seem to be clustered around the 5% error line for approximately 90% of the 2 to 11 GHz frequency range. This technique appears to work for not only Rexolite, but also for Teflon.
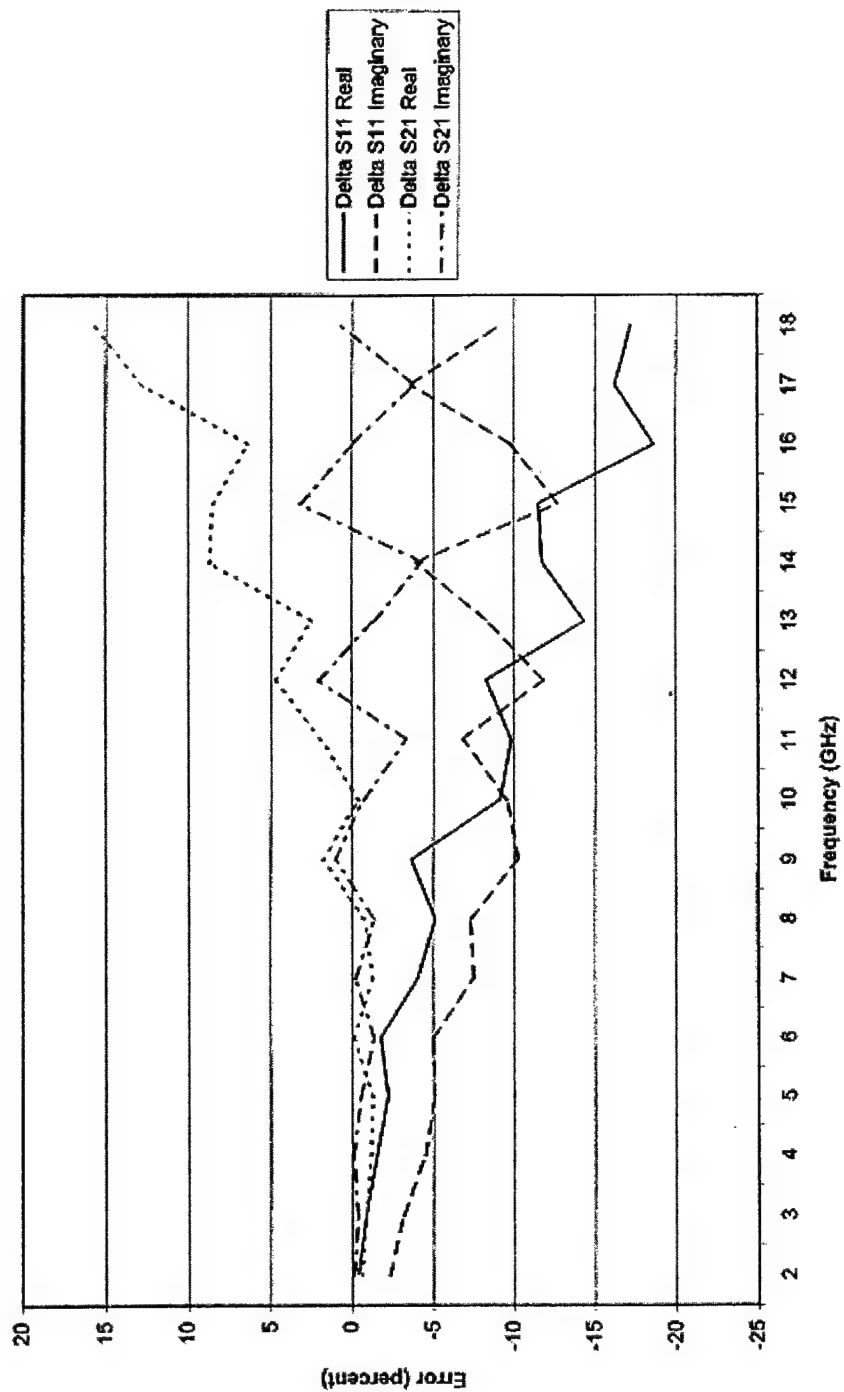
Figure 13. Error in percent for the comparison of NIST theory for S11 and S21 to measurements of S11 and S21 of 0.125 inch thick Rexolite 1422.

247
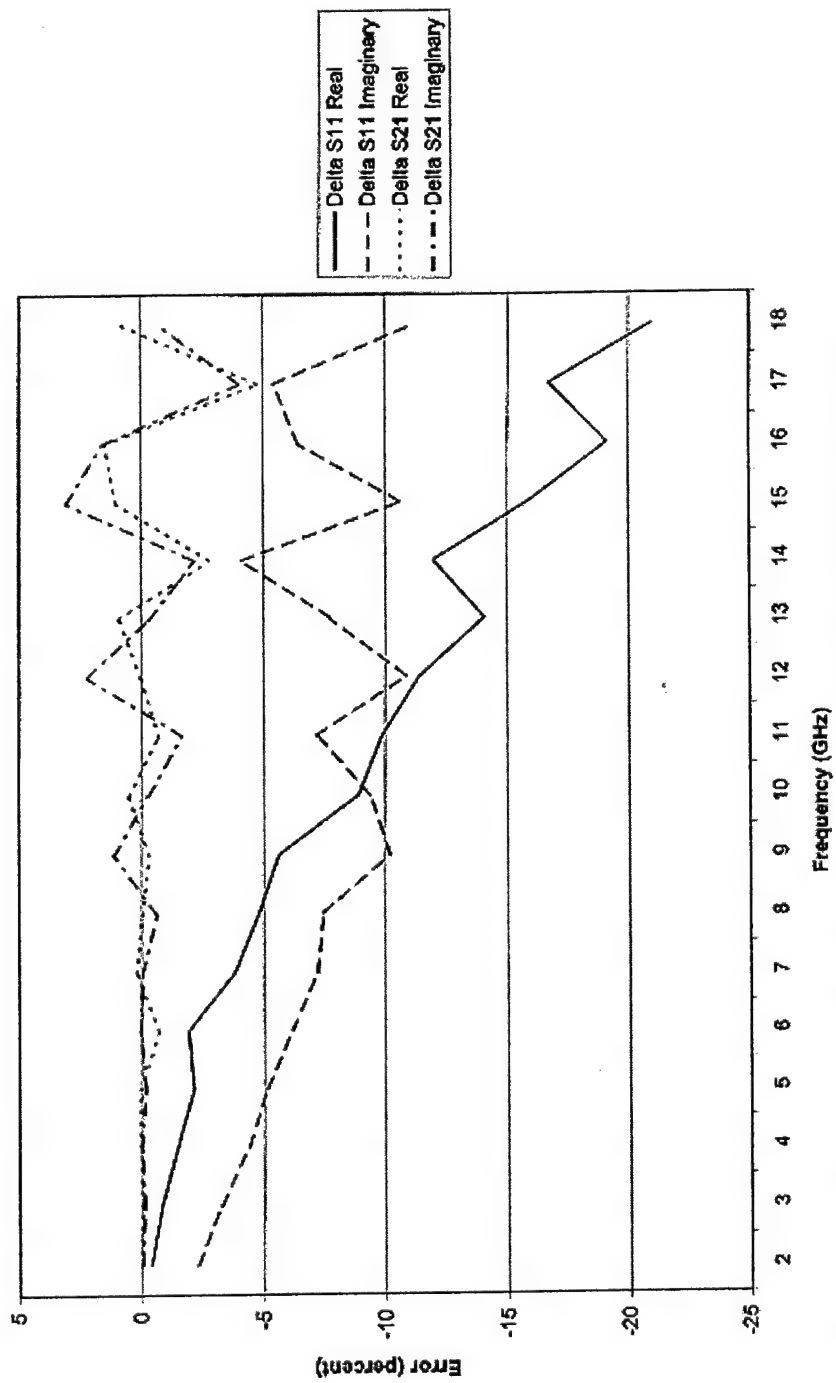
Figure 14. Error in percent for the comparison of NIST theory for S11 and S21 to measurements of S11 and S21 of 0.25 inch Thick Rexolite 1422.

248
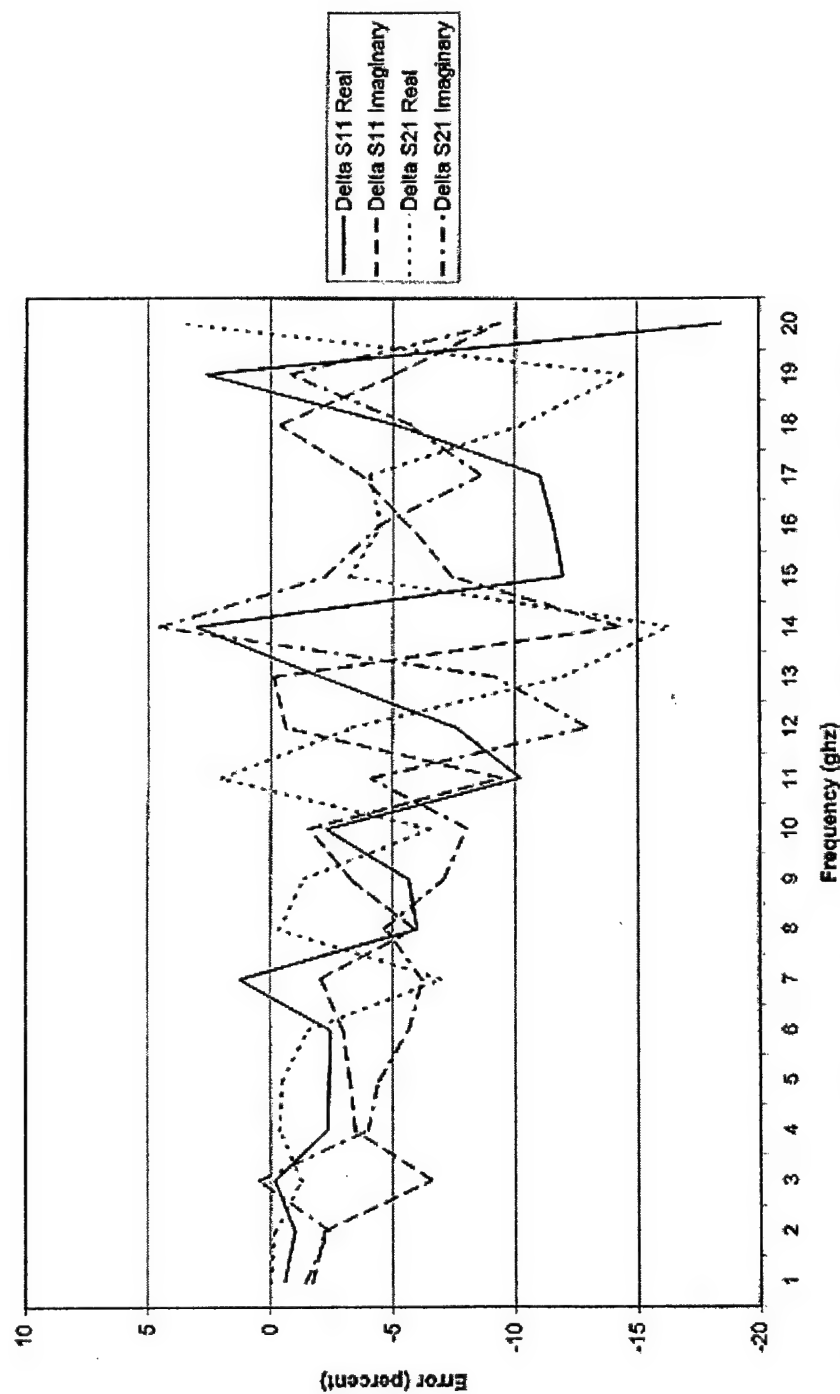
Figure 15. Error in percent for the comparison of NIST theory for S11 and S21 to measurements of S11 and S21 of 0.0165 inch thick teflon.

9.0 Limitations in Novel Measurement Technique

The limitations in this measurement technique must be balanced against the accuracy of the analytic codes, the models and the parameters input into the models when determining the error bounds. The variance of relative dielectric constant with frequency must be accounted for.

The practical limit of error allowance, of 10% maximum, is well within the constraints of what is presently available from material manufacturers. This is not the case if the manufacturer uses cavity measurements to determine the relative dielectric constant, but the limitation due to the cavity is over a limited (not octave) frequency range. This measurement technique does provide adequate measurement accuracy on relatively low loss materials over approximately two and one-half octaves. In fact it is strongly believed, that this measurement technique, with the developed readily made coaxial probes, can provide accurate measurements over the range of 45 MHz to 12 GHz using the correctly calibrated HP 8510C network analyzer. This is readily seen in all the data collected and the comparisons made since all the data was less than 1% error at 2 GHz.

The problem with high loss materials and the thin substrates is primarily air gap driven. It is known that 0.056 picofarad of capacitance can drive the value of the real part of S_{11} down by between 0.1 and 0.2. This in itself can cause at least 20% error in the measurement of the relative dielectric constant.

The coaxial probes are easily, cheaply, and readily made using available and appropriate frequency range connectors. Attention needs to be paid to the type of connector used versus the frequency band that the measurements are to be made. All waveguide have a lower cutoff frequency just as connectors have a maximum useable frequency. The probes developed are quite easy to change out connectors, on the order of 10 minutes. In order to perform cold measurements a real cryogenic connector should be used. The room temperature range can easily use available connectors as long as one checks probe flatness across the coaxial probe interface before every measurement.

The inaccurate measurement of the thin substrates is still of extreme value in terms of diagnostics. Making the material measurement over the 2 to 18 GHz frequency range provides the full 2-port data that can be inspected in order to determine which side of the substrate the thin film is located. This can be determined by looking at the reflection coefficient (Return Loss on the network analyzer). This can be determined both at room temperature and at other temperatures.

The dual flanged coaxial probes exhibit resonances, that do follow integer multiples, as seen in both measured and predicted data. The cavity method was modified for calculation of ε_r', for the inverse problem where sample thickness did not match the cavity size. The 0.25 inch thick Rexolite 1422 was well within

5% for ε_r', while air was with in 10% below 8.92 GHz. The 0.0165 inch thick Teflon sample was not within 10%, but exhibited a trend towards 10% as the frequency increased.

10.0 Conclusion

A method and procedure for calibrating to the coaxial flanged probes, over 2 to 18 GHz, using the full 2-port method has been generated. This method deletes the subjective delay based on wrapping around a point on the Smith chart, known as probe extension, for a short or open. This method is expandable over the entire useable frequency range of the network analyzer used for material measurements. The method does use the modified calibration data set [31].

A method and set of example, readily made coaxial probes have been described and used in the HP 8510C network analyzer testing environment. The developed probe technique uses commercially available off the shelf connectors that can cover the entire frequency measurement range of the network analyzer. The frequency measurement range of the probes is only limited by the operational frequency range of the type of connector installed in the coaxial probe flange.

A limitation, to the only dual coaxial probe analysis, known to date, was discovered. This discovery, impacts the calculation, for the forward problem, where the S-parameters are determined. The limitation was that the material boundary condition, between the flanges was set to infinity, as well as the probes. The practical use for this analysis uses finite flanges that require additional formulation for the discontinuity at the flange edges. This limitation implies that the measured data presented in this dissertation is closer to the theoretical than stated on the comparison data plots.

A finite element model was developed, using the High Frequency Circuit Simulator (HFSS) analytic code. Several problems were discovered in the materials and S-parameter calculations of this analytic code. The model generated worked over the full 2 to 18 GHz frequency range for the air material measurement between the dual coaxial probes. The model aided in the discovery of how the dual coaxial probes should really need to be modeled. The predicted data matched, within 20%, the location of the measured resonances in the measured data.

The comparison between the HFSS and the measured data provided the discovery of how the dual coaxial probe materials measurement technique is actually working. The measurement technique is actually behaving as a lossy resonator. Calculations do show that the material to free space edge acts like a total reflection point and behaves like a metallic wall of a cylindrical cavity. The

251

Research community to date, has not looked at this materials measurement technique as a cavity resonator.

The determination that the dual coaxial probe technique is actually a cavity resonator was verified with measured field probe data for the 0.25 inch thick air space measurement. The data is provided in the dissertation for the radial electric field from the feed point to the outer edge of the probe flanges. This data shows, with measured data, that the electric field is approximately zero at the outer flange edges. This supports the premise that the electric field is not radiated out of the coaxial flange assembly, but is reflected back into the coaxial assembly. This enables the assembly to act as a lossy cavity resonator with material walls by the impedance mismatch at the flange edges.

The measured data is compared to the TportFor analytic model with results illustrating the adequacy of the measurement technique for use from a minimum of 2 to 12 GHz for various thicknesses of Teflon and Rexolite, that is , low loss materials. The predicted versus measured S-parameters exhibit errors, in this frequency range, of less than 10%. All measured material results show that the measured data closely matches the low frequency end predicted data, suggesting that the analytic model is accurate at the lower frequencies. It also shows that the measured data is accurate at the lower frequencies as compared to TportFor S-parameter data.

A transmission line model was derived for this dual coaxial flanged probe assembly. The assembly approximates a radial line transmission line once it is recognized that only the electric field in the z-direction and the magnetic field in the axial direction exist due to the circumferential symmetry of the problem. The equations derived illustrate the complexity of the problem due to the need for Hankel functions of order 2 with complex arguments. The method follows power conservation, and knowing the input and output power of the probes, the power absorbed in the material can be calculated. This then allows the forward problem to be analyzed for the complex dielectric constant, but not easily.

11.0 References

[1]   A. M. Nicolson and G. F. Ross, "Measurements of the Intrinsic Properties of Materials by Time-Domain Techniques," IEEE Trans. Instrum. Meas., Vol. IM-19, No. 4, pp. 377-382, November, 1970.

[2]   W. B. Weir, "Automatic Measurement of Complex Dielectric Constant and Permeability at Microwave Frequencies," Proc. IEEE, Vol. 62, No. 1, pp. 33-36, January, 1974.

[3] J. Munk and A. Dominek, "Calibration of Automatic Network Analyzers," Report723224-1, ElectroScience Laboratory, The Ohio State University, September,1990.

[4] P. W. Stemp and I. J. Youngs, "Reproducibility, Traceability and Uncertainty of Dielectric Measurements Using Automated Vector Network Analysis," Seventh International Conference on Dielectric Materials, Measurements and Applications, Conf. Pub. No. 430, 23-26 pp. 1-3, September, 1996.

[5] J. Baker-Jarvis, and M. D, Janezic, "Analysis of a Two-Port Flanged Coaxial Holder for Shielding Effectiveness Dielectric Measurements of Thin Films and Thin Materials," IEEE Trans. Elect. Comp, Vol. 38, No. 1, pp. 66-70, February, 1996.

[6] A. Kraszewski, M. A. Stuchly, and S. S. Stuchly, "ANA Calibration Method for Measurements of Dielectric Properties," IEEE Trans. Instrum. Meas., Vol. IM-32, No. 2, pp. 385-387, June, 1983.

[7] T. W. Athey, M. A. Stuchly, and S. S. Stuchly, "Measurement of Radio Frequency Permittivity of Biological Tissues with an Open-Ended Coaxial Line: Part I," IEEE Trans. Microwave Theory Tech., Vol. MTT-30, No. 1, pp. 82-86, January, 1982.

[8] J. R. Mosig, J. E. Besson, M. Gex-Fabry, and F. E. Gardiol, "Reflection of an Open-Ended Coaxial Line and Application to Nondestructive Measurement of Materials," IEEE Trans. Instrum. Meas., Vol. IM-30, No. 1, pp. 46-51, March, 1981.

[9] N. E. Belhadj-Tahar, O. Dubrunfaut, and A. Fourrier-Lamer, "Broad-Band Microwave Characterization of a Tri-Layer Structure Using a Coaxial Discontinuity with Applications for Magnetic Liquids and Films," IEEE Trans. Microwave Theory Tech., Vol. 46, No. 12, pp. 2109-2116, December, 1998.

[10] S. O. Nelson and P. Bartley, Jr., "Open-Ended Coaxial-Line Permittivity Measurements on Pulverized Materials," IEEE Trans. Instrum. Meas., Vol. 47, No. 1, pp. 133-137, February, 1998.

[11] W. R. Humbert and W. R. Scott, "A New Technique for Measuring the Permittivity and Loss Tangent of Cylindrical Dielectric Rods," IEEE Microwave and Guided Wave Letters, Vol. 6, No. 7, pp. 262-264, July, 1996.

[12] Zulkifly Abbas, R. D. Pollard, and R. W. Kelsall, "A Rectangular Dielectric Waveguide Technique for Determination of Permittivity of

Materials at W-Band," IEEE Trans. Microwave Theory Tech., Vol. 46, No. 12, pp. 2011-2015, December, 1998.

[13] M. A. Stuchly, S. S. Stuchly, and G. Kantor, "Diathermy Applicators with Circular Aperture and Corrugated Flange," IEEE Trans. Microwave Theory Tech., Vol. MTT-28, No. 3, pp. 267-271, March, 1980.

[14] J. A. Berrie and A. K. Dominek, "Measurement of Electrical Parameters for Planar Materials," Report 720964-16, ElectroScience Laboratory, The Ohio State University, January, 1992.

[15] G. S. Smith and J. D. Nordgard, "Measurement of the Electrical Constitutive Parameters of Materials Using Antennas," IEEE Trans. Antennas Propagat., Vol. Ap-33, No. 7, pp. 783-792, July, 1985.

[16] L. S. Anderson, G. B. Gajda, and S. S. Stuchly, "Analysis of an Open-Ended Coaxial Line Sensor in Layered Dielectrics," IEEE Trans. Instrum. Meas., Vol. IM-35, No. 1, pp. 13-18, March, 1986.

[17] J. Ayer, "Measurement of Dielectric Constant at RF and Microwave Frequencies," RF Design, pp. 44-47, April, 1987.

[18] C. H. Durney, H. Massoudi, and M. F. Iskander, Radiofrequency Radiation Dosimetry Handbook, Fourth Edition, USAFSAM-TR-85-73, Brooks AirForce Base, October, 1986.

[19] D. Blackham, "Permittivity Measurements Using an Open-Ended Coaxial Probe," AMTA Workshop on Electromagnetic Characterization of Materials, Date, Paper 3-1.

[20] J. Baker-Jarvis, C. Jones, B. Riddle, M. Janezic, R. G. Geyer, J. H. Grosvenor, Jr., and C. M. Weil, "Dielectric and Magnetic Measurements: A Survey of Nondestructive, Quasi-Nondestructive, and Process-Control Techniques," Springer-Verlag, New York, Inc., pp. 117-136, 1995.

[21] D. Misra, M. Chabbra, B. R. Epstein, M. Mirotznik, and K. R. Foster, "Noninvasive Electrical Characterization of Materials at Microwave Frequencies Using an Open-Ended Coaxial Line: Test of an Improved Calibration Technique," IEEE Trans. Microwave Theory Tech., Vol. 38, No. 1, pp. 8-14, January, 1990.

[22] M. A. Stuchly, M. M. Brady, S. S. Stuchly, and G. Gajda, Equivalent Circuit of an Open-Ended Coaxial Line in a Lossy Dielectric," IEEE Trans. Instrum. Meas., Vol. IM-31, No. 2, pp. 116-119, June, 1982.

[23] B. G. Colpitts and J. S. Ployer, "Finite-Difference Time Domain Model of a Coaxial Probe," Symposium on Antenna Technology A. (ANTEM'94), Conf. Proc., Winnipeg, Canada, pp. 357-361, 1994.

[24] C. Gabriel, T. Y. A. Chan, and E. H. Grant, "Admittance Models for Open Ended Coaxial Probes and Their Place in Dielectric Spectroscopy," Phys. in Medicine and Biology, Vol. 39, pp. 2183-2200, 1994.

[25] T. Ando, "Determining Complex Permittivity by Measuring the Scattered Waveform from a Dielectric Circular Cylinder," IEEE Trans. Instrum. Meas., Vol. 38, No. 5, pp. 1012-1014, October, 1989.

[26] R. Afzalzadeh, "Dielectric Constant Measurement of Finite-Size Sheet at Microwave Frequencies by Psuedo-Brewster's Angle Method," IEEE Trans. Microwave Theory Tech., Vol. 46, No. 9, pp. 1307-1309, September, 1998.

[27] J. Baker-Jarvis, M. D. Janezic, P. D. Domich, and R. G. Geyer, "Analysis of an Open-Ended Coaxial Probe with Lift-Off for Nondestructive Testing," IEEE Trans. Instrum. Meas., Vol. 43, No. 5, pp. 711-718, October,.

[28] C. H. Riedel, M. B. Steer, M. R. Kay, J. S. Kasten, M. S. Basel, and R. Pomerleau, "Dielectric Characterization of Printed Circuit Board Substrates," IEEE Trans. Instrum. Meas., Vol. IM-39, No. 2, pp. 437-440, April, !990.

[29] S. Ramo and J. R. Whinnery, Fields and Waves in Communication Electronics, 2nd edition, John Wiley and Sons, NewYork, pp. 395-400, 1984.

[30] R. C. Collin, Field Theory of Guided Waves, 2nd Edition, IEEE Press, Piscataway, New Jersey, 1991.

[31] T. R. Holzheimer, Broadband Nondestructive Materials Measurements Using Readily Made Dual Coaxial Probes, Ph.D. Dissertation, University of Texas at Arlington, May, 2000.

[32] Network Analysis: Specifying Calibration Standards for the HP 8510 Network Analyzer, Product Note 8510-5A, February 1, 1998.

Bandwidth and Efficiency of Some Electrically Small Antennas

Paul E. Mayes and Paul W. Klock
Professors Emeritus, Electromagnetics Laboratory
Department of Electrical and Computer Engineering
University of Illinois, Urbana, IL 61801

Abstract: **The miniaturization of antennas always meets limitations on bandwidth and/or efficiency. However, there appears to be room for performance enhancement for antennas that are only moderately small in electrical size. The first self-resonance of a thin linear dipole occurs when the tip-to-tip length is approximately equal to one-half of the operating wavelength. Shorter dipoles can be made resonant by adding an inductor at the feed point. An alternative structure that also produces linearly polarized omnidirectional radiation is a biconical antenna. A cone defined by polar angle near ninety degrees has small vertical dimension, but resonates when the radius is approximately one-quarter wavelength. The radial dimension at (parallel) resonance can be reduced, without altering the pattern appreciably, by placing inductors around the periphery of the wide-angle cone.**

This paper discusses the published theoretical limits on the bandwidth performance of electrically small antennas and shows theoretical and experimental evaluation of the performance of some small dipole, monopole and wide-angle conical antennas.

1. Introduction

The dramatic reduction in size of electronic components in recent years has led to an increasing demand for smaller antennas. However, there are both theoretical and practical limitations to reducing antenna size to a small fraction of the operating wavelength. Within these limitations there is room for enhancing the performance of electrically small antennas.

The literature on electrically small antennas extends from about 1947 to the present. The classical works are by Wheeler [1,2] and Chu [3]. They introduce the concept of relating the bandwidth to the volume of a sphere that encloses the antenna. Taking the radius of the sphere to be a, the enclosed

antenna is said to be electrically small whenever $ka=2\pi a/\lambda<1$. Wheeler [4] suggested a measurement technique for efficiency that has been adopted by Newman, et al, [5] and widely used since. The theoretical results of Chu have been extended and simplified by succeeding authors, especially Collin/Rothschild [6], Hansen [7] and McLean [8]. The similarity between the impedance of an electrically small antenna and a resonant circuit have led to the extension of the concept of quality factor, Q. Hansen's review paper suggests that increases in bandwidth should be possible by making better use of the spherical volume, but his formula for Q (which has been used extensively by later authors) was shown by McLean to be in error, particularly for *ka* near unity.

The procedure for determining a lower bound on the Q of an electrically small antenna (introduced by Chu and later used by several other authors) examines the fields outside the spherical volume that contains the antenna. Various means have been used to separate the radiated power from the energy stored in the region outside the sphere. The minimum Q is given by

$$Q = \frac{2\omega W}{P_{rad}} \tag{1.1}$$

where ω is the radian frequency, W is the larger of the electric or magnetic stored energy, and P_{rad} is the radiated power. Putting expressions for stored energy and radiated power into this formula gives a lower bound on Q since the radiated power is independent of the size of the sphere and any energy stored inside the sphere can only increase the value of Q. A value of the minimum Q can be associated with each modal field, the lowest order (TM$_{01}$) mode being dominant in electrically small antennas. Hansen reduced Chu's result for the TM$_{01}$ mode to

$$Q_H = \frac{1+3k^2a^2}{k^3a^3(1+k^2a^2)} \tag{1.2}$$

However, McLean asserts that Hansen's equation should have the form

$$Q_M = \frac{1+2k^2a^2}{k^3a^3(1+k^2a^2)} \tag{1.3}$$

Collin and Rothschild replaced Chu's approximations with exact fields and found the minimum value of Q for the TM$_{01}$ mode to be given by

$$Q_{CR} = \frac{1}{k^3 a^3} + \frac{1}{ka} \qquad (1.4)$$

The same result was later derived by McLean in a more direct manner [9].

All of the plots of minimum Q shown in Figure 1 display a dramatic increase in Q for small values of ka. However, there is a region below the value of $ka = 1$ where the increase in Q with decreasing ka is relatively small. Utilization of antennas that fall in this region would seem to be possible with little deleterious effect.

Chu, and others after him, based his calculation of Q upon the similarity between the frequency dependence of the impedance of a small antenna near a (tuned) resonance and that of a series RLC circuit. For the circuit case, where the resistance is fixed and the inductive reactance is proportional to frequency, the Q is given by the ratio of inductive reactance at resonance to the resistance. The fractional bandwidth FBW (between half-power points) is the reciprocal of Q. At the half-power points of an antenna attached to matched load, the magnitude of the reflection coefficient is 0.707 and the SWR is 5.8. Although such a high value of SWR is not likely to be acceptable in many antenna systems, it has nevertheless become a widely used definition for band limits for electrically small antennas.

2. Theoretical determination of Q for short resonant dipoles

When the antenna input impedance is known, theoretically or experimentally, the FBW can be determined directly without invoking circuit approximations. For example, the input impedance Z_{in} of an electrically short dipole of length $2H < \lambda/4$ is approximately given by [10]

$$Z_{in} = 20k^2 H^2 - jZ_{0d} ctn(kH) \qquad (2.1)$$

where

$$Z_{0d} = 120(\ln \frac{2H}{d} - 1) = 60\Omega - 203.2 \qquad (2.2)$$

and d is the diameter of the dipole and $\Omega = 2\ ln(H/d)$ is the dipole thickness parameter [11]. For resonance, a series inductor may be added at the input. The expression for the impedance of the antenna and tuning inductor can be normalized to the resistance at resonance ($k = k_0$) and an algebraic approximation used for the transcendental function of small argument.

$$Z_{innor} = \left(\frac{kH}{k_0H}\right)^2 + j\frac{Z_{0d}}{20(k_0H)^3}\left(1 - \frac{k_0H}{kH}\right) \qquad (2.3)$$

Some simplifying definitions lead to a short expression for the normalized input impedance. Let $x = \dfrac{kH}{k_0H}, K = \dfrac{Z_{0d}}{20(k_0H)^3}$, then

$$Z_{innor} = x^2 + jK\left(\frac{x-1}{x}\right) = R_{innor} + jX_{innor} \qquad (2.4)$$

Writing the magnitude squared of the reflection coefficient $|\Gamma|^2$ in terms of the real and imaginary parts of the normalized input impedance leads to a polynomial equation that must be satisfied for a given degree of mismatch. When $|\Gamma|^2 = \dfrac{1}{2}$, the real roots (x_1, x_2) of

$$x^6 - 6x^4 + (1+K^2)x^2 - 2K^2x + K^2 = 0 \qquad (2.5)$$

define the half-power points for the case of a loaded (matched) antenna. Since the roots are proportional to frequency, the loaded FBW can be computed directly.

$$FBW = \frac{x_2 - x_1}{\sqrt{x_1 x_2}} \qquad (2.6)$$

The computation of loaded Q, wherein the power dissipated in the generator or load impedance is included, yields half the unloaded value. Thus, when the theoretical results for minimum Q are converted to maximum fractional bandwidth, the values of FBW for a matched antenna are twice those for an unloaded antenna. In Figure 2, values of unloaded Q computed for $\Omega = 8$ and $\Omega = 20$ have been added to the plot for minimum unloaded Q from Figure 1. This plot shows that, even for "fat" ($\Omega = 8$) dipoles, the Q is significantly greater than the theoretical minimum.

Some confidence in the theoretical results of Figure 2 has been established by making comparison with independent data. Figure 3 is a sketch of a physical monopole antenna that has been both analyzed and measured [??]. This antenna is self supported tower insulated from the ground and fed at its base. The tower is 91.44 meters in height but the transverse dimensions are unknown at this writing. The antenna has been analyzed across the 100 to 400 KHz band by V. Trainotti [??] using the WIPL code developed at Syracuse University [??]. His computed

259

values are plotted in Figure 4 along with the results from the theory of Section 2. The agreement with a linear antenna of $\Omega = 20$ are seen to be very good. The measured impedance of this antenna has been reported by C. Smith and E. Johnson. The values of Q obtained from their measurements are plotted in Figure 5 along with those computed for a lossless antenna and the theoretical minimum for a lossless antenna. The effect of the increasing ground loss at the lower frequencies is evident in the growing discrepancy between the values of Q obtained from the measurements and those that were computed for an antenna with no losses. This is corroborating evidence for the broadened bandwidths that result when losses are included in the determination.

3. Efficiency and bandwidth

For a meaningful comparison of bandwidths of various electrically small antennas, it is necessary to have reasonably accurate values for the efficiency of each antenna. The effect of antenna losses upon the Q of the antenna is easy to obtain. For a lossless antenna

$$Q_1 = \frac{2\omega W}{P_{rad}}$$

(3.1)

where P_{rad} is the power radiated. For a lossy antenna

$$Q_2 = \frac{2\omega W}{P_{rad} + P_{loss}}$$

(3.2)

where P_{loss} is the power dissipated in the antenna. Hence, the efficiency, e, is given by

$$e = \frac{P_{rad}}{P_{rad} + P_{loss}} = \frac{Q_2}{Q_1} = \frac{FBW_1}{FBW_2}$$

(3.2)

Since the power dissipated in the generator or load impedance is included, the computation of loaded Q yields half the unloaded value. Thus, when the theoretical results for minimum Q are converted to maximum fractional bandwidth, the values of FBW for a matched antenna are twice those for an

260

unloaded antenna. Since the condition $|\Gamma|^2 = 1/2$ implies a matched source, the values of loaded Q are plotted for small antennas in Figure 2.

Two moment method codes have been used for the computations in this paper. The first code is the Finite Element Radiation Model (FERM) developed at the Lincoln Laboratories of Massachusetts Institute of Technology [12]. However, it was discovered that FERM had limited capability to handle patch geometries with wide variations in patch sizes. While this was no problem with simple antennas, such as the blade dipole, it proved to restrict the accuracy with which detailed geometry of feed regions could be modeled in more complex antennas. A new code (LFMOM) was recently developed by W. C. Chew and J. Zhao at the Center for Computational Electromagnetics, Electromagnetics Laboratory, University of Illinois at Urbana-Champaign [13]. This new code extended the range of available basis functions from the conventional RWG (Rao, Wilton, Glisson) [14] to the loop-tree [15]. This feature of the new code makes it possible to use a very wide range of patch sizes in the analysis of antennas, even electrically small ones. The procedure utilizes the capability of extensions of FERM to generate files that describe the physical structure of an antenna. These files are then converted to input files for the Low-Frequency Method of Moments (LFMOM) code which provides fast methods for solution of the MoM integral equation.

Two procedures have been used to compute the approximate efficiency. In one, the input impedance is first calculated for a lossless antenna in order to find the radiation resistance. Then, loss is added to the antenna and the input impedance is recalculated. The efficiency is obtained from

$$e = \frac{P_{r1}}{P_{in2}} = \frac{I_{in1}^2 R_r}{I_{in2}^2 (R_r + R_{loss})} \approx \frac{R_r}{R_{in}}$$

where I_{in1} is the input current for the lossless case and I_{in2} is the input current when losses are present. To the degree that the addition of losses changes the input current only slightly, these two input currents will be approximately equal. The assumption inherent in this procedure is that the current distribution is not affected by the difference in the impedances of the lossless and lossy cases.

The second procedure has been incorporated into the LFMOM code and gives the efficiency at each frequency considered by the code. The approximations involved include: the usual ones associated with replacing the integral equation with a set of linear equations, the computation of far-zone fields

from a discretized representation of the antenna current, the numerical integration of the far-zone fields to find the power radiated. The efficiency is obtained from

$$e = \frac{power\ radiated}{power\ delivered} = \frac{\oiint_\Sigma P_d dS}{P_{in}}$$

where P_d is the power density on the closed surface Σ in the far zone.

4. Example: a short blade dipole

To serve as a benchmark for other electrically small antennas, the FBW and efficiency have been computed for some small blade dipole antennas. Figure 6 shows the patch geometry used in the analysis of a base-loaded blade dipole. The dipole was positioned with its axis coincident with the z-axis of a Cartesian coordinate system. Twenty subsections were used along the length, between $z=-H$ and $z=+H$. The blade was located in the xz-plane between $x=-w/2$ and $x=+w/2$. Only one subsection was used in x. The dipole was excited by a delta-gap generator located at $z=0$. Lumped inductors at the feedpoint were simulated by specifying a surface impedance for the patches adjacent to the source.

Figure 7 shows the real and (absolute value of) the imaginary parts of the input impedance of a 14.6-cm long dipole that is base-loaded to achieve resonance at 400 MHz ($\lambda = 75$ cm). The value of ka for this antenna is 0.61, moderately small electrically. The unloaded FBW from Figure 7 is seen to be

$$FBW = \frac{403.4 - 397.0}{\sqrt{(403.4)(397.0)}} = 0.016$$

In any practical situation losses will be present in the antenna and in the tuning inductor. The effect of loss in the inductor are illustrated by the computed results of Figure 8. The ratio of reactance to resistance of the inductor (quality factor, Q) was chosen to be equal to 100 at the resonant frequency of 400 MHz. From the computed input resistance and reactance shown in Figure 8 it is seen that the unloaded *FBW* is increased to 0.024.

Figure 9 illustrates that the results from the two methods for computing the efficiency of the blade dipole are in good agreement. Note that the ratio of FBW_1, for the lossless case, and FBW_2, for the lossy case, is 0.625, also in fair agreement with the data of Figure 9. Also shown in Figure 10 is the efficiency

computed using LFMOM after adding copper loss to the blade dipole. It is apparent that the tuning inductor is dominant in determining the efficiency.

Assessment of the change in performance of the short blade dipole with frequency is facilitated with the LFMOM code. The directive gain (DG) is computed by integrating the far-zone power density. The power gain (PG) is computed by comparing the power radiated to the input power. The working gain (WG) is computed by finding the mismatch loss from the solution for the input impedance. These quantities are plotted for the short blade dipole (with no copper loss) in Figure 11. Since the pattern of the short antenna changes very little with frequency, the directive gain is essentially constant over the small band near resonance. The change in efficiency from 0.64 to about 0.666 makes very little difference in the power gain over the same band. Hence, the frequency dependence in the performance of this small antenna is almost all caused by the variation in the input impedance. Note that limiting this variation to 3 dB produces band limits in Figure 11 of 391 and 410 MHz, a FBW of 0.47, corresponding to the loaded case, approximately twice that of the unloaded case with efficiency of 0.65.

6. Another example: wide-angle conical radiating resonator

Some applications requiring vertically polarized omnidirectional radiation also have restrictions on height. The wide-angle conical radiating resonator (CRR) [16] has been studied as a low-profile alternative to shortened dipoles or monopoles. The vertical height of a CRR is adjustable to quite low values by choosing the polar angle of the cone(s) to be near ninety degrees. The height, as well as the radius, is also reduced by using inductive loading between the rims of the cones that form the upper and lower walls of the resonator. Inductive loads spaced at ninety-degree intervals have been found to adequately preserve the omnidirectional characteristic of the radiation.

Figure 12 is a side view of an edge-loaded wide-angle CRR as represented for moment method analysis. This model uses planar triangular patches to approximate all conducting surfaces of the antenna. The edge inductors are simulated by patches with a specified surface impedance. The real part of the surface impedance can be adjusted to represent the loss in a coil with a specific value of Q. The resonator is excited by a ring of delta-gap voltage sources which encircles the mid-plane of a central polygonal conducting column. The radius of this feed column is meant to correspond to the dimension of the center conductor of a coaxial cable that would be used to excite a physical antenna. Accurate modeling of the feed proved to be impossible with FERM and led to the

263

development of the LFMOM code for antennas.

Computed results for a CRR with polar angle of 80 degrees and radius of 7.3 cm are shown in Figure 13. The resonator is terminated with four strips having surface reactance of 7.9 ohm/sq at 100 MHz, which translates into an inductance of approximately 12 nH.. In the results of Figure 13, no losses are considered. Since the lowest frequency of resonance for the CRR resembles that of a parallel RLC circuit (inductive below resonance; capacitive above), the computed results are shown as conductance and susceptance versus frequency. As before, the intersections of the conductance and absolute susceptance curves define the half-power points. Although there is some uncertainty caused by the numerical noise in the susceptance plot, the band limits can be estimated rather accurately and the FBW is approximately 0.0033. The plot labeled "DGNOR" was obtained by doubling the values of normalized conductance. This provides means for approximating the loaded FBW in the same manner as for the unloaded FBW.

The computations were repeated for terminations with $Q=100$ at 400 MHz. This choice leads to a value of 0.316 ohms for the resistance of the inductors. Figure 14 shows the values of normalized conductance and absolute susceptance as computed with LFMOM. The fractional bandwidth of the unloaded antenna is now equal to 0.0085. Based upon the results shown in Figures 13 and 14, the efficiency of the CRR would be 0.388. The efficiencies computed with LFMOM for the cases where lossy inductors ($Q = 100$ at 400 MHz) are added to a perfect conducting CRR and to a copper CRR are shown in Figure 15. The efficiency at 400 MHz is found to be 0.377 with pec and 0.363 with copper.

7. Comparison on the basis of equal height

The comparison of antennas of equal radian spheres is somewhat academic. In practice, an antenna is rarely allocated the space of a spherical volume. Likely, there will be reasons (economic, aerodynamic, esthetic, camouflage, or other) to constrain the shape of the designated space to be quite different from a sphere. Hence, there are pragmatic reasons to compare the performance of wide-angle CRR's to other antennas having low profile.

The 80-degree cone of radius 7.3 cm considered above has a maximum height (at the rim of the cone) of 1.29 cm. A dipole with half-length of 1.29 cm ($kH=0.11$) would require a high value of inductance to tune to 400 MHz. The reduced radiation resistance and increased losses in the base coil would greatly affect the efficiency. Repeating the analysis of Section 3, maintaining the height-to-width ratio of 7.3, it was determined that a base inductor of approximately 1

μH would be required. Using this value as a starting point, repeated analysis with LFMOM found that an inductance of 1.018 μH produced resonance at 400 MHz. Figure 16 shows the input impedance of the tuned dipole without losses as computed with LFMOM. The FBW determined from this figure is 0.0001, a value of Q equal to 10,000. The value of Ω for this antenna is 5.36. If this data point is compared to Figure 2, it falls between the curves for $\Omega = 8$ and $\Omega = 20$, illustrating the sensitivity to error of computations in this area of the plot.

When the above computations are repeated, first with a lossy inductor, with a Q of 100 at 400 MHz, and then with copper loss added, the resulting efficiencies are both 0.0436. Comparing all of these data to those for the conical radiating resonator of Section 6, the CRR shows superiority in all cases. Although the argument can be made that a vertical monopole is simpler than a CRR, it is debatable whether the CRR requires more horizontal space when the ground screen for the monopole is taken into account.

8. Multiple resonators

When the bandwidth obtained within a height restriction is not adequate, techniques for increasing the bandwidth without unduly increasing the height are desirable. A possible procedure involving nested CRR's connected in series has been previously suggested [13]. Figure 17 shows the patch model of two such resonators. Either the impedance bandwidth or the degree of mismatch of such a structure can be adjusted by controlling the separation between the resonances of the two resonators. Figure 18 shows a Smith chart plot of the input impedances calculated for a given structure with various external (series) inductors. The loci are approximately circles that can be approximately centered on the Smith chart by adding an ideal tranformer. For example, adding a lossless 5.57 nH inductor and a 0.235:1 transformer produces the impedance locus of Figure 19. Allowing the transformed locus to essentially coincide with the $|\Gamma| = 0.707$ circle on the chart gives the largest attainable half-power bandwidth.

Two aspects of the performance of this antenna require further study. The position of the circular impedance locus on the chart is greatly influenced by the details of the feed region. Essential to evaluation of the overall performance of any electrically small antenna is accurate data for the efficiency. The tools for performing these studies are now available in the LFMOM code. Figure 20 indicates for the example of Figures 18 and 19, it is the efficiency, not impedance match, which limits the useful bandwidth

10. Conclusions and future plans

Several techniques for evaluating the impedance bandwidth and efficiency of electrically small antennas have been shown to be in good agreement. The efficacy of a new code, LFMOM, has been shown, particularly in treating the details in the small region around the feed point of electrically small antennas. Preliminary results from applying LFMOM to edge-loaded conical radiating resonator (CRR) antennas have been presented. The results from LFMOM continue to validate the capability of extending the impedance bandwidth of CRR antennas by using multiple resonators. More complete study of the effect of varying the numerous parameters of these antennas is needed and is currently underway.

11. Acknowledgement

12. References

[1] H. A. Wheeler, "Fundamental Limitationsof Small Antennas", Proc. IRE, vol. 35, pp. 1479-1486, December 1947.

[2] H. A. Wheeler, "Small Antennas", IEEE Trans. Ant. Propagat., vol. AP-23, pp. 462-469, July 1975.

[3] L. J. Chu, "Physical Limitations of Omni-Directional Antennas", Jour. Apl. Phys., vol. 19, pp. 1163-1175, December 1948.

[4] H. A. Wheeler, "The Radiansphere Around a Small Antenna", Proc.IRE, vol. 47, pp. 1325-1331, August 1959.

[5] E. H. Newman, P. Bohley and C. H. Walter, "Two Methods for the Measurement of Antenna Efficiency", IEEE Trans. Ant. Propagat., vol. AP-23, pp. 457-461, July 1975.

[6] R. E. Collin and S. Rothschild, "Evaluation of Antenna Q", IEEE Trans. Ant. Propagat., vol. AP-12, pp.23-27, January 1964.

[7] R. C. Hansen, "Fundamental Limitations in Antennas", Proc. IEEE, vol. 69, pp. 170-182, February 1981.

[8] J. McLean, "A re-examination of the fundamental limits on the radiation Q of electrically small antennas", IEEE Trans. Ant. Propagat., vol. AP-44, pp. 672-676, May 1996.

[9] E. C. Jordan and K. G. Balmain, Electromagnetic Waves and Radiating Systems, p. 387, Englewood Cliffs, New Jersey, 1968.

[10] S. Lee, D. A. Shnidman and F. A. Lichauco, "Numerical modeling of RCS and antenna problems", Tech. Rep. No. 785, Lincoln Laboratory, Massachusetts Institute of Technology, December 1987.

[11] J.-S. Zhao, W. C. Chew and P. E. Mayes, "Accurate Analysis of Electrically Small Conical Antennas by Using the Low-Frequency Method", Proc. Antenna Applications Symposium, Allerton Park, Illinois, October 2001.

[12] S. M. Rao, D. R. Wilton and A. W. Glisson, "Electrolmagnetic Scattering by Surfaces of Arbitrary Shape", IEEE Trans. Ant. Propagat.,vol. AP30, pp. 409-418, May 1982.

[13] P. E. Mayes and W. Gee, "Using Multiple Resonant Radiators for Increasing the Impedance Bandwidth of Electrically Small Antennas", *Proc. 24th Annual Antenna Applications Symposium,* Allerton Park, Illinois, September 2000.

Comparison of Collin-Rothschild (QCR), Hansen (QH) and MacLean (QM)
Formulas for the Minimum Q of Antennas Radiating the TM01 Mode
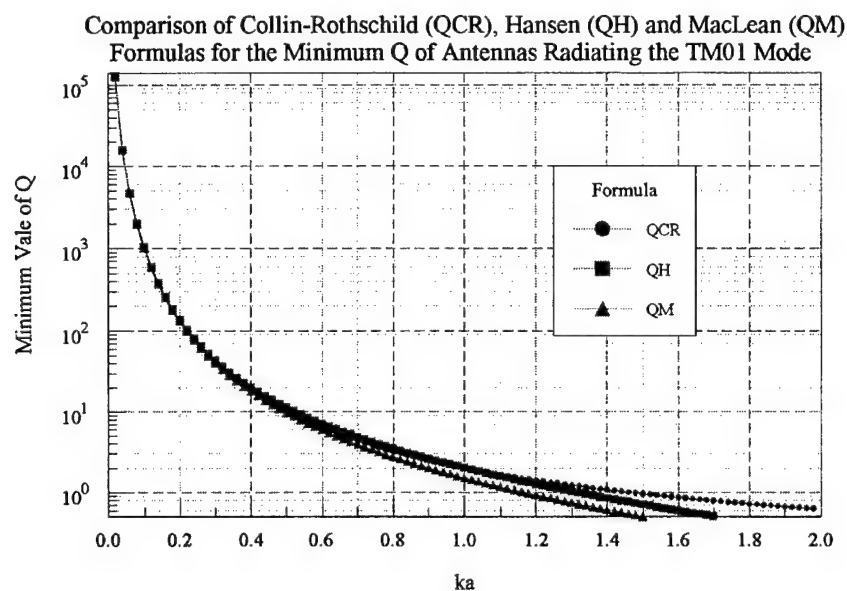
Figure 1. Plots of minimum Q values versus *ka* for antennas radiating the TM$_{01}$ mode, computed from three different formulas.

QCRM - Collin/Rothschild/McLean formula for minimum Q
Q8U - Computed unloaded Q, short dipole, omega=8
Q20U - Computed unloaded Q, short dipole, omega=20
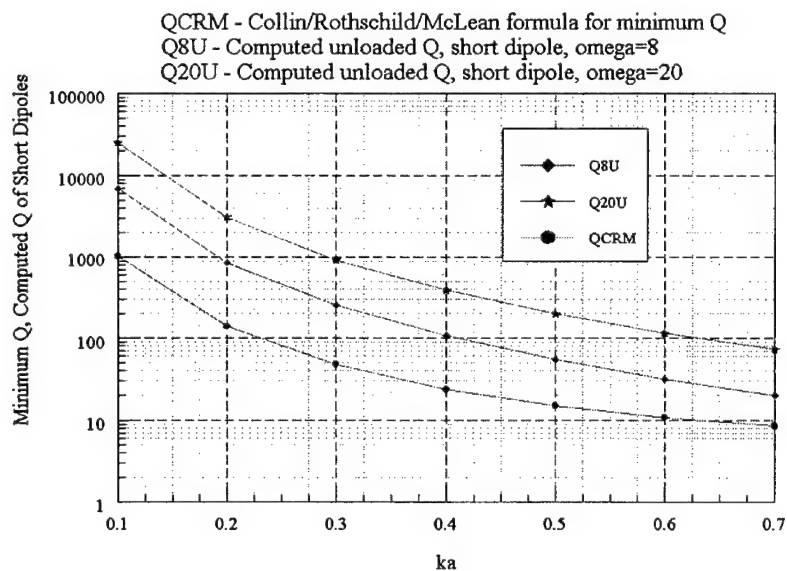
Figure 2. Values of unloaded *Q* for short dipoles (Ω = 8 and 20) compared with the values computed for the minimum unloaded *Q* as a function of antenna size.

268
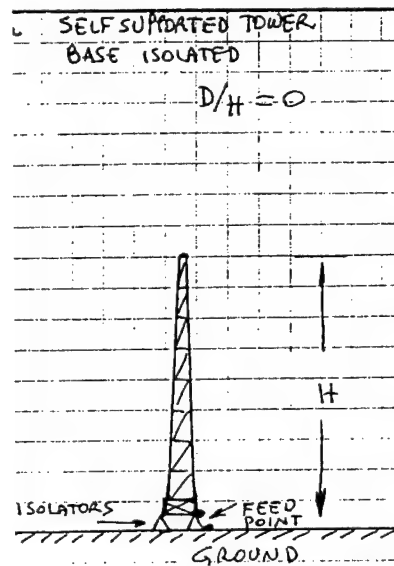
Figure 3. Sketch of short broadcast monopole of type used for the measurements and computations of Figures 4 and 5. The value of Ω for this antenna is unknown.
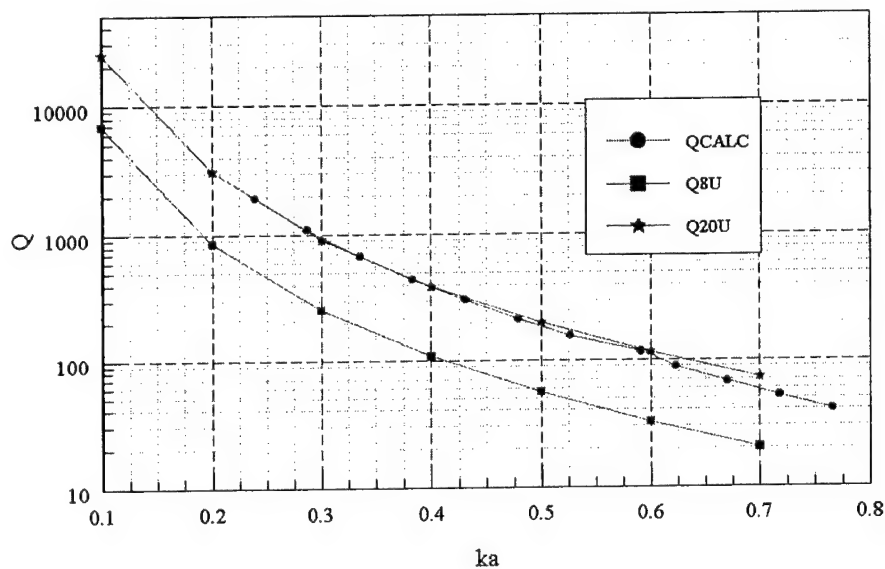
Figure 4. Comparison of the values of Q computed for the antenna of Figure 3 with the WIPL code* and those computed from Equation (1.10) for $\Omega = 8$ and 20. *Kolundzija, Ognjanovic, Sarkar and Harrington, Syracuse University (V. Trainotti, private communication).
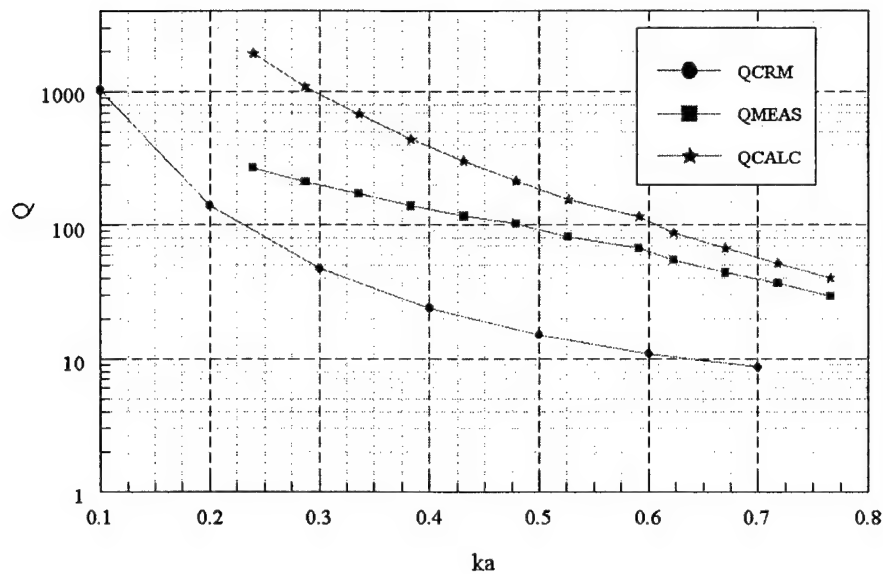
Figure 5. Comparison of the values of Q measured* and calculated** for the antenna of Figure 3 and the minimum unloaded Q as given by Equation (1.4). *C. Smith and E. Johnson, PIRE, Oct. 1947. **V. Trainotti, private communication.
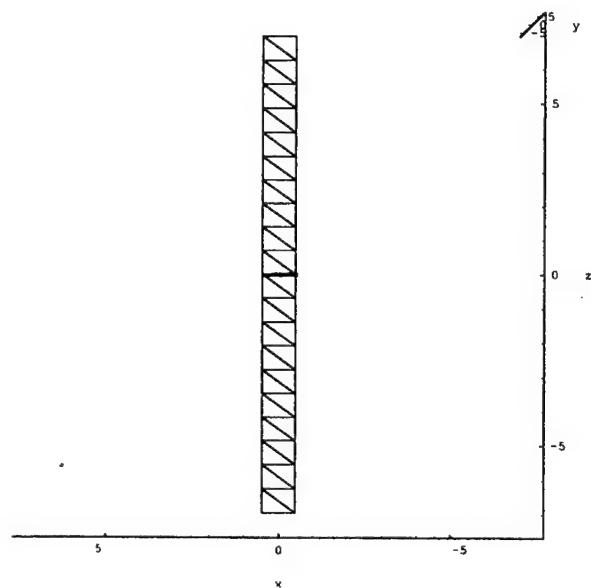
Figure 6. Patch geometry for analysis of a blade dipole by the method of moments.

270

Base-Loaded Blade Dipole, Half Length (H)=7.3cm, Width=1 cm
Inductive Load, Rsurf=0.0, Xsurf=78 ohms/sq (100 MHz), L=180 nH
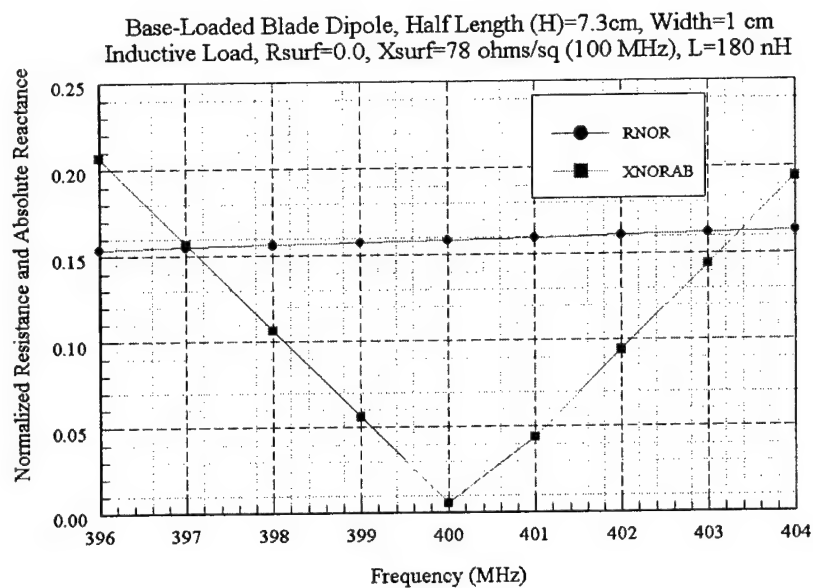
Figure 7. Normalized resistance (RNOR) and absolute value of normalized reactance (XNORAB) computed for a lossless blade dipole using LFMOM code. The short (*ka=0.61*) dipole is tuned to 400 MHz with a base inductor of 180 nH. The unloaded FWB is 0.016.

Inductive Load, Rsurf=3.12, Xsurf=78 ohms/sq (100 MHz), L=180 nH
Q=100 @ 400 MHz
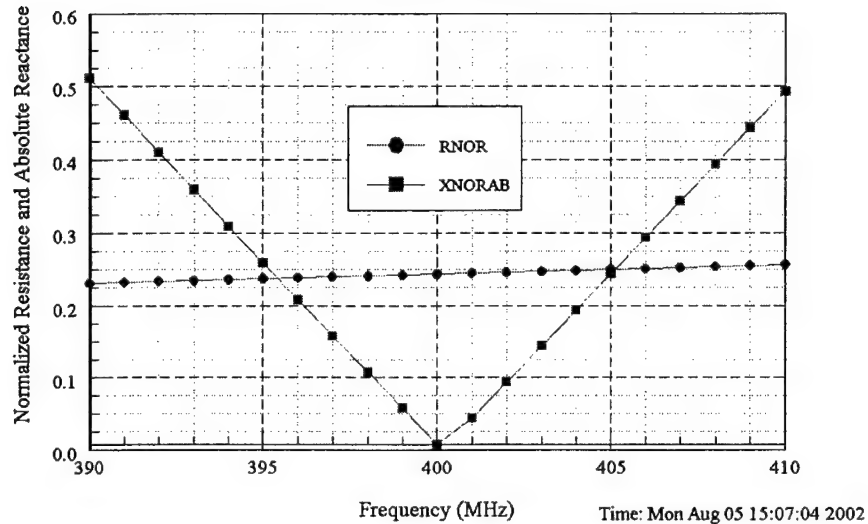
Figure 8. Normalized resistance (RNOR) and absolute value of normalized reactance (XNORAB) computed for a base-loaded blade dipole using LFMOM code. The short (*ka=0.61*) dipole is tuned to 400 MHz with a base inductor of 180 nH having Q = 100 at 400 MHz. The unloaded FWB is 0.024.

Base-Loaded Blade Dipole, Half-Length (H)=7.3 cm, Width= 1 cm
Inductive Load, Rsurf=0 (Case 1), = 3.12 (Case 2), Xsurf=78 ohms/sq (100 MHz)
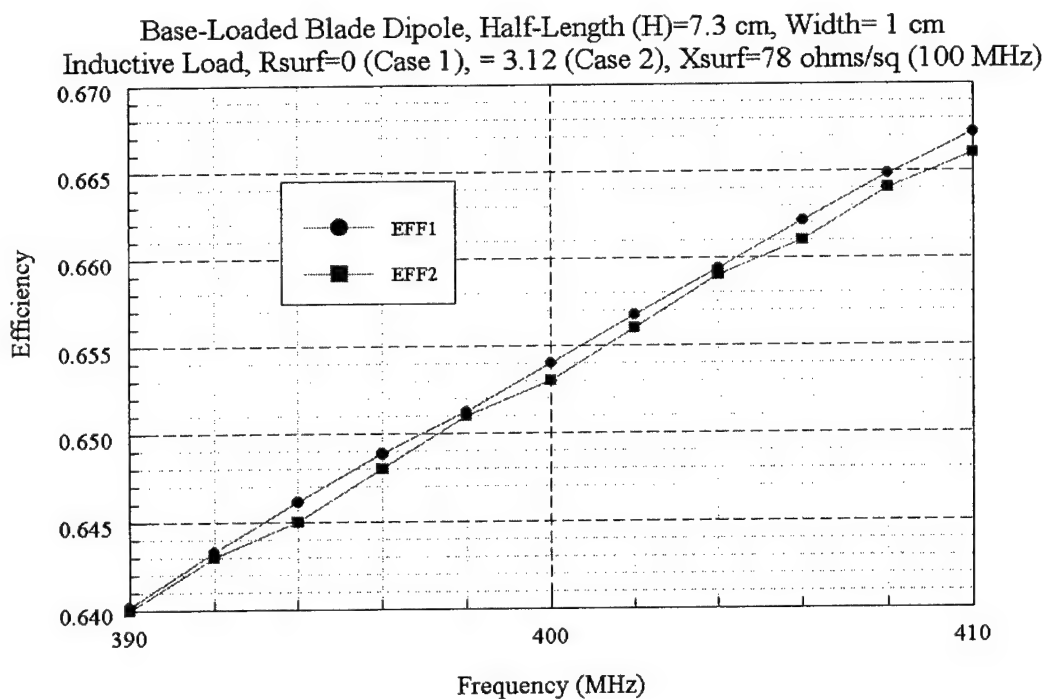
Figure 9. Efficiency computed for a base-loaded blade dipole using LFMOM code in two ways. The short (*ka=0.61*) dipole is tuned to 400 MHz with a base inductor of 180 nH having *Q* = 100 at 400 MHz. EFF1 is computed using Equation (1.15); EFF2, with Equation (1.16).

Base-Loaded Blade Dipole, Half-Length (H)=7.3 cm, Width= 1 cm
Inductive Load, Rsurf=3.12, Xsurf=78 ohms/sq (100 MHz), Rscu=0.0053 ohms
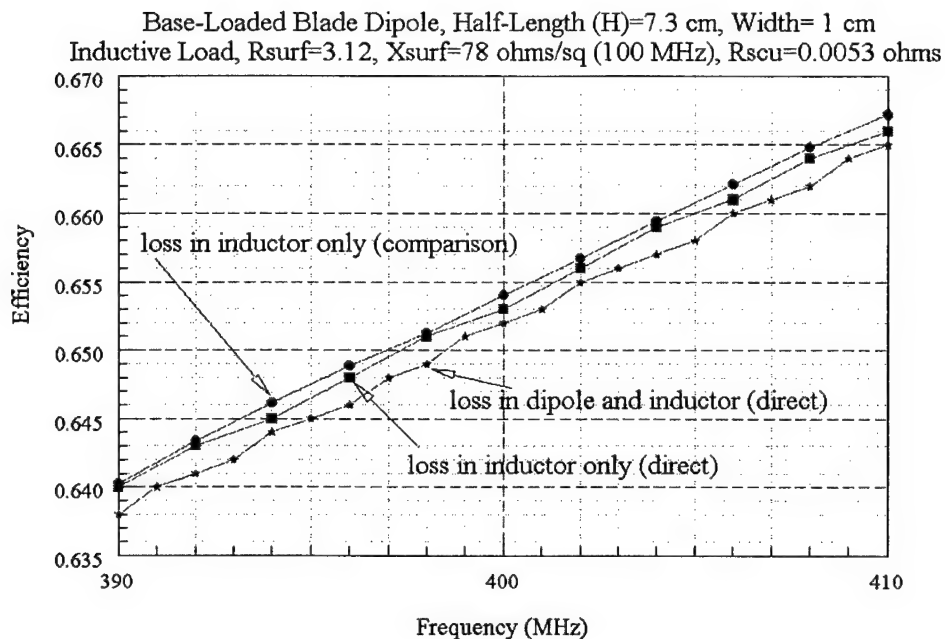
Figure 10. The results from computing the efficiency of a base-loaded dipole antenna. In the upper curves the loss was confined to the inductor. In one case the loss was computed by comparing data for lossless and lossy cases. The center curve gives the results obtained directly from the LFMOM code. In the lower curve the loss in the copper conductor of the antenna was included.

274
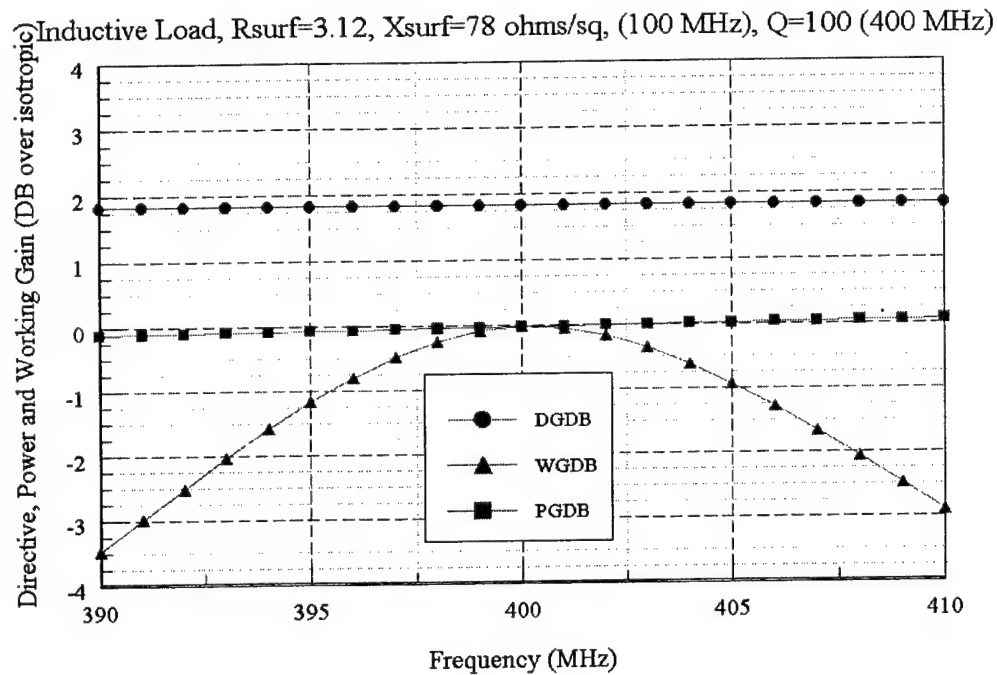
Figure 11. Directive (DGDB), power (PGDB), and working (WGDB) gains computed for a base-loaded blade dipole using LFMOM code. The short (*ka=0.61*) dipole is tuned to 400 MHz with a base inductor of 180 nH having $Q = 100$ at 400 MHz. Note that the loaded FWB determined by the 3-dB decrease from maximum of the working gain is (410 – 391)/400 = 0.047.
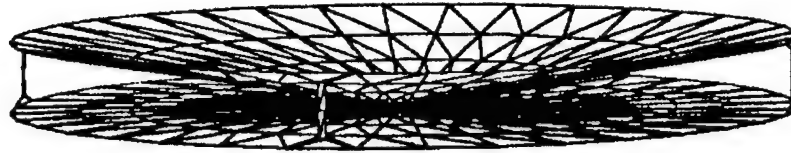
Figure 12. Single conical radiating resonator with inductive surface impedances on narrow strips connected around the periphery. Sketch shows the boundaries of patches used in the moment method analysis.

Single Conical Resonator, Theta1=90, Theta2=80 deg, Radii: Outer=7.3, Inner=0.0635 cm
Four Inductive Loads, Rsurf=0, Xsurf=7.9 ohms/sq (100 MHz)
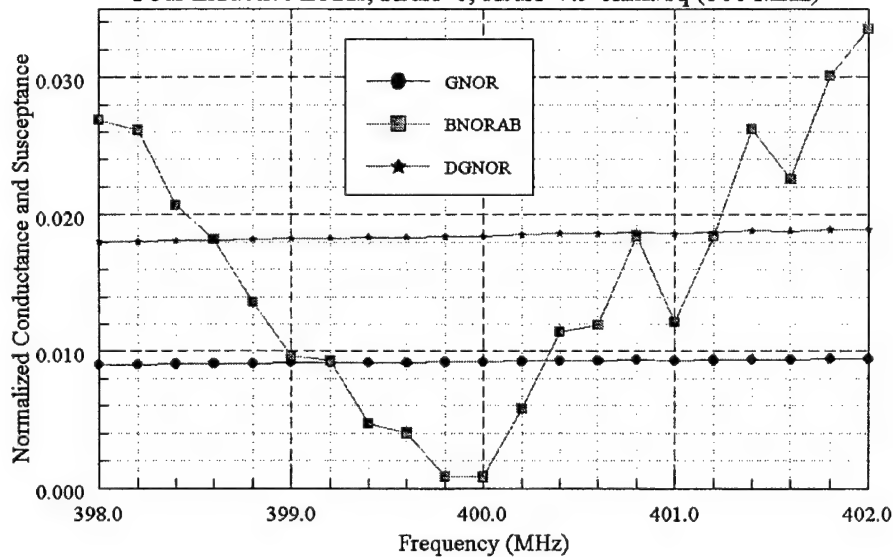
Figure 13. Normalized conductance (GNOR) and absolute value of normalized susceptance (BNORAB) computed for a single CRR using LFMOM code. The small (*ka=0.61*) radiatng resonator is tuned to 400 MHz with four lossless rim inductors of 12.7 nH. The unloaded FWB is approximately 0.0035.

276

Single Conical Resonator, Theta1=90, Theta2=80 deg, Radii: Outer=7.3, Inner=0.0635 cm
Four Inductive Loads, Rsurf=0.316, Xsurf=7.9 ohms/sq (100 MHz)
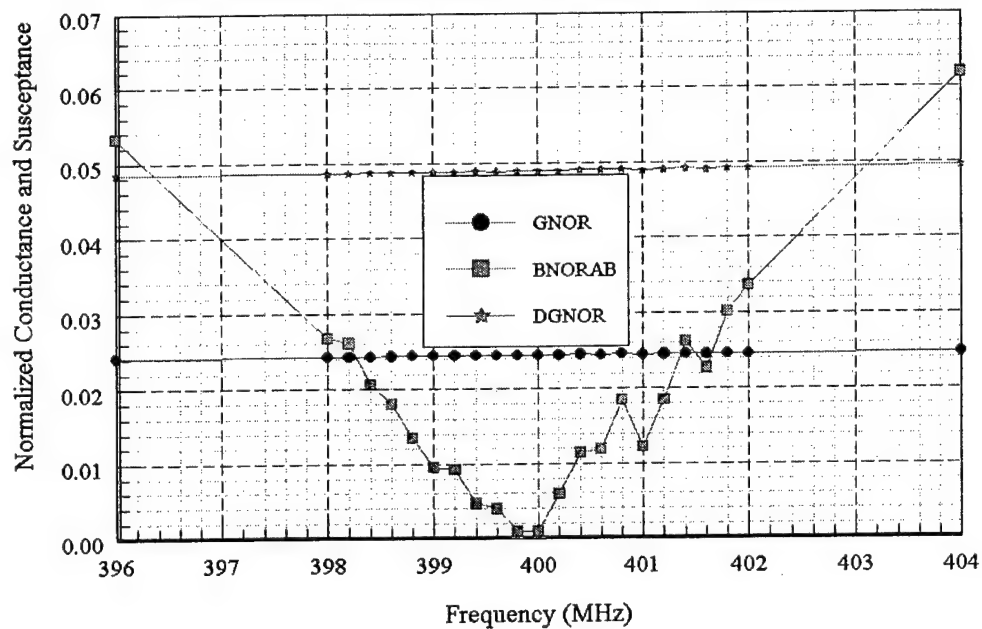
Figure 14. Normalized conductance (GNOR) and absolute value of normalized susceptance (BNORAB) computed for a single CRR using LFMOM code. The small ($ka=0.61$) radiatng resonator is tuned to 400 MHz with four rim inductors of 12.7 nH with $Q = 100$ at 400 MHz. The unloaded FWB is approximately 0.0085.

277

Single Conical Resonator, Theta1=90, Theta2=80 deg, Radii: Outer=7.3, Inner=0.0635 cm
Four Inductive Loads, Rsurf=0.316, Xsurf=7.9 ohms/sq(100 MHz), Rs=0.0053 ohms (Cu)
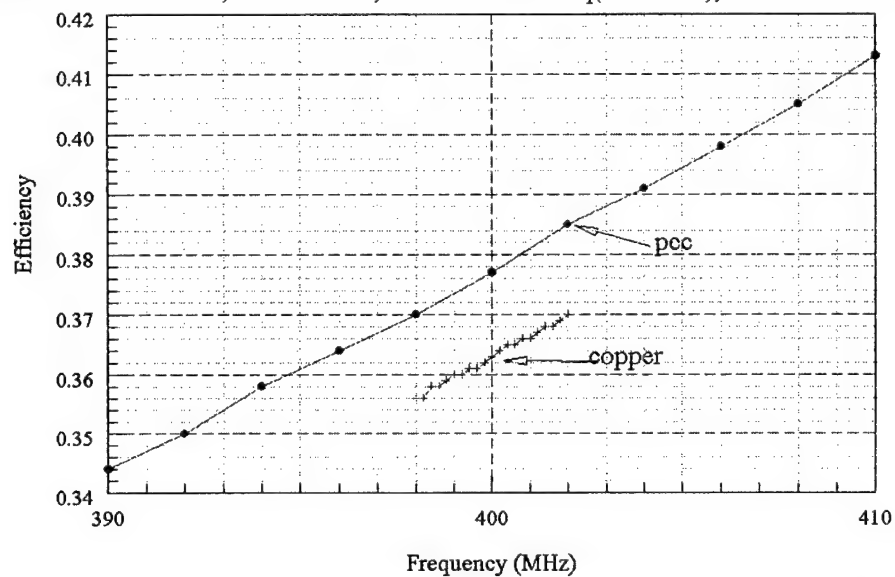
Figure 15. Efficiencies computed for a single CRR loaded with inductors having Q=100 at 100 MHz. The upper curve is computed assuming all conductors are perfect; the lower, conductors are copper.
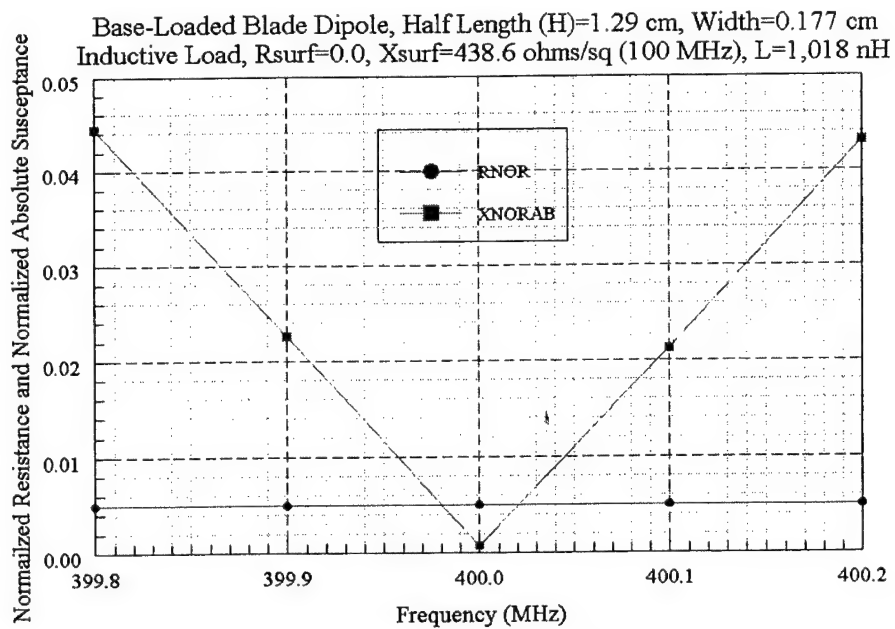
Figure 16. Normalized resistance (RNOR) and absolute value of normalized reactance (XNORAB) computed for a base-loaded blade dipole using LFMOM code. This very short (*ka=0.11*) dipole is tuned to 400 MHz with a lossless base inductor of 1 µH. The unloaded FWB is approximately 0.0001.

279
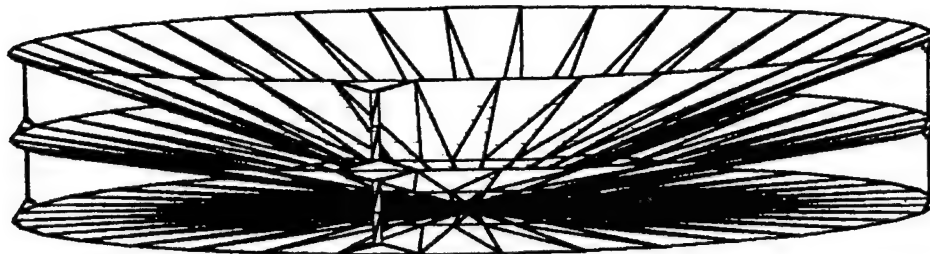
Figure 17. Nested set of two conical radiating resonators with feed region arranged for series connection, four inductive straps arranged symmetrically around the periphery of each resonator.

Theta1=90, Theta2=80, Theta3=70 deg
Radii: Outer=18.75, Inner1,3=0.2, Inner2=0.3 cm
Xs1=12.6, Xs2=9.0 ohms/sq, Q1,2=100 @ 100 MHz

Frequency, 89 - 100 MHz in 0.5 MHz steps
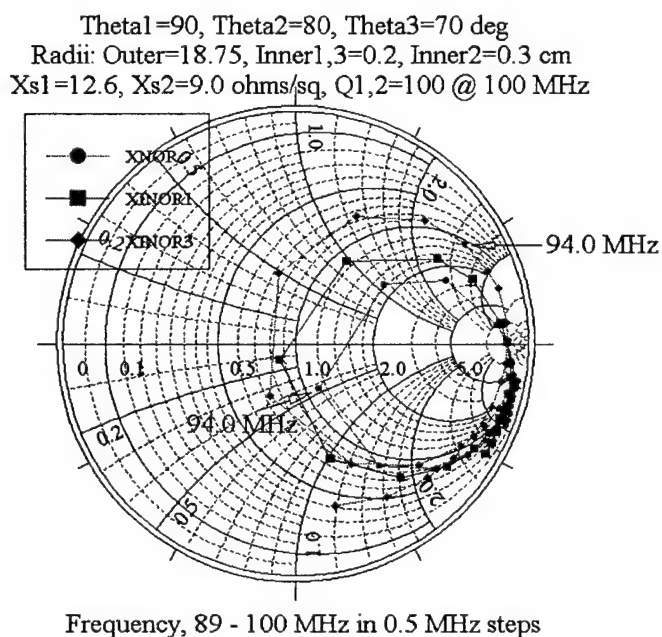
Figure 18. Computed impedance loci for double resonator (DR) antenna (XNOR), DR antenna plus a 2.4 nH inductor (XINOR1), and DR antenna plus a 6.37 nH inductor (XINOR3).

280

Theta1=90, Theta2=80, Theta3=70 deg
Radii: Outer=18.75, Inner1,3=0.2, Inner2=0.3 cm
Xs1=12.6, Xs2=9.0 ohms/sq, Q1,2=100 @ 100 MHz
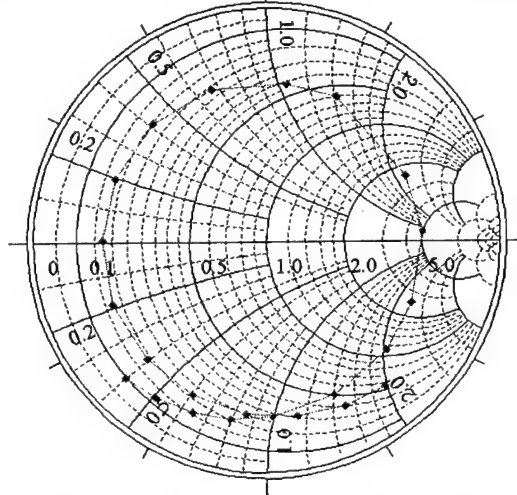
Frequency, 89 - 100 MHz in 0.5 MHz steps
Series Reactance = 0.035 Frequency (MHz)
Transformer Ratio = 0.236:1

Figure 19. Computed impedance loci for double resonator (DR) antenna plus a 5.57 nH inductor and a 0.236:1 transformer.
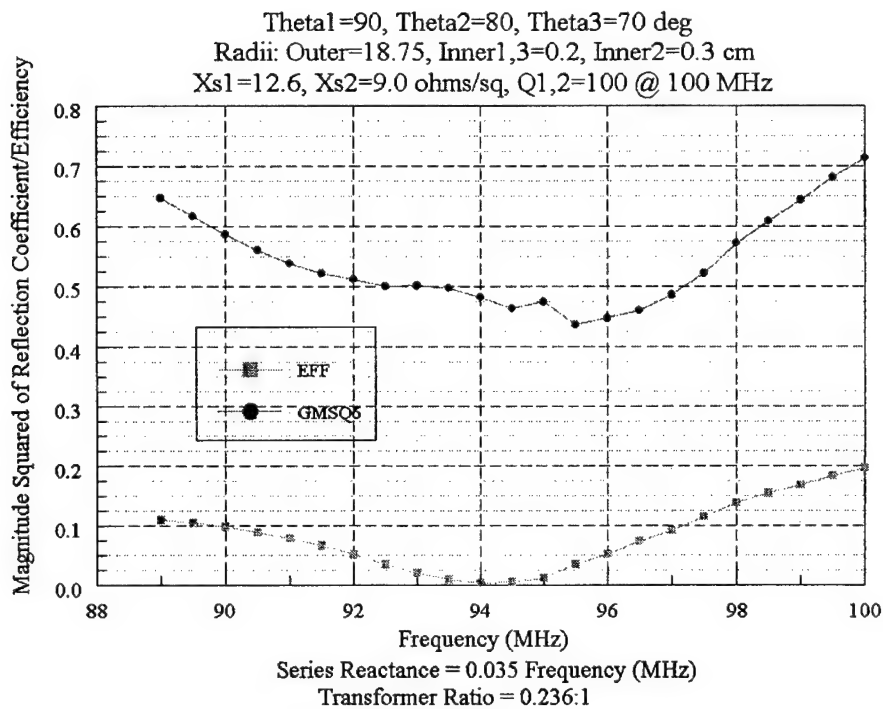
Figure 20. Magnitude squared of reflection coefficient for double resonator antenna with a 5.57 nH inductor and an ideal 0.236:1 transformer. Efficiency values are for antenna only, no losses have been included for the inductor and transformer. When determined on the basis of impedance match alone, the FBW for this antenna is 0.0425. At 100 MHz, *ka*=0.42.

A DISCUSSION ON THE EFFECTIVE VOLUME AND RADIATION PROPERTIES OF SMALL NON-EUCLIDEAN WIRE MONOPOLE ANTENNAS

Steven R. Best
8 Tamarack Lane
Townsend, MA 01469
srbest@att.net

Abstract: The radiation properties of several small non-Euclidean wire monopole antennas are considered. The antennas discussed here include the normal mode helix, the meander line antenna, and several arbitrarily shaped monopole antennas. The radiation properties of these antennas are compared as a function of their total wire length and geometry. The effective volume of these antennas is determined and compared. It is demonstrated that the radiation properties of these antennas are directly a function of the antenna's effective height and effective volume, which are established as a function of both total wire length and geometry. It is shown that these antennas are resonant at the frequency where they exhibit the greatest effective volume. Additionally, it is shown that when the total wire length and g eometry o f t hese a ntennas a re c onfigured s uch t hat t hey e xhibit t he same effective height and volume, their radiation properties are essentially identical, independent of any differences in their total wire length and geometry. Finally, it demonstrated that antennas with greater effective volume exhibit the lowest Q.

1. Introduction

Antenna geometry has become a topic of considerable interest in the optimization of the performance properties of electrically small antennas [1] – [3]. In some instances, it has been presumed that certain antenna geometries may be useful in enhancing or optimizing the performance of electrically small monopole antennas. While this has been specifically suggested in the case of fractal monopole antennas [1], it has been shown that these fractal shaped monopole antennas offer no inherent advantages over other small antennas of similar size and total wire length [4], [5].

The electromagnetic behavior of a linear wire monopole antenna is a function of all its physical properties, which include its overall height, total wire length, geometry and wire diameter. With any antenna geometry, it is inherently obvious that increasing the antenna's total wire length, while maintaining a fixed overall height, lowers the antenna's resonant frequency. Presuming that the antenna's overall height and wire diameter are fixed, the question to consider is whether its possible to optimize the antenna's performance properties by adjusting the antenna's total wire length and geometry. To maintain a standard of reference for comparison of the antenna's performance properties, the antenna's resonant frequency must remain fixed as the total wire length and geometry are adjusted.

In the study presented here, the relative performance characteristics of several small non-Euclidean monopole antennas are considered. These geometries include the normal mode helix, the meander line antenna and several arbitrarily shaped antennas. The performance characteristics of these antennas are considered as a function of their total wire length and geometry where both their overall height and wire diameter remain fixed. The performance properties considered are the antenna's resonant impedance and Q, which provides a measure of the antenna's resonant bandwidth. Additionally, the effective volume of these antennas is determined and compared, providing a better understanding of how the antenna's physical properties translate into its electromagnetic behavior.

Initially, the performance properties of several antennas are compared where they have the same height, wire diameter, and total wire length. In this case, the antennas exhibit different resonant frequencies as a function of differences in their geometry. Next, the total wire length and geometry of several antennas are adjusted such that they are resonant at the same frequency. In this case, their performance properties are compared where their overall height relative to the resonant wavelength remains fixed.

In analyzing the relative performance properties of different antennas, it is demonstrated that when their total wire length and geometry are adjusted such that they are resonant at the same frequency, they exhibit similar effective height and volume, and therefore similar radiation properties. Their resonant performance properties are essentially independent of the differences in total wire length and geometry, indicating that the overall height of the antenna relative to the resonant wavelength is the primary factor in determining the antenna's performance characteristics. It is also demonstrated that the antennas' are resonant at a frequency where they exhibit the greatest effective volume and that their resonant Q decreases with increasing effective volume.

2. The Small Antenna Limit and Effective Antenna Volume

In defining an antenna to be electrically small, the antenna is considered to have certain electrical performance characteristics that can essentially be characterized as a function of the antenna's size with respect to the operating wavelength. Typically, the electrical performance characteristics considered are the antenna's impedance (radiation resistance and input reactance) and Q or bandwidth properties. Electrically small antennas have a maximum physical dimension that is very small with respect to the operating wavelength and they generally have impedance properties where the radiation resistance is very low and the input reactance is very high [6] - [12].

One of the most ambiguous topics in the discussion of electrically small antennas is the small antenna limit (SAL), which is defined as the upper frequency boundary at which an antenna can be considered electrically small. In many instances, this boundary is determined from the frequency at which $ka = 1$, where k is $2\pi/\lambda$ and a is the radius of a sphere encompassing the maximum physical dimension of the antenna [1], [13], [14]. A sphere of radius $a = 1/k = \lambda/2\pi$, is defined as the *radiansphere* and is typically the boundary of the transition between the near-field and far-field for a small antenna [9], [15]. The question that remains however, is the boundary limit for an electrically small antenna determined by the frequency at which the antenna's maximum dimension can be encompassed within the *radiansphere*? In the case of a short dipole antenna, this would define the SAL boundary to occur at a frequency where the dipole's overall length, l, is equal to λ/π ($ka = 1$). This limit translates into an overall dipole length of approximately 0.318 λ, or 64% of the dipole's resonant length.

Numerous approximations for the boundary at which an antenna can be considered electrically small have been stated in the literature. These boundary approximations range from the obvious statement that the antenna size must be very much smaller than the operating wavelength, to more specific boundaries such as the antenna must be smaller than $1/10^{th}$ λ [15], [16]; $1/8^{th}$ λ [17]; or $1/4^{th}$ λ [18]. In his early work on the fundamental limitations of antennas, Wheeler stated that *"the small antenna to be considered is one whose maximum dimension is less than the radianlength,"* [6] where the *radianlength* is defined as a dimension of $\lambda/2\pi$. Adler, Chu and Fano [19], in discussing the theory of the short dipole, also defined the short dipole to be one whose overall length, l, is less than $\lambda/2\pi$. A short monopole is therefore defined to be one whose overall height, h, is less than $\lambda/4\pi$. This boundary limit is significant in that it establishes a small antenna boundary or limit determined from $ka = 0.5$, resulting in a small antenna frequency limit of ½ of that which would be determined from $ka = 1$. The

significance of the small antenna frequency limit being determined from $ka = 0.5$ has been demonstrated in comparing the radiation resistance properties of the Koch fractal monopole, normal mode helix and meander line antennas [20]. When these antennas are self-resonant above this small antenna limit, their radiation resistance converges near this limit, to that of a Euclidean monopole having the same total height, independent of the difference in the antenna's total wire length and geometry.

Wheeler [6]-[7] and Chu [19], [21] essentially equated the electrically small antenna to a simple lumped capacitor or inductor. In doing so, Wheeler equated the electrically small antenna to a cylindrical volume capacitor of an effective height, d, and an effective area, A. In this case, *"the effective area is the area of an idealized parallel-plate condenser, with plates separated by the effective height, which would have the same capacitance as the antenna."* As discussed by Wheeler and Chu, the radiation resistance of the electrically small antenna is primarily determined by the antenna's effective height. At the same time, Wheeler demonstrated that the electrically small antenna's reactance (its capacitance) is a function of both the antenna's effective area and its effective height through a general relationship given by

$$C = \varepsilon \frac{A}{d}$$

(1)

where ε is the electric permittivity of air. Additionally, the equivalent capacitance of the antenna can be written as a function of the antenna's effective volume, $V_e = Ad$, and its effective height as follows

$$C = \varepsilon \frac{V_e}{d^2}$$

(2)

If several electrically small antennas have the same radiation resistance and therefore the same effective height, then any differences in their input reactance properties can be attributed to differences in their overall effective volumes, which, when considering the cylindrical volume capacitor model, indicates that these antennas have different effective cylindrical areas.

Wheeler also went on to discuss that the antenna's effective volume, V_e, can be written in terms of an effective spherical radius, r, given as a function of the antenna's power factor, p, as follows [10]:

$$r = \frac{\lambda}{2\pi} \left(\frac{9}{2} p\right)^{1/3} \tag{3}$$

The antenna's power factor, p, is defined to be equivalent to $1/Q$. Using equation (3), the spherical radius of the effective volume can be determined from the antenna's power factor thus allowing for a comparison of the relative effective volume of the different antenna geometries considered here. Additionally, the effective height of these antennas is compared as a function of both total wire length and geometry.

3. The Normal Mode Helix and Meander Line Antennas

In the case of thin diameter normal mode helix and meander line antennas, it has been demonstrated that they exhibit essentially identical radiation impedance properties when they are made to be resonant at the same frequency [4], [5]. This behavior is independent of the differences in the antennas' total wire length and geometry. Here, the effective height and volume of several wide diameter normal mode helix and meander line configurations are considered and discussed in terms of their relation to the radiation properties of these antennas. The objective here is to determine if adjusting the total wire length and geometry of the antenna can lead to an optimization of the antenna's resonant performance characteristics. Optimization of the antenna's performance properties includes increasing the antenna's resonant radiation resistance and decreasing the resonant Q (increasing bandwidth).

The geometries of the normal mode helix antennas, designated NMH1, NMH2, and NMH3, are depicted in Figure 1. In each case, their overall height is 6 cm and their wire diameter is fixed at 0.5 mm. The overall diameter of these antennas is 1 cm. The other physical properties of these antennas are detailed in Table1. Having a height of 6 cm, the small antenna limit for these antennas, as determined from $ka = 0.5$, is approximately 400 MHz. In evaluating the relative resonant behavior of these antennas a resonant frequency near this small antenna limit is chosen.

287

NMH1   NMH2   NHM3
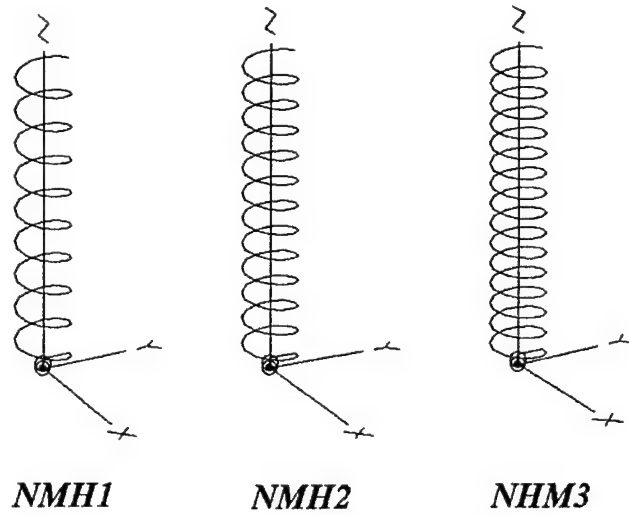
Figure 1. Geometry of the Normal Mode Helix Antennas.

Antenna	Height (cm)	Total Wire Length (cm)	No. of Turns
NMH1	6	29.25	9
NMH2	6	38.42	12
NMH3	6	47.65	15

Table 1. Physical Properties of the Normal Mode Helix Antennas.

The impedance properties of these antennas were determined over a frequency range of 50 through 500 MHz and are presented in Figure 2. The NEC 4.1 engine of EZNEC Pro [22] was used to model the performance properties of these antennas. In each case, the antenna was modeled as being lossless so that the radiation resistance could be directly determined.   The lossless Q of these antennas was determined using the following expression [1], [23].

$$Q = \frac{\omega}{2\,R_{IN}} \left(\frac{\partial X_{IN}}{\partial \omega} + \left| \frac{X_{IN}}{\omega} \right| \right) \qquad (6)$$

288

and is presented in Figure 3 as a function frequency. Using equation (3), the spherical radius of the effective volume of the each antenna was determined and is presented in Figure 4.
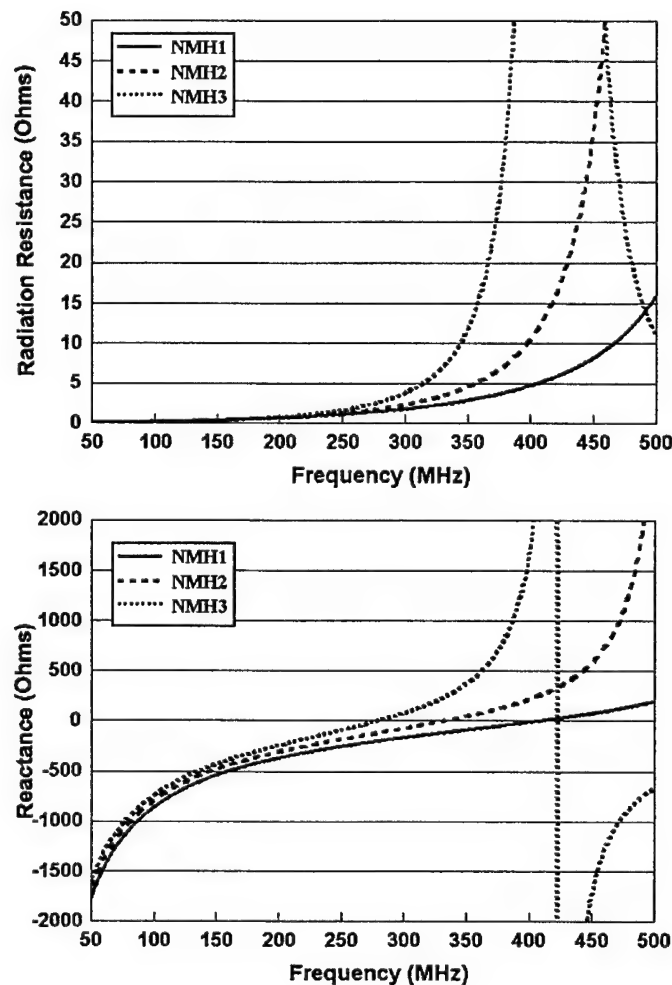
Figure 2. Impedance Properties of the Normal Mode Helix Antennas.

Examining the impedance properties of these antennas as presented in Figure 2, it is evident that as the total wire length increases, the antenna's resonant frequency and resonant radiation resistance decrease. Additionally, at frequencies below the small antenna limit, the radiation resistance of these antennas converges indicating that their effective height converges at low frequencies. However, at

289

these low frequencies, the input reactance of the antenna does not converge to the same extent. From the relationships described in equations (1) and (2), this implies that the antenna's total effective volume does not converge to the same extent.
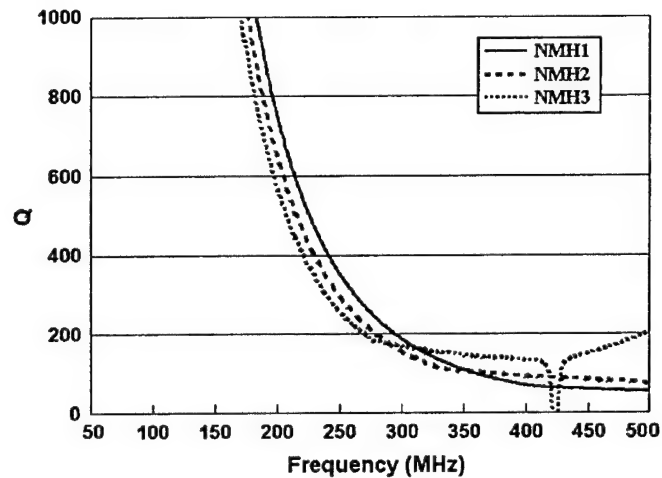
Figure 3. Q **of the Normal Mode Helix Antennas.**
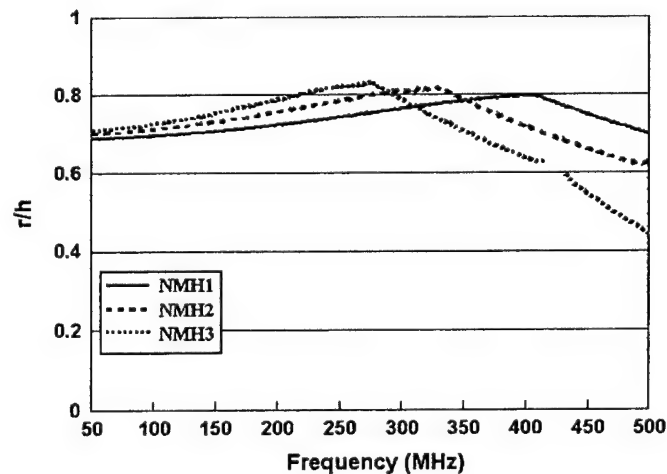
Figure 4. Radius of Effective Spherical Volume for the Normal Mode Helix Antennas.

Examining the Q of these antennas, which is depicted in Figure 3, it is evident that the antenna having the longest total wire length and lowest resonant frequency exhibits the lowest Q at very low frequencies. This relative behavior is maintained until the operating frequency approaches each antenna's resonant frequency. At resonance, the Q of these antennas "breaks" in that it no longer continues to asymptotically decrease. At frequencies above an antenna's resonance, the antenna having the least total wire length and higher resonant frequency exhibits the lowest Q. From the Q data presented in Figure 3, it is also evident that at any given frequency, the self-resonant antenna exhibits the lowest Q.

When the effective volume of these antennas is examined as a function of frequency, the relative differences in their performance properties can be explained in relation to their physical properties. Figure 4 presents the equivalent spherical radius of the antenna's effective volume, r, normalized to the antenna's physical height, h. In each case, the antenna is resonant at the frequency where it exhibits the greatest effective volume. With these normal mode helix antennas, the effective volume increases and the resonant frequency decreases with increasing total wire length. However, with increasing total wire length, the resonant resistance decreases and the resonant Q increases because the effective height and volume of the antenna are smaller with respect to the resonant wavelength. The relative resonant properties of these antennas are summarized in Table 2.

Antenna	Resonant Frequency (MHz)	Radiation Resistance (Ohms)	Q
NMH1	408.2	5.1	66
NMH2	331.4	3.5	115
NMH3	278.4	2.6	184

Table 2. Resonant Properties of the Normal Mode Helix Antennas.

To optimize the performance properties of the electrically small monopole antenna at any given frequency, it is first necessary to maximize its effective volume at that frequency, thus causing it to become self-resonant. Further optimization of the antenna's performance properties require that both the effective height and the effective volume be increased, which increases the radiation resistance and decreases the antenna Q, respectively.

291

The objective of further study at this point is to determine if altering the monopole antenna's total wire length and geometry can be an effective method to optimize the antenna's effective height and volume and hence its resonant performance properties. In all cases, the antenna height and wire diameter remain fixed. For a first reference comparison of performance, the simple meander line monopole is compared with the normal mode helix.

The meander line monopole antennas considered here are depicted in Figure 5 and are designated M1, M2, M3, M4 and M5. These antennas have an overall height of 6 cm and a wire diameter of 0.5 mm. The other physical properties of these antennas are detailed in Table 3.
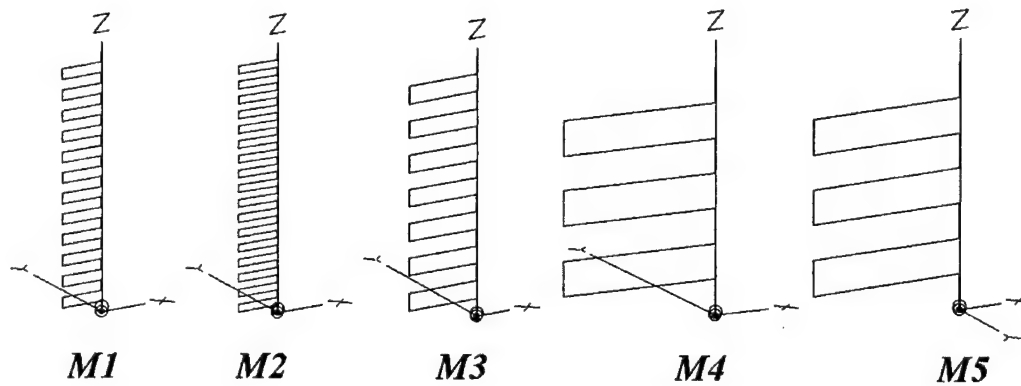
Figure 5. Geometry of the Meander Line Antennas.

Antenna	Height (cm)	Total Wire Length (cm)	Meander Width (cm)
M1	6	29.25	0.97
M2	6	38.42	0.95
M3	6	29.25	1.66
M4	6	29.25	3.87
M5	6	28.16	3.7

Table 3. Physical Properties of the Meander Line Antennas.

The physical properties of M1 and M2 meander line configurations were chosen to essentially match those of the NMH1 and NMH2 normal mode helix configurations, respectively. Using EZNEC, the resonant frequencies of meander line M1 and M2 were determined to be 567.5 and 528.7 MHz, respectively, indicating that their maximum effective volume occurs at a higher frequency. A comparison of their effective volumes is presented in Figure 6. It is evident that the normal mode helix geometry is more effective in terms of exhibiting a lower resonant frequency as a function of total wire length.
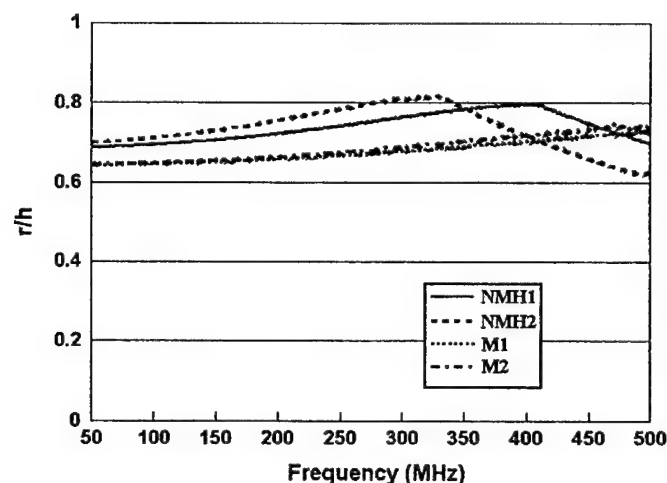
Figure 6.   Effective Spherical Volume Radius of the Meander Line and Normal Mode Helix Antennas.

To lower the resonant frequency of the meander line configurations to match that of the normal mode helix antenna, specifically that of the NMH1 configuration, which is self-resonant at 408.2 MHz, the physical volume of the meander line antenna can be increased while maintaining the same total wire length. The physical volume of the meander line antenna is increased by increasing the meander line diameter as done in the M3, M4 and M5 configurations. The M3 meander line configuration has a width of 1.66 cm lowering its resonant frequency to 497.1 MHz. The meander line M4 configuration has a width of 3.87 cm lowering its resonant frequency to 395.0 MHz. Since the M4 configuration has a lower resonant frequency than that of the NMH1 configuration, its total wire length and diameter can be decreased until its resonant frequency matches that of the NMH1 helix. When the total wire length is reduced to 28.16 cm and the

meander width is reduced to 3.7 cm, the meander line antenna has a resonant frequency of 408.2 MHz. This is the M5 meander line configuration.

A similar process can be undertaken with the normal mode helix antenna. The total wire length in the NMH1 configuration can be reduced simultaneously with an increase in the helix diameter while maintaining the same resonant frequency. In this case, a fourth normal mode helix configuration was implemented, NMH4, having a total wire length of 21.99 cm and a diameter of 3.7 cm. The NMH4 helix configuration has approximately 1-2/3 turns. A visual comparison of the NMH1 and NMH4 configurations is presented in Figure 7. Both of these antennas are resonant at 408.2 MHz.

NMH1   NMH4
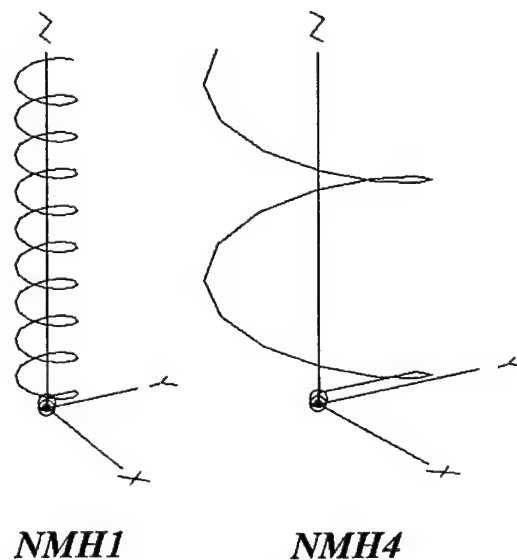
Figure 7. The NMH1 and NMH4 Normal Mode Helix Configurations.

To examine the significance of geometry in relation to the resonant antenna performance, the impedance properties of the NMH1, the M5 and the NMH4 antennas were determined and are compared in Figure 8. The Q and the spherical radius of the effective volume of these antennas were determined and are compared in Figures 9 and 10, respectively. A summary of the resonant radiation properties of these antennas is presented in Table 4. From the performance data presented in Figures 8, 9 and 10 and Table 4, it is evident that these antennas

294

exhibit remarkably similar behavior considering the significant differences in their physical properties. One of the differences in performance is the radiation resistance, which is higher in the NMH1 configuration, indicating that the narrower, longer wire structure exhibits a slightly greater effective height. The other performance difference is the antenna Q which is lower in the M5 and the NMH4 configurations, which can be attributed to their slightly greater total effective volume, which results from their increased physical diameter.
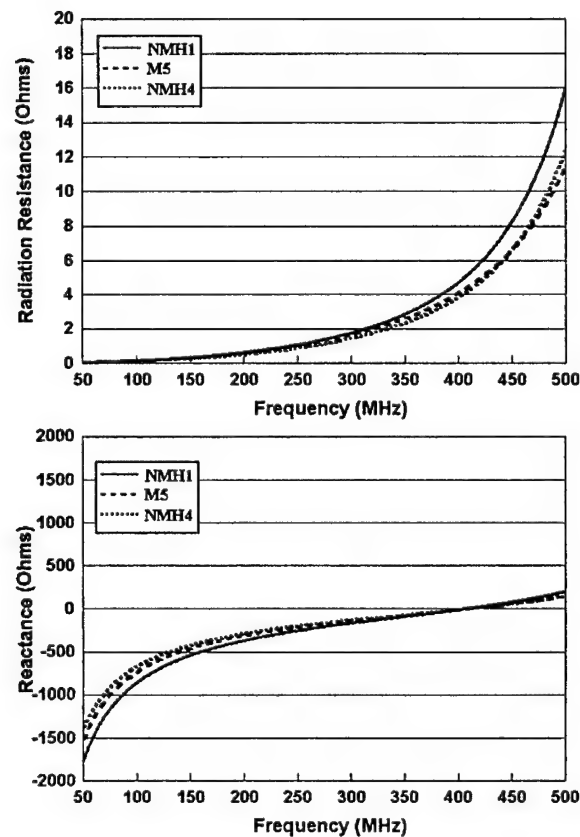
Figure 8.   Impedance Properties of the NMH1, M5 and NMH4 antenna configurations.
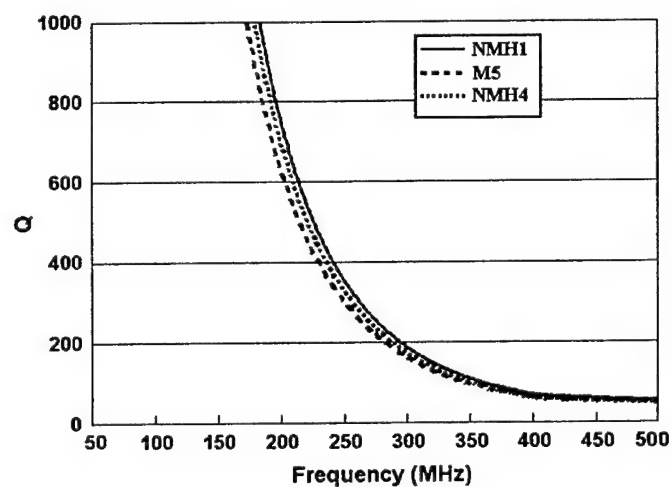
Figure 9. *Q* Properties of the NMH1, M5 and NMH4 Antenna Configurations.
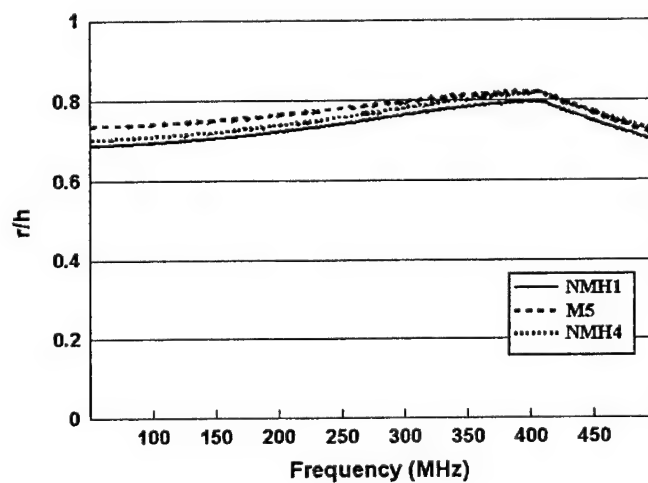
Figure 10. Effective Spherical Volume Radius of the NMH1, M5 and NMH4 Antennas.

Antenna	Height (cm)	Total Wire Length (cm)	Width (cm)	Resonant Frequency (MHz)	Radiation Resistance (Ohms)	Q	r/h
NMH1	6	29.25	1.0	408.2	5.1	66	.80
M5	6	28.16	3.7	408.2	4.4	61	.82
NMH4	6	21.99	3.7	408.2	4.2	61	.82

Table 4. Radiation Properties of the NMH1, M5 and NMH4 Antennas.

4. The Arbitrary Geometry Monopole Antennas

To further consider the significance of the antenna's total wire length and geometry in determining the resonant performance properties of small monopole antennas, several arbitrarily shaped monopoles are considered. These antennas have the same height and similar occupied physical volume. In each case, the antennas have a total height of 6 cm and are enclosed within a cube having a width and length of 6 cm. The wire diameter of these antennas is 0.5 mm. The total wire length and geometry of each antenna is adjusted such that their resonant frequency is approximately 408.2 MHz, matching that of the NMH1 configuration discussed in the previous section. Five arbitrarily shaped monopole antennas were designed and are designated A1, A2, A3, A4 and A5. Depictions of these antennas are presented in Figure 11.

The performance properties of these antennas were determined using the NEC engine in EZNEC pro. The impedance and Q properties of these antennas are presented in Figure 12 and 13, respectively. The radius of the effective spherical volume of these antennas is presented in Figure 14. A summary of the resonant performance properties of these antennas is presented in Table 5. Examining the performance characteristics of these antennas it is again evident that their resonant properties are remarkably similar given the significant difference in their physical properties. As with the physically wider meander line and normal mode helix antennas, these antennas exhibit a lesser radiation resistance than the NMH1 normal mode helix antenna. Differences in their radiation resistance can be attributed to the difference in the antenna's effective height. Additionally, the antennas having the greatest effective volume exhibit the lowest Q.

297

A1 **A2** **A3**

A4 **A5**
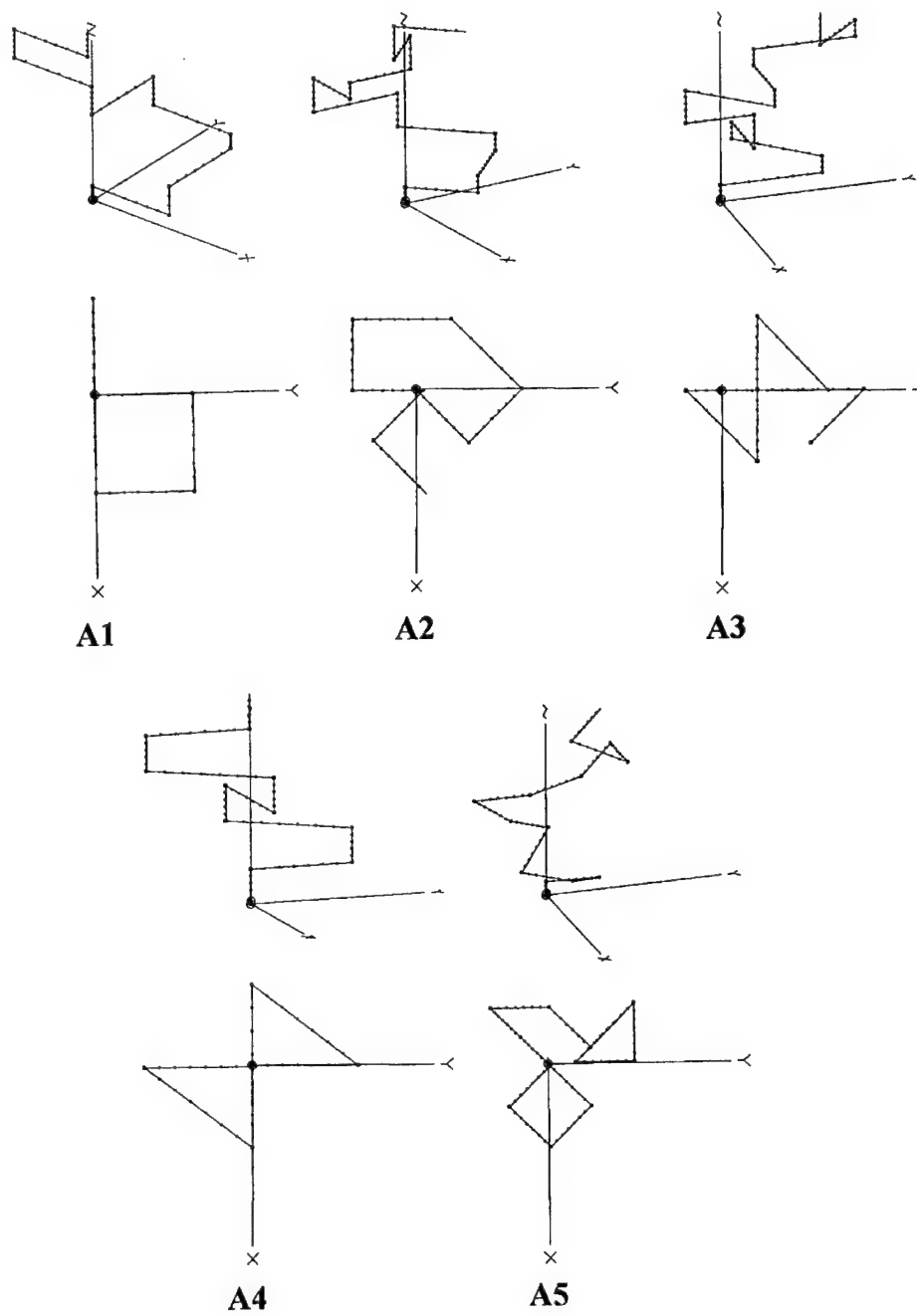
Figure 11. The Arbitrarily Shaped Monopole Antennas.
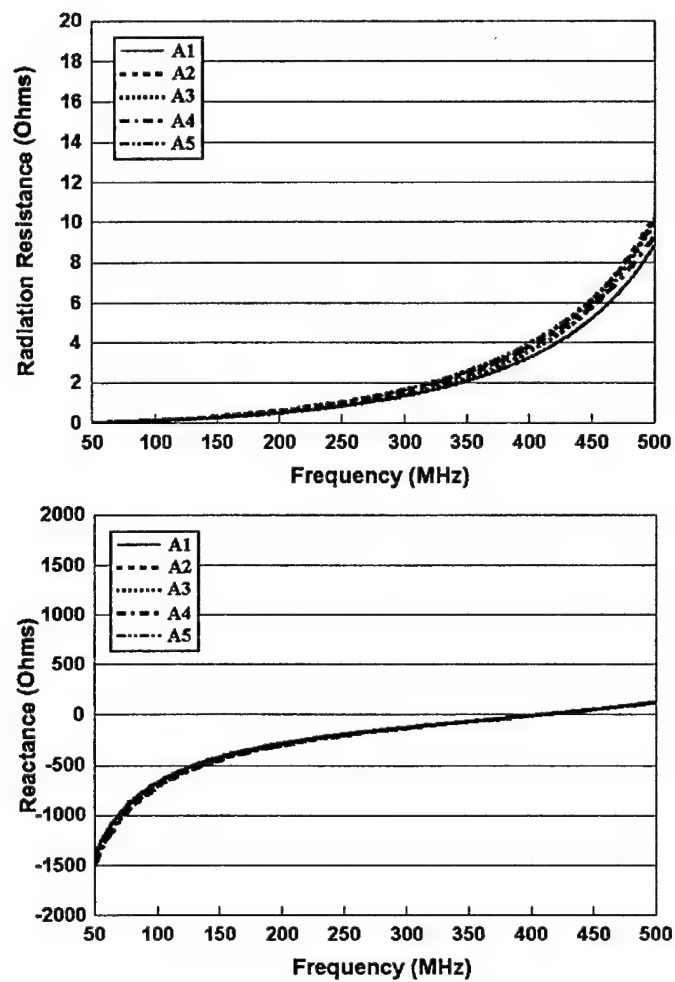
Figure 12. Impedance Properties of the Arbitrarily Shaped Monopole Antennas.

299
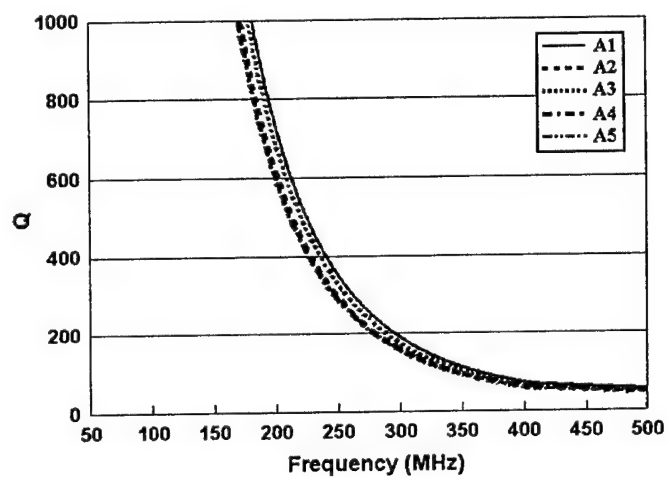
Figure 13. Q Properties of the Arbitrarily Shaped Monopole Antennas.
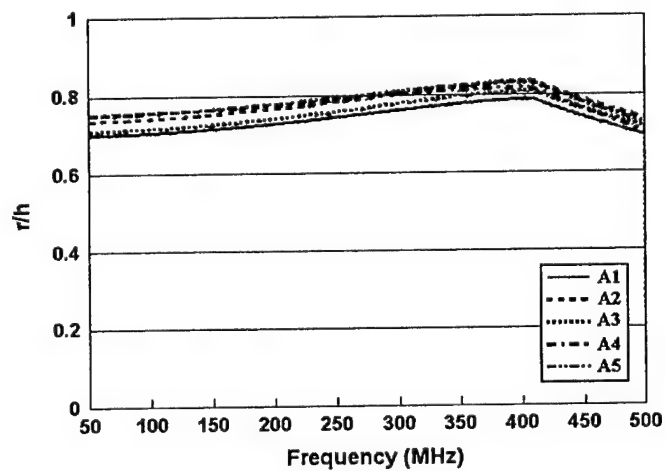
Figure 14. Radius of the Effective Spherical Volume of the Arbitrarily Shaped Antennas.

Antenna	Height (cm)	Total Wire Length (cm)	Maximum Width (cm)	Resonant Frequency (MHz)	Radiation Resistance (Ohms)	Q	r/h
NMH1	6	29.25	1.0	408.2	5.1	66	.80
A1	6	23.85	6 x 6	408.3	3.5	68	.79
A2	6	23.96	6 x 6	408.1	4.1	58	.83
A3	6	25.95	6 x 6	408.1	3.8	63	.81
A4	6	24.13	6 x 6	408.2	4.1	61	.82
A5	6	24.61	6 x 6	408.1	4.3	58	.83

Table 5. Radiation Properties of the Arbitrarily Shaped Antennas.

5. The Modified Normal Mode Helix Antennas

The final group of antennas considered as part of this study consists of several normal mode helix antennas. These antennas have a height of 6 cm and a wire diameter of 0.5 mm. These antennas have differing total wire lengths and diameters but are made to be resonant at the same frequency as the NMH1 normal mode helix antenna. The diameter of these antennas was made to increase gradually from 1 cm to 3.2 cm to better illustrate the relationship between the antenna's physical properties and its resonant performance characteristics. The physical properties of these normal mode helices, designated H1 through H6 are detailed in Table 6.

Antenna	Height (cm)	Total Wire Length (cm)	Diameter (cm)	No. of Turns
H1	6	29.25	1.0	9
H2	6	27.45	1.24	6 ¾
H3	6	26.05	1.50	5 ¼
H4	6	25.09	1.77	4 ¼
H5	6	23.63	2.31	3
H6	6	22.36	3.18	2

Table 6. Physical Properties of the Normal Mode Helix Antennas.

The impedance, Q and radius of the effective spherical volume of these antennas are presented in Figures 15, 16 and 17 respectively. A summary of their

301

performance characteristics is presented in Table 7. As with the antennas discussed in the previous section, increasing the physical diameter of the antenna reduces its effective height and radiation resistance but increases the antenna's overall effective volume, thus reducing the antenna Q. Again, however, the resonant properties of these antennas are not notably different considering the difference in their physical properties.
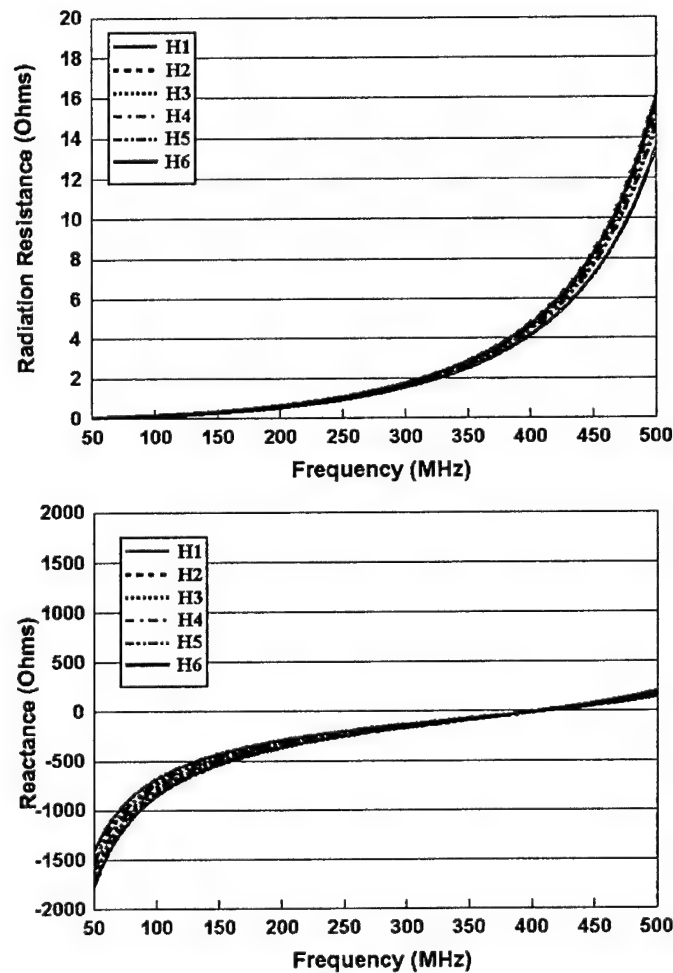
Figure 15. Impedance Properties of the Normal Mode Helix Antennas.
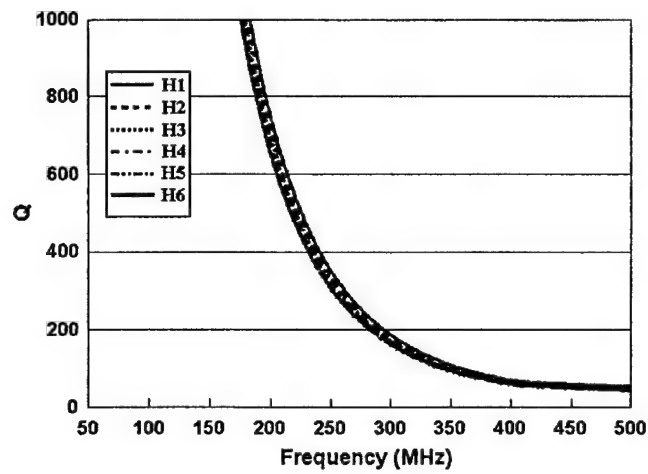
Figure 16. *Q* **Properties of the Normal Mode Helix Antennas.**
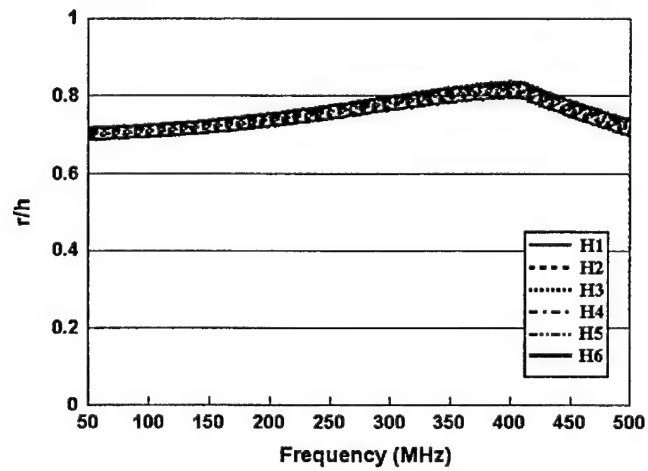
Figure 17. Radius of the Effective Spherical Volume of the Normal Mode Helix Antennas.

Antenna	Resonant Frequency (MHz)	Radiation Resistance (Ohms)	Q	r/h
H1	408.2	5.13	66	.80
H2	408	5.18	63	.81
H3	408.3	5.11	61	.82
H4	408.2	5.03	59	.82
H5	408.3	4.85	57	.83
H6	408.2	4.55	57	.84

Table 7. Resonant Properties of the Normal Mode Helix Antennas.

6. Discussion

In the previous sections, the radiation properties of several small self-resonant monopole antennas were considered. In each case, the total wire length and geometry of the antennas were adjusted such that all of the antennas were made to be resonant at the same frequency. Remarkably, the radiation properties of these antennas were essentially the same independent of the significant differences in their physical properties. Optimization of the antenna's radiation resistance and Q properties requires that both the antenna's effective height and volume be increased to the greatest extent.

Although this work may not represent a sufficiently comprehensive study, it is evident that the narrower diameter monopole structures require significantly more total wire length to achieve resonance than their wider diameter counterparts. Additionally, the narrower diameter monopole structures exhibit a greater effective height and therefore a greater resonant radiation resistance. The wider diameter structures require less wire length to achieve resonance and they exhibit a greater effective volume and therefore a lower value of resonant Q. However, the resonant performance properties were not significantly different for any of the monopole configurations.

From these results, it appears that for a fixed height monopole, the antenna's total wire length and geometry together establish the antenna's resonant frequency and that for a given resonant frequency, the antenna's radiation properties are essentially the same independent of any differences in total wire length and geometry. This indicates that the primary factor determining the antenna's resonant properties is its overall height relative to the resonant wavelength.

304

This being the case, the value in optimizing the antenna geometry becomes a function of how much total wire length is required to achieve self-resonance. Geometries requiring less total wire length to achieve resonance will be more efficient as the total loss in the structure will be minimized.

These results are considered to be valid for simple linear monopole structures similar to that described here. Other monopole structures such as top loaded monopoles and folded monopoles will exhibit different performance characteristics and would likely provide better solutions as they typically have greater radiation resistance as a function of height.

7. References

[1]   Carles Puente-Baliarda, J. Romeu and A. Cardama, "The Koch Monopole: a Small Fractal antenna," *IEEE Trans. Antennas and Propagat.*, Vol. 48, pp. 1773 – 1781, Nov. 2000.

[2]   Edward E. Altshuler, "Electrically Small Self-Resonant Wire Antennas Optimized Using a Genetic Algorithm," *IEEE Trans. Antennas and Propagat.*, Vol. 50, pp. 297 – 300, Mar. 2002.

[3]   K. J. Vinoy, K. A. Jose, V. K. Varadan, and V. V. Varadan, "Hilbert Curve Fractal Antenna: A Small Resonant Antenna for VHF/UHF Applications," Microwave Opt. Technol. Lett., Vol. 29, No. 4, pp. 215 – 219, May 2001.

[4]   Steven R. Best, "The Koch Fractal Monopole Antenna: The Significance of Fractal Geometry in Determining Antenna Performance," *25th Annual. Antenna Applications Symposium Conference Proceedings*, pp. 194-205, University of Illinois, October, 2001.

[5]   Steven R. Best, "On the Performance Trade-offs Associated with Fractal Antenna Designs," *25th Annual Antenna Applications Symposium Conference Proceedings*, pp. 206-213, University of Illinois, October, 2001.

[6]   Harold. A. Wheeler, "Fundamental limitations of small antennas," *Proceedings of the IRE*, Vol. 35, pp. 1479-1488, Dec. 1947.

[7]   H. A. Wheeler, "Fundamental Relations in the Design of a VLF Transmitting Antenna," *IRE Trans Antennas Propagat.*, Vol. 6, pp. 120-122, Jan. 1958.

[8]   H. A. Wheeler, "Fundamental Limitations of a Small VLF Antenna for Submarines," *IRE Trans. Antennas Propagat.*, Vol. 6, pp. 123-125, Jan. 1958.

[9]   H. A. Wheeler, "The Radiansphere Around a Small Antenna," *Proceedings of the IRE*, Vol. 47, pp. 1325-1331, Aug. 1959.

[10] H. A. Wheeler, "Small Antennas," *IEEE Trans. Antennas Propagat.*, Vol. 23, pp. 462-469, Jul. 1975.

[11] R. C. Hansen, "Fundamental Limitations in Antennas," *Proceedings of the IEEE*, Vol. 69, pp. 170-182, Feb. 1981.

[12] H. A. Wheeler, "Antenna Topics in My Experience," *IEEE Trans. Antennas Propagat.*, Vol. 33, pp. 144-151, Feb. 1985.

[13] James S. McLean, "A Re-Examination of the Fundamental Limits on the Radiation Q of Electrically Small Antennas," *IEEE Trans. Antennas Propagat.*, Vol. 44, pp. 672-676, May 1996.

[14] K. Fujimoto *et al*, "Small Antennas," Research Studies Press, England; John Wiley and Sons, New York, 1987.

[15] Constantine A. Balanis, "Antenna Theory – Analysis and Design," John Wiley and Sons, New York, 1982.

[16] Warren L Stutzman and Gary Thiele, "Antenna Theory and Design," John Wiley and Sons, New York, 1998.

[17] Sergei A. Schelkunoff and Harald T. Friis, "Antennas – Theory and Practice," John Wiley and Sons, New York, 1952.

[18] K. Hirasawa *et al*, "Analysis, Design, and Measurement of Small and Low Profile Antennas," Artech House, Norwood, 1992.

[19] Richard B. Adler, Lan Jen Chu, and Robert M. Fano, "Electromagnetic Energy Transmission and Radiation," John Wiley & Sons, New York, 1960.

[20] Steven R. Best, "On the Performance of the Koch Fractal and Other Bent Wire Monopoles as Electrically Small Antennas," 2002 *IEEE Antennas and Propagation International Symposium*, Vol. 4, pp. 534-537, June 2002.

[21] Lan Jen Chu, "Physical Limitations of Omni-Directional Antennas," *Journal of Applied Physics*, vol. 10, pp. 1163-1175, Dec. 1948.

[22] EZNEC/4 Antenna Modeling Software, Roy Lewallen, P.E., http://www.eznec.com.

[23] Wen Geyi, Perry Jarmuszewski, and Yihong Qi, "The Foster Reactance Theorem for Antennas and Radiation Q," *IEEE Trans. Antennas Propagat.*, Vol. 48, No. 3, pp. 401 – 408, Mar. 2002.

INVESTIGATION OF POLARIZATION PURITY AND PORT ISOLATION IN LINEARLY AND CIRCULARLY POLARIZED MICROSTRIP PATCH ANTENNAS WITH GROUND PLANE SERRATIONS

G. H. Huff, G. Cung, and J. T. Bernhard
Electromagnetics Laboratory
Department of Electrical and Computer Engineering
University of Illinois at Urbana-Champaign
Urbana, IL 61801

Abstract: This paper investigates the application of serrations to the ground plane of a diagonal fed and dual fed microstrip patch antenna. Polarization characteristics as well as port isolation for the dual fed case are examined. Previous studies on polarization purity enhancements with serrated ground planes have shown as much as a 10dB reduction in cross polarization radiation for a probe fed linearly polarized microstrip antennas on finite ground planes. Along with greater polarization purity, moderate increases in the 3dB beamwidth and tunability also arise from the use of serrations along the ground plane in the single fed linearly polarized case. With this in mind, serrations are applied to similar patch geometries with different feeding schemes to attain dual orthogonal linear polarization as well as circular polarization. Measurements of both cases highlight effects of serrations on radiation parameters, impedance, and port isolation in the dual fed case.

1. Introduction

Poor polarization purity and port isolation in microstrip patch antennas can cause spurious coupling and interference, resulting high error rates in received or transmitted data. In many cases, a finite ground plane may exaggerate these problems. Along with the effects of cross-polarization coupling, the action of circulating edge currents may also act to deteriorate the radiated fields of the antenna by means of diffraction from the surface along the edge boundaries of the finite ground plane. This diffraction can cause interference that decreases the radiation pattern beamwidth and can also affect the impedance of the structure.

To partially remedy this phenomenon, ground plane serrations have been proposed in [1] as a ground plane edge treatment for the reduction of spurious

307

radiation caused by the diffraction of circulating edge currents. In addition to this, serrations can also provide a pseudo-polarizing effect for currents on the ground plane, giving as much as a 9 dB reduction in cross polarization signal levels in the single fed square microstrip antenna. Serrations, originally considered as an edge treatment for compact range reflectors [2-7], are now studied for the enhancement of dual linearly and circularly polarized microstrip patch antennas in an effort to decrease undesired coupling between ports and thereby increase the polarization purity, boosting the antenna's performance.

2. Background

The use of serrations has been thoroughly investigated [2-7] and is usually considered as a cost-efficient solution in the design of compact reflector ranges as well as other range designs to eliminate the undesired effects from diffraction around the reflector, as well as the test fixture and other components for other antenna measurements (such as the Gregorian sub-reflector in [8]). For the compact range reflector specifically, the use of serrations has been implemented as an edge treatment that acts to reduce the error generated from the diffracted fields along the edges of the reflector. In doing so, the overall quality of the reflector for antenna and scattering measurements is improved through an increase the quiet zone, supporting a larger and more uniform plane wave with an improved constant phase front. Other edge treatments such as blended, or rolled, edges have also been well examined and compared to serrations [9]. Rolled edges tend to be more effective; however the fabrication of such edge treatments is considerably more expensive than the planar serrations technique.

Very little has been studied concerning the direct application of serrations to other antennas, planar geometries or otherwise. In the case of the linearly polarized microstrip patch antenna, serrations have been studied in [1], in which the most significant effect is the considerable decrease in cross-polar radiation as the length of the serration is increased. This phenomenon may be due to the fact that the serrations along the edges of the ground plane act to diminish the circulating action of the currents along the outer boundary of the ground plane. Their presence creates a pseudo-polarizing effect that translates into a significant decrease in cross-polar radiation. The energy previously in the cross-polar component appears to be distributed to both the forward- and back-plane directions as co-polar radiation, decreasing the front-to-back ratio and decreasing the maximum gain slightly.

3. Antenna Geometry

To investigate the effects of serrating the ground plane of a microstrip patch antenna, three identical square ($L = W = 40.23$ mm) antennas are designed for operation at 2.44 GHz and fabricated. The square geometry is chosen to represent microstrip antenna design most conducive to cross polarization effects. Figure 1 shows the geometries for the three antenna structures. For this set of antennas, a single diagonal feed for dual orthogonal linear polarizations as well as dual feeds for circular polarization are considered, with all three antennas for each feed configuration residing on equal sized square dielectric slabs (Duroid® 5880 substrate, $\varepsilon_r = 2.2$, $h = 1.52$ mm) with the patch elements centered over their respective ground planes and SMA probe feeds ($D_{Probe} = 1.23$ mm) identically positioned. The feed location for the diagonally fed antenna is at $X_f = Y_f = 13.4$ mm from the corner of the patch. To extend this treatment to the circularly polarized case, the feed locations are $(X_f, Y_f) = (W/2, 13.4)$ and $(13.4, L/2)$ for the dual fed case. The extension of the ground plane in all planar dimensions from the patch edges was fixed at a distance of 7h ($\approx \lambda_{eff}/10$) allowing the serrations to become comparable to a wavelength. For two of the antennas, triangular serrations are then removed from the edges of the ground plane inward to create the three cases. The only dimension altered during the course of the experiment was the depth of the serration Δ_{serr} (measured from the outer edge of the ground plane toward the patch).

4. Experimental Results

4.1 Diagonally Fed Antenna for Dual Orthogonal Linear Polarizations

Measurements of the input impedance, VSWR, and radiation patterns for the diagonally fed antenna can be seen in Figures 2-5. Figure 2 shows the input impedance for the three cases. For the two serrated antennas a slight frequency shift is introduced with the new geometry of the ground plane, which is created by the variation of the serration depth and the resulting effects on the current distribution on the antenna. For these antennas, there exists a slight decrease in beamwidth in the E-plane (xz-plane) and a slight increase in beam width in the H-plane (yz-plane). Since the antenna is dual linearly polarized and symmetric, similar polarization characteristics are seen in the E- and H-planes of the antenna, and are in good agreement with the results in [1].

4.2 Dual Fed Antenna for Circular Polarization

Measurements of the input impedance, VSWR, and radiation patterns for the dual

fed antenna can be seen in Figures 7-9. For the dual fed antennas, the behavior is quit similar to the diagonally fed case, and is in good agreement with the results in [1]. In Figure 7, symmetric placement of the two ports (see Figure 1) on the individual antennas achieves a near-identical impedance match for each probe position, with the exception of the moderately serrated antenna's port 2. For this probe feed, a slight fabrication tolerance error occurred, which accounts for the slight variation in port impedance. Although there are slight impedance variations, the 2:1 VSWR bandwidths for each port on the respective antennas remain very close to each other.

Also for the dual fed case, the individual radiation measurements of port 1 and port 2 are similar to [1], and exhibit radiation characteristics similar to the E- and H-plane behavior seen in the diagonally fed case previously discussed. Therefore, only the circularly polarized measurements are presented. To measure the circular polarization characteristics, a 90° hybrid coupler was used to obtain an equal power split and the needed phase difference between the two ports. The sense of circular polarization was chosen to be left hand (LHCP), and the standard gain horn was set up in a similar manner to measure LHCP and RHCP of the antennas. In the LHCP configuration the antenna experiences little deviation in the pattern characteristics across the serration cases. For RHCP, the antenna experiences a 2-3 dB reduction in "cross polarization" at boresight, and begins to exhibit higher levels of cross-polarization as the serration length is increased. In the fully serrated case, this dramatic increase in cross-polar radiation is greatest, and can be attributed to a combination of two factors. The first is the higher back-plane radiation that arises from increasing the serration penetration depth, which can be seen in the diagonally fed antennas (Figures 4-6). The second is that when the antenna under test is facing away from the standard gain horn, where the back-plane radiation appears to be RHCP.

4.3 Port Isolation in Dual Fed Antenna

The final aspect of the serrated ground plane to be discussed is the port isolation in the dual fed case. Figure 10 shows the isolation characteristics between port 1 and 2 (S_{21}). From this plot, which is only representative of the overlapping of 2:1 VSWR bandwidth of all three antennas where a legitimate comparison can be made, it can be seen that the application of serrations yields encouraging results. At the center of this bandwidth there is a 3.01 and 8.24 dB reduction in coupling between ports for the moderately and fully serrated antenna respectively. In the moderately serrated antenna, this reduction is not maintained over the entire bandwidth considered, however for the fully serrated antenna a significant reduction is seen across the entire bandwidth.

310

An application with possible improvements arising from the use of serrated ground planes is the active reflect-array element discussed in [10]. In such an application, polarization purity, which is tied directly to port isolation, is essential for proper operation of the device. The design specifics and geometry for the antenna are similar to the dual fed circularly polarized antenna discussed below, with the exception of a square portion of conductor, which is removed with the diagonals diametrically opposed and located on the normal feeding positions, shown in Figure 11. Within this area of removed conductor, an amplifier can be inserted to receive one polarization (at port 1 for example), amplify and transmit in the other polarization (continuing the example, port 2). For the integrated amplifier application previously discussed, such a decrease in coupling between ports can represent a significant increase in the polarization purity and achievable gain of the amplified signal.

5. Conclusions

In this paper, the application of serrations to the ground plane of a square microstrip patch antenna for both dual linear and circular polarization has been studied. In the Diagonal fed configuration, the pattern symmetry in each plane is in good agreement with previous work on the serration of the microstrip antenna ground planes. For the dual fed (two port) scenario, the effects of serrations have differing effects depending on the application being considered. For circular polarization, the effects of serrations decrease the 'cross polarization' at boresight, but increase quickly from there on and degrade the predicted performance of the antenna. However, in the context of application to an active reflectarray, the effect of the pseudo-polarizing effect of the serrated ground plane acts to significantly decrease the coupling between ports and shows promise for future applications and investigation. In general, the effect of serrations on the impedance of the antenna is minimal, where as the effect on radiation is significant, and is under investigation for other types of antenna designs.

6. Acknowledgments

7. References

[1] G.H. Huff, and J.T. Bernhard, "Improvements in the performance of microstrip antennas on finite ground planes through ground plane edge serrations," *IEEE Microw. Wireless Comp. Lett.*, vol. 12, no. 8, pp. 308 –310, Aug. 2002.

[2] Yu-Kuan Mao and Xian-Hong Cheng, "The design principle of compact range antennas," *1989 IEEE AP-S. Dig.*, pp. 318 –319, 1989.

[3] R. Mompo, J. Molina, M. Calvo, and J.L Besada, "Compact range antenna analysis," *Proc. of 1989 Electrotechnical Conf. on Integrating Research, Industry and Education in Energy and Communication Engineering*, pp. 497 –500, 1989.

[4] J.P. McKay and Y. Rahmat-Samii, "Quiet zone evaluation of serrated compact range reflectors," *1990 IEEE AP-S Dig.*, pp. 232 –235, 1990.

[5] G. Parini and M. Philippakis, "Use of quiet zone prediction in the design of compact antenna test ranges," *IEE Proc. Microw. Antennas and Propagat.*, vol. 143, pp. 193 –199, June 1996.

[6] C.G. Parini and M. Philippakis, "Compact antenna test range reflector edge treatment," *Electronics Letters*, vol. 32, pp. 82 –83, Jan. 1996.

[7] I.J. Gupta, D.G. Brown, W.D. Burnside, and W. Lin, "A serrated edge Gregorian subreflector for dual chamber compact range systems," *IEEE Trans. on Antennas and Propagat.*, vol. 39, pp. 1258 –1261, Aug. 1991.

[8] Teh-Hong Lee and W.D Burnside, "Performance trade-off between serrated edge and blended rolled edge compact range reflectors," *IEEE Trans. on Antennas and Propagat.*, vol. 44, pp. 87 –96, Jan. 1996.

[9] Teh-Hong Lee and W.D. Burnside, "Compact range reflector edge treatment impact on antenna and scattering measurements," *IEEE Trans. on Antennas and Propagat.*, vol. 45, pp. 57 –65, Jan. 1997.

[10] R. Clark, G.H. Huff, and J.T. Bernhard, "An integrated active microstrip reflectarray element with an internal amplifier," To appear in *IEEE Trans. on Antennas and Propagat.*, May 2003.
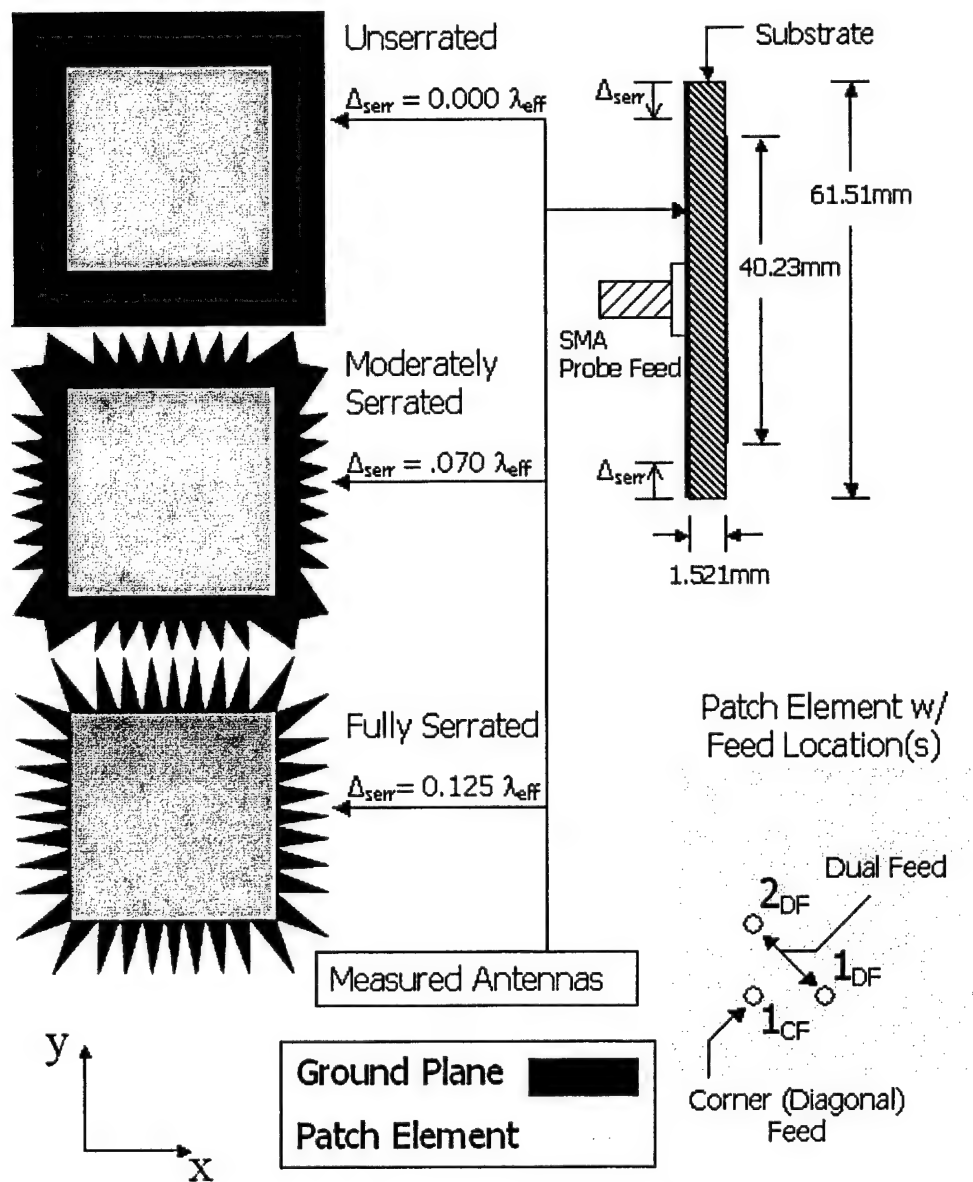
Figure 1: Antenna geometry and feed locations for the antennas considered.
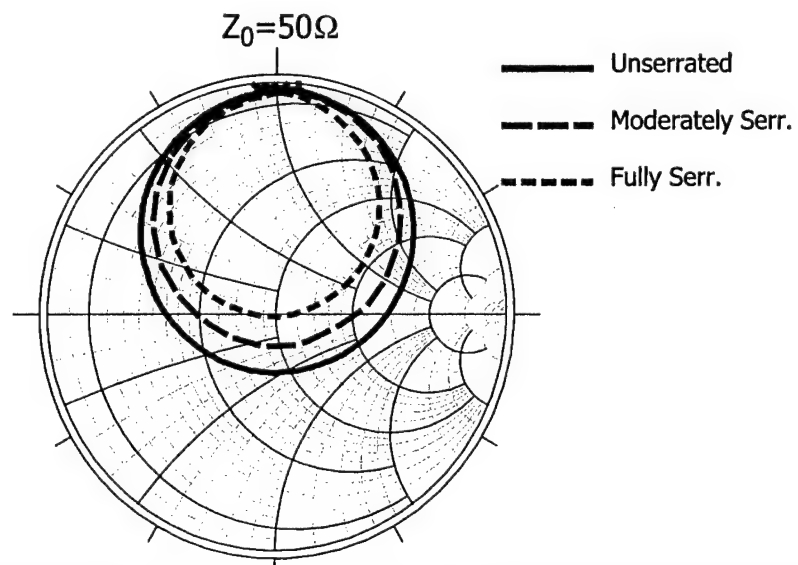
Figure 2: Measured input impedance for the diagonally fed (dual linear) antenna over the range of 2–3 GHz.
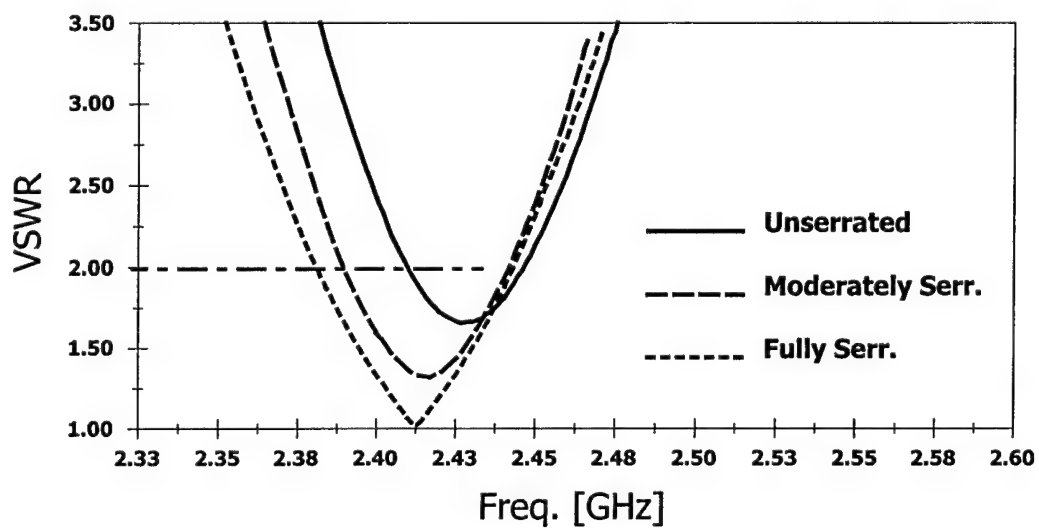
Figure 3: Measured 2:1 VSWR for the diagonally fed (dual linear) antenna.

314
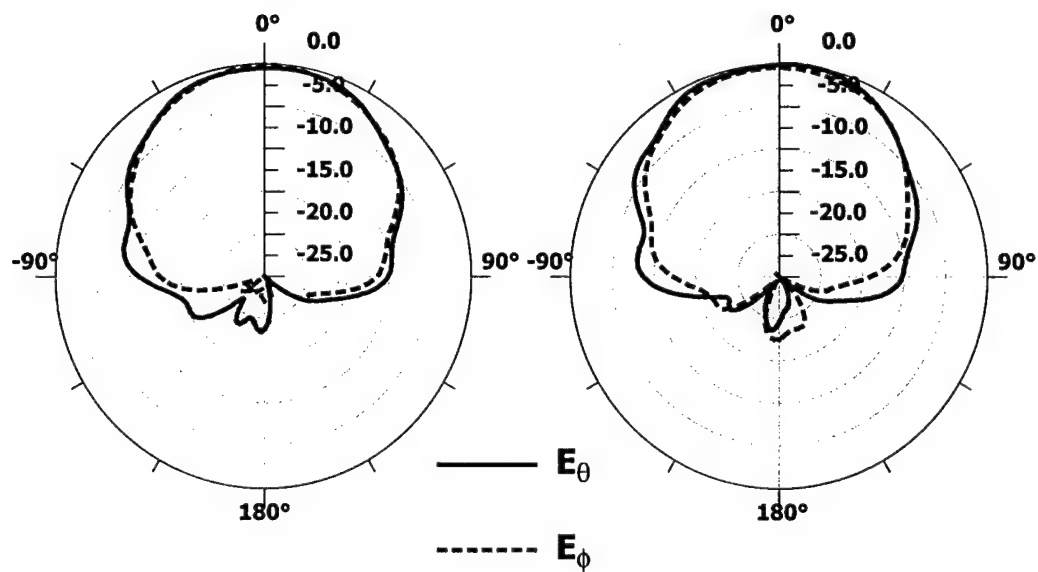
Figure 4: Measured E-plane (left) and H-plane (right) elevation radiation patterns for the diagonally fed unserrated ground plane at 2.43 GHz.
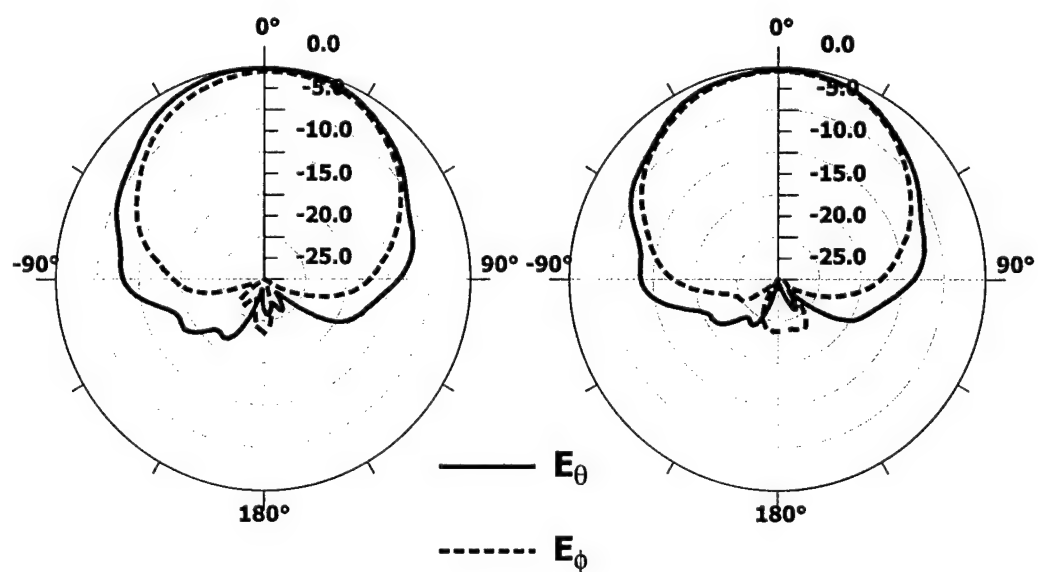
Figure 5: Measured E-plane (left) and H-plane (right) elevation radiation patterns for the diagonal fed moderately serrated ground plane at 2.43 GHz.
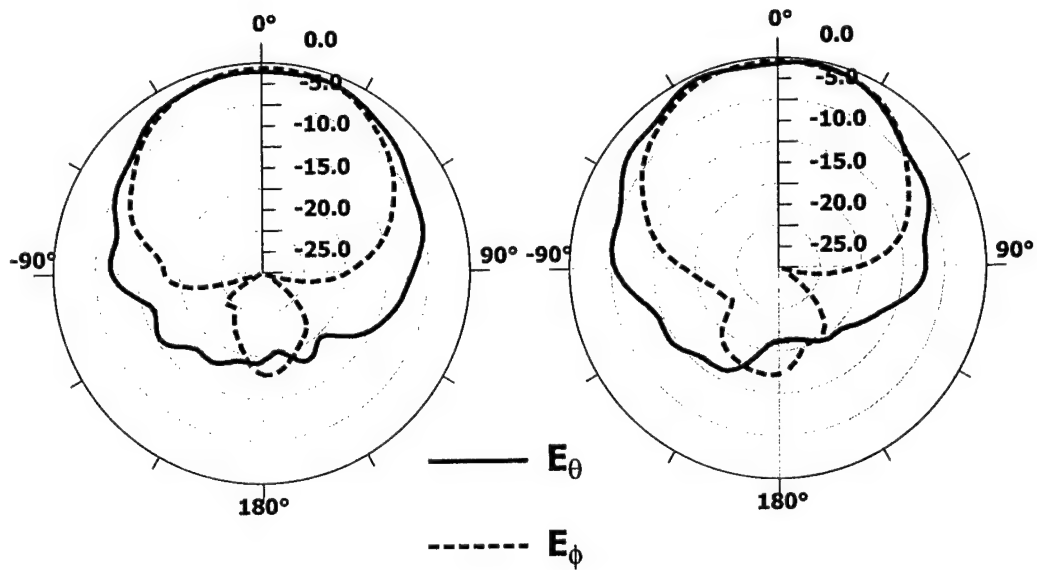
Figure 6: Measured E-plane (left) and H-plane (right) elevation radiation patterns for the diagonally fed fully serrated ground plane at 2.43 GHz.

	3dB	8dB	10dB	Front to Back
Unserr. E_θ	82.67°	155.83°	180.8°	18.71 dB
Unserr. E_ϕ	78.86°	134.69°	163.43°	22.06 dB
Mod. Serr. E_θ	90.76°	178.12°	194.99°	21.29 dB
Mod. Serr. E_ϕ	83.09°	139.49°	156.91°	18.6 dB
Fully Serr. E_θ	95.8°	199.84°	226.51°	14.46 dB
Fully Serr. E_ϕ	79.86°	133.78°	148.48°	12.92 dB

Table 1. Beamwidth analysis at 2.43 GHz for all three cases of the diagonally fed antenna.

316
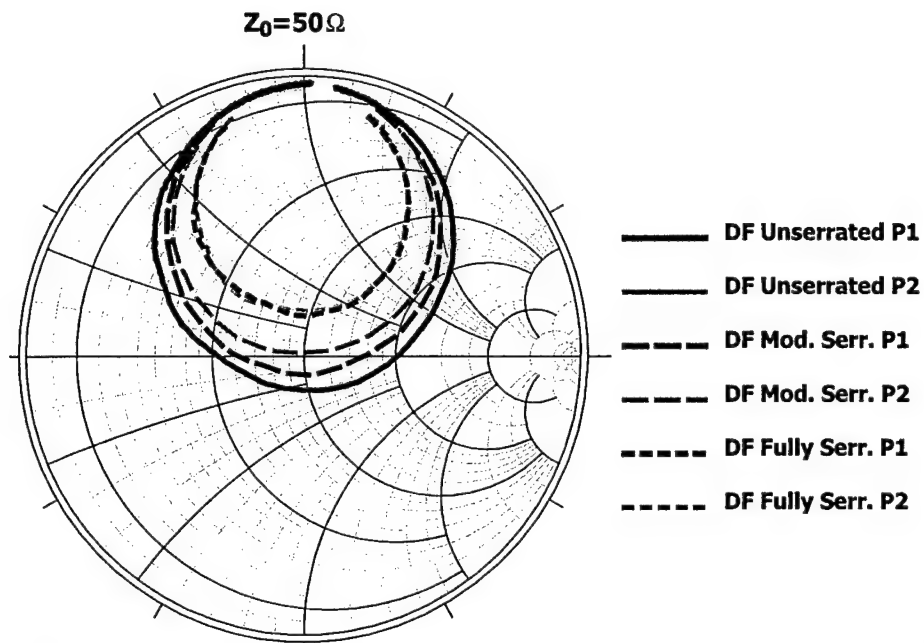
Figure 7: Measured input impedance for the dual fed antennas (for circular polarization) over the range approximately 2–3 GHz.
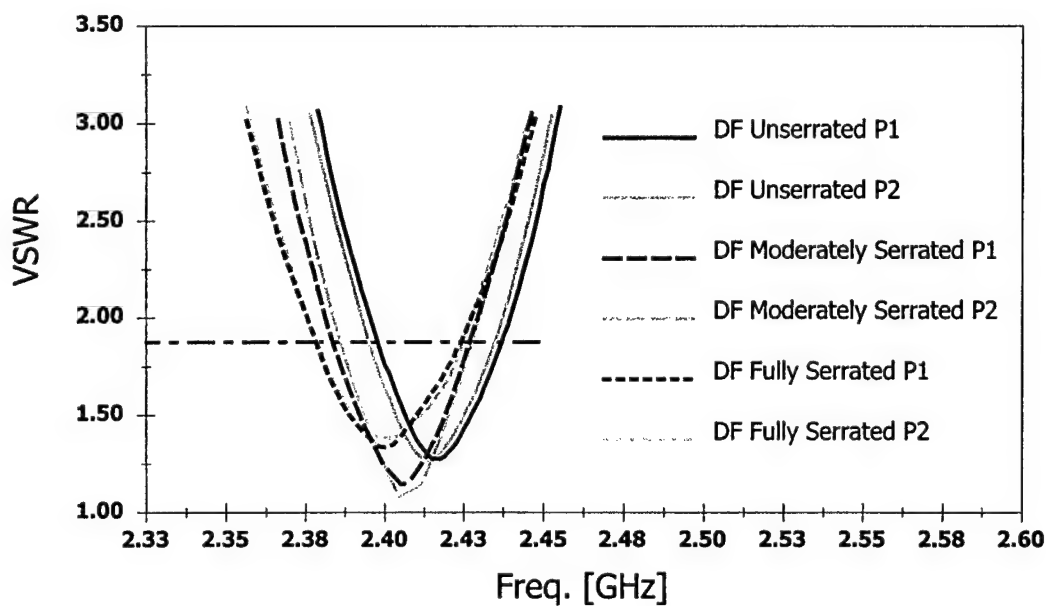
Figure 8: Measured VSWR of the dual fed antennas (for circular polarization), port 1 in black and port 2 in gray.
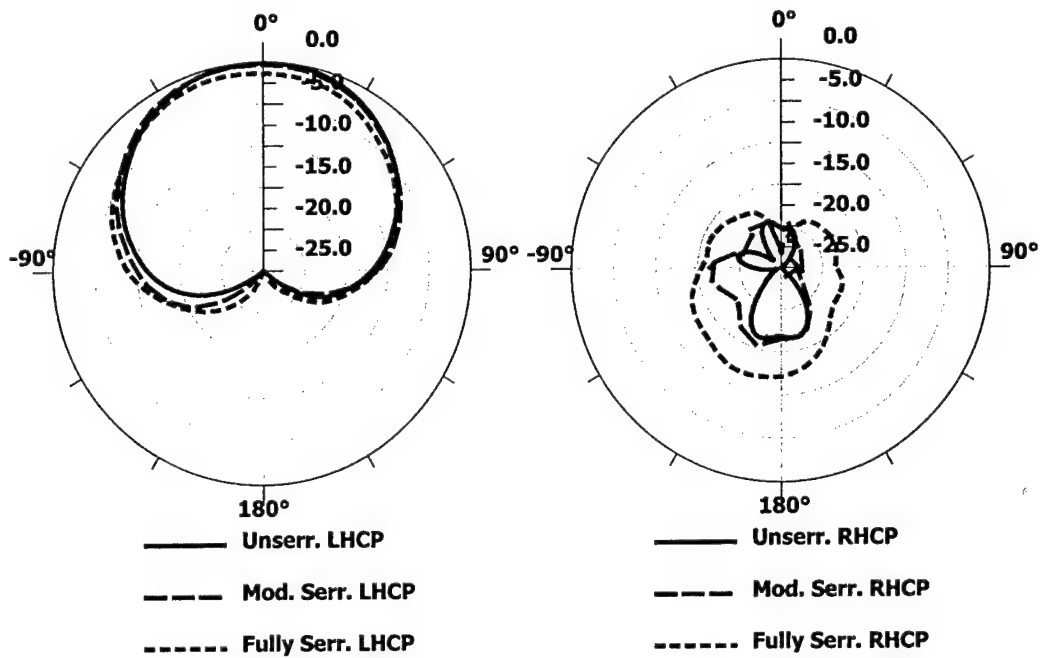
Figure 9: Measured LHCP ('co-polar' - left) and RHCP ('cross-polar' - right) for the three antennas at 2.41 GHz.

Serration and Polarization	3dB & (%Diff)	8dB & (%Diff)	10dB & (%Diff)	Front to Back [dB]
Unserr. LHCP	84.93°	144.06°	165.12°	26.3
Mod. Serr. LHCP	88.46° (+1.78 %)	154.67° (+7.10 %)	177.85° (+7.42 %)	29.18
Fully Serr. LHCP	95.9° (+12.13 %)	169.17° (+16.03 %)	190.9° (+14.48 %)	28.39

Table 2: Beamwidth analysis at 2.41 GHz for all three cases of the dual fed antenna (for circular polarization).

318
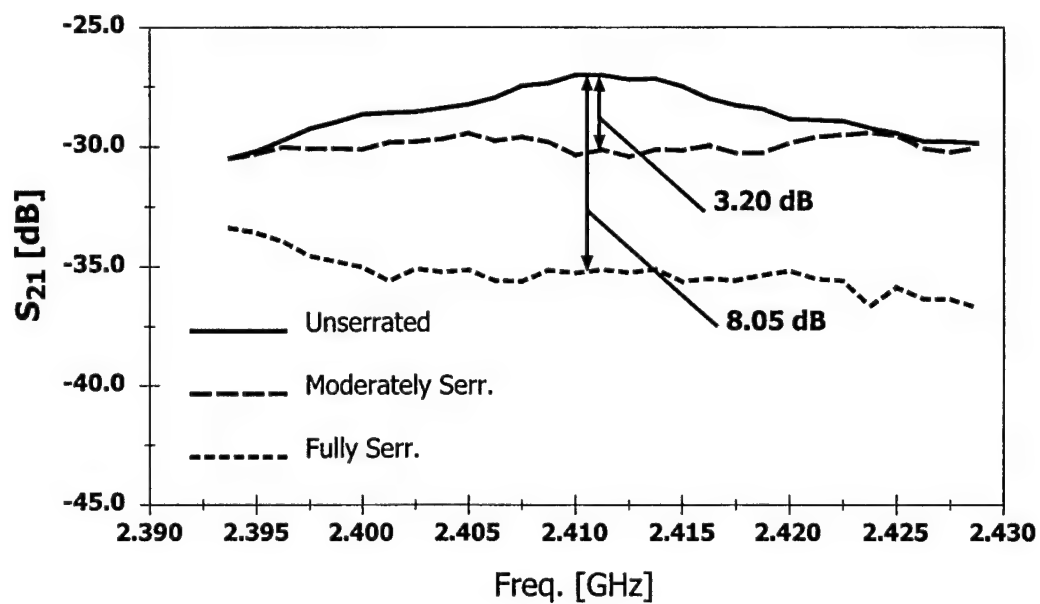
Figure 10: Port isolation in the dual fed case. Markers represent center of overlapping 2:1 VSWR bandwidth (see Figure 8), 2.413 GHz, for all three antennas.
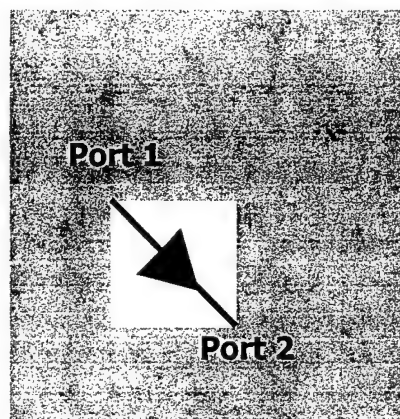
Figure 11: Active reflectarray element as designed in [10].

ON THE PERFORMANCE PROPERTIES OF A MULTIBAND CONICAL MONOPOLE ANTENNA

Steven R. Best
8 Tamarack Lane
Townsend, MA 01469
srbest@att.net

Abstract: The multiband behavior of the self-similar Sierpinski Gasket monopole has been extensively considered in the literature. While the Sierpinski Gasket monopole exhibits a certain degree of multiband behavior in terms of its impedance characteristics, its overall performance properties are less than desirable. Specifically, the Sierpinski Gasket monopole exhibits relatively narrow bandwidths in each of its operating bands and its radiation patterns exhibit poor omnidirectionality because of its asymmetrical 2-dimensional bow-tie shape. Here, a multiband conical monopole antenna is presented that is designed to operate in the same frequency bands as the Sierpinski Gasket. The conical monopole antenna, being a three-dimensional design, offers increased impedance bandwidths and an improvement in radiation pattern performance.

1. Introduction

The multiband behavior of the self-similar Sierpinski Gasket monopole antenna has been described in the literature and has been shown to be a direct function of its gap structure [1]–[3]. Specifically, it has been demonstrated that its multiband behavior is a direct function of the four gaps located along the central axis of the antenna [4], [5]. While the Sierpinski Gasket exhibits a certain degree of multiband behavior, its bandwidths are relatively narrow and its radiation patterns are less than ideal. Typically, the Sierpinski Gasket exhibits a multi-lobe pattern in the elevation sweep plane and it exhibits a high degree of bi-directionality in the azimuth sweep plane.

To improve the radiation characteristics of the Sierpinski Gasket antenna, a three-dimensional conical monopole antenna is derived from the details of the Sierpinski Gasket's gap structure that primarily defines its multiband behavior. This three-dimensional conical monopole exhibits broader impedance bandwidths and improved radiation pattern performance.

2. The Sierpinski Gasket Monopole

The Sierpinski Gasket monopole antenna is comprised of four self-similar sub gaskets, as illustrated in Figure 1. The Sierpinski Gasket considered here has an overall height of 15.24 cm. The extent and height of each self-similar sub gasket are also illustrated in Figure 1. The measured multiband behavior of this Sierpinski Gasket monopole is illustrated in Figure 2, which depicts the return loss characteristics of the antenna relative to 50 ohms characteristic impedance. The return loss characteristics of this antenna were measured over a frequency range of 50 MHz to 12 GHz. The Sierpinski Gasket was mounted directly over a 120 cm by 120 cm conducting ground plane and was base fed using an SMA connector. There are five primary operating bands exhibited by the Sierpinski Gasket. The first is created by the basic structure of the bow-tie monopole itself. The second is created by both the basic bow-tie structure and the largest gap introduced by the first fractal iteration. The remaining three operating bands are created by the second, third and fourth fractal iterations.
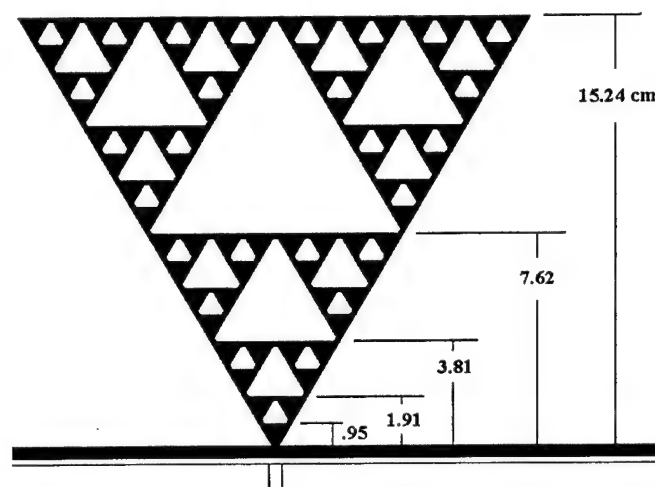
Figure 1. The Sierpinski Gasket Monopole Antenna.

However, the full gap structure introduced by each fractal iteration is not required to create the operating bands. It has been demonstrated that the multiband behavior of the Sierpinski Gasket is primarily a function of the four main gaps located along the central vertical axis of the structure [4], [5]. Additionally, these gaps can be significantly truncated as illustrated in Figure 3, and the operating

321

bands of the Sierpinski Gasket will essentially be maintained [6]. The measured return loss characteristics of this modified Gasket are compared with those of the Sierpinski Gasket in Figure 4. From these return loss characteristics, it is evident that the modified Gasket exhibits essentially identical or improved operating band characteristics.
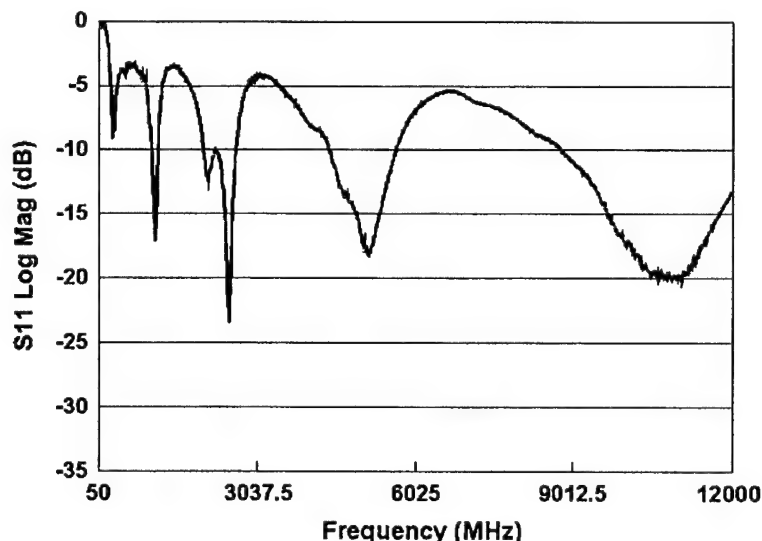
Figure 2. Input Return Loss of the Sierpinski Gasket Monopole.

Two of the performance disadvantages associated with the Sierpinski Gasket include its relatively narrow bandwidths in its lower operating bands and its asymmetrical radiation patterns, which are depicted in Figure 5. To measure the radiation patterns of the Sierpinski Gasket monopole, it was base fed and mounted over a 60 cm diameter circular ground plane. While the finite edge of the ground plane impacts the radiation pattern characteristics of the monopole antenna, it does not contribute to the pattern asymmetry occurring between the $\phi = 0°$ and $\phi = 90°$ sweep planes. This asymmetry is a direct function of the 2-dimensional nature of the Sierpinski Gasket's structure. Additionally, the radiation patterns in the $\phi = 0°$ sweep plane exhibit a high degree of lobing with increasing operating frequency due the array factor associated with the fact that the current is primary concentrated along the two edges of the gasket structure [6].

322
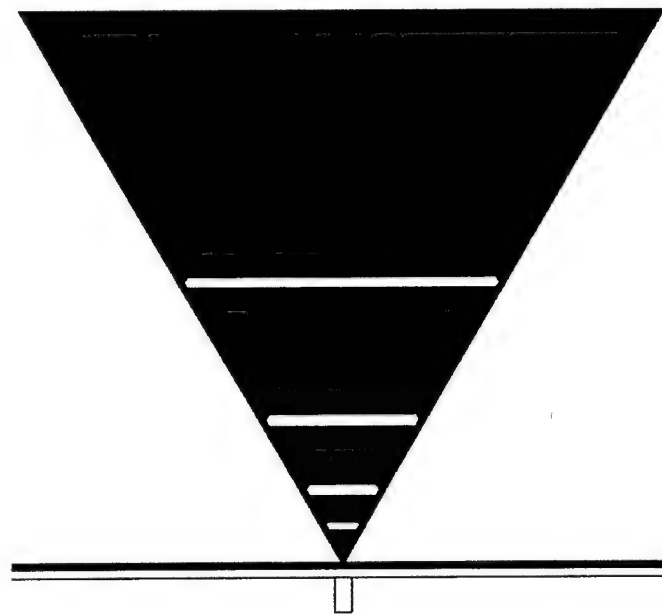
Figure 3. Modified Gasket Monopole Antenna.
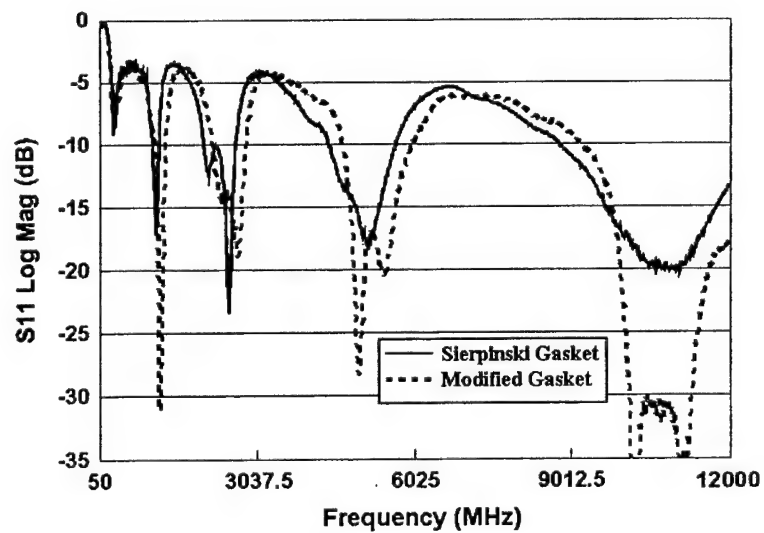
Figure 4. Return Loss Comparison between the Sierpinski Gasket and the Modified Gasket.

323
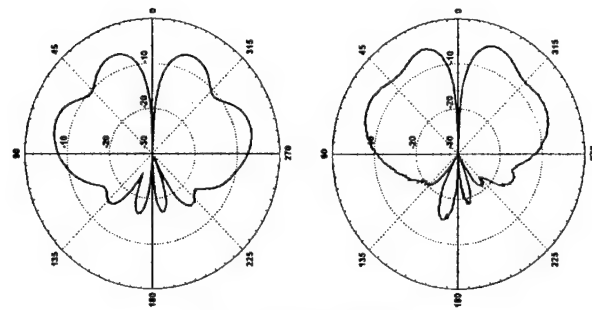
(a) 1125 MHz
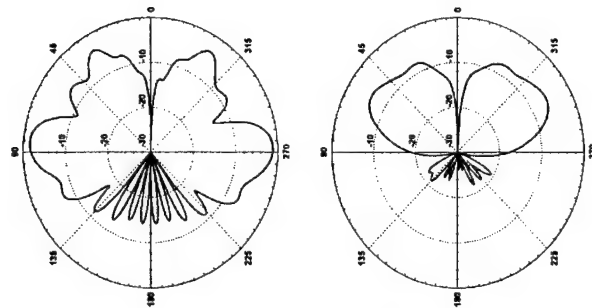
(b) 2440 MHz

(c) 5083 MHz

$$\phi = 0^{o} \qquad\qquad \phi = 90^{o}$$
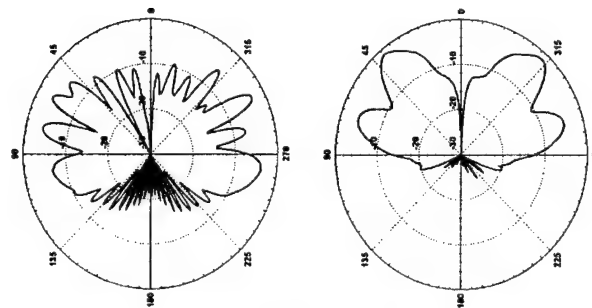
Figure 5. Radiation Patterns of the Sierpinski Gasket Monopole Antenna.

To improve the radiation characteristics of the Sierpinski Gasket, the modified Gasket depicted in Figure 3, is converted into a 3-dimensional structure.

3. The Multiband Conical Monopole Antenna

To improve the radiation pattern symmetry of the Sierpinski Gasket, the 2-dimensional nature of its bow-tie structure must be made more symmetrical, which requires that it be made into a 3-dimensional conical shape. This will improve the omnidirectionality of its radiation patterns and should also increase the operating bandwidth because of the increase in the overall width of the structure. Given the complexity of the Sierpinski Gasket's fractal gap structure, conversion to a 3-dimensional conical shape would be difficult. Fortunately, conversion of the modified Sierpinski Gasket to a 3-dimensional conical shape is relatively simple. The 3-dimensional implementation of the modified Sierpinski Gasket is depicted in Figure 6.
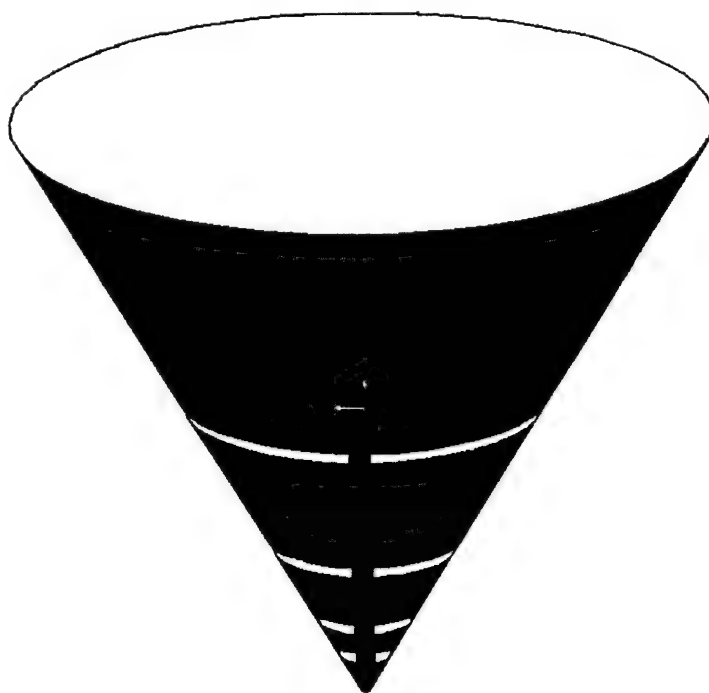
Figure 6. 3-Dimensional Conical Monopole Antenna.

This conical monopole antenna has the same height as the Sierpinski Gasket and the same gap placement. A comparison of the measured return loss of this conical monopole and the Sierpinski Gasket is presented in Figure 7. The conical

monopole antenna was base fed and mounted over the same 120 cm by 120 cm ground plane. Examining the return loss characteristics of this antenna, it is evident that it exhibits multiband behavior similar to that of the Sierpinski Gasket. While there is some upward shift in the operating bands at higher frequencies, this antenna exhibits a significant improvement in terms of both the impedance match and operating bandwidth in each band. In fact, the SWR of this antenna is better than 2:1 over most of the entire frequency band from 300 MHz through 12 GHz.
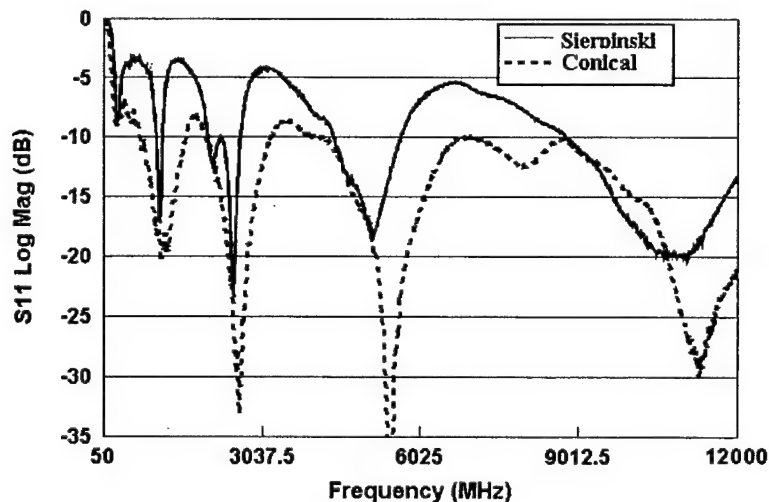
Figure 7. Comparison of the Return Loss Characteristics of the Conical Monopole and the Sierpinski Gasket.

The radiation patterns of the conical monopole antenna were also measured on the 60 cm circular ground plane. Radiation patterns for this antenna, in the $\phi = 0°$ sweep plane are presented in Figure 8. These patterns were measured at the points of minimum return loss. There is a significant improvement in the pattern lobe structure and symmetry as these patterns are duplicated in the $\phi = 90°$ sweep plane. It is also significant to note that these radiation patterns exhibit a greater degree of similarity between operating bands than those of the Sierpinski Gasket.

While, these preliminary results demonstrate that this 3-dimensional conical monopole offers significant performance improvement over the 2-dimensional Sierpinski gasket, further study is required. Further pattern measurements are required to study the full pattern omnidirectionality and lobe structure over the full extent of each operating band. Additionally, a dipole version of this antenna

is to be constructed and compared with the dipole version of the Sierpinski Gasket. Finally, modification of the gap structure is to be implemented to see if the broadband impedance characteristics of this antenna can be further improved.

(a) 1125 MHz   **(b) 2650 MHz**

(c) 5500 MHz
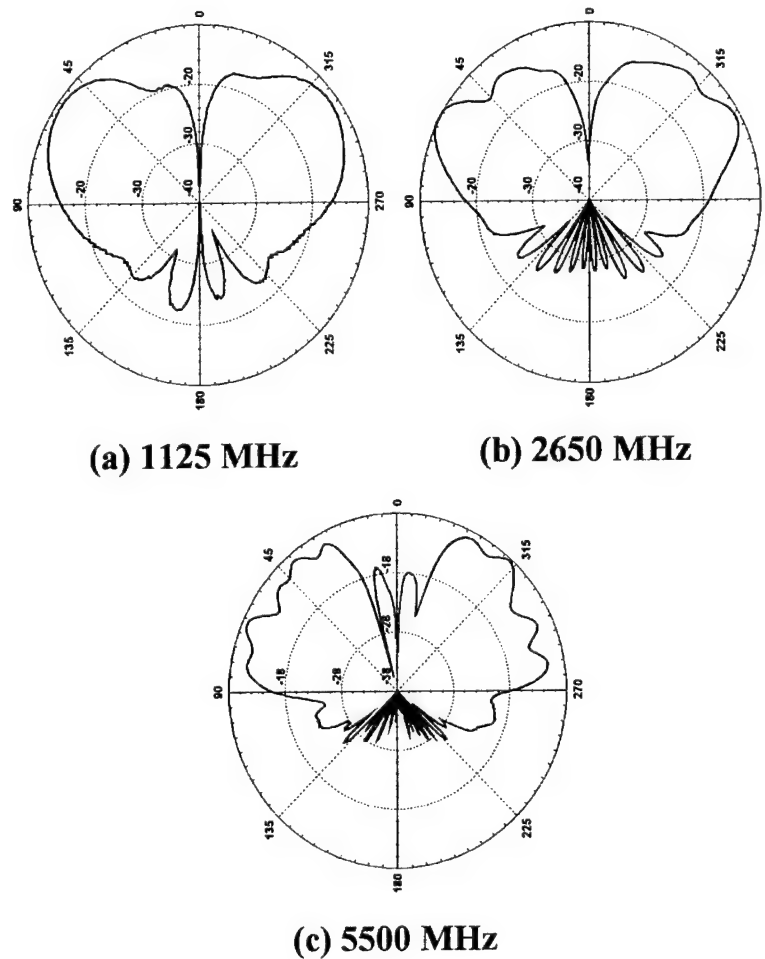
Figure 8. Radiation Patterns of the Multiband Conical Monopole Antenna.

4. Discussion

A 3-dimensional conical monopole antenna was derived from the gap structure of the Sierpinski Gasket that primarily defines it multiband behavior. This conical monopole offers improved impedance matching and operating bandwidths.

Additionally, preliminary results demonstrate that it offers improved radiation pattern performance. Further study is required to investigate the full radiation properties of this antenna in each of its operating bands in both the monopole and dipole configurations.

5. References

[1] C. Puente, J. Romeu, R. Pous, X. Garcia and F. Benitez, "Fractal Multiband Antenna Based on the Sierpinski Gasket," *IEE Electronic Letters*, Vol. 32, No. 1, pp. 1-2, January 1996.

[2] C. Puente, J. Romeu, R. Pous, and A. Cardama, "On the Behavior of the Sierpinski Multiband Fractal Antenna," *IEEE Transactions on Antennas and Propagation*, Vol. 46, No. 4, pp. 517 – 524, April 1998.

[3] C. Puente, J. Romeu, R. Bartoleme, and R. Pous, "Perturbation of the Sierpinski Antenna to Allocate Operating Bands," *IEE Electronic Letters*, Vol. 32, No. 24, pp. 2186-2188, November 1996

[4] S. R. Best, "On the Significance of Self-Similar Fractal Geometry in Determining the Multiband Behavior of the Sierpinski Gasket Antenna," *IEEE AWPL*, Vol. 1, No. 1, pp. 22-25, 2002

[5] S. R. Best, "Operating Band Comparison of the Perturbed Sierpinski and Modified Parany Gasket Antennas," *IEEE AWPL*, Vol. 1, No. 1, pp. 35-38, 2002

[6] M. Navarro, J. M. Gonzalez, C. Puente, J. Romeu, and A. Aguasca, "Self-Similar Surface Current Distribution on Fractal Sierpinski Antenna Verified with Infra-red Thermograms," *Proceeding of the IEEE Antennas and Propagation Society International Symposium*, Vol. 3, pp. 1566 – 1569, Orlando, FL, July 1999.

MINIATURIZATION OF MICROSTRIP PATCH ANTENNAS USING THE SIERPINSKI FRACTAL GEOMETRY

Kiyun Han[1,2], Frances J. Harackiewicz[1] and Seokchoo Han[1]
Department of Electrical & Computer Engineering, Southern Illinois
University Carbondale[1]
Carbondale, IL 62901
Vector Fields Inc.[2]
1700 N. Farnsworth Ave.
Aurora, IL 60505

Abstract: Fractal geometries have been applied to antenna design to make multiband and broadband antennas. In addition, fractal geometries have been used to miniaturize the size of antennas. However, miniaturization has been mostly limited to the wire (dipole and loop) antennas. In this paper, microstrip patch antennas are miniaturized using a modified Sierpinski carpet fractal geometry and are compared with the conventional rectangular patch antenna.

Second and third iteration Sierpinski carpet apertures are made on a square patch. The Sierpinski geometry is modified by leaving a thin strip-shape conductor at the middle of the center aperture. This modification allows the probe position to be shifted to obtain 50 ohms. As a result, a 2.184 GHz square Sierpinski patch is about 17.43 % smaller than the conventional 2.184 GHz square patch with the same material. In addition, in this design, which uses probe feeding, the overall antenna volume is smaller than other microstripline-fed fractal antennas, found in the market. Finally, measurement results are compared to FDTD simulation results.

1. Introduction

Fractal antennas have received much attention from antenna designers since Nathan Cohen introduced the fractal antenna in 1988 [1]. After that many fractal geometries have been applied to antenna design. Self-similarity, in which the same geometry repeats with different size, makes fractal antennas a good

candidate for multiband antennas. The single triangle Sierpinski gasket with different iterations has been used to make multiband monopole and dipole antennas [2]. Stacked triangle and carpet Sierpinski gaskets have been used for broadband antennas [3, 4]. Fractal geometries have also been used to miniaturize the size of antennas. Koch curve and Minkowski geometries are used for monopole, dipole and loop antennas to make them smaller [5, 6]. However, miniaturization is mostly limited to the wire antennas and relatively small attempts were made to the microstrip patch. In [6], a torn-square fractal patch is fabricated and compared with a rectangular patch. The Koch curve is applied to the length of the resonant rectangular patch for 5 GHz to reduce the length. As a result, 38 % shorter length is achieved but bandwidth is also decreased to 0.4%. Another new technique to reduce the size of a microstrip antenna with a partially filled high permittivity substrate is proposed in [7]. With that proposed technique, over 50% antenna dimension reduction is achieved compared to the conventional antenna with an air layer placed into the whole volume under the patch.

In this paper, a modified Sierpinski fractal microstrip patch antenna is proposed to reduce the size of the antenna compared to conventional square microstrip patch antenna. The design procedure will be explained and measurement results will be compared with Finite Difference Time Domain (FDTD) simulation results.

2. Design and Results

2.1 Design

Modified second and third iteration Sierpinski carpet geometries are applied to a 2.4 GHz square microstrip patch as follows. First, a single square microstrip patch is designed around 2.4GHz, using 31-mil thickness Rogers RT/Duroid 5870 (ε_r = 2.33) for the substrate. A program 'PATCHD' in [8] is used to decide the patch size. Second, the width and length of the patch is divided by 3 equal lengths. The center square is removed but leave the strip at the center for matching purpose. To make the second iteration Sierpinski carpet apertures, divide the width and length of the patch by 9 equal lengths and remove the center squares from 8 sub-squares. To make the third iteration Sierpinski carpet apertures, divide the width and length of the patch by 27 equal lengths and remove the center squares from 64 sub-squares. The final shapes of the second and third iteration fractal patches are in Figure 1 (a) and (b) respectively.

Several fractal patches are made with different iterations and different center strip widths to observe the frequency shift. Three second iteration fractal patches are fabricated with 4.47 mm, 3.48 mm, and 1.45 mm widths of the center strip and one third iteration fractal patch is fabricated with 1.45 mm width of the

330

center strip. All patch antennas are fabricated in the Antenna and Propagation Lab at Southern Illinois University Carbondale. The antennas are carefully printed using printed-circuit technology on copper clad substrate. The size of all antennas is 4.02 cm x 4.02 cm and all antennas are made with ε_r = 2.33 and 31-mil thickness substrate with probe feed to reduce the overall volume compare to the transmission feed. The pictures of the fractal antennas and 2.4GHz square patch antenna are shown in Figure 2. Later, a 2.2 GHz square microstrip patch was made to compare the size and SWR with the antenna (b) in Figure 2.

2.2 Results

Simulations are generated with Vector Fields' Concerto software. The measured and simulated return loss versus frequency are compared for the solid square patch and iteration 2 with 1.45 mm wide center strip fractal patch in Figure 3. To obtain 50 ohms, for the second iteration fractal patch antenna, the feed point is shifted from 1.426 cm to 1.633 cm from the edge of the patch. The results between measurement and simulation show about 2.2% and 1.4% differences for the antenna (b) and (d) respectively. As we can see from the Figure 3, the measured resonant frequency is shifted by 7.4% from 2.38 GHz to 2.204 GHz. The size of 2.204 GHz patch is 4.383 cm x 4.383 cm with the same material. Thus with this proposed design, a 15.88% smaller size is achieved compared to the conventional design. Next, iteration 3 with 1.45 mm wide center strip fractal patch is tested. In that case, the resonant frequency is shifted by 8.4% from 2.384 GHz to 2.184 GHz and a 17.4% smaller size is achieved compared to the conventional design. The sizes of two antennas are compared in Figure 4. Measured return losses for various fractal antennas and square patch antenna are shown in Figure 5.

It is found that if more area is removed, the input impedance increases. As a result, the feed point is shifted from 1.426 cm to 1.652 cm from edge of the patch for antenna (e) to (a) to obtain 50 ohms. The typical input resistance values at the edge of the patch are in the 150 – 300 ohms. However in the Sierpinski fractal patch, the values are increased as higher iteration and thinner center strip are used. Thus the input resistance changes rapidly with the position of the feed point. To find an accurate feed point, many simulations were needed. The relation between the resonant frequencies and the amount of removed area from the solid patch and feed points are summarized in Table1.

	Area removed		Frequency shifted	
	Cm^2	%	GHz	%
Antenna (e)	0	0	2.384	0
Antenna (d)	2.9624	18.33	2.26	5.2
Antenna (c)	3.0992	19.18	2.248	5.71
Antenna (b)	3.3698	20.85	2.204	7.55
Antenna (a)	4.7528	29.41	2.184	8.39

Table 1. Area removed and frequency shifted.

Measured bandwidths (SWR < 2) for each antenna are shown in Table 2. Antenna (d) maintains 15 MHz of the same bandwidth with the square patch antenna (e). However, as more area is removed from the patch, the bandwidth is decreased. The rest of the fractal antennas show 12MHz bandwidth. In Figure 6, the SWR of antenna (b) is compared with a 2.2GHz square patch antenna. Antenna (b) shows a little narrower bandwidth than the 2.2 GHz square patch antenna. All bandwidths of the fractal antennas (0.6% - 0.7%) are slightly larger than that (0.4%) in [6].

	f_r (GHz)	Bandwidth (SWR<2)	%
Antenna (a)	2.184	12.0 MHz (2.178 GHz – 2.190 GHz)	0.55
Antenna (b)	2.204	12.0 MHz (2.197 GHz – 2.209 GHz)	0.54
Antenna (c)	2.248	12.0 MHz (2.242 GHz – 2.254 GHz)	0.53
Antenna (d)	2.260	15.0 MHz (2.253 GHz – 2.268 GHz)	0.66
Antenna (e)	2.384	15.0 MHz (2.374 GHz – 2.389 GHz)	0.63

Table 2. Bandwidth of the antennas.

The far-field patterns are simulated with Vector Fields' Concerto for the antenna (b) and square antenna (e). The results are shown in Figure 7 (a) and (b). Figure 7 (a) shows the E Plane pattern of the antenna (b) and (e) at 2.156 GHz and 2.38 GHz respectively and Figure 7 (b) shows the H Plane pattern of the antenna (b) and (e) at 2.156 GHz and 2.38 GHz respectively. Both the E and H Planes show very similar patterns between the two antennas.

3. Conclusion

The modified Sierpinski fractal geometries have been applied to square patch antennas. It is shown that making the Sierpinski carpet shape apertures on the square patch leads to a lower resonant frequency. As a result, a 17.34% smaller 2.184 GHz fractal patch antenna is made compared to the conventional 2.184 GHz square patch antenna without losing the characteristics. The bandwidth was a little narrower but the simulated pattern was very similar to the square patch. Since this proposed technique uses only a single layer and probe feed, the overall volume is smaller than that of the miniaturization technique using a partially filled high permittivity substrate [7]. In the future, other fractal geometries (Koch curve) will be studied for more size reduction and broadband or multiband patch antennas.

4. Acknowledgement

5. References

[1] N. Cohen, "Fractal Antennas Part 1: Introduction and the Fractal Quad," *Communication Quart.*, pp. 7-22, Summer 1995.

[2] C. Puente, J. Romeu, R. Pous, X. Garcia and F. Benitez, "Fractal Multiband Antenna Based on the Sierpinski Gasket," *IEE Electronics Lett.*, vol. 32, pp. 1-2, Jan. 1996.

[3] G. J. Walker and J. R. James, "Fractal Volume Antennas," *IEE Electronics Lett.*, vol. 34, no 16, pp.1536-1537, Aug. 1998.

[4] C. T. P. Song, P. S. Hall, H. Ghafouri-Shriaz and D. Wake, "Fractal Stacked Monopole with Very Wide Bandwidth," *IEE Electronics Lett.*, vol. 35, no. 12, pp. 945-946, June 1999.

[5] C. Puente Baliarda, Jordi Romeu, and A. Cardama, "The Koch Monopole: A Small Fractal Antenna," *IEEE Trans. Ant. Propagat.*, vol. AP-48 (11), pp. 1773-1781, Nov. 2000.

[6] J. P. Gianvittorio and Y. Rahmat-Samii, "Fractal antennas: A Novel Antenna miniaturization Technique, and Applications," *IEEE Ant. Prpopagat. Magazine*, vol. 44(1), Feb. 2002.

[7] B. Lee, and F. J. Harackiewicz, "Miniature Microstrip Antenna with a Partially Filled High permittivity Substrate," *IEEE Trans. Ant. Propagat.* to appear August 2002.

[8] R. A. Sainati, *CAD of Microstrip Antennas for Wireless Applications*, Boston: Artech House Inc., 1996.
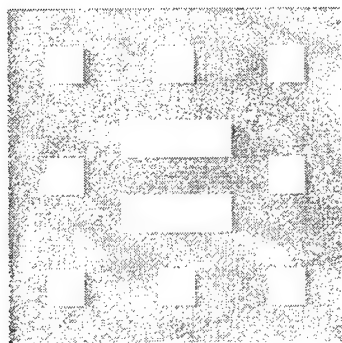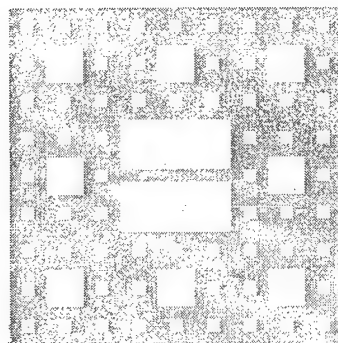
Figure 1. Modified fractal patch after second and third iteration. (a)After second iteration. (b) After third iteration.
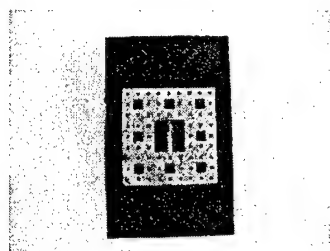
(a) Antenna (a)
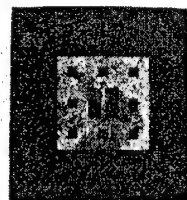
(b) Antenna (b)
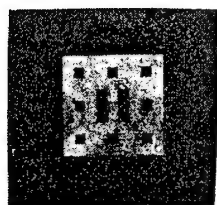
(c) Antenna (c)
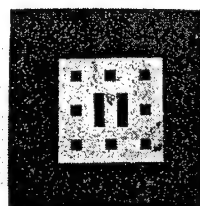
(d) Antenna (d)
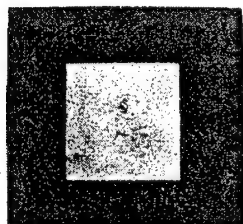
(e) Antenna (e)

Figure 2. Pictures of fractal patch antennas and square patch antenna.
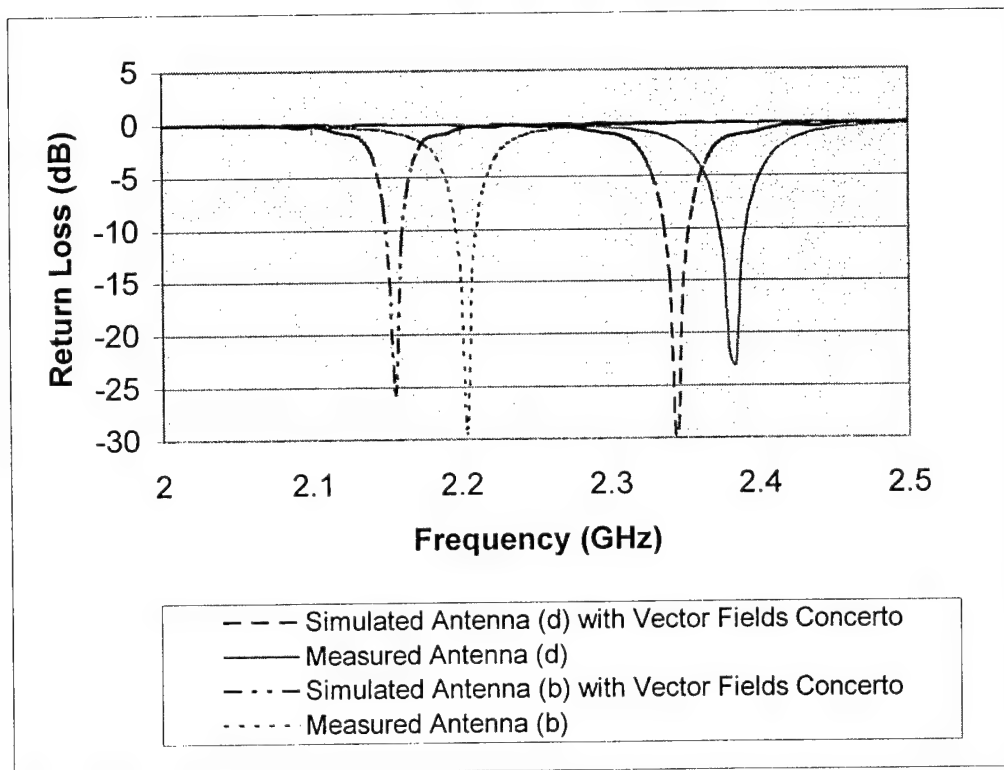
Figure 3. Similated and measured return lossess of antenna (b) and antenna (d).
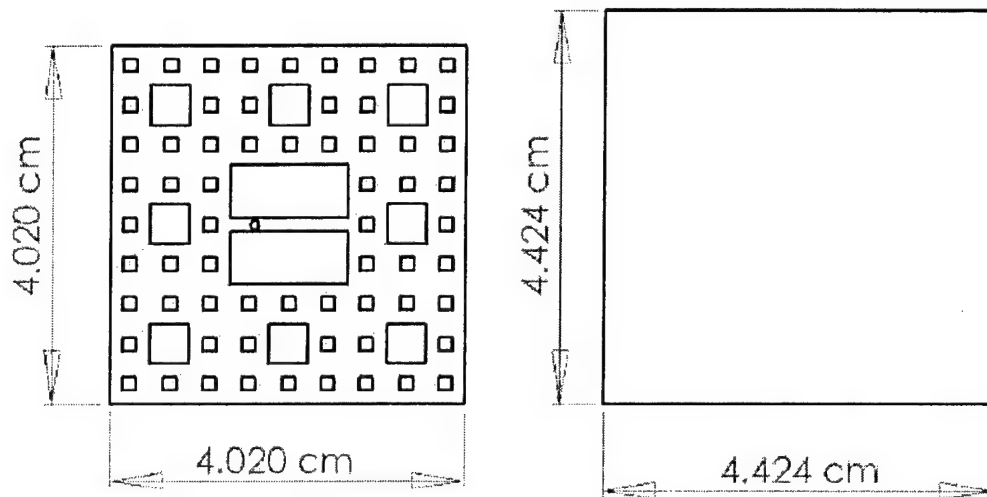
Figure 4. Comparision of the size between antenna (a) and 2.184 GHz square patch. Both antennas have the same resonant frequency but antenna (a) has 17.4% smaller size than square patch antenna.
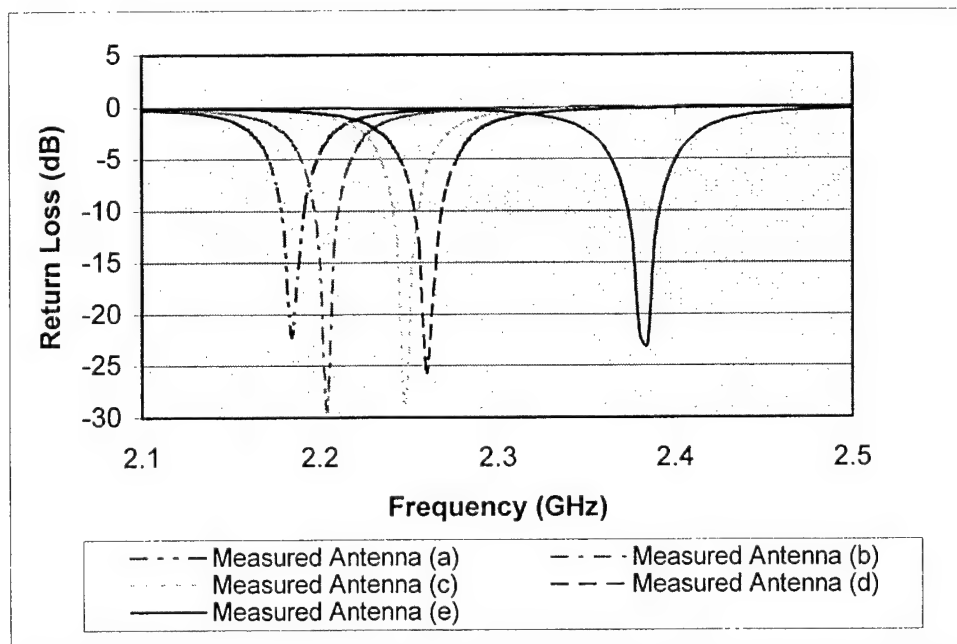
Figure 5. Measured return losses of fractal patch antennas and square patch antenna.
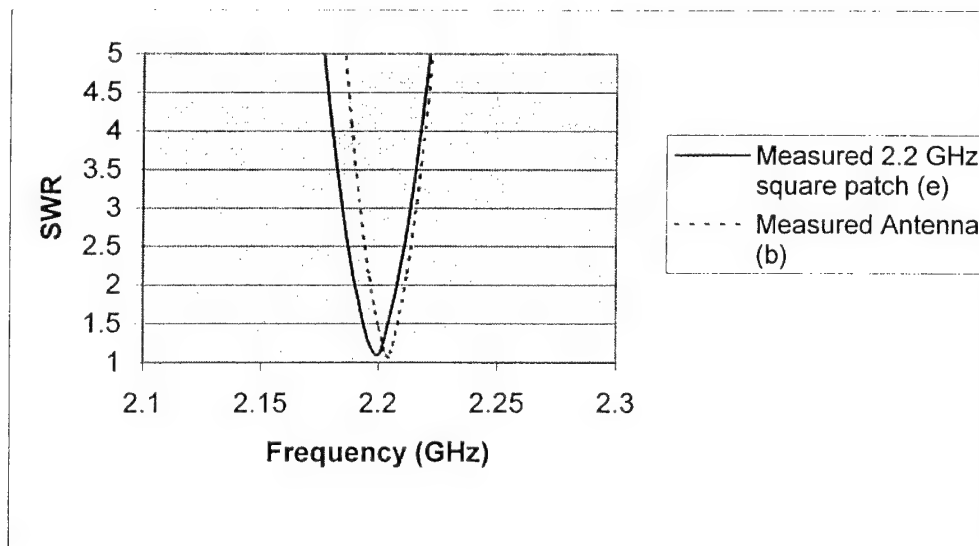
Figure 6. Measured SWR of fractal antenna (b) and 2.2 GHz square patch antenna (e).
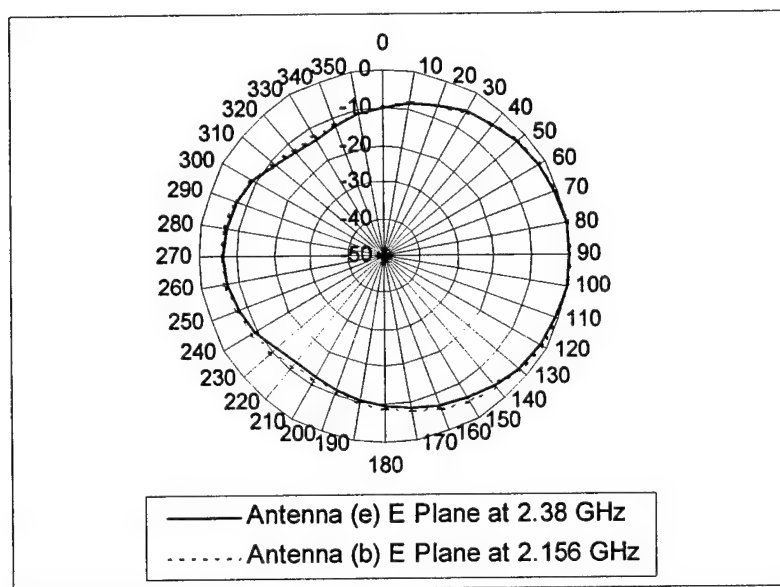
(a)
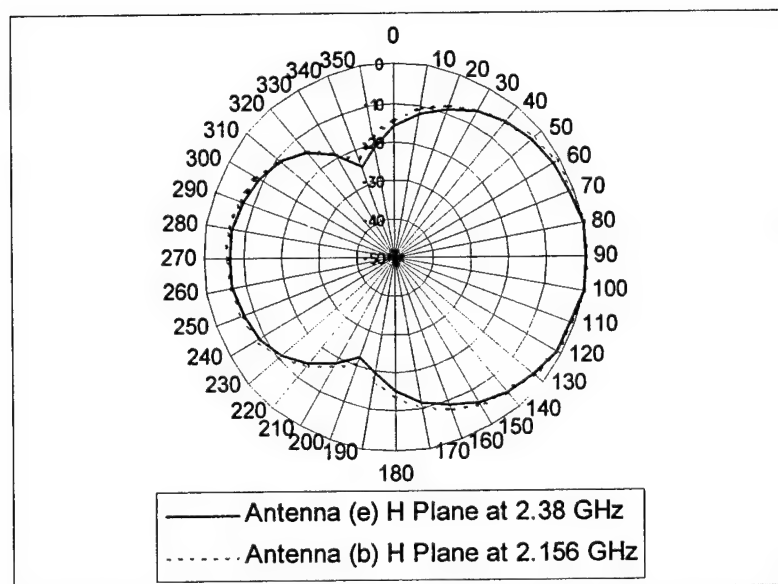
(b)

Figure 7 (a). E Plane patten of the antenna (b) and (e) at 2.156 GHz and 2.38 GHz respectively. (b). H Plane patten of the antenna (b) and (e) at 2.156 GHz and 2.38 GHz respectively.

341

Ultra Wide-Band Radiating Element for Cellular Wireless Applications

Narian Izzat[1], Fred Hunt[1], Kevin Linehan[1]

[1]Andrew Corporation, Orland Park, Illinois IL 60462

Abstract

Concept designs for a wide-band radiating element are presented together with results from theoretical models and practical realizations of the element. The element is designed to cover the frequency range: 860 MHz to 2.17 GHz. The element is vertically polarized, with wide azimuth beam width and input VSWR of 2:1. The maximum dimension of the element is approximately 4 inch for operation at frequencies down to 860 MHz.

1. Introduction

Ever increasing usage of the RF radio spectrum for cellular and micro-cellular wireless applications creates the need for multi-band/wide band radiating elements and antennas. For micro-cellular applications, the antenna typically comprises a single radiating element. For cellular base station applications sector antennas comprising a linear array with single or dual polarity are usually considered.

The present contribution summarizes efforts to develop a wide band vertically polarized element. Ideal requirements for such an element are constant azimuth beamwidth over the frequency band of operation, compact size for use in a wide-band array and a good input match.

In this contribution a wide-band element covering the frequency range of 860 MHz to 2.17 GHz is presented. The concept design is developed as an evolution and modification of the planar log periodic element, the zig-zag element and the sinuous log element and by consideration of self-similarity and frequency scaling.

Theoretical results are presented on the element from electromagnetic modeling tools and measured results are presented from a practical realization. These results show the element to be capable of achieving input VSWR of better than 2:1 with wide azimuth beamwidth. The element is compact with dimensions of approximately 4 inch for operation down to a frequency of 860 MHz.

2. Concept design

In order to achieve wide-band performance, it is important to consider self-similarity and frequency scaling. The concept of self-similarity has received increasing attention over the past few years as a result of perceived future antenna requirements for operation over multiple frequency bands and wide bandwidth. Log-periodic elements are an important subset of self-similar antennas. A wide variety of log-periodic antenna designs are available. The generalized log periodic element is a compound or multi-dimensional element. It can be described in terms of several degrees of freedom. These degrees of freedom are often represented by "sector" angles. Designs for the various types of log periodic antennas generally follow add hoc rules of thumb, which define ranges for the sector angles in order to achieve required values of input impedance and radiated pattern. With increasing computational power, log periodic antennas are nowadays more amenable to analysis through electromagnetic modeling. It is important however to consider the principle of operation of the element from a conceptual point of view.

Figure 1 below outlines the concept design of the element. This shows a twin armed radiating element. Each arm of the element consists of radial sections of an arc. Each section is joined at its end to the next radiating section giving a sequence. Two sector angles define this geometry α and β. The width and spacing of individual sections of the radiating element may be related to each other by a constant scale factor to give a log periodic sequence or alternatively the radius and spacing between the elements may be a constant linear factor.

The two arms of the element are rotationally symmetric through 180°. They may lie in the same plane or alternatively the angle between the two planes of the arms may be varied. In order to realize a vertically polarized element suitable for use as a sector antenna, the arms are rotated by 90 degrees to the x-y plane so as to lie parallel to each other and at a height h above a reflecting ground plane (Figure 2).

These parameters give several degrees of freedom to allow optimization of beamwidth and input impedance. Higher frequency resonant sections of the element are closer to the ground plane compared to lower frequency sections, which reduces variation in azimuth beamwidth with frequency. The height of the element, scale factor and sector angles α, β maybe changed to optimize maximum extent of element for given frequency of operation, input impedance and azimuth beamwidth. The present contribution considers radial arc sections for the element. Radial arms with a sinuous variation may also be considered.
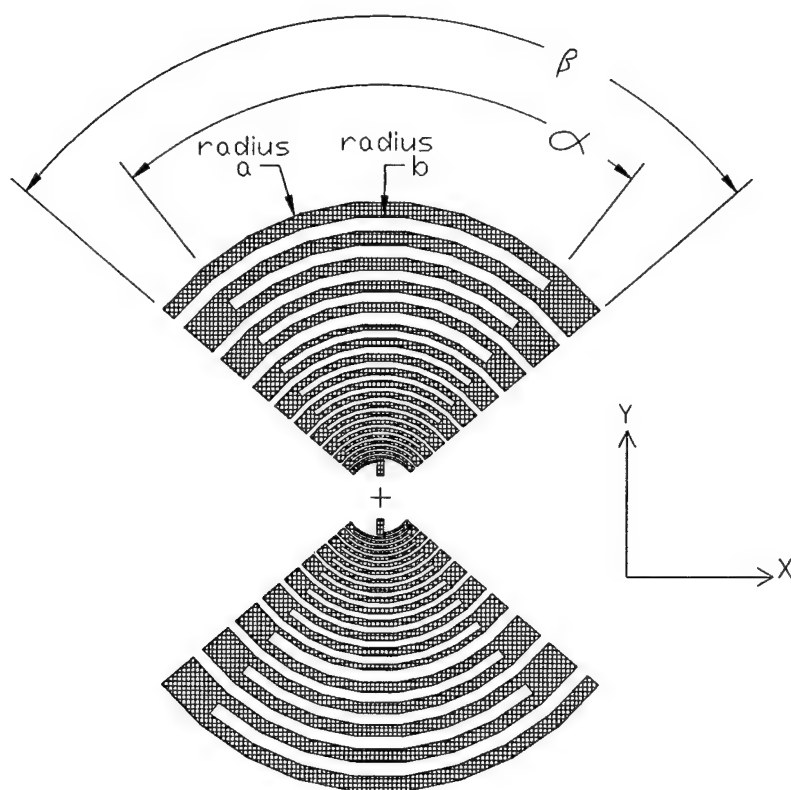
Figure 1. Concept Design for Wide Band Radiating Element
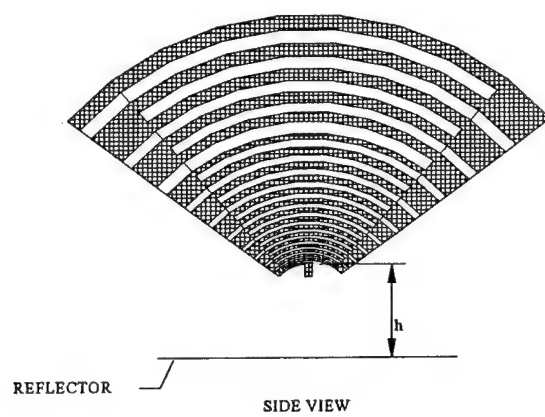
Figure 2. Side view of element at height h above ground.

3.0 Practical realization of the element

An example element was considered based on the above concept. The geometry of the element was modeled using electromagnetic modeling software tools and practically realized on PCB material. The element was modeled for input reflection better than 10 dB down to an operating frequency of 860 MHz and wide azimuth beamwidth.

The element was realized on Taconic RF30-60 printed circuit board material with the two arms of the element etched on either side of the printed circuit board. The element had a maximum extent of approximately 4 inch for operation down to 860 MHz and a height above reflector of approximately 1.5 inch. The height of element above ground is varied in order to optimize the quality factor of the individual resonant sections in the element.

The element was fed using a tapered balun transformer. The transformer consisted of two sections. The first section of the transformer consisted of a triangular taper. This was terminated onto a micro-strip tapered feed line and ground. The input impedance was transformed using this arrangement from a balanced 100-150 Ω down to unbalanced 50 Ω micro-strip feed line.

Figure 3 details the geometry considered for element.
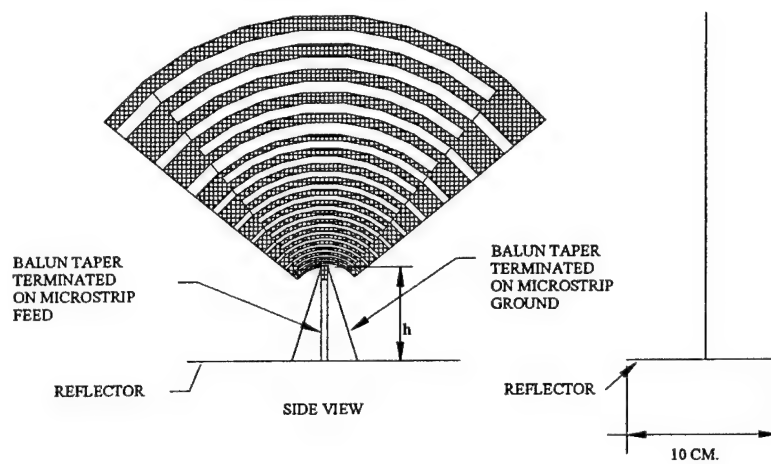
Figure 3. Side and end view of element above reflector ground (10 cm wide). h=3.5 cm. α=33 degree, β=120 degree. Radius of outer-most arc=6 cm.

4.0 Results of measurements on the element

The following section summarizes measured results on the element shown in Figure 3.

Return loss: Return loss of approximately 10 dB was achieved down to an operating frequency of 860 MHz.

Measured patterns: Co-polar and cross-polar patterns for the low frequency band: 860 MHz to 960 MHz and the high frequency band: 1710 MHz to 2170 MHz were measured in an anechoic test facility. These are shown in Figures 4 and 5 respectively.
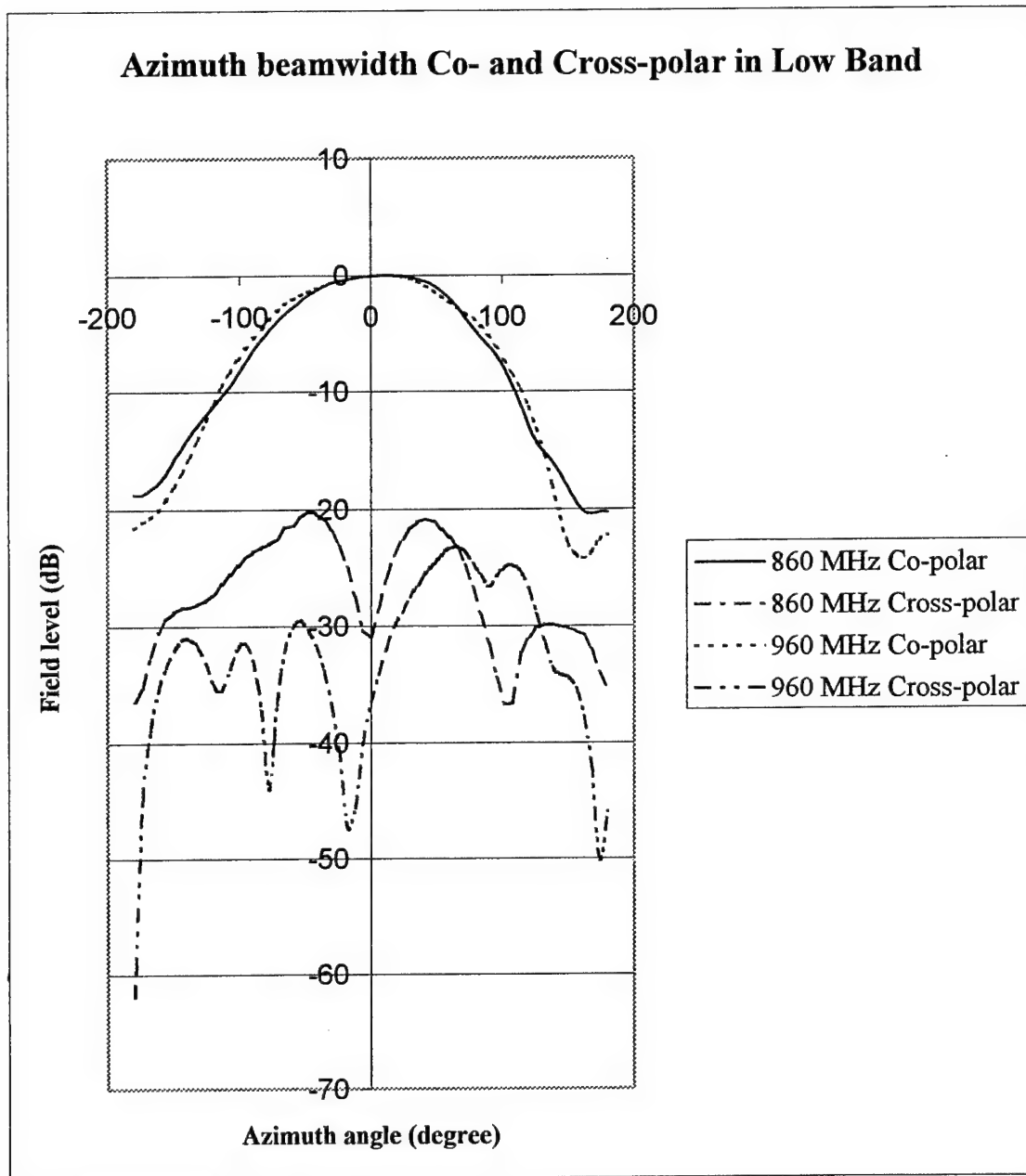
Figure 4. Co- and Cross-Polar Patterns in the frequency band: 860-960 MHz
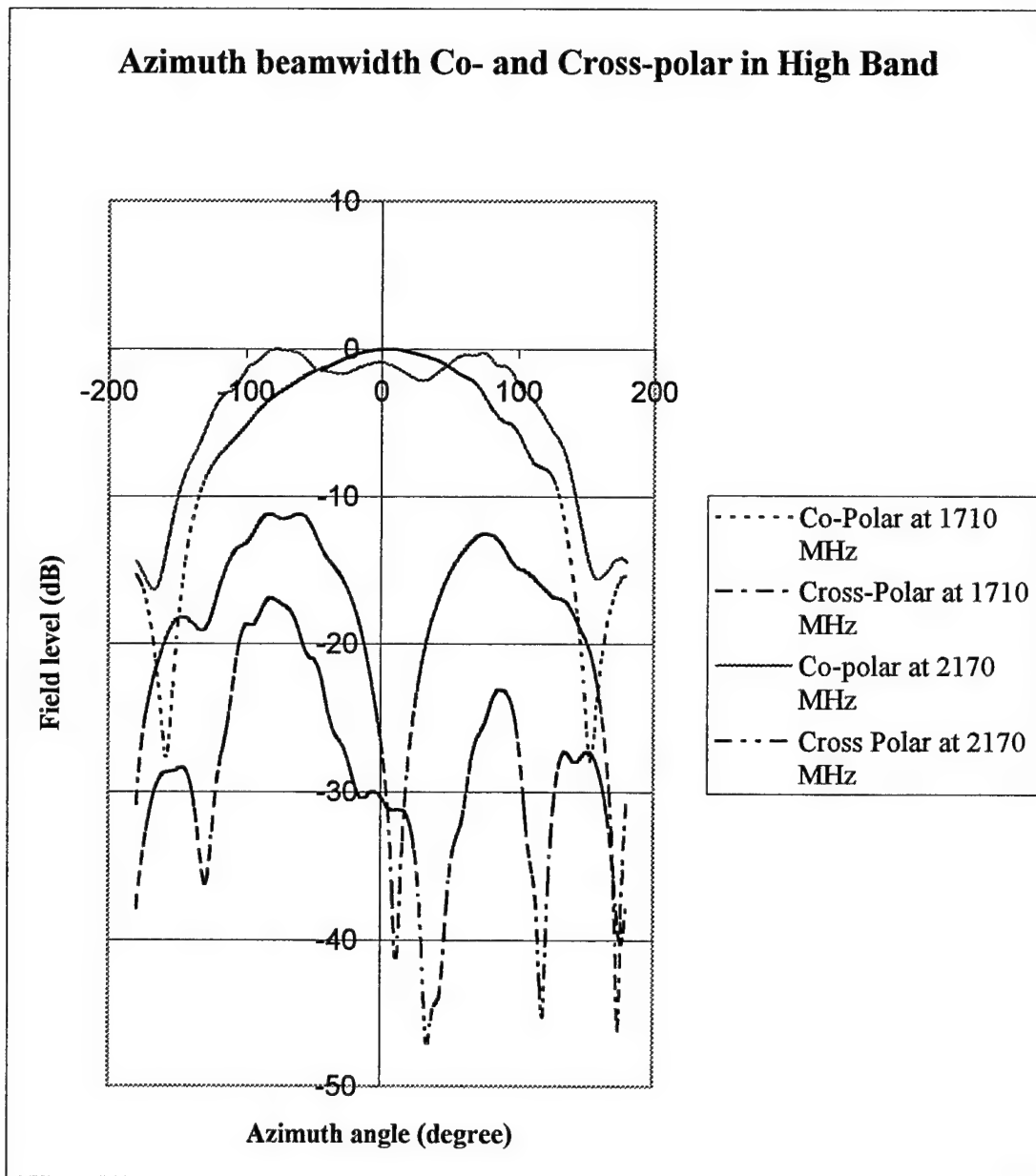
Figure 5. Co- and Cross-Polar Patterns in the frequency band: 1710-2170 MHz

Computed 3 dB beamwidth from the above patterns is tabulated in Table 1 below.

Frequency	Azimuth beam width (degrees)
860 MHz	135
960 MHz	145
1710 MHz	150
2040 MHz	230
2170 MHz	225

Table 1. Measured 3 dB beamwidth for the element.

It should be noted that while a constant beamwidth is measured in the lower operating frequency range, dispersion in azimuth beamwidth is recorded towards the upper end of the frequency band. This may be corrected by varying the height, h, of element above ground or by introducing side-walls in the reflector geometry in order to influence beamwidth in the higher frequency band of operation.

Gain: Gain of the element was measured in the 1710-2170 MHz in the anechoic chamber by gain substitution against a known gain standard. Results from the measurement, indicate a gain for the element in the range of 3-4 dBi.

5.0 Results from EM models

The geometry of Figure 3 was also modeled using electromagnetic modeling tools and the following results obtained:

Return Loss: Better than 10 dB.

Measured patterns: Computed beam width is tabulated in Table 2 below

Frequency	Azimuth beam width (degrees)
860 MHz	170
960 MHz	171
1710 MHz	205
2040 MHz	210
2170 MHz	210

Table 2. Computed 3 dB beam width for a simulation model of the element

Directive Gain: Directive gain was computed for the element based on the computed patterns. Table 3 below gives the computed directivity.

Frequency	Directivity
860 MHz	5.5
960 MHz	5.4
1710 MHz	4.67
2040 MHz	4.43
2170 MHz	4.46

Table 3. Computed Directivity of the element

Comparing directive gain from model results with measured gain for the actual element, it can be seen in general that measured gain is some 1-1.5 dB below directive gain. This is consistent with the overall loss budget of the antenna when we consider Input reflection of −10 dB and loss in the micro-strip feed line section.

Conclusions

General concept design, measured and modeled results are presented for a compact wide band element. The element has a maximum extent of approximately 4 inch for operation down to a frequency range of 860 MHz with wide azimuth beamwidth and return loss better or equal to 10 dB.

Although this contribution presents a design for a vertically polarized configuration with wide azimuth beamwidth, the concept design can be modified for alternative configurations of dual polar or vertically polarized with narrow azimuth beamwidth.

IMPROVED IMPEDANCE BANDWIDTH PREDICTION OF STACKED RECONFIGURABLE BOWTIE ANTENNAS

J. Hazen and J. T. Bernhard
Electromagnetics Laboratory
Department of Electrical and Computer Engineering
University of Illinois at Urbana-Champaign
Urbana, IL 61801

Abstract: This paper presents continuing work on the stacked reconfigurable bowtie antenna, following presented data at Antenna Applications Symposium 2001. Previous work introduced a stacked, dual-polarized microstrip bowtie using a mixed dielectric substrate and ground-plane isolated switches, with a potential impedance bandwidth of 36% for a single band. Previously simulated data modeling has now been updated using finite difference time domain methods with perfectly-matched layer boundaries to gain increased accuracy between simulated and measured results. Additionally, a transmission-line model has been developed to provide insight into the antenna's behavior. Particular attention has been devoted to probe-feed modeling. The new models provide improved agreement with measured data and heightened understanding of the antenna operation. Measured impedance bandwidth derived from the new computational models is presented.

1. Introduction

Preliminary results for a Stacked Reconfigurable Bowtie (SRB) antenna were presented at the 2001 Antenna Applications Symposium [1] . The present work extends our analysis of the SRB using the Finite Difference Time Domain (FDTD) method and transmission-line modeling of antenna components.

The SRB antenna consists of a stacked bowtie antenna in quadrature formation, with layered substrates. The current version of the antenna was designed to operate in the S-band for the lower elements and the X-band for the upper elements. Figure 1 depicts the single element geometry of the SRB and Figure 2 shows a single linear bowtie element of the SRB antenna.
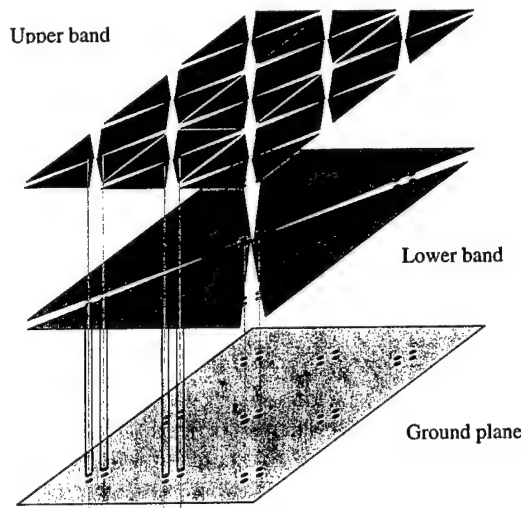
Figure 1: Stacked Reconfigurable Bowtie concept. Lower and upper band elements are alternatively activated using RF MEMS switches below the ground plane.
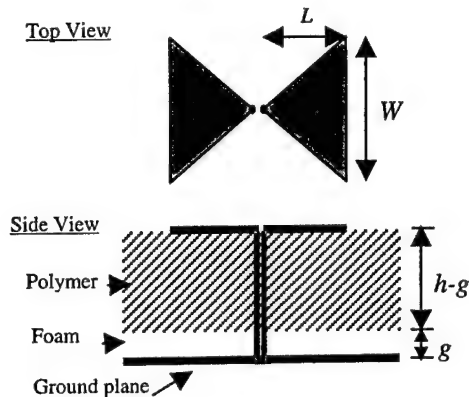
Figure 2: Top and side view of the linear bowtie element.

This paper is organized as follows: Section 2 presents the FDTD impedance simulations of the SRB antenna and compares them to updated IE3D [2] simulations of the same antenna and measured S-parameters. Section 3 describes transmission-line modeling of the linear bowtie antenna, particularly the balanced feed. Finally, Section 4 discusses the results and provides directions for future work.

2. Finite Difference Time Domain Simulation with XFDTD

The finite difference time domain (FDTD) method has several advantages over IE3D's 2D-Planar Method of Moments code for simulating the SRB antenna. XFDTD is a FDTD simulation package that was used to model the SRB antenna [3]. A finite ground plane and substrate, which mimics the fabricated antennas, adds no computational complexity to XFDTD as it does for IE3D. IE3D uses an infinite ground plane for its simulation by default, so a finite ground plane must be drawn separately and requires considerable resources for a convergent solution. Also, whereas an S-band linear stacked bowtie antenna approaches the maximum limitation for the number of unknowns in IE3D, the full SRB can be simulated in XFDTD since FDTD complexity is based on the size of the simulation space and material properties rather than on a maximum number of

354

unknowns. Therefore, for the stacked antenna, XFDTD becomes the simulation tool of choice.

2.1 Linear S-Band Bowtie

In the present work, the Linear S-Band Bowtie that was fabricated and presented in [1] was measured again with port extension calibration to account for the coaxial feed length. IE3D simulations were re-run with 0.9 mm diameter square feeds. The measurements were then compared to the IE3D and XFDTD simulated data, with the results shown in Figures 3 and 4.
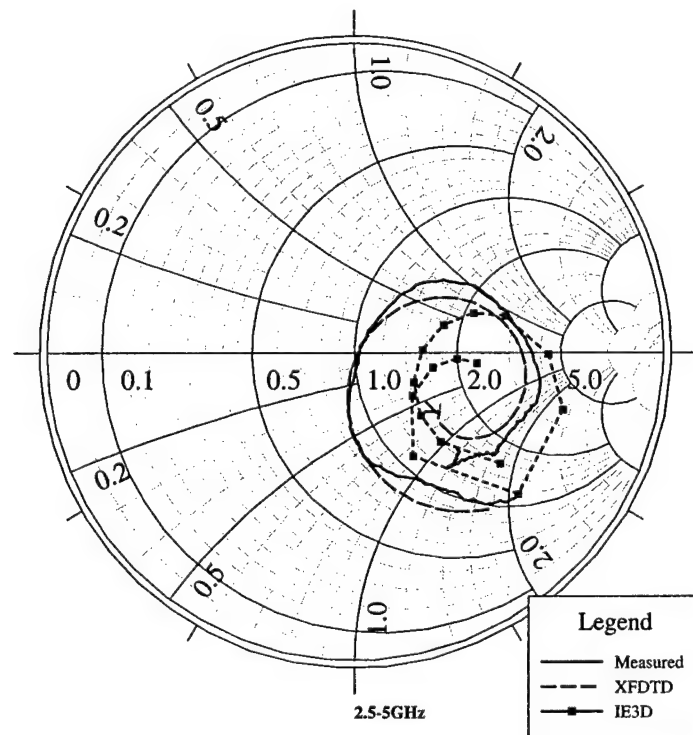
Figure 3: Smith chart S_{11} data for the S-band linear Bowtie.
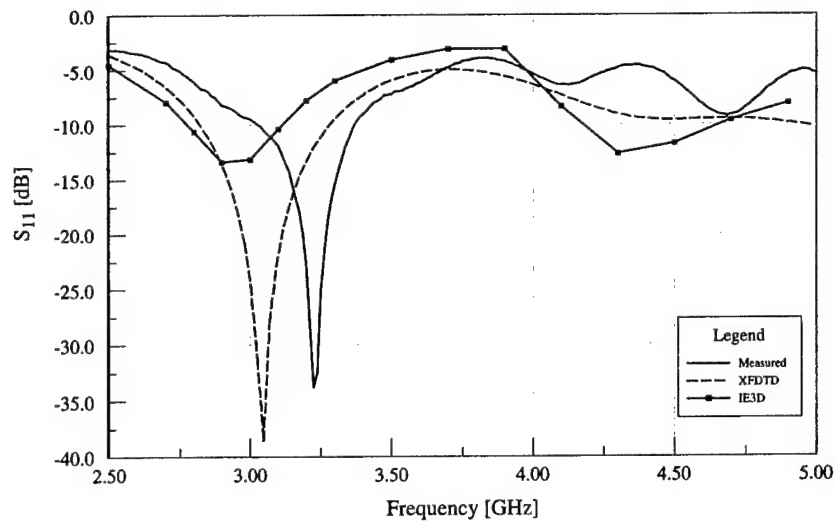
Figure 4: S_{11} Log-magnitude data for the S-band linear bowtie.

In general, XFDTD better models the measured data than IE3D, except for a negative frequency shift. Differences between the simulated and measured results could be due to the necessity to stack multiple layers of dielectric to achieve the desired thickness for the measured prototype. This stacking creates small airgaps between layers that can lower the effective permittivity of the substrate. Other fabrication discrepancies, particularly at the ground-plane junction, that are not accounted for by port-extension measurement could also account for a portion of the disparity.

2.2 Linear X-Band Bowtie

The Linear X-Band bowtie has been newly designed and fabricated to produce the Version 2 simulated and measured results presented in Figures 5 and 6. Version 2 of the Linear X-Band bowtie is similar to Version 1, which was presented in [1] ; however, it uses 0.3 mm diameter feeds with 1.2 mm spacing between the feeds and LCP substrate rather than PTFE substrate. The measured S_{11} is well predicted using XFDTD, as displayed in Figures 5 and 6.
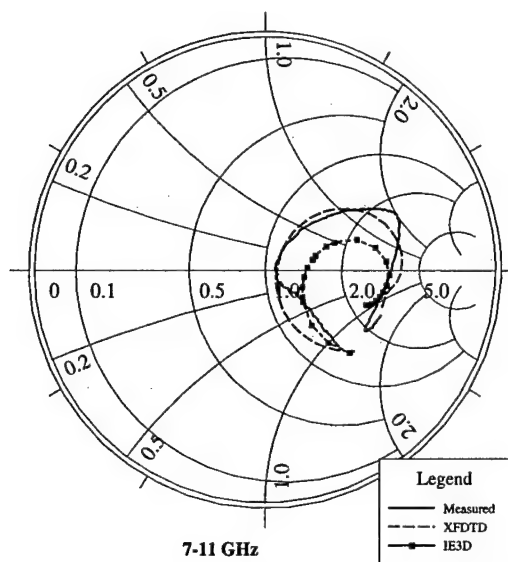
Figure 5: S_{11}, simulated and measured for the Linear X-band Bowtie, Version 2.
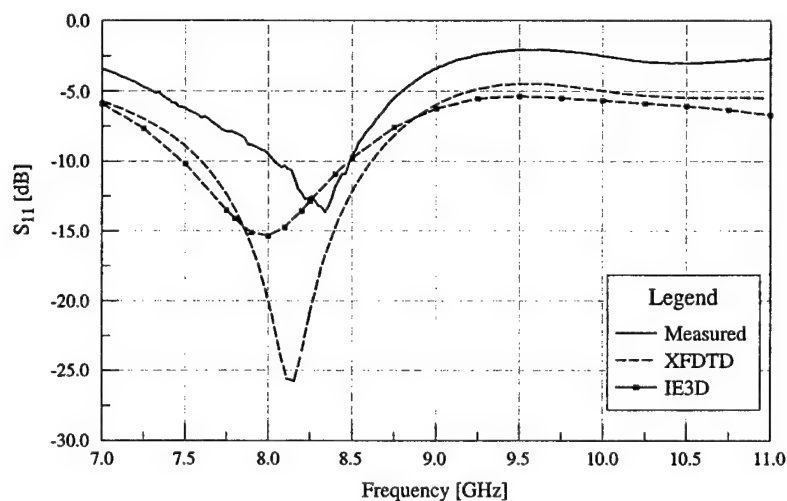
Figure 6: Log-magnitude simulated and measured S_{11} data of the Linear X-band Bowtie, Version 2.

Again, the simulated data has a negative frequency shift from the measured data. Discrepancies between simulated and measured results are probably due to fabrication tolerances.

2.3 Quadrature S-Band Bowtie
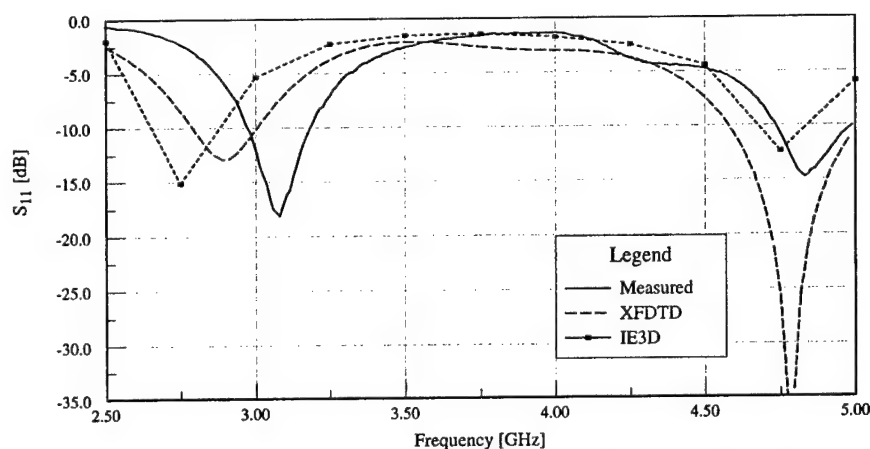
Figure 7: Log-magnitude simulated and measured S_{11} data of the Quadrature S-band Bowtie.

Figure 7 shows the simulated and measured data for the Quadrature S-band bowtie. For the Quadrature bowtie, the XFDTD simulation again better matches the measured data, this time with $|S_{11}|$ minimums closer using XFDTD than IE3D.

2.4 Stacked antenna with no X-Band feeds

Simulation and measurement of the SRB antenna, without X-Band feeds, is given in Figure 8. Again, XFDTD simulates the antenna much better than IE3D does.
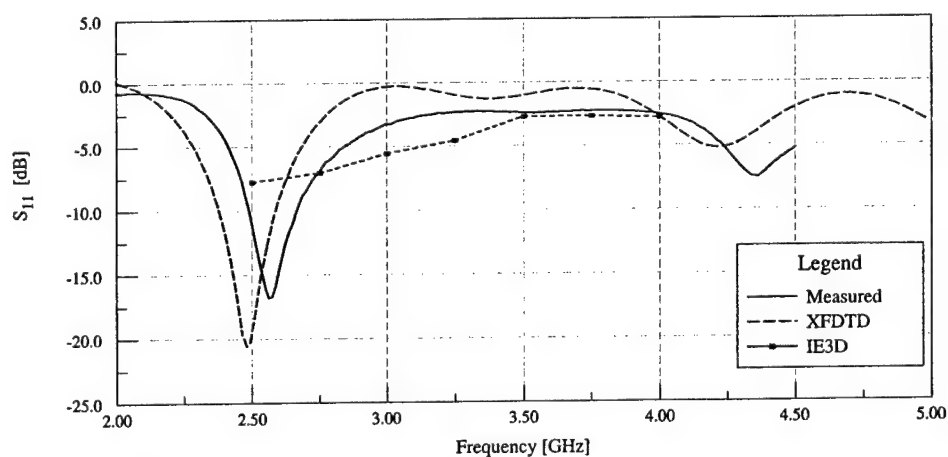
Figure 8: Log-magnitude simulated and measured S_{11} data of the SRB, without X-Band feeds.

358

3. Transmission line modeling of the Linear S-band antenna feeds

To gain a better understanding of how the antenna feeds affect the overall impedance bandwidth of the SRB antenna, we studied the S-band linear bowtie feeds using transmission line theory. The input impedance of a balanced fed linear S-band bowtie was compared to the simulation and measured results of the same structure over several S-band frequencies.

3.1 Transmission Line Model

Lumped element modeling of feeds has been described in [4] and elsewhere. Since h, for $h=h_1+h_2$ as shown in Figure 9 below, is on the order of $\lambda/10$ for both frequency bands of interest, we investigated whether the feeds of the antenna could be modeled as a balanced transmission line. The following diagram illustrates this transmission line modeling, assuming that the two ports are fed with signals of equal magnitude and opposite phase.
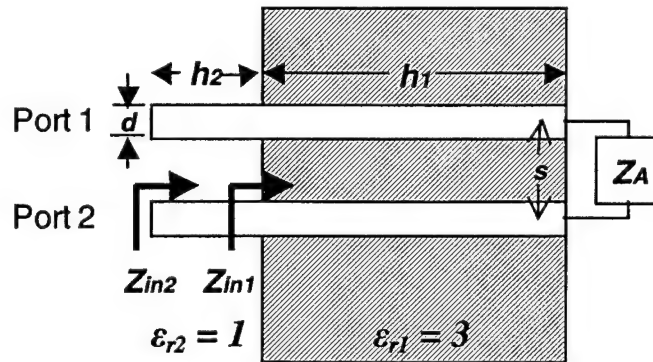
Figure 9: Transmission line model for the linear bowtie antenna.

Z_A, the input impedance of the linear bowtie antenna without its feeds, is acquired using XFDTD with one feed at the center of the bowtie. Z_{in1} is the input impedance of the feed transmission line, looking towards the antenna, at the junction between the substrate and air. Z_{in2} is the input impedance at the ground-plane junction.

359

In reference to the diagram in Figure 9, the well-known twin-wire transmission line equations are given as follows:

$$Z_0 = \sqrt{\frac{L}{C}} = \frac{377\,\Omega/m}{\pi\sqrt{\varepsilon_r}}\cosh^{-1}\left(\frac{s}{d}\right) \tag{1}$$

$$Z_{in1} = Z_{01}\frac{Z_A + jZ_{01}\tan(\beta h_1)}{Z_{01} + jZ_A\tan(\beta h_1)} \tag{2}$$

$$Z_{in2} = Z_{02}\frac{Z_{in1} + jZ_{02}\tan(\beta h_2)}{Z_{02} + jZ_{in1}\tan(\beta h_2)} \tag{3}$$

where $\beta = \dfrac{\omega\sqrt{\varepsilon_r}}{c}$

3.2 Model Comparison to Simulated and Measured Results.

The circuit model in Figure 10 was used to compare the simulated and measured S-parameters to the transmission line model data. Each feed is a port in XFDTD and for the fabricated and measured antenna; however, in a balanced and differential antenna mode, two feeds would be considered a single port with input impedance Z_{in2}. The basic form of this model comes from [5] . Knowing that the voltages at port 1 and 2 are equal and opposite in phase, that $Z_{11} = Z_{22}$ due to antenna symmetry, and $Z_{12} = Z_{21}$ due to passive components and reciprocity, $|I_1| = |I_2|$ and $Z_{in2} = 2(Z_{11} - Z_{21})$.
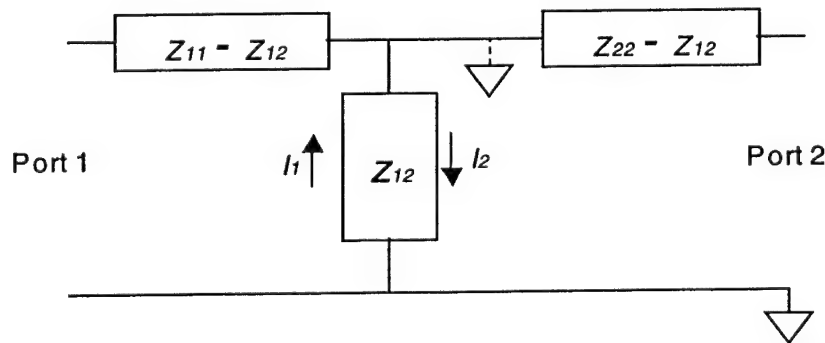
Figure 10: Port description in Z-Parameters of the balanced twin-wire feed.

2.5-5 GHz

Legend
——— T-Line Model, Zin2
– – – XFDTD, Zin2
- - - - - Measured, Zin2
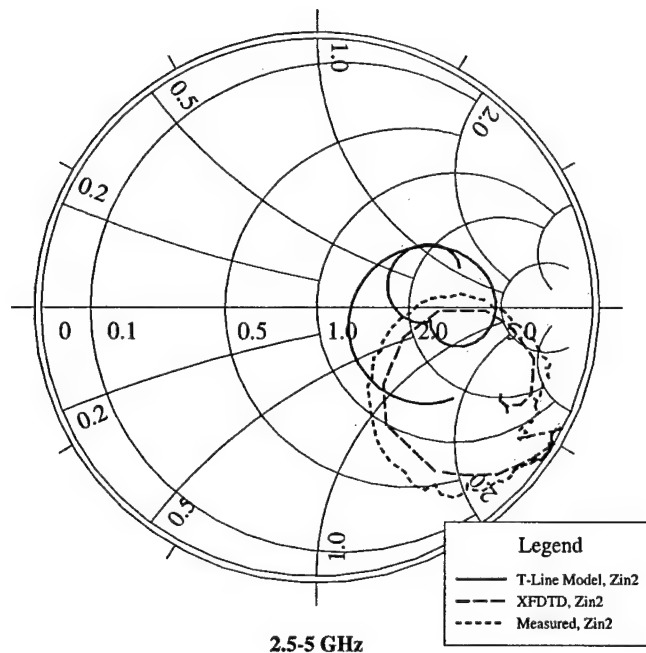
Figure 11: Transmission line model with equivalent XFDTD and measured Z_{in2}.

Figure 11 shows the transmission line model of the S-band linear bowtie antenna along with the same model in XFDTD and the derived data from measurements in balanced mode. The XFDTD plot uses measured S_{21} data in its computation of Z_{in2}, rather than XFDTD simulated S_{21} data. Some low-frequency discrepancies can be accounted for due to x-directional dispersion from the XFDTD calculation of Z_A. Other discrepancies could be due to coupling between the feeds and the bowtie, which is not present in Z_A, scattering and radiation from the feeds, and small variations between the FDTD simulation and fabricated geometries.

4. Conclusions and Future Work

The FDTD simulation better models the linear bowtie antennas and some quadrature and stacked antennas than does a 2.5D, Method of Moments code. Transmission line modeling of the twin-wire feed gives increased understanding to how the feed geometry affects the impedance bandwidth by allowing analysis of variations of feed diameter and spacing.

Future work on the SRB includes modeling the SRB with X-band feeds and analyzing radiation pattern data. Further FDTD simulation and transmission line modeling of the linear bowties will characterize the effect of critical antenna

361

design parameters (especially the feed dimensions) on impedance bandwidth and radiation characteristics.

5. References

[1] J. Hazen, R. Clark, P. Mayes, and J.T. Bernhard, "Stacked reconfigurable antennas for space-based radar applications," *Proc. 2001 Antenna Applications Symposium*, 2001, pp. 59-69.

[2] IE3D, version 8.0. Zeland Software Inc.

[3] XFDTD, version 5.3. Remcom Inc.

[4] B.M. Alarjani and J.S. Dahele, "Feed reactance of rectangular microstrip patch antenna with probe feed," *Electronics Letters*, vol. 36, pp. 388-390, 2 March 2000.

[5] D. M. Pozar, *Microwave Engineering,* New York John Wiley & Sons, Inc. 1998.

STRUCTURE INTEGRATED PATCH ELEMENT FOR X-BAND APPLICATION

Robert Sekora
EADS Deutschland GmbH, Military Aircrafts
P.O.Box 80 11 60
81663 Munich

ABSTRACT

This paper describes the development, design, manufacturing and testing of a patch element for airborne applications in the X-band. The advantage of this design was that the radiating element has to fulfill the electrical requirements as well as the mechanical requirements.

On modern fighter or mission aircrafts more and more antennas have to be integrated. But the proposed antenna locations are limited due to restrictions on the aircraft surface. These constraints require the design and development of antennas, which can be integrated in the aircraft structure.

From our point of view a structure integrated antenna is also a conformal antenna, but a conformal antenna is not always structure integrated. A conformal antenna solution does not fulfill the mechanical requirements of the aircraft structure. These type of antenna leads to a weakness of the aircraft structure which must be compensated by additional measures. An increasing mass for structural parts is inevitable.

The used materials for the antenna layers were a mixture of microwave substrates and typical aircraft materials. This was the reason thatthere must be a trade of within the design process between the electrical and structural requirements.

Because of the layout structure an antenna design with a stacked patch element has been preferred. These type of radiation element allows an integration in a planar antenna array with an electrical beam steering over a wide frequency range.

The requirements for the patch elements has been derived from an antenna system which is used in a commercial data link system.

For the electromagnetic design an in-house software has been used.

The electrical and mechanical requirements has been verified with an representative engineering model. The first test results will be shown in this paper.

1. Requirements

In commercial state of the art data link systems for X-band applications center fed reflector antennas were used as standard components. This antennas require a very large radome which is hard to be integrated in the aircraft structure. These radomes have also great disadvantage for the aerodynamic performance of the aircraft.

The requirements for the patch element has been derived from an data link antenna system. The following design parameters have been specified:

Frequency Range:	9.0 to 10.0 GHz
VSWR:	better 2.0:1 within defined frequency range
Gain of patch Element:	better 4.0 dBi
Polarization:	LHCP or RHCP
Axial Ratio:	better 3.0 dB
Impedance:	50 Ohms

Additional to the electrical requirements the structural performance of the aircraft surface has to be fulfilled. The design parameters were derived from the surface structure of the center fuselage of the Typhoon fighter aircraft.

2. Description of Patch Layers

Based on the requirement that the radiating element should be integrated in the outer aircraft structure a patch antenna solution has been preferred. The elements should be easy integrated in a planar antenna array.

The electrical performance of the patch element is restricted due to the material limitations. The structural materials, e.g. quartz glass does not fulfill the strong requirements of typical microwave substrates. This was the reason that a compromise between electrical and mechanical performance has to be accepted.

Under these restrictions the applicable materials has to be chosen very carefully. Up to the final design many analysis and pretest has been performed to find the right structural stack up. For the design process the following layer structure has been defined:

Material	Function
PU-Caapcoat	Rain erosion protection layer
Espanex Foil	carrier for the upper patch element
Quartz-Glass	Impact protection
RO4003	Microwave substrate containing the lower patch
RO4003	Microwave substrate containing the coupling slots and feeding network
Syncore	Structural material
CFK	Aircraft structure

Tab. 1 Dielectric Layers and there Function

The layers have been bonded with an adhesive, which will be used in a modern aircraft manufacturing process. The microwave substrates has been laminated with an applicable prepreg. The layer definition has to be considered that the integration process fits to the aircraft integration process.

3. Electromagnetic Design

The electromagnetic parameters could be now deviated from the layer design and the applicable materials. These were important parameters for the electromagnetic modeling and optimization process. Each layer must be defined by

- Material
- Dielectric constant
- Material losses
- Thickness

Within the electromagnetic design the following topics have to be considered:

- planar construction
- applicable for single radiating element or within an array
- aperture coupling caused by lightning constraints
- realization within standard manufacturing process

Having taken all these requirements into account within the design phase the following patch design has been chosen:
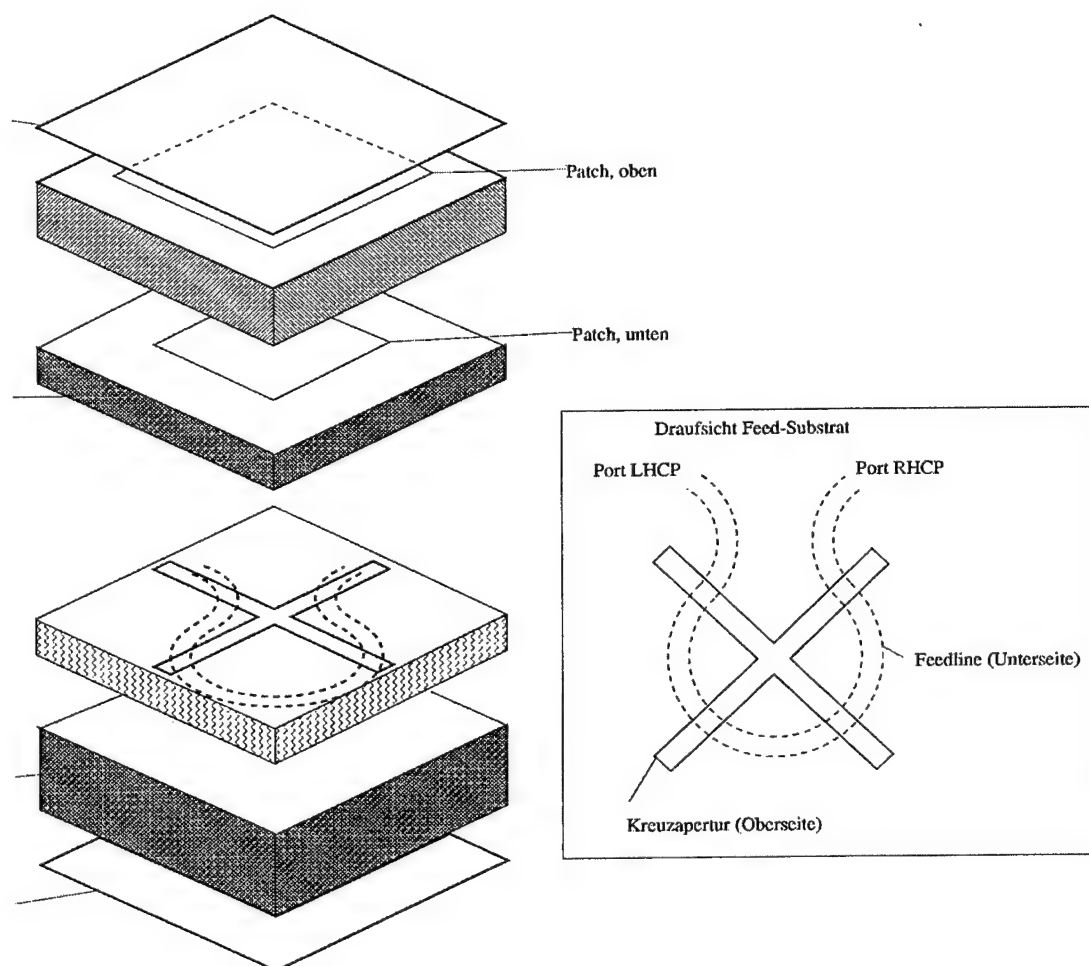
Fig. 3-1 Proposed Patch Design

This layout combines many advantages. The patch could be left hand or right hand circular polarized. The stacked patch guarantees a well matched patch element over wide frequency range. And the requirements could be fulfilled under the application of structural materials.

This design has been taken into account for the optimization process.

The patch geometry has been optimized with respect to gain and return loss within the defined frequency range. If you can use microwave materials for stacked patch applications the VSWR is better than 2.0:1 over a bandwidth 20%. But this

requires on the one hand a thick substrate relative to the wavelength and a material with a low dielectric constant, nearly 1.0. Both requirements are not available. Because the quartz glass is required for impact protection and has a dielectric constant of about 3 and the thickness is limited due to mass requirements. From these constraints results a limited bandwidth of 10%.

The size of the patch element, and therefore the gain of the element depends also on the applicable materials, respectively the dielectric constant. Materials with low dielectric constants leads to a larger patch element with higher gain values than materials with an higher dielectric constant. The outer dimensions of the radiating elements are smaller than typical patch elements and therefore the gain will be the typically achieved values.

The performance could be achieved by varying the dimension of the patches, slots and stripline width.

4. Design of the Antenna Demonstrator

The electrical and mechanical requirements have to be verified with an antenna demonstrator. This demonstrator should be designed and built in accordance with the final antenna manufacturing process. The production is derived from the standard integration process the Typhoon fighter aircraft program.

Several patch elements should be integrated in the demonstrator model. With the prototype the following parameters should be verified

- manufacturing process
- positioning accuracy
- variation of material thickness
- electromechanical requirements
- mechanical requirements

The overall dimensions of the demonstrator were 340 x 250 mm.

The antenna demonstrator is shown in the following figure:
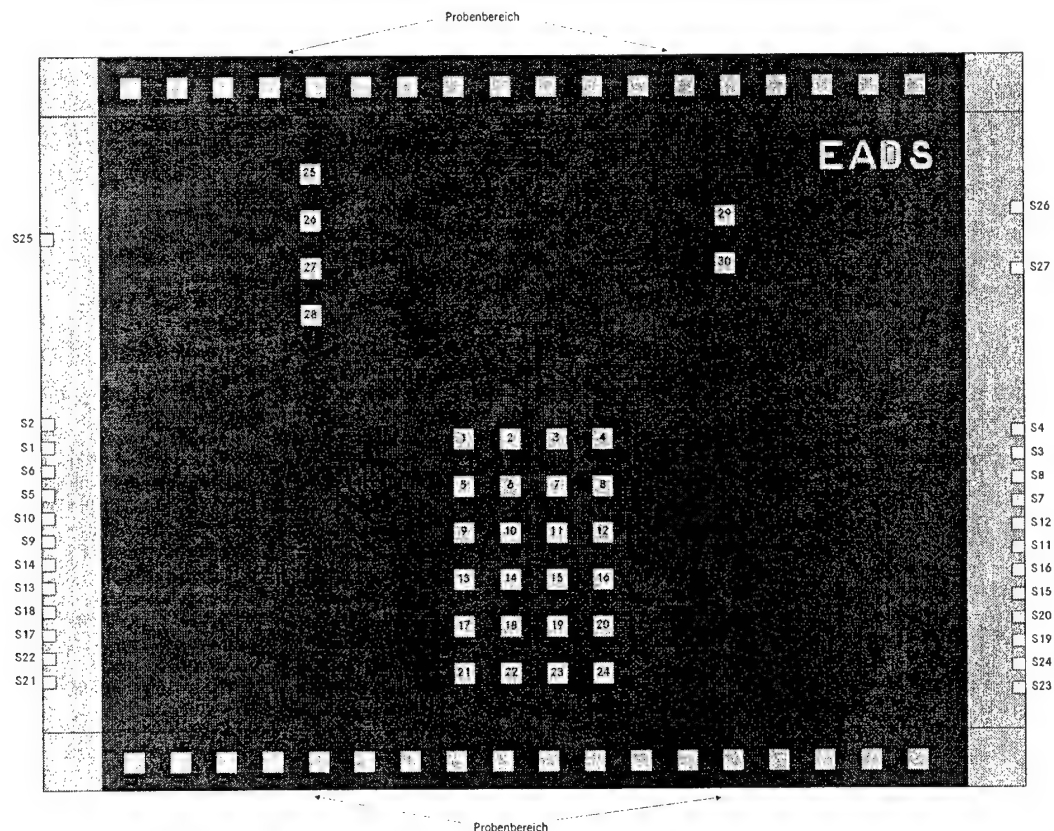
Fig. 4-1 Antenna Demonstrator Model

The demonstrator contains four areas. At the upper and lower edge there is the probe area. These probes were prepared for bending tests and measurement of the layer thickness. In the center area there are 30 radiating element for electromagnetic performance verification. In this area also the positioning accuracy should be measured with X-ray testing.

The two radiating elements on the right side are right hand circular and left hand circular polarized. Additional to return loss measurement of these elements the decoupling of each one should be verified.

All patches were fed via a SMP type coaxial connector. This connector is applicable over a wide frequency range up to 18.0 GHz. Each elements in the center have his own dedicated port. With this feeding technique the array properties could be verified in the first step. Because of manufacturing technique in this realization phase only side mounted connectors could be integrated. Other

requires on the one hand a thick substrate relative to the wavelength and a material with a low dielectric constant, nearly 1.0. Both requirements are not available. Because the quartz glass is required for impact protection and has a dielectric constant of about 3 and the thickness is limited due to mass requirements. From these constraints results a limited bandwidth of 10%.

The size of the patch element, and therefore the gain of the element depends also on the applicable materials, respectively the dielectric constant. Materials with low dielectric constants leads to a larger patch element with higher gain values than materials with an higher dielectric constant. The outer dimensions of the radiating elements are smaller than typical patch elements and therefore the gain will be the typically achieved values.

The performance could be achieved by varying the dimension of the patches, slots and stripline width.

4. Design of the Antenna Demonstrator

The electrical and mechanical requirements have to be verified with an antenna demonstrator. This demonstrator should be designed and built in accordance with the final antenna manufacturing process. The production is derived from the standard integration process the Typhoon fighter aircraft program.

Several patch elements should be integrated in the demonstrator model. With the prototype the following parameters should be verified

- manufacturing process
- positioning accuracy
- variation of material thickness
- electromechanical requirements
- mechanical requirements

The overall dimensions of the demonstrator were 340 x 250 mm.

Fig. 5-1 Antenna demonstrator after integration process

The antenna model with some integrated connectors and rain erosion protection coating is shown in the following figure.
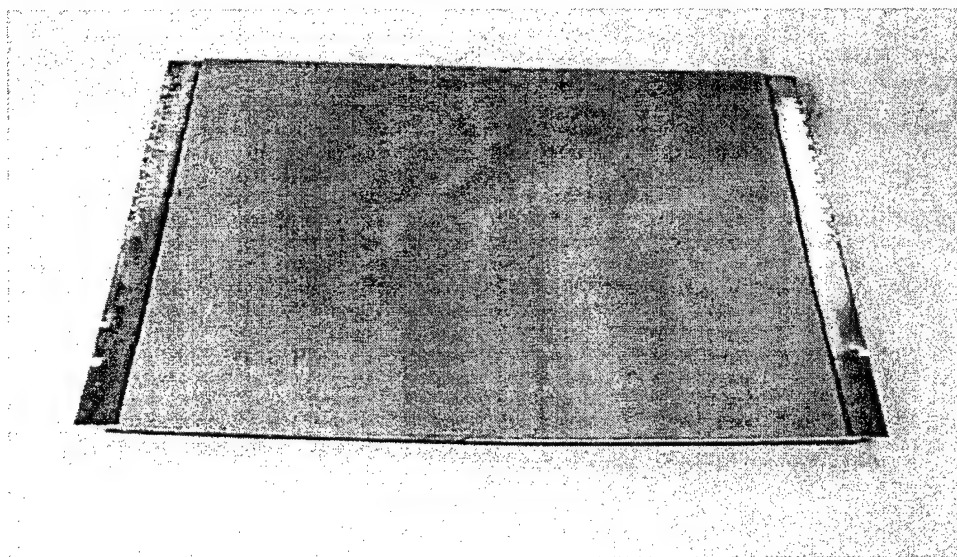
Fig. 5-2 Antenna demonstrator final version

6. Structural and Electrical Verification

Within the verification process the following results should be documented:

- Manufacturing Tolerances
- Structural Requirements
- Electromagnetic Requirements

The manufacturing tolerances would be verified with the probes taken from the edge of the antenna demonstrator. Special grinding probes has been prepared in our laboratories. The results after the evaluation shows that the requirements for positioning accuracy has been fulfilled. Depending from the material layers deviations from the nominal thickness occur up to 60 %. But this problem could be closed with an optimization in the manufacturing process. A horizontal positioning accuracy of less than 5% could be achieved with our tooling concept. But for future designs a better positioning accuracy should be achieved.

The structural requirements has been also verified with a complex test program. Special probes have been manufactured, tested and verified. The structural requirements, which has been foreseen for this antenna applications, has been fulfilled.

For the electrical aspects the return loss has been still measured. Within the required frequency range from 9.0 to 10.0 GHz the return loss was better than – 10 dB. The electromagnetic verification program will be closed with a detailed pattern, gain and axial ratio measurement program.

7. Summary

The demonstrator model described in this paper has shown that a structural integrated antenna can be realized. Due to material restrictions an acceptable electrical performance can be achieved. Also the mechanical requirements has been verified within a new integration process.

The results of this demonstrator model will be a good basis for the ongoing work. This will be realized in a structure integrated antenna with a curved surface and probably an integrated beam forming network with passive components.

Infinite Arrays of Tapered Slot Antennas
With and Without Dielectric Substrate

S. Kasturi, A.O. Boryssenko and D.H. Schaubert
Antenna Laboratory
University of Massachusetts
Amherst, MA 01003

Abstract: The impedance of Tapered Slot Antennas in an infinite array have been calculated by using full-wave method of moments techniques to assess the effects of key design parameters, including dielectric substrate permittivity. The slotline cavity is found to be extremely important to the operation of the antenna, and dielectric loading is seen to improve the resistance. For a fixed overall depth of the antenna, adjustment of the exponential opening rate and the slotline cavity size provide substantial control over the resistance and reactance of the antenna. The observed trends can be used to create a new design or to improve an existing design.

1. Introduction

Tapered Slot Antennas (TSA), also known as Vivaldi and notch antennas, are the primary contender for ultrawide bandwidth antenna arrays. The wide bandwidth potential of notch antenna arrays was identified thirty years ago [1], but the realization of that potential required nearly twenty years of experimental and analytical development. The advent of modern techniques for computational electromagnetics and of affordable, high-performance computing have hastened the development and understanding of these antenna arrays over the past decade [2,3,4].

Despite many recent successful developments of ultrawide bandwidth TSA arrays, many aspects of their design and performance remain largely unexplored. Most of the analyses that have been used to date employ the infinite array approximation whereby only a single unit cell of the array must be modeled in the computational domain. However, some recent work to analyze finite arrays of TSA has yielded interesting results [5,6]. As of now, the effects of truncation remain largely unexplored for these ultrawide bandwidth arrays. Also, although many of the designs that have been implemented employ stripline feed circuits, the effects of varying the dielectric permittivity have not been published, nor have comparisons of dielectric-free antennas to similar geometries employing stripline

feeds. This paper begins to illuminate the effects of substrate permittivity by presenting the results of a parameter study involving 27 variations of a reasonably good TSA array. The parameter study was conducted by using the infinite-array analyses [3,7,8,9] that have been developed at UMass and verified by comparison to waveguide simulator experiments and to other computational methods. Furthermore, all 27 variations were analyzed as dielectric-free antennas *and* as stripline-fed antennas with $\varepsilon_r = 4$. Stripline-fed antennas with $\varepsilon_r = 2.2$ have been analyzed also, but those results are not presented here.

The two cases that were selected, dielectric-free and stripline-fed with $\varepsilon_r = 4$ (Figure 1), yield sufficiently different results to indicate the impact of ε_r on array performance and they span the range of substrates that are often considered for TSA array fabrication. The dielectric-free cases are of considerable interest because the cost and weight of microwave substrates used in stripline-fed arrays are too high for many applications. Dielectric-free antennas are comprised of a metal fin and fed by a balanced circuit or by microstripline on a small piece of substrate covering only a small portion of the antenna near the narrowest part of the slotline.
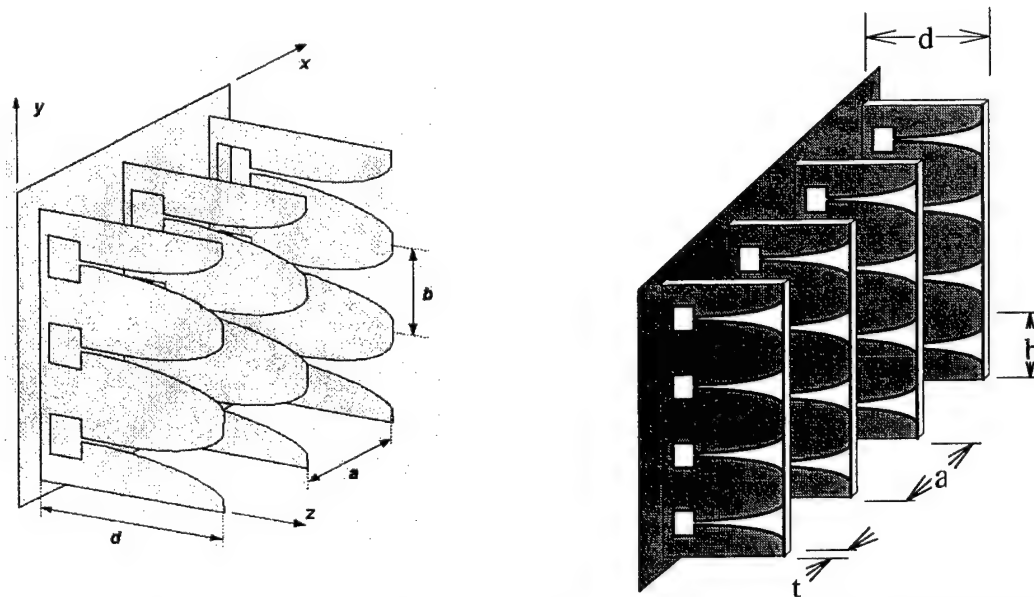
Figure 1. (a) Single-polarized TSA array without dielectric. (b) Single-polarized TSA array with dielectric.

Achieving good ultrawide bandwidth and scanning characteristics requires optimization of several parameters that define the TSA array. Previous studies

373

[10,11,12] have shown, nonetheless, that TSA array performance is particularly impacted by three geometrical parameters (see Fig. 2); exponential opening rate (Ra), slotline cavity size (Dsl), and antenna depth or length (D or L). The wideband input impedance of arrays are compared for three values of each of these parameters, 27 cases for dielectric-free and for $\varepsilon_r = 4$. Some of the trends that were observed for $\varepsilon_r = 2.2$ studies in the past are evident in the results here. However, the new results show that changing the dielectric substrate adds flexibility to control certain aspects of these trends. For example, the average value of input resistance of most of the geometries increases with frequency for the dielectric-free antennas, whereas it is more constant for $\varepsilon_r = 4$. In some cases, trends that were noted for the $\varepsilon_r = 2.2$ cases in [10] are altered for other values of ε_r.

The next section describes the antenna geometry and the way the study was performed. Presentation of the parameter study results and discussion follows.

2. Important Design Parameters and Method of Analysis

a) Design Parameters:

The design parameters involved in the geometry of the Vivaldi antenna element for both configurations (with and without dielectric) are shown in Figures 1 through 4. Figure 1 depicts the overall antenna array geometry. The geometry of the metal layers in the case of dielectric antenna is defined by the same parameters as that of the metal element in the dielectric-free antenna, as shown in Figure 2. The stripline feed geometry is shown in Figure 3.

The design parameters can be classified into element parameters, array parameters, and substrate parameters. Element parameters are further classified into metal layer parameters and feed-stub parameters. In this paper, a discussion of the array's performance with variation of the most important element parameters, viz., exponential opening rate (Ra), element depth (D) and cavity size (Dsl) is presented. Previous studies have used the tapered slot length (L) as a parameter. This may be a more fundamental parameter controlling array performance than the depth D. However, there is a one-to-one correspondence between D and L, and they are completely equivalent if Lg, Dsl and Lt are fixed. Furthermore, design requirements often specify the total available depth for the array. Therefore, in this paper we selected the depth D as the length parameter. The rest of the parameters are fixed according to guidelines obtained from earlier work [10,11]. The H-plane and E-plane array spacings (a and b) are 8 cm, which is half the wavelength at 1.875GHz.
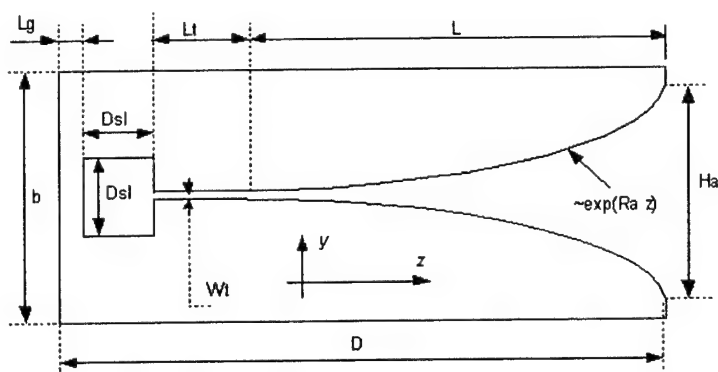
Figure 2. Vivaldi antenna element geometry.
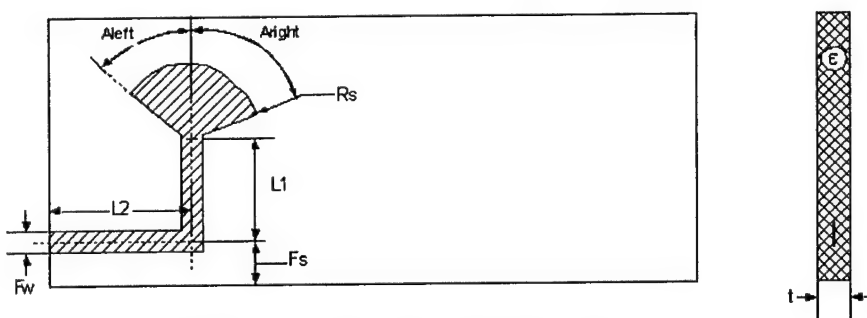
Figure 3. Feed geometry for dielectric antenna.
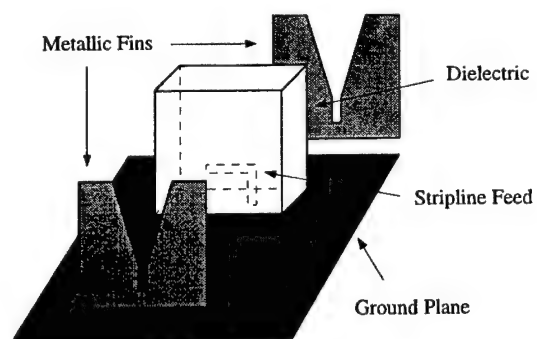
Figure 4. Exploded view of dielectric antenna element.

375

The specifications for the antenna parameters are:

Element parameters:

Metal layer parameters:

        b = 8.00 cm: width of the antenna

        D = variable (24, 32, 40 cm): overall depth of the antenna element

        Ha = 7.00 cm: height of antenna aperture

        Ra = variable (0.1, 0.2, 0.3 cm^{-1}): exponential opening rate

        Ls = 1.5 cm: length of linear slot

        Ws = 0.2 cm: width of the linear slot

        Dsl = variable (1.5, 2, 2.5 cm): length and width of the square slotline cavity

        Lg = 1.5 cm: backwall offset

Feed- stub parameters:

        Fw=0.2 cm: width of stripline feed

        Rs=1.5 cm: radius of radial stripline stub

        Aleft=30°: left angle of radial stripline stub sector

        Aright=78°: right angle of radial stripline stub sector

Array parameters:

        a = 8.00 cm: H-plane spacing

        b = 8.00 cm: E-plane spacing

Substrate parameters:

        ε_r = 4: dielectric constant

        t = 0.32 cm: substrate thickness

<u>b) Analysis Tools.</u>

Two MoM codes are used for the analysis of the dielectric-free and dielectric antenna arrays. The MoM formulation for dielectric-free cases employs rectangular and parallelogram meshing over the metal surface to calculate the electric current distribution, using the Green's function-method of moments formulation [7]. The analysis for dielectric cases employs triangular meshing in the slot region to calculate magnetic currents using the Green's function-MoM formulation for stripline-fed geometries [3]. These codes analyze the unit cell and

hence are applicable for infinite arrays. Both codes calculate the input impedance of the corresponding antenna over the required frequency range.

For the dielectric-free antenna, the input impedance is calculated at the center of the linear slotline of length Lt, where a delta-gap voltage generator is applied as shown in Figure 5. For the dielectric antenna however, the input impedance is calculated at the port point (at the start of the stripline feed) as shown in Figure 6.
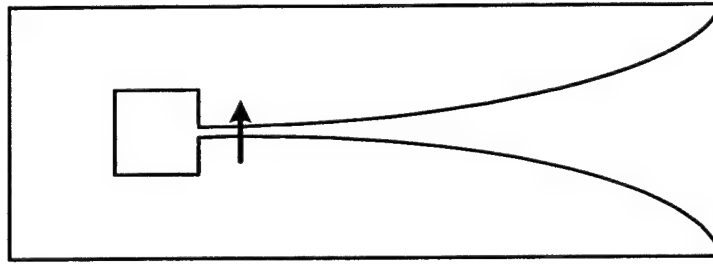
Figure 5. Feed mode on dielectric-free antenna element.
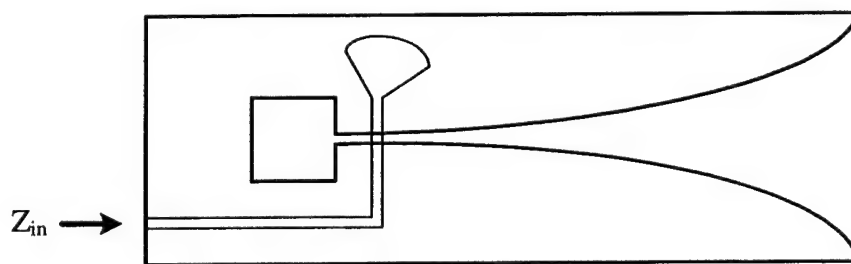
Figure 6. Feed mode for dielectric antenna element.

For comparison of the two different antenna configurations, the impedance of only the metal fins that compromise the radiating portion of the dielectric antenna is obtained by:

    a) Moving the reference point along the transmission line from the feed point in Figure 6 to the stripline-slotline transition, which is located at the feed point for the comparable dielectric-free antenna;

    b) Subtracting the reactance of the radial stub from the active impedance at the stripline-slotline transition, according to the equivalent circuit shown in Figure 7.
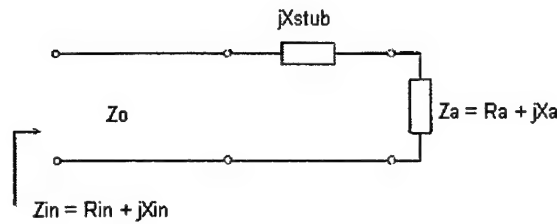
Figure 7. Equivalent circuit.

3. Results and Discussion

A total of 27 geometries have been analyzed, with and without dielectric. Only the broadside beam position is considered in this paper. Based on previous work, these results are indicative of characteristics for other scan angles. The parameters are varied through the following values:

Opening rate **Ra**: 0.1, 0.2, 0.3 cm^{-1}
Depth of the element **D**: 24, 32, 40 cm
Size of cavity **Dsl**: 1.5, 2, 2.5 cm

The impedances and VSWR, along with inferences drawn from them are presented below. The data are plotted according to the following criteria:

- The dielectric antenna impedance has been obtained as described above. Characteristic impedance of the stripline is 45Ω.
- The reactance of the radial stub is calculated using the MoM code for dielectric antennas but using modes *only on the feedline and stub*. This corresponds to analyzing a non-radiating stripline circuit. Previous work has shown that the stub reactance obtained from such an analysis yields good results when combined with the equivalent circuit of Figure 7 and full-wave analysis of the complete antenna structure.
- For the dielectric-free case, the VSWR is calculated with respect to a normalizing impedance of 80Ω, which yields the best wide-band VSWR possible for most of the geometries.
- For the dielectric case, the VSWR is calculated by normalizing to the impedance value that yields the best VSWR through the whole band. It was found that this normalizing impedance

378

usually varies around 50Ω, +/-10Ω. The characteristic impedance of the stripline is in the same range, 45Ω.

- In the dielectric case, the impedance used to calculate the VSWR includes the radial stub reactance, since the capacitance of the stub is an integral part of the actual antenna and it usually improves the wideband VSWR.

Opening rate (Ra):

For all variations in depth of the antenna element and cavity size, the effects of changing opening rate were observed. Representative cases are shown in figures 8-11 for dielectric and dielectric-free cases.
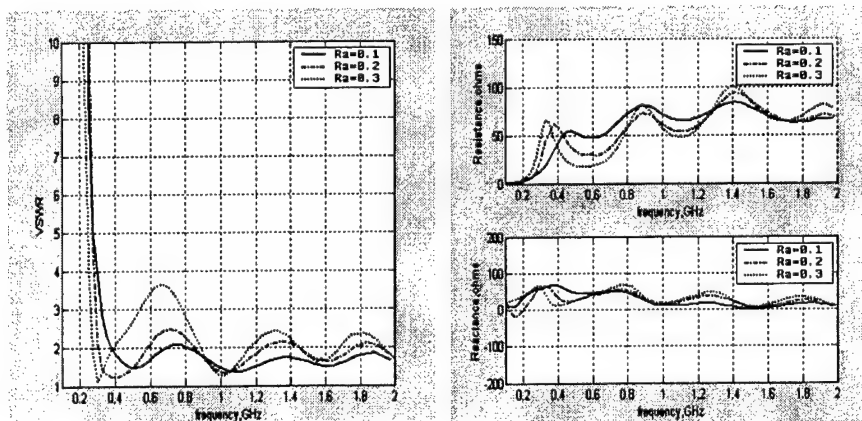
Figure 8. Variation of opening rate (Ra) 0.1, 0.2, 0.3 in dielectric antenna. Dsl = 1.5 cm, D= 24 cm, ε_r = 4, broadside beam.

379
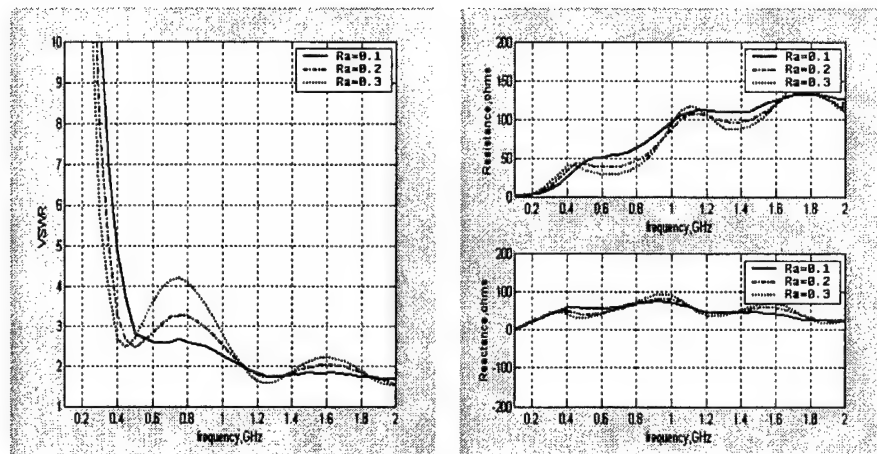
Figure 9. Variation of opening rate (Ra) 0.1, 0.2, 0.3 in dielectric-free antenna. Dsl = 1.5 cm, D= 24 cm, broadside beam.
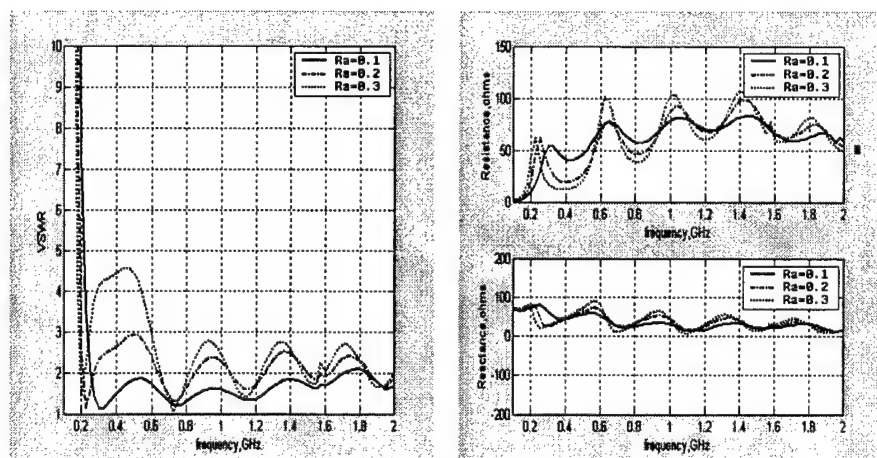
Figure 10. Variation of opening rate (Ra) 0.1, 0.2, 0.3 in dielectric antenna. Dsl = 2 cm, D= 32 cm, ε_r = 4, broadside beam.
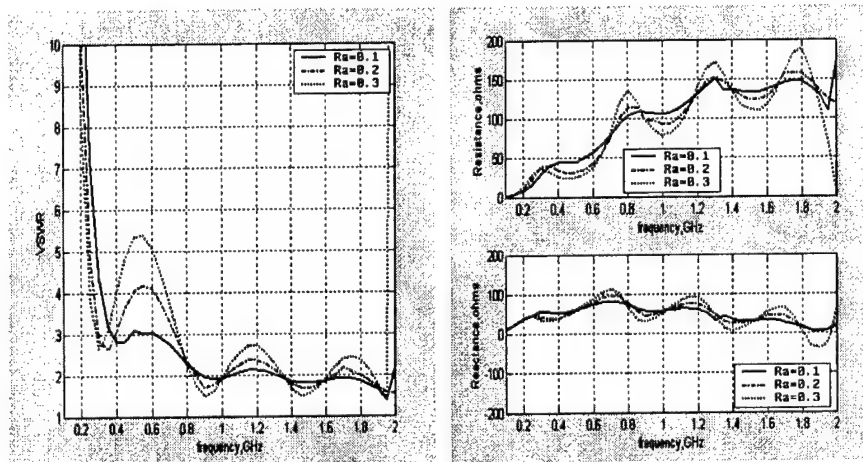
Figure 11. Variation of opening rate (Ra) 0.1, 0.2, 0.3 in dielectric-free antenna. Dsl = 2 cm, D= 32 cm, broadside beam.

Salient trends in dielectric case:

- The amplitude of the variation in resistance (and reactance) increases with opening rate. These excursions from the mean value lead to prominent excursions in the VSWR profile, which limit the usable frequency range.
- At low frequencies, the resistance for different opening rates rises to more or less the same level (+/- 10Ω), but with different slopes. The smallest opening rate rises slowest, while the largest Ra rises fastest. This reduces the lowest operating frequency for the largest opening rate.
- The resistance at frequencies above the first peak falls rapidly for large opening rates. The minimum value of resistance for larger opening rates is low enough to cause a large hump in the VSWR plot, which exceeds operational limits.

Salient trends in dielectric-free case:

- The average resistance increases continually over the frequency range. This reduces the usable frequency range because it is not possible to select a normalizing impedance for which the VSWR is within acceptable limits. This trend (R

381

increasing with frequency) will be shown below to depend on cavity size, Dsl, and dielectric permittivity.

- The amplitude of resistance and reactance variation increases with opening rate, as seen in the dielectric case.

Depth of the antenna element (D):

The effects of changing the depth of the antenna element are shown for a few cases in figures 12 through 15, and the following inferences can be made from these results plus other comparisons not shown here.
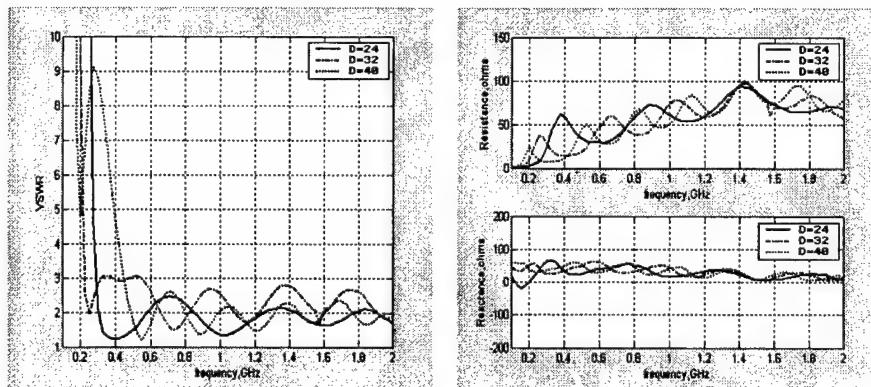
Figure 12. Variation of depth of the antenna element (D) 24, 32, 40 cm in dielectric case. Dsl= 1.5 cm, Ra= 0.2, $\varepsilon_r = 4$, broadside beam.
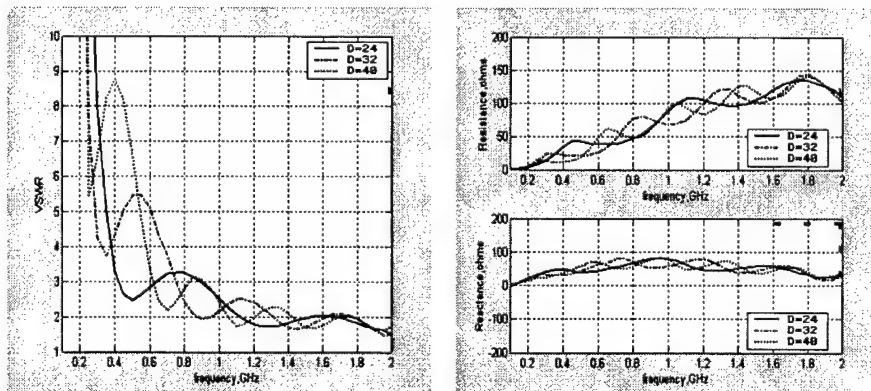
Figure 13. Variation of depth of the antenna element (D) 24, 32, 40 cm in dielectric-free case. Dsl= 1.5 cm, Ra= 0.2, broadside beam.

382
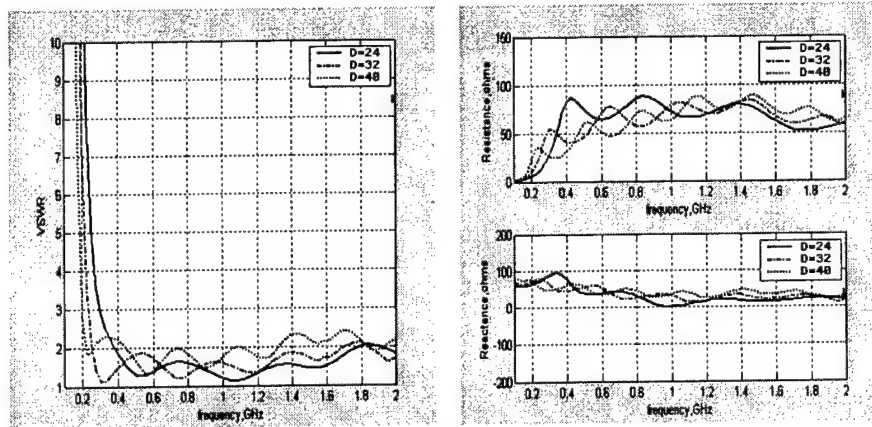
Figure 14. Variation of depth of the antenna element (D) 24, 32, 40 cm in dielectric case. Dsl= 2 cm, Ra= 0.1, ε_r = 4, broadside beam.
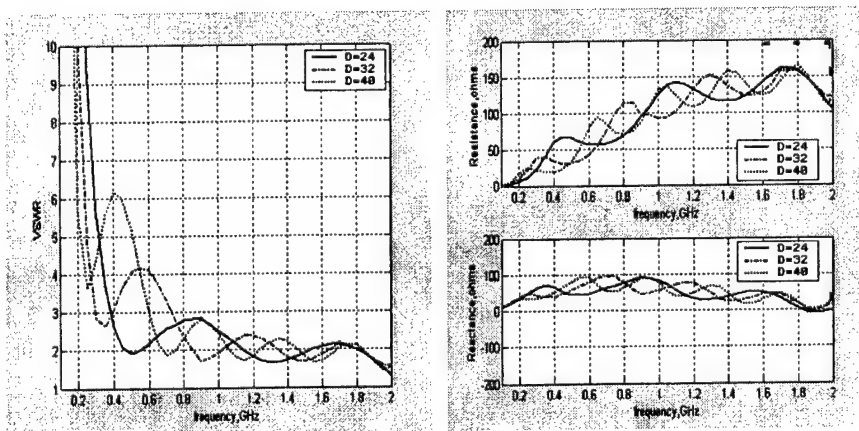
Figure 15. Variation of depth of the antenna element (D) 24, 32, 40 cm in dielectric-free case. Dsl= 2 cm, Ra= 0.1, broadside beam.

Salient trends in dielectric case:

- The resistance for different lengths rises to different levels, at almost the same slope, with the longest antenna reaching its

383

peak first and attaining the lowest value. The shortest antenna reaches its peak last and attains the highest value. Furthermore, at frequencies above the first resistance peak, a trough in the resistance can lead to a poor impedance match in this frequency range. If the long antenna reaches its peak too fast (and hence too low), a good match is not obtained. The lower is the peak that is attained, the lower is the first trough. If a long antenna attains a high enough resistance to give a good match, we obtain the lowest operating frequency, since it rises soonest.

- The number of resonances (oscillations) increases with length, and there appears to be a scaling: an increase in length of half-wavelength (at highest frequency-1.875GHz) leads to the addition of one resonant peak in the resistance plot.

Salient trends in dielectric-free case:

- As in the dielectric case, the resistance increases to different levels at almost the same slope. The value of the first resistive peak is a little lower for the dielectric-free antennas than for the dielectric antennas, and fewer peaks occur for a given antenna depth than for the dielectric antenna.
- The number of resonances increases with length, scaling similar to that in the dielectric case.

Cavity size (Dsl):

Figures 16 through 19 show the effects of different sizes of the slotline cavity on the input impedance of dielectric and dielectric-free cases, respectively.
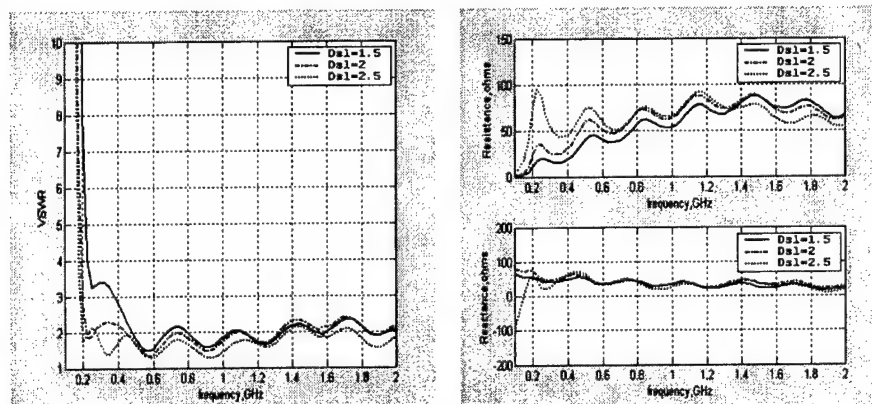
Figure 16. Variation of cavity size (Dsl) 1.5, 2, 2.5 cm in dielectric case. D= 40 cm, Ra= 0.1, ε_r = 4, broadside beam.
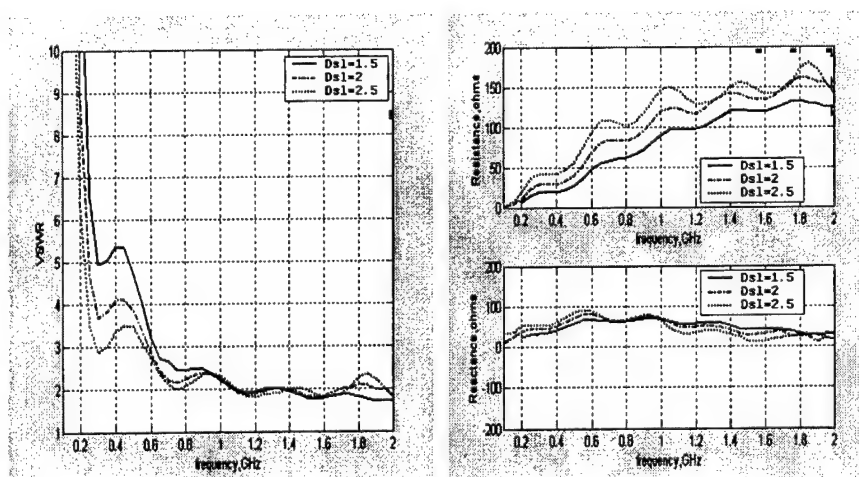
Figure 17. Variation of cavity size (Dsl) 1.5, 2, 2.5 in dielectric-free case. D= 40 cm, Ra= 0.1, broadside beam.
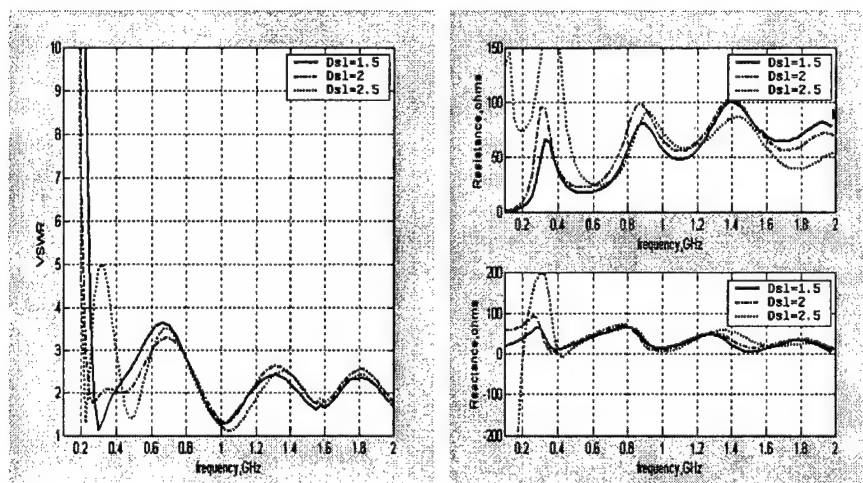
Figure 18. Variation of cavity size (Dsl) 1.5, 2, 2.5 cm in dielectric case. D= 24 cm, Ra= 0.3, ε_r = 4, broadside beam.
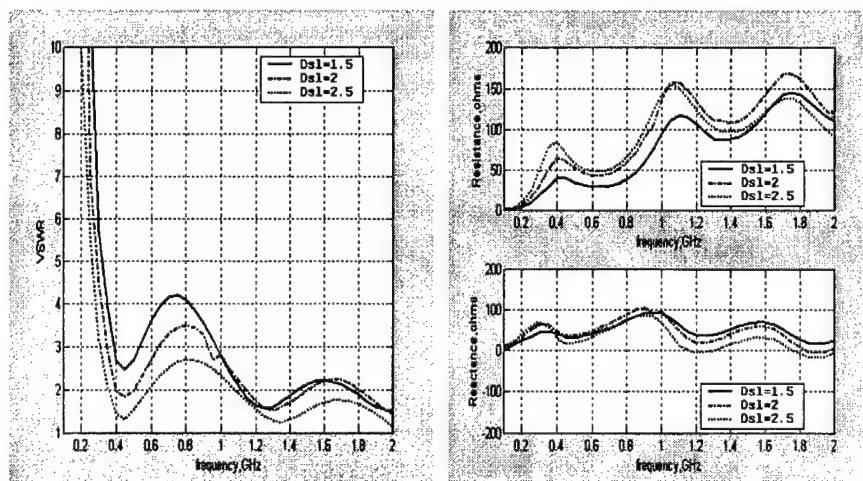
Figure 19. Variation of cavity size (Dsl) 1.5, 2, 2.5 cm in dielectric-free case. D= 24 cm, Ra= 0.3, broadside beam.

Salient trends in dielectric case:

- All resonances (peaks of the resistance) occur at nearly the same frequencies for all sizes of the cavity. However, with increase in size, the lower frequency peaks (especially the first peak) increase. Unlike the opening rate data in Figures 8 and 10, a higher peak doesn't result in a lower trough, so the VSWR remains good throughout the low frequency range.
- The resistance increases with Dsl up to mid band; above midband, the resistance decreases when Dsl increases.
- A larger cavity results in more low-frequency inductance being added, as seen in the reactance plots. However, this effect is seen only until a certain value of cavity size, beyond which the total reactance becomes capacitive at low frequencies.

Salient trends in dielectric-free case:

- All resonances occur at nearly the same frequencies for all sizes of the cavity.
- A larger cavity adds to the inductance at the lower frequencies.
- A larger cavity increases the resistance throughout most of the band. However, as can be seen from Figure 20, cavity sizes of 3 cm and higher reveal the high frequency reversal observed for dielectric antennas.
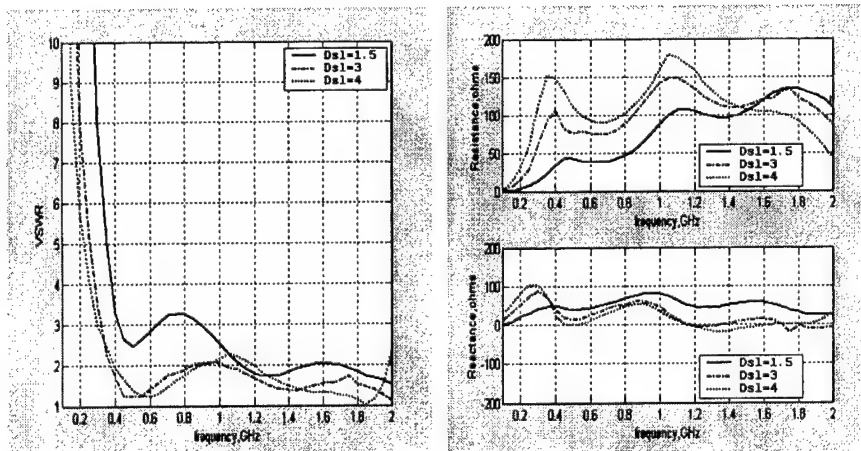
Figure 20. Variation of cavity size (Dsl) 1.5, 3, 4 in dielectric-free case. D=24 cm, Ra=0.2, broadside beam.

387

4. Summary

Considering the data from dielectric and dielectric-free cases, some common trends are observed such as:

- The reactance of the antenna starts out inductive at low frequencies, and gradually approaches the capacitive region towards high frequencies.
- The curvature of the "average" resistance is strongly affected by Dsl and less affected by D, Ra and ε_r. The average resistance of the smallest cavity size antenna continually increases throughout the band, while the average resistance of the largest cavity size antenna peaks just beyond midband and then decreases.
- Dielectric loading usually improves the lower end performance as is seen when a dielectric and dielectric-free case are compared.

Guidelines for design improvement can be inferred from the trends seen, and are similar for dielectric and dielectric-free antennas:

a) Increasing opening rate results in a lower minimum operating frequency, but with larger VSWR oscillations. Reducing the antenna depth or increasing the cavity size can reduce the magnitude of the oscillations.

b) Increasing antenna depth improves low-frequency performance, but also leads to VSWR humps, which can be countered by smaller opening rates or larger cavity size.

c) Large cavity size improves low-frequency performance considerably.

d) The presence of the capacitive stub in the dielectric antennas improves the wideband performance of the array by offsetting some of the low-frequency inductance of the antenna. This effect can be created in a dielectric-free antenna by including a series capacitor at the feed point.

e) The average value of the resistance attains higher values at low frequencies for dielectric antennas than for dielectric-free antennas. Also, the average resistance of dielectric-free antennas tends to increase over the entire operating band, whereas the resistance of dielectric antennas moves gradually up then down around a median value.

388

5. Acknowledgement

6. References

[1] L.R. Lewis, M.Fasset and J. Hunt, " A broadband stripline array element", IEEE Antennas & Propag. Symp., pp. 335-337, June 1974.

[2] P.S. Simon, K. McInturff, R.W. Jobsky and D.L. Johnson, "Full-wave analysis of an infinite, planar array of linearly polarized, stripline-fed, tapered notch elements", IEEE Antennas & Propag. Symp., pp. 334-337, 1991.

[3] D.H. Schaubert, Jon Anders Aas, M.E. Cooley and N.E. Buris, "Radiation and scattering analysis of infinite stripline-fed tapered slot antenna arrays with a ground plane", IEEE Trans. Antennas & Propag., vol.42, pp. 1161-1166, Aug 1994.

[4] Nick Schuneman, James Irion and Richard Hodges, "Decade bandwidth tapered notch antenna element", Proc.2001, Ant. Appln. Symp., pp. 283-294, Monticello, IL.

[5] H. Holter and H. Steyskal, "On the size requirement for finite phased-array models", IEEE Trans. Antennas & Propag., vol.50, pp. 836-840, June 2002.

[6] A. Boryssenko and D.H. Schaubert, "Predicted performance of small arrays of dielectric-free tapered slot antennas", Proc.2001, Ant. Appln. Symp., pp. 250-279, Monticello, IL.

[7] Michael E. Cooley, D.H. Schaubert, Nicholas E. Buris and Edward A. Urbanik, "Radiation and scattering analysis of infinite arrays of endfire slot antennas with a ground plane", IEEE Trans. Antennas & Propag., vol.39, pp. 1615-1625, November 1991.

[8] D.H. Schaubert, "TSAAIR-analysis of tapered slot antennas with air dielectric", Elect. And Comput. Engg., Univ. of Massachusetts, Amherst, MA, December 1991.

[9] J. Shin, "Improved method of moments computations applied to tapered slot antenna arrays", M.S. Thesis, Elect. Comput. Engg., Univ. of Massachusetts, Amherst, MA, September 1994.

[10] J. Shin and D.H. Schaubert, "A parameter study of stripline-fed vivaldi notch-antenna arrays", IEEE Trans. Antennas & Propag., vol.47, pp. 879-886, May 1999.

[11] J. Shin and D.H. Schaubert, "Towards a better understanding of wideband vivaldi notch-antenna arrays", proc.1995, Ant. Appln. Symp., Monticello, IL.

[12] Tan-Huat Chio and D.H. Schaubert, "Parameter study and design of wideband widescan dual-polarized tapered slot antenna arrays", IEEE Trans. Antennas & Propag., vol.48, pp. 879-885, June 2000.

ARO Sponsored Programs in Antenna Research

Dr. W. Devereux Palmer, Ph.D., P.E.
Electromagnetics Program Manager
US Army Research Office
Engineering Sciences Directorate

Agenda

- The US Army Research Office

- Current programs in antennas

- Future interests

Dev Palmer • US Army Research Office • 919-549-4246 • dpalmer@aro.arl.army.mil

1

The U.S. Army Research Office mission is to seed scientific and far reaching technological discoveries that enhance Army capabilities.

Dev Palmer • US Army Research Office • 919-549-4246 • dpalmer@aro.arl.army.mil

ARO Structure

Office of the Director
Dr. C.I. Chang

Engineering Sciences Directorate Dr. David Skatrud	Physical Sciences Directorate Dr. Andrew Crowson	Research & Technology Directorate LTC David Camps
Computing & Information Sciences Division	Biological Sciences Division	OSD Programs Office
Electronics Division	Chemical Sciences Division	Small Business Programs Office
Mechanical & Environmental Sciences Division	Materials Sciences Division	Technology Integration Office
Mathematics Division	Physics Division	

50 Program managers
$160M in funded programs

Dev Palmer • US Army Research Office • 919-549-4246 • dpalmer@aro.arl.army.mil

ARO History and Recognition

- Established 1951 as the Office of Ordnance Research
- Renamed Army Research Office in 1961
- Sponsors extramural basic research as part of the Army Research Laboratories and the Army Materiel Command

ARO-sponsored researchers have received:
- 32 National Medal of Science awards
- 27 Nobel Prizes (4 of the last 6 in physics and chemistry)
- 2 Royal Swedish Academy of Sciences Crafoord Prizes

ARO Programs

- Single-investigator "core" programs
  - Subject areas in biannual BAA
    http://www.aro.army.mil
- OSD Programs: MURI, DURIP, DEPSCOR
  - Multidisciplinary University Research Initiative
  - Defense University Research Instrumentation Program
  - Defense Program to Stimulate Competitive Research
- SBIR/STTR
  - Small business prime with university, large business, non-profit subcontract options
- Management of other Army and DoD projects

ARO Interests In Electromagnetics And Antennas

- Integration technologies for millimeter-wave/microwave circuits with small size, light weight, low cost, and high reliability
- Electromagnetic analysis, simulation, and modeling
  - Circuits, systems, packages, and antennas
- Modeling and simulation for RF propagation and scattering
- Antennas
  - Innovative approaches to increasing the performance and decreasing the size and signature of tactical antennas
  - Designs for multifrequency, multiband operation
  - Novel ideas for ultra-wideband radar

Army Interests In Electromagnetics And Antennas

- Adaptive arrays
- Wireless and radar propagation theory and simulation
- EM numerical techniques
- Power-efficient RF components
- Advanced MMW circuit and antenna integration, integrated transmission lines
- Optical control of array antennas
- Mobile tactical wireless and printed antennas

4

FCS Communications

http://www.darpa.mil/ato/images/programs/fcs_comm.jpg
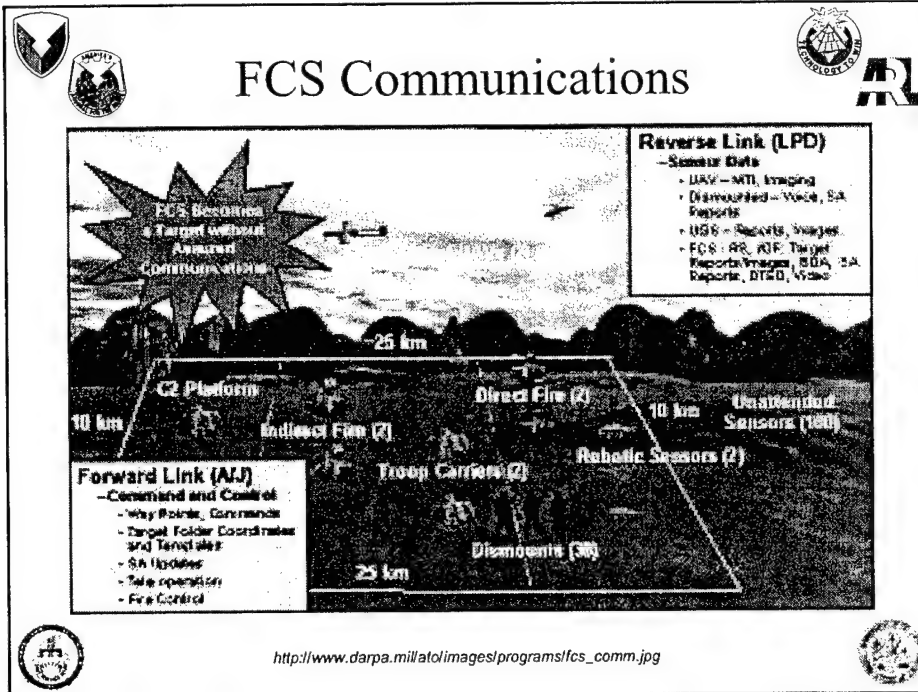
FCS Comms Requirements

- Assured, available, secure
  - Networked force cannot tolerate a <u>probability</u> of communication
- High bandwidth
  - Comms, radar, CID, GPS, situational awareness
- Low-power, compact
  - Man-portable, reduced logistics tail

Dev Palmer • US Army Research Office • 919-549-4246 • dpalmer@aro.arl.army.mil

Current Military Platforms

- Aegis cruiser has 150 antennas, 450 comms/radar functions
- JSTARS airframe carries 6 types of radar, 2 digital data links, 15 voice radios
- C4I ground vehicle may have 25 comms/radar functions
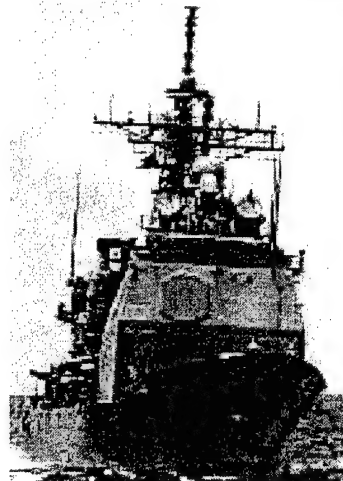
Problem: Congestion of RF Systems in Frequency Spectrum and Physical Space

Solution	Technology
• Higher frequency systems *Higher bandwidth for added functionality* *Access to unused spectrum* *Tighter beam enables frequency reuse*	• mm-wave circuits • Terahertz circuits • Optical communications and sensors
• Multifunctional systems • Adaptive/Agile systems	• Antennas • RF circuits • Global, multi-physics simulation and modeling

ARO "Blue Sky" Work

- Multiple-resonance antennas that apply filter theory to achieve very wide bandwidth (30:1)
- Very small printed antennas (1:30)
- Novel structures
  - Photonic band gap antennas with organic hi-Q filters
  - Magnetic synthetic slot antennas
- Novel materials
  - High permittivity, high permeability composites

ARO Antenna Programs

- Spatial power combining and quasi-optics
- Multi-physics modeling and simulation
  - Faster, more efficient algorithms
  - Full-wave E&M integration with SPICE-like device models
- Novel antenna structures and materials
- mm-wave scaled-range
  - Provides well-characterized wave propagation problem for model validation

49 Element Ka Band Array

Clemson MURI "Quasi-Optical Power Combining"

11.6 dB of gain
31.9 GHz center frequency
1 GHz, 3-dB bandwidth

Quasi-Optical Devices - Planar

5-W, 37-GHz Grid Amplifier

David Rutledge, UC Berkeley

Zoya Popovic, University of Colorado at Boulder

Dev Palmer • US Army Research Office • 919-549-4246 • dpalmer@aro.arl.army.mil

398

8

Dielectric Resonator Antennas

Dr. Ahmed Kishk • U Mississippi Electrical Engineering • 662-915-5385 • ahmed@olemiss.edu

Miniaturized HF-UHF Antenna
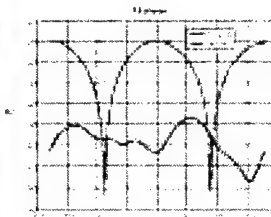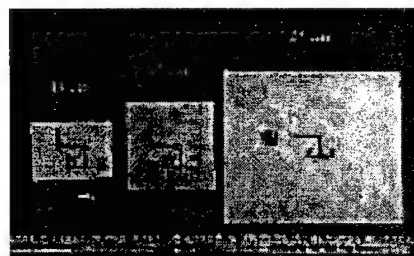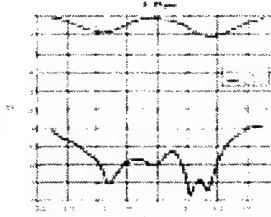
Dr. Kamal Sarabandi • U Michigan EECS • 734-936-1575 • saraband@umich.edu
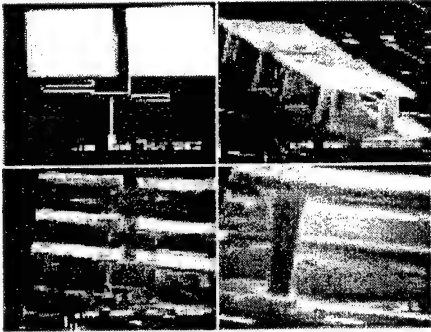
Micromachined 94 GHz Dipole Array

Quasi-optic antenna processing
-Third generation

UCSB

Height 150um
Patch size, 400 x 310um

Dipole array with TS HBT IC technology
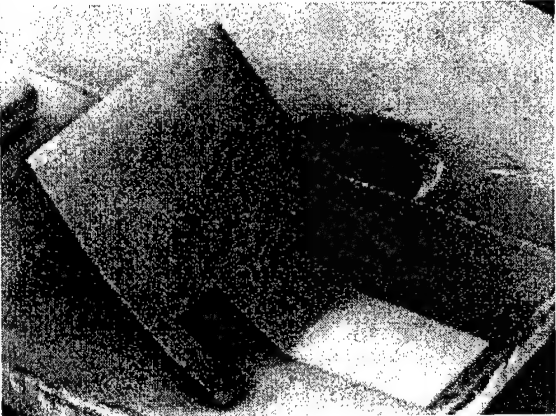-feed by micro strip Wilkinson power divider, height 150 um

Dev Palmer • US Army Research Office • 919-549-4246 • dpalmer@aro.arl.army.mil

Micromachined Wide-Band Element For Phased Arrays

26 GHz low-profile microstrip antenna constructed using plastic deformation magnetic assembly (PDMA)

Dr. Jennifer Bernhard • UIUC ECE Department • 217-333-0293 • jbernhar@uiuc.edu

A ROTMAN LENS IMPLEMENTATION FOR MULTI-FUNCTION RF ANTENNA APPLICATIONS

Robert Dahlstrom, and Andrew Bayba
U.S. Army Research Laboratory
2800 Powder Mill Road
Adelphi, MD 20783
dahlstrom@arl.army.mil

Abstract: An electronic scanning antenna (ESA) that uses a beamformer for scanning the beam has the advantage of being able to form multiple beams for multimode, shared-aperture applications. This scanning approach is achieved at a reduced parts count for the antenna subassembly and therefore at a lower cost than approaches that use phase-shifting elements for controlling the beam. The beamforming technology used in this effort is the Rotman lens. The desirable feature of this beamformer is that it can be produced (either on a dielectric or in a cavity) for low-loss, planar operation at frequencies designated for current and future Army weapons platforms (i.e., K_u and K_a bands). Since beam formation is accomplished through true time delay, the antenna is wideband and will accommodate multiple operational modes.

The objective of this effort is to generate simultaneous multiple beams through the lens. We will address the use of low-loss M x N switching networks (e.g., PIN-diode, and photonic actuated switches) to meet the requirements of a shared multibeam aperture. Eventually, the lens will be coupled and matched to a broadband low-sidelobe aperture array to focus and scan the beams in elevation. For this paper, however, the open-ended waveguide outputs of the Rotman lens assembly will be used as the array element.

Ultimately, we would like to reduce the size, weight, and cost of vehicle-mounted sensors by combining multiple sensor functions into one ESA. In the current design, the antenna scans 45 degrees horizontally. A beam-switching network at the input ports of the Rotman lens selects two beams to be used at any given time, thereby providing electronic scanning for two simultaneous channels. The system bandwidth is 36 to 40 GHz. We will describe the design and fabrication of the Rotman lens assembly and present the results of measurements of its performance.

1. INTRODUCTION

The U.S. Army Research Laboratory (ARL) is currently pursuing key technologies for low-cost, advanced battlefield sensors for multimode radar and communication platforms. These radar and communication functions include active/passive target acquisition, combat identification, weapons guidance, secure point-to-point communications, active protection, networks for situational awareness, and signal intercept. Typically, each of these functions is performed by a separate piece of equipment specifically designed for that purpose, with its own electronics package and antenna. As more of these functions are added to a vehicle, the available space suitable for antennas is quickly depleted, and costs and weight increase rapidly. Incorporating multiple-use components into these systems can considerably reduce total system size, weight, and cost. By sharing a single antenna aperture, one can time- and/or frequency-multiplex both radar and communications functions, or, in the case of multiple-beam antennas, perform them simultaneously. One such approach, described herein, uses one K_a-band, multipurpose, electronic scanning antenna (ESA) to perform the functions required by several systems.

2. SYSTEM DESCRIPTION

In the K_a-band ESA being developed, we achieve the simultaneous performance of multiple functions by combining a multiple-beam antenna array with a PIN-diode or photonic switching network while maintaining a broad overall system bandwidth of better than 36 to 40 GHz. The complete antenna system consists of a 16 (vertical) x 32 (horizontal) array of slot-fed microstrip patch radiators fed by the Rotman lens. The lens has 19 input ports, with the port on each end intended to be terminated to provide a symmetric environment for the remaining ports. The center 17 ports correspond to azimuth beam-scanning positions covering ±22.5 degrees from broadside. A dual-channel beam-switching network (BSN) is used to select one of the beams for each channel. Ultimately, amplifiers will be inserted between the lens and the patch array to increase the gain.

3. ESA OPERATION

Operation in an electronically scanned mode involves remotely controlling the BSN to switch either of the signal source inputs to any of the 17 beam ports of the Rotman lens, in a sequential or random scan, as desired. Adding time-multiplexed functions requires only that the appropriate beam selection be made at the same time as the input signal is switched. A fixed-beam communication channel can be added by coupling to the appropriate beam port. In a similar

manner, incorporating additional functions merely adds to the complexity of the BSN, not of the antenna itself.

4. ROTMAN LENS

The key to achieving a low-cost, compact, multibeam antenna is the use of a Rotman lens to provide the appropriate phasing to each element of the array. The
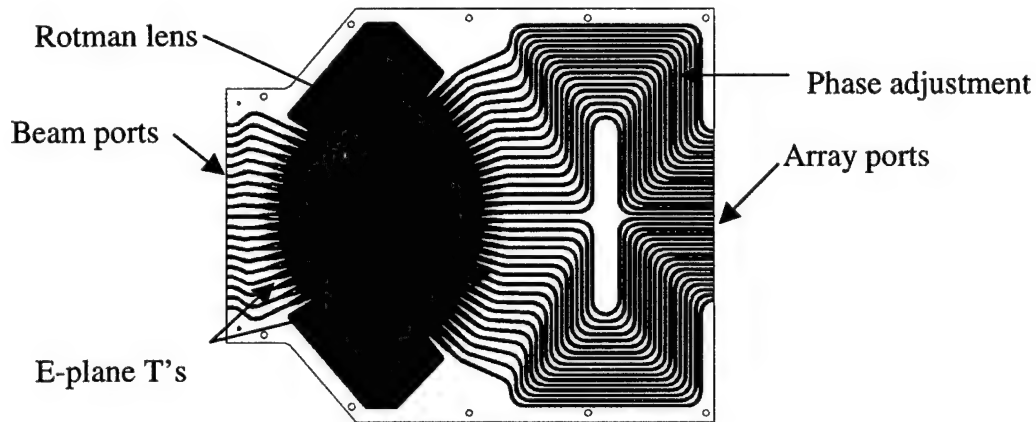

Figure 1. Rotman lens - Shaded areas show signal paths

lens has 19 beam ports (shown on the left in figure 1) that couple the signal into the broad parallel-plate region of the lens. The lens' geometry is chosen so that each beam port, by virtue of its position, produces the desired array phasing for its associated beam angle at the output ports. The direction of the beam radiating from the antenna can therefore be controlled by selection of an appropriate beam port. In addition, the amplitudes at the outputs are somewhat greater in the center, aiding sidelobe suppression

The Rotman lens design differs from that of other lenses in that it has three perfect focal points on the beam feed, with the other sources approximated on a circular focal arc. In other words, when a source is turned on at one of these foci, a linear phase taper appears across the linear array of output ports. The small phase errors at the intermediate positions do not significantly degrade antenna performance. The Rotman lens is an inherently wide-bandwidth device, because the path lengths to the output ports correspond to a true time delay, rather than just providing the desired phase. Therefore, the correct phasing is achieved independently of frequency. The medium used for this lens is waveguide, with the E field oriented parallel to the broad walls of the lens to reduce reflections at the input and output ports. In this orientation, the wavelength of the signal

403

traveling through the lens is a function of the wall spacing. The corresponding variation of the velocity of propagation of the signal in the lens causes a shift in beam angle with frequency for angles off broadside. Using an E field oriented perpendicular to the broad walls of the lens could eliminate this effect, but over the limited frequency range used here, the beam shift is small, about ±4%. The Rotman lens design is based on one provided to ARL by the Georgia Tech Research Institute shown in figure 2. The Georgia Tech antenna assembly consisted of a beam-port manifold mounted on top, connected to the Rotman lens by 19 U-shaped waveguides, which was in turn connected to another manifold below the lens by 34 U-shaped waveguides, which provided the desired output spacing to feed a 34-element sectoral horn. This arrangement makes a compact package for scanning a beam horizontally.

In the application addressed here, vertical scanning capability was needed as well. To add that capability, the sectoral horn was replaced with a patch array that provides scanning in elevation, which is described in detail in a separate report [1]. Two lenses were needed, one for transmit and the other for receive. Other factors considered in adapting the Georgia Tech design to the MFRF requirements
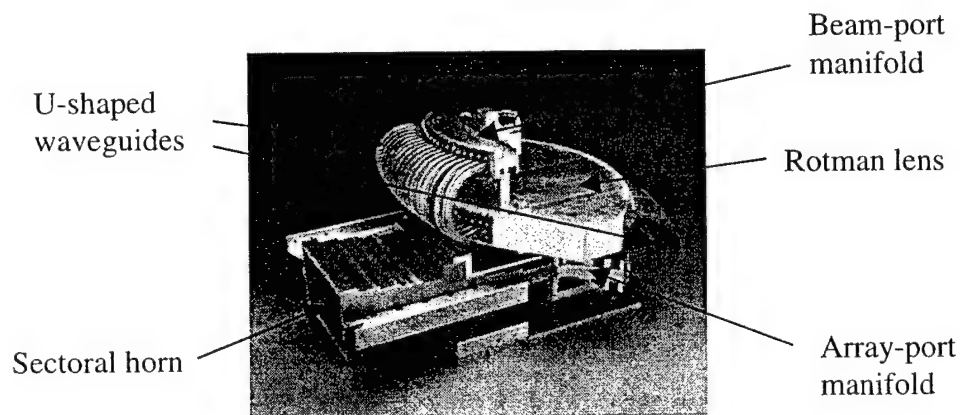

Figure 2. Georgia Tech Rotman lens antenna

were reducing size, cost, and weight, and improving manufacturability. To achieve these goals, the lens, the input and output manifolds, and the U-shaped waveguide phase adjustment were incorporated into a single package as shown in figure 1. In addition, replacing the Magic T's with E-plane T's and eliminating the aperture tapering attenuators simplified the design. Finally, careful reduction in manufacturing tolerances improved manufacturability with a minimal impact on performance.

5. COMBINED LENS, PHASE ADJUSTMENT, AND MANIFOLDS

The Rotman lens configuration was changed to a planar design to reduce the size of the overall system. The input and output interfaces of the separate manifolds were duplicated at each end of the planar package with the array phase adjustment incorporated into the internal waveguide interconnects. Beam port phase adjustment was not included, but could be added with an adapter, if needed. The planar design could be mounted to a vehicle's exterior surface, as is often preferred, by attaching a patch array to its broad face and routing its array ports to that array. For this application, however, transmit and receive lens assemblies are used as the top and bottom of the MFRF system package with the patch arrays mounted in between as shown in figure 3 to reduce overall system size.

6. FOLDED E-PLANE T DESIGN

The magic T's of the original design were simplified to folded E-plane T's for this one to save the cost of machining the waveguide ports for the terminations and the cost of the 53 terminations, themselves. The split ports of an E-plane T are not matched, with an S_{22} and S_{33} of about 6 dB, which would seem to be a prohibitive mismatch. However, as used in the Rotman lens, the split ports are always fed with similar amplitudes and phases. The phase difference is greatest at an end
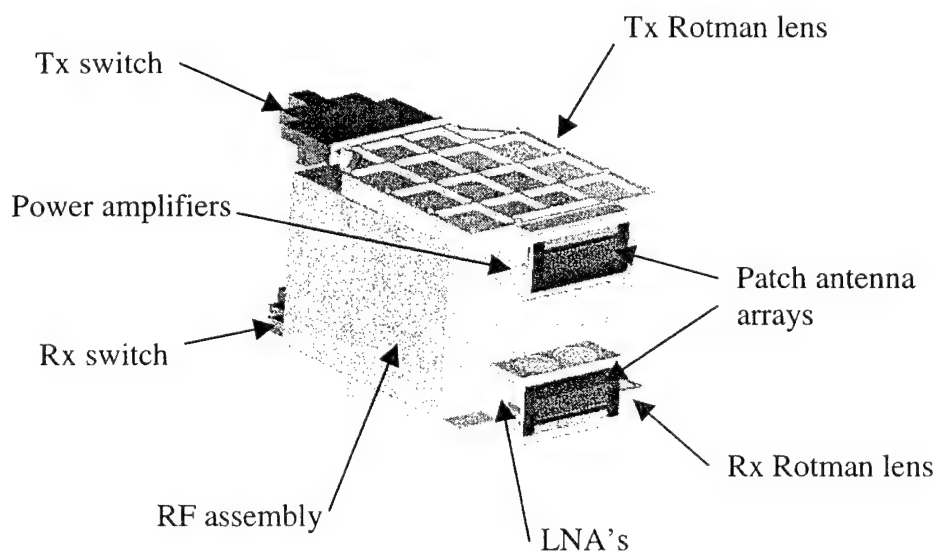

Figure 3. MFRF antenna configuration

405

array port when fed from an end beam port, estimated to be 58 degrees. Figure 4 shows the mismatch as a function of this phase difference. It shows how the mismatch increases from 0 dB at the center of scan to about 6 dB for the edge array ports at the scan extremes. The consequence of the mismatch would be to reflect signal back into the lens, which could increase the sidelobe level at the scan extremes. This degradation was expected to be minimal.
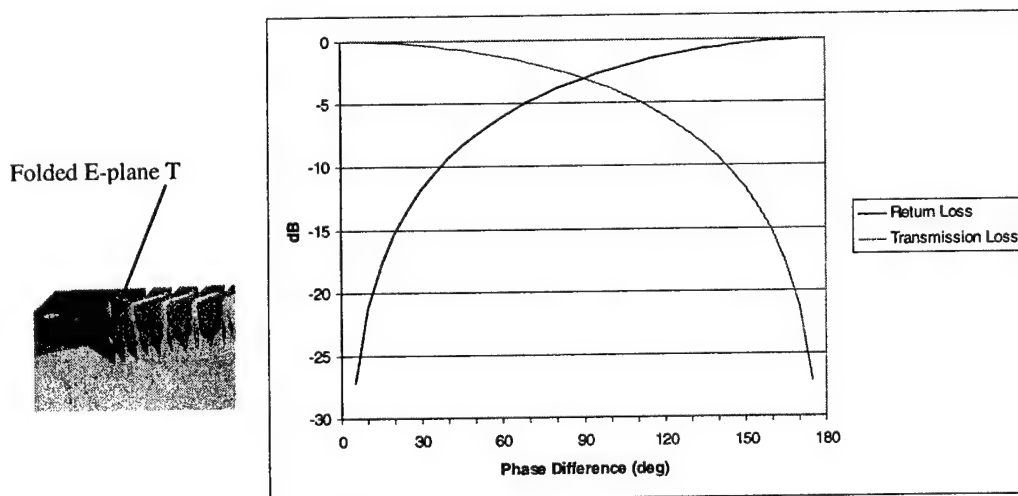

Figure 4. Mismatch due to folded-T junction

7. ELIMINATING APERTURE TAPERING ATTENUATORS

A Taylor distribution was applied to the array ports in the original design to reduce sidelobes by adding an attenuator in line with each port. The attenuators vary in phase shift requiring compensation in the waveguide interconnect path lengths. This cost and the cost of the attenuators themselves were saved by eliminating the attenuators. The resulting aperture distribution is nearly uniform, and a corresponding increase in the first sidelobes to about 13 dB would, therefore, be expected.

8. MECHANICAL DESIGN & FABRICATION

The parameters carrying the greatest importance in the fabrication of the Rotman lens were cost, weight, manufacturability, and electrical performance. Other parameters that impacted the configuration were overall size, port mating

constraints, and dimensional stability (with temperature and loading). In the case of the lens, cost and manufacturability are strongly tied. Tradeoffs between these parameters led to material selection, geometric design details (e.g. minimizing I/O waveguide lengths), tolerance specifications, limits on minimum feature sizes, and exclusion/modification of certain electrical design features. As an example of the last point, the original design contained matched T-junctions at the waveguide-to-cavity transitions; however, the electrical performance gained by incorporating these features was not sufficient to justify the large increase in fabrication cost, and the design was modified to exclude them.
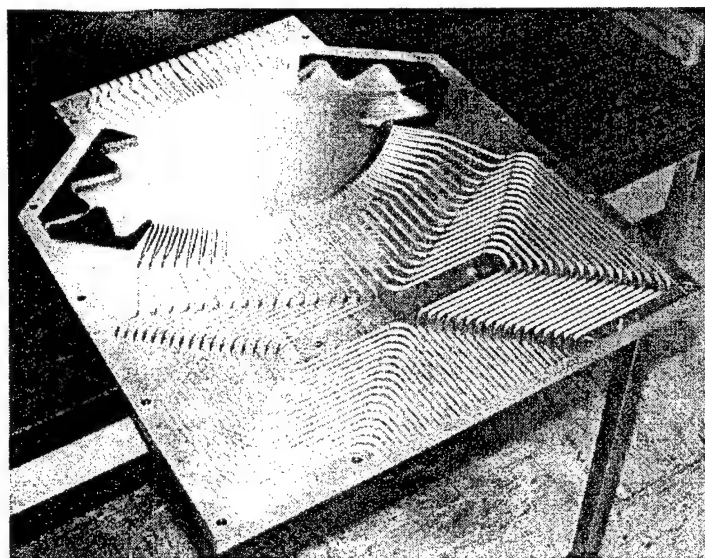
Figure 5. MFRF Rotman lens - one half shown, with absorber

The lens was fabricated from rectangular blocks in symmetric halves as shown in figure 5 with absorber installed. This splits the waveguides in the center of the broad wall, where the current is at a minimum, and also reduces vertical cutting depth for the dimensionally sensitive features. The thickness of the lens was made substantially greater than the waveguide height (7X) for structural rigidity (bending stiffness is increased by nearly 300X). The penalty is increased mass. However, pocketing the non-lens side of the blocks reduced the weight. For fabrication tolerances, it was determined that critical side-to-side dimensions should be held to +/- .003", but that the tolerance for the depth should be limited to +/-.0005". Of particular concern was flatness and alignment of the mating surfaces of the two halves. To address the alignment, pins were incorporated; and

to ensure contact of mating surfaces, fourteen ¼-20 bolts were used – together producing a nominal contact pressure of 250 psi. The material chosen was aluminum (alloy 6061-T6). This material is easy to machine, light, corrosion resistant, and not costly. To reduce out-of-plane warping, the use of other aluminum alloys and adding an annealing step to the fabrication process after the primary machining run were considered (due to residual stress), but were found to be unnecessary.

The lens input and output ports had to be designed to mate with the planar switch array output and the planar input of the T/R modules/antenna array, both K_a-band waveguide. This is nontrivial because the waveguide transitions to the lens cavity are of necessity along concave surfaces; and in addition, on the antenna side, all waveguides must have identical electrical lengths. To reduce the cost and complications of constructing one of a kind, independent waveguides, which were used in the previous design, the waveguide was cut directly into the block of the cavity. The overall size of the lens was reduced by parametrically minimizing the lengths of these waveguides.
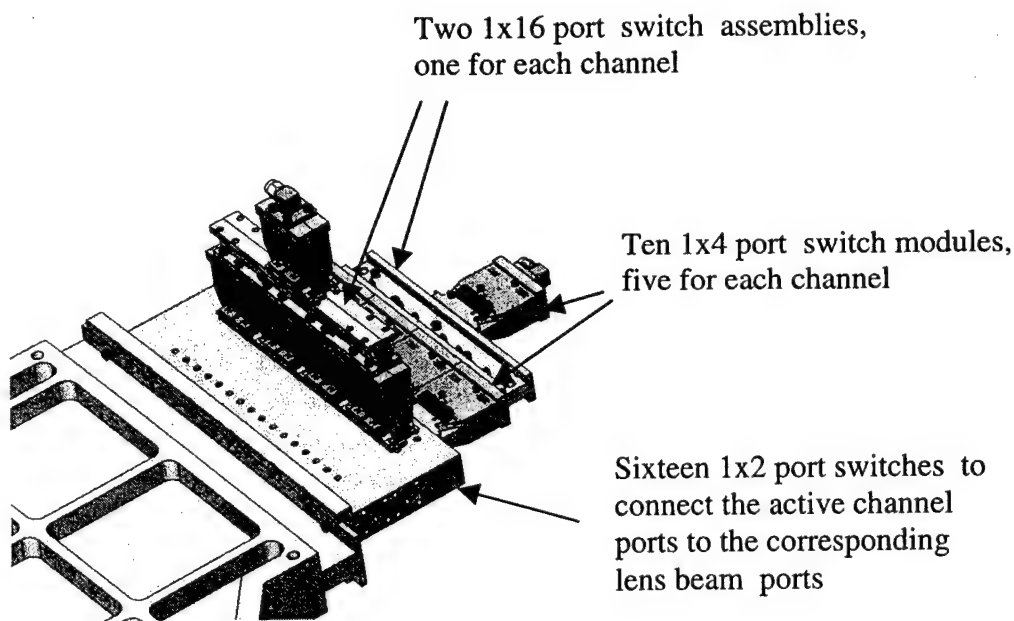

Figure 6. Trex Enterprises 2x16 PIN diode switch

9. BEAM-SWITCHING NETWORK

Two different approaches are being pursued to develop a 2x16 BSN that operates from 36 to 40 GHz. They are PIN-diode (Trex Enterprises) and photonic-actuated silicon-tab [2] (JJW Consulting) based designs. The PIN-diode design is shown in figure 6. Both designs use SPDT switch elements in four successive stages to achieve 1x16 switching. To achieve 2x16 switching, each of these 1x16 switches is followed by an array of sixteen SPDT switches to connect the selected output of

Parameter	Specification
Antenna gain	19-22 dBi (Open-end waveguide elements)
Azimuth beamwidth	2.6° nominal at 38 GHz
Azimuth sidelobes	15 dB peak
Polarization	Horizontal
Beam scan	±22.5° azimuth (17 beams)
Size	18 x 15 x 2 in.
Weight	14 lb.

Table 1. Rotman lens beamformer performance
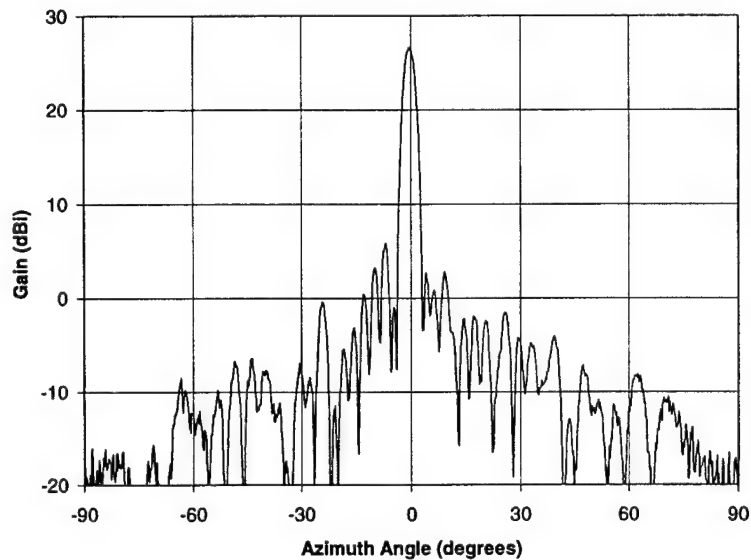
Figure 7. Radiation Pattern of GA Tech Rotman Lens Antenna
Sectoral Horn Output

409

each to the corresponding lens beam port. In addition, additional switching is provided to terminate unused ports. Since the signal passes through six stages of
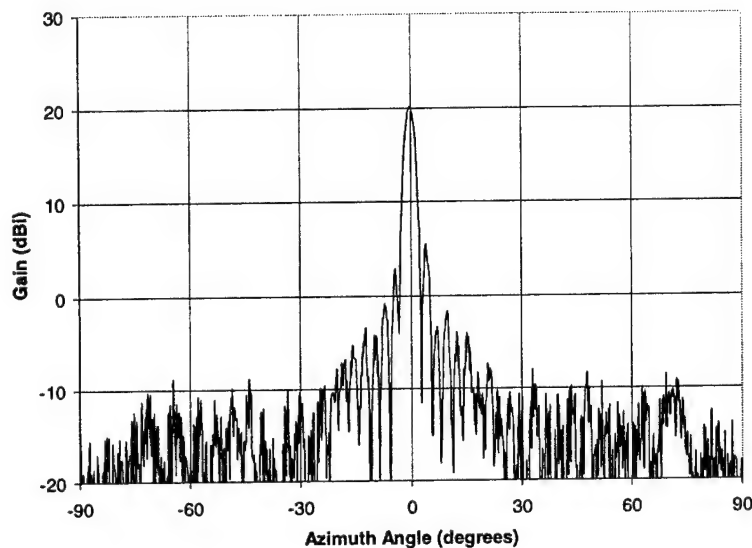

Figure 8. Radiation pattern of ARL Integrated Rotman Lens
Open-end Waveguide Output

switching in the 2x16 configuration, it is important that the loss of each stage be minimized. Even with a loss of only 1 dB per stage, additional losses due to transitions and interconnects in a microstrip package will bring the total insertion loss to about 10 dB.

Since both this loss and the maximum input power are marginal for many applications, other technologies are being investigated. Overall lower losses and the ability to handle higher input power would correspond to improved system specifications with regard to receiver noise figure and increased transmitted power.

10. ANECHOIC CHAMBER MEASUREMENTS

The antenna was tested in an anechoic chamber at ARL. The system was operated in a receive mode, and beam scanning in azimuth was measured to be greater than ±22°. The radiation pattern at 38 GHz of a center beam port is given in figure 8, compared to our measurements of the Georgia Tech antenna in figure 7. The superimposed measured patterns of all 19 beam positions are shown in figure 9. The measured performance is summarized in table 1.

410

11. FUTURE PLANS

Ongoing efforts related to this work include reducing the size, weight, and loss of the Rotman lens and creating switch technologies that are reliable, compact, and low loss. Architectures under evaluation include cavity-based designs and stripline configurations using various dielectrics. In the area of BSN development, we are continuing our work in PIN-diode arrays, using a traditional 2 x 16
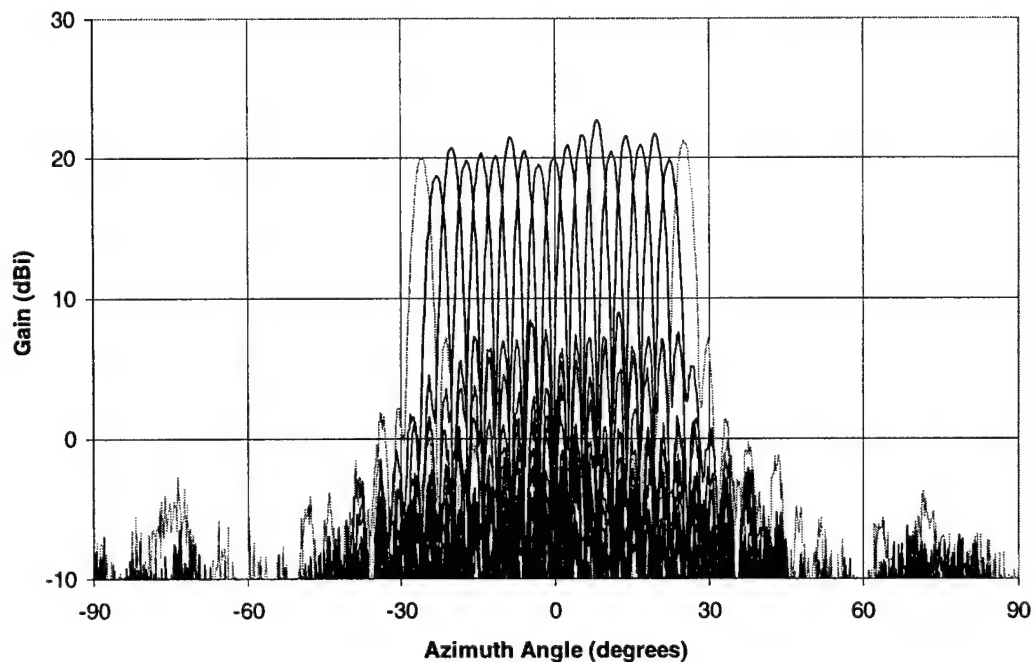
Figure 9. Superimposed measured patterns of all 19 beam ports

End-of-scan ports are not normally used but are shown for completeness.

architecture. In the future, we will pursue crossbar or tapped-line designs as well as continuing to address the photonic-actuated silicon-tab switch matrix.

12. CONCLUSION

An electronically scanned antenna system has been described that has the potential to meet the needs of one or more radar or communications systems residing on a single platform. Sharing the antenna aperture in this way makes it unnecessary to have separate antennas for each system. The advantages of this

411

technique include smaller total size, less weight, and lower cost. With further enhancements in Rotman lens architectures, BSNs, and wideband apertures; multimode and multibeam affordable ESA's will surely have a great impact on future combat systems.

REFERENCES

1. S. Weiss, R. Dahlstrom, O. Kilic, E. Viveiros, S. Tidrow, F. Crowne, E. Adler, "Overview of the Multifunction RF Effort – An Army Architecture for an Electronically Scanned Antenna," *Proceedings of the 2002 Antenna Applications Symposium*, pp. 119-129.

2. R. Augeri, J. Taub, J. Whelehan, S. Gellar, H. Malik, "Photonic Crossbar Switch" *GOMAC 2000 Digest*, vol. 25, pp. 328-33, March 2000.

3. R. Dahlstrom, P. Phu, B. Scheiner, E. Adler, J Lilly, "A Wideband Rotman Lens Electronic Scanning Antenna For Multimode Sensing Systems," *GOMAC-99 Digest of Papers*, vol. 24, pp. 502-505, March 1999.

4. E. O. Rausch, A. F. Peterson, and W. Wiebach, "A Low Cost, High Performance, Electronically Scanned MMW Antenna," *Microwave J.,* vol. 40, no. 1, pp. 20–32, January 1997.

5. E. O. Rausch, A. F. Peterson, and W. Wiebach, "Millimeter Wave Rotman Lens," *Proceedings of the 1997 IEEE National Radar Conference*, pp. 78–81, May 1997.

6. T. Katago, S. Mano, and S. Sato, "An Improved Design Method of Rotman Lens Antennas," *IEEE Trans. Antennas and Propagation,* vol. AP-32, no. 5, pp. 524–527, May 1984.

7. H.-H. Fuchs, D. Nüßler, "Design of Rotman lens for beamsteering of 94 GHz antenna array," *Electronic Letters*, vol. 35, no. 11, pp. 854-855, 27 May 1999.

A Two-Dimensional Millimeter Wave Phase Scanned Lens Utilizing Analog Photonic Band Gap Waveguide Phase Shifters

James B. West, John C. Mather, Jonathan P. Doane
Rockwell Collins, Inc.
400 Collins Rd
Cedar Rapids, IA 52498

Hao Xin, Hooman Kazemi, Aiden Higgins
Rockwell Scientific Co.
Thousand Oaks, CA 91360

Abstract: The electrical and mechanical design, top-level array calibration, and the measured scan performance of a 38 GHz 16-element proof-of-concept two-dimensional space fed phased array lens is described. A unique feature of the lens is the use of phase shifters developed at the Rockwell Scientific Company (RSC) that utilize tunable Photonic Band Gap (PBG) waveguide sidewalls to generate a 360° analog phase shifter at each radiating element to realize electronic beam scanning within a few microseconds. The waveguide phase shifter insertion loss performance is detailed and plans for further improving insertion loss are discussed. It is anticipated that the average insertion loss will be improved to be less than 2.0 dB at an operating frequency of 38 GHz for a GaAs substrate based PBG structure with planar Schottky diode tuning elements.

1. Introduction

Photonic Band Gap structures are well known devices that can function as a high impedance surface [1]. It has been shown that these "Electro-Magnetic Crystals" (EMXTs) can support a TEM mode when used as sidewalls in a rectangular waveguide. With the addition of active varactors, these tunable TEM waveguides can be used as 360° analog phase shifters [2]. By constructing a matrix of such devices, a waveguide phased array is realized. The array is excited by a simple space feed consisting of a single feed horn that illuminates the waveguide lens. The combination of the EMXT waveguide phase shifters and the space fed architecture results in a low cost, simple phased array.

This work presents a proof-of-concept 4x4 array demonstration. The size of the array was chosen to be large enough to demonstrate beam steering, yet small enough to design, build, and test a unit in a time efficient and cost effective manner. The eventual move to a larger, more practical aperture is anticipated in this paper and the projected consequences are noted.

1.1   Array Architecture

The architecture consists of a space fed constrained 4x4 (16 element) Transverse Electro-Magnetic (TEM) waveguide phased array lens. Each TEM waveguide utilizes the Rockwell Scientific Company's (RSC) unique and innovative tunable Photonic Band Gap EMXT (Electro-Magnetic Crystal) technology as waveguide sidewalls. The surface impedance of the EMXT sidewalls varies with DC bias. Variable, analog phase shift through each waveguide radiating element is possible by modulating the sidewall surface impedance which in turn modulates the waveguide propagation constant (β, or k) for the waveguide at a fixed frequency. The change in β initiates the variable insertion phase through the waveguide [2]. The phase shifters collimate the beam and add the required phase gradients across the array to activate two-dimensional electronic beam scanning.

A conceptual sketch of the array is shown in Figure 1.1-1 below.
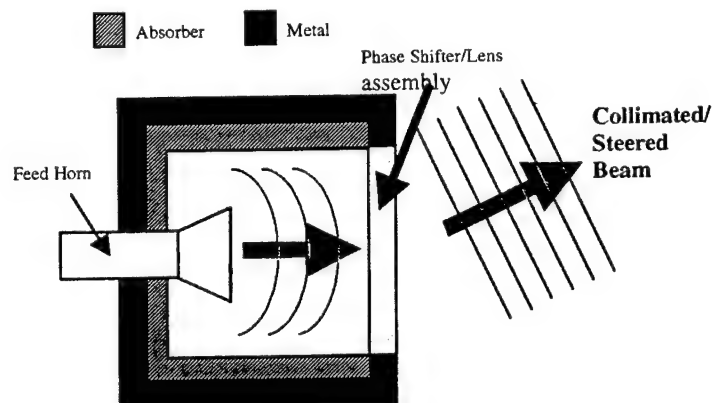
Figure 1.1-1. Array conceptual diagram

414

The array architecture using the EMXT phase shifters has several advantages, as delineated below:

- 360° analog phase shift is possible
- High Digital to Analog Converter (DAC) resolution provides a high effective phase shifter bit count.
- Real-time phase-based pattern synthesis is possible:
    - Fan beam
    - Agile pattern null forming
    - Possible to approximate one-dimensional $csc^2(\theta)$ radiation pattern for imaging modes
- Amplitude based pattern synthesis is feasible by "turning off" selected elements (at the cost of reduced array efficiency)
- No quantization side lobes or minimum steering increment normally associated with digital phase shifters
- Very fast phase shifter switching speeds
    - On the order of a few μsec is feasible
    - Limited by beam steering controller (BSC) hardware and control software
- Space feed significantly cuts down the array RF distribution network complexity
- BSC and DAC design approach simplifies bias interconnect scheme

1.2   EMXT Phase Shifter Technology

Figure 1.2-1 shows a waveguide element with high impedance EMXT sidewalls. The top and bottom surfaces of the waveguide are metallic conduction surfaces while the sidewalls are made up of high impedance surfaces, as shown.   Tuning elements are incorporated within the EMXT to realize similar behavior at a constant center frequency.

Indium Phosphide (InP) was chosen for the initial device substrate because of the mature InP processes already in place at the Rockwell Scientific Company (RSC). A current effort is underway to migrate the design to a Gallium Arsenide (GaAs) substrate that will provide a higher performance, lower loss device.
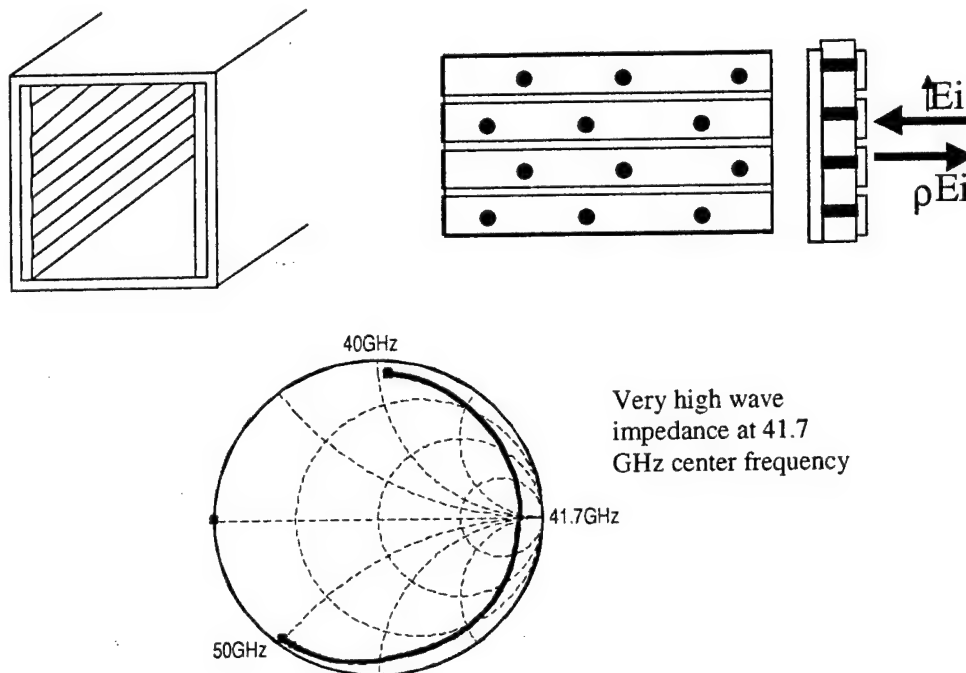
Very high wave
impedance at 41.7
GHz center frequency

Figure 1.2-1. TEM waveguide sidewall is a high impedance surface exhibiting a +1
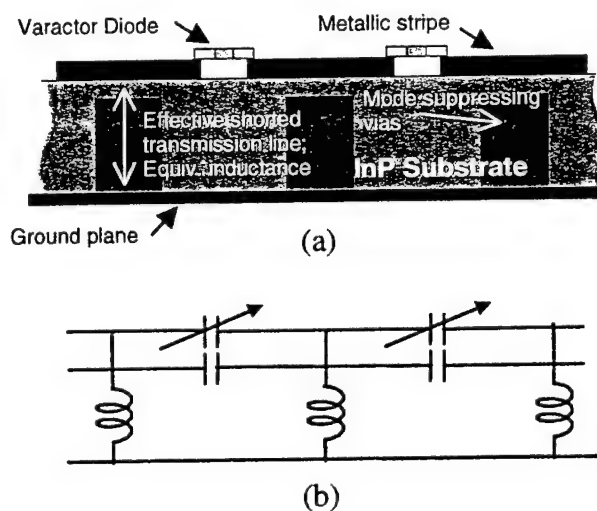reflection coefficient over the band of interest around a center resonance frequency

(a)

(b)

Figure 1.2-2. Phase shifter showing (a) physical implementation and (b) equivalent
resonant LC circuit.

The periodic arrangement of stripes on the EMXT forms a resonant structure, which can be thought of as an effective LC circuit, as shown in Figure 1.2-2 (b). The capacitance is created by the gap between the stripes as well as tunable InP varactor diodes placed across the gap. The substrate can be thought of as a transmission line, shorted out by the ground plane. An electrically short, grounded transmission line approximates an inductive reactance. The blind vias in the substrate are designed to prevent the propagation of undesired higher ordered modes within the EMXT substrate. The LC equivalent circuit exhibits a bandstop response and behaves as a high impedance surface for a range of frequencies. By adjusting the bias on the varactors, the overall capacitance changes, thus shifting the resonant frequency. For a fixed frequency, the impedance of the surface is a function of bias voltage. This causes a variable phase velocity for the wave traveling through the waveguide, which in turn realizes an analog variable waveguide phase shifter.
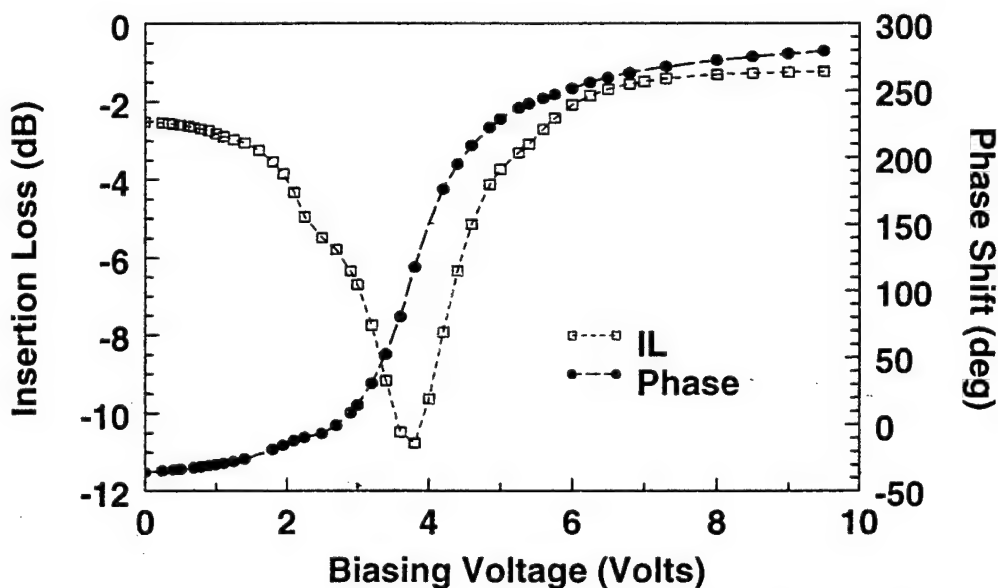
Figure 1.2-3. Representative InP Total Element Phase Shift Phase and Insertion Loss as a Function of Bias Voltage

Phase shift as a function of the varactor bias voltage for InP sidewalls is shown in Figure 1.2-3. The loss of the initial InP EMXT structure is quite high and varies as a function of bias voltage. The high insertion loss is attributed to two factors: a parasitic resonance within the EMXT structure, and the series resistance (Rs) of the InP varactor diodes. The next generation GaAs EMXT design is in process to remove the parasitic resonance and lower the diode series resistance.

2. Antenna Electrical Design

2.1 Lens Design

The lens is the component of the antenna that collimates the beam into a plane wave and scans the beam to the desired position. See Figure 2.1-1 for images of the final prototype 4x4 lens. The elements are spaced uniformly at $\lambda_o/2$. A slight rectangularity of the aperture produces an impedance of approximately 440Ω, resulting in theoretical mismatch loss of 0.7 dB relative to free space.
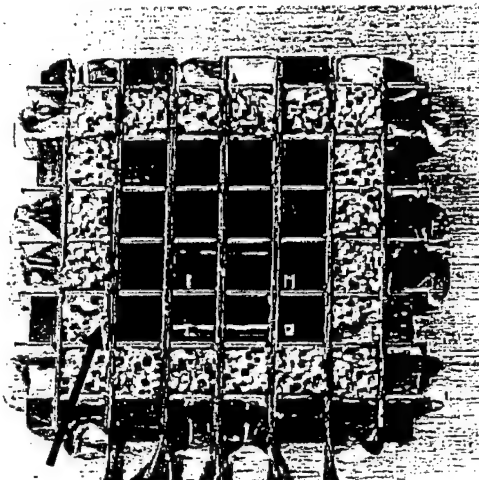
Lens Front Surface Absorber in non-active cells
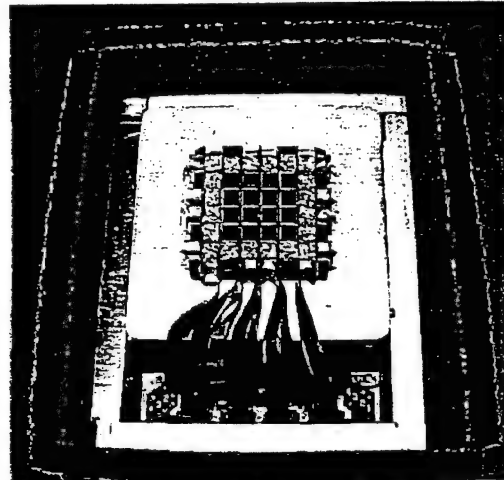
Lens with Bias Interconnect. Front absorber cover removed for clarity

Figure 2.1-1. Egg-Crate Lens Construction

2.2 Horn Design

The amplitude distribution of the horn was designed for a 10 dB taper, as this would provide low sidelobes and minimal spillover past the edges of the lens. The initial feed position was set to create an f/d ratio of ½. For ease in construction, the horn was designed as an E-Plane sectoral horn. A first order design was completed, assuming a 10dB taper in the far field at 45 degrees, which is the angle between the phase center of the horn and the edge of the lens for the given f/d ratio. Standard far field equations were used, along with PCAAD (Personal Computer Antenna Analysis and Design) [3], a general-purpose antenna design software package. This analysis was only approximate, as the far field behavior does not ensure such a pattern in the near field. This design was then modeled in Ansoft HFSS (High Frequency Structure Simulator) [4], which was used to calculate the antenna's near field response.

Comparison of contour cuts of the near field at varying distances away from the horn verified the proper amplitude illumination over the equivalent lens area.

Once the horn design and placement were set, the phase of the pattern incident onto the lens was analyzed in HFSS. Phase shift commands could then be given to the lens that would remove the natural spherical spreading of the signal, and therefore collimate the beam.

2.3   Feed Box Design

A self-contained feed box assembly lined inside and out with absorbing foam was designed to emulate a free space environment so that would energy flow between the feed and the lens without spurious reflections. A separate cavity was designed for the bias lines to pass through and remain fully shielded and unobtrusive to the radiated field of the antenna, see Figure 2.3-1. The box's dimensions were chosen to maximize the performance of the absorber in terms of the incident angle of the fields impinging on the absorber. A coax-to-waveguide transition was used to excite the horn. The feed horn was mounted to a precision linear positioning table, with a micrometer dial, which allowed precise adjustment of the horn placement (f/d ratio).

Feed Horn Assembly & Bias Connectors w/o Lens

F/D Adjustment Assembly

Feed Input

Top-Level Assembly
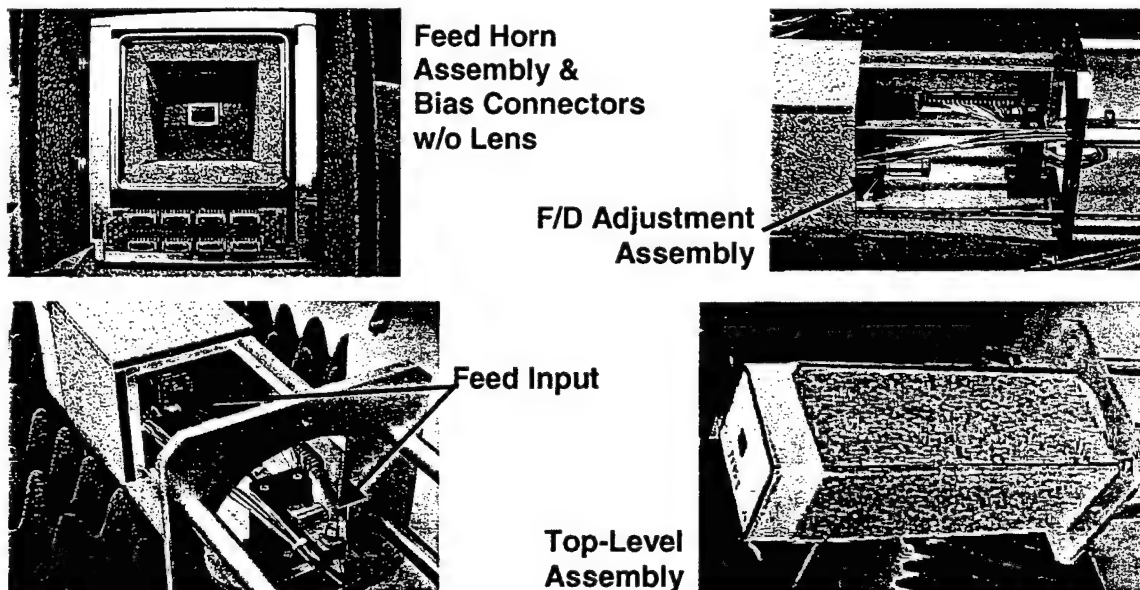
Figure 2.3-1. Feed Box Construction

2.4   Feed/Lens Interaction

Several factors that contribute to loss in the antenna are discussed below. The general performance of a space feed is expected to improve with an electrically larger array,

and the phase shifter insertion loss should dramatically reduce with the next generation EMXT design.

- **Spillover from the feed**. The absorber lining within the box absorbs energy that is not incident on the lens. HFSS analysis predicted approximately 1.5 dB of loss.

- **Reflection off of the face of the lens**. Some of the incident energy hits the sidewalls end on and is not transmitted optimally. The metal edge reflections and a slight reactive mismatch between the impedance of the TEM mode waveguide and free space also causes reflections. From HFSS analysis, the reflection from these factors contributes approx. 1.5dB of loss (see Figure 2.4-3). Top side bias requirements of the InP devices require metallic interconnect in the active area of the lens. This bias scheme causes a parasitic reflection that creates an additional 1 dB of loss.
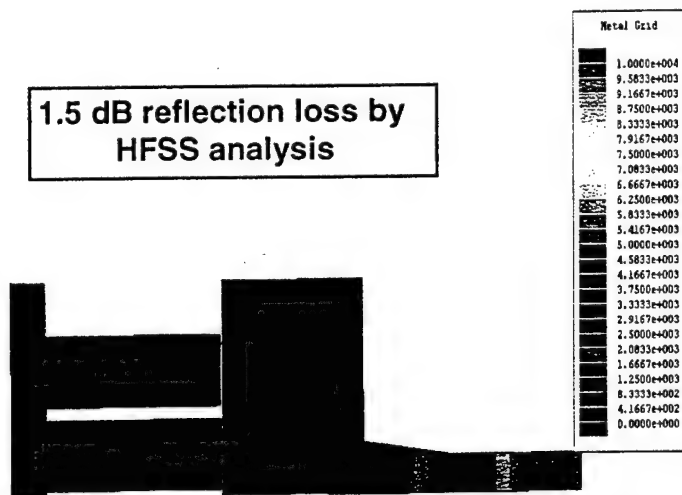
Figure 2.4-3. Reflection from Lens in Ansoft HFSS

- **InP EMXT Resistive Losses**. The InP EMXT based waveguide phase shifter exhibited from 2 to 11dB of loss through one waveguide, according to the HFSS Poynting vector-based analysis. This loss varied significantly with applied bias on the individual elements. The overall average loss tended to remain around 10 dB, but fluctuated moderately as the beam was steered.

Overall, average expected losses sum to approximately 14dB. The expected loss budget is given in Table 2.4-1.

Directivity	+ 16.5 dBi
Illumination	- 1.5 dB
Reflection	- 1.5 dB
Bias Scheme	- 1.0 dB
Average InP EMXT Losses	-10.0 dB
Total Gain	**2.5 dBi**

Table 2.4-1. Loss Budget for Array

2.5   Space Feed Design Issues

The space feed arrangement for phased array antennas offers the significant advantage of a greatly simplified millimeter wave feed network for arrays that are large in terms of a wavelength.   There are, however, some disadvantages of this approach.

The space fed, constrained waveguide phased array, also referred to as a transmission lens array in the literature, suffers from primary and secondary face reflections [5, 6]. Global reflections off the primary face scatter spherically in the back lobe, while secondary face reflections collimate in the feed horn at boresight. These reflections are related to mutual coupling. In addition, the focal point of the reflected energy moves with beam scanning, and secondary reflections can be manifest as parasitic forward side lobe energy. Space feeds are not "lossless", as in the case of a matched, isolated constrained feed. In addition, the space feed is not "perfectly matched" from secondary to primary faces.

The use of a Wide Angle Impedance Matching (WAIM) structure, as discussed in Section 2.6 below, would minimize mutual coupling and should reduce the effects of primary and secondary face reflections. In addition, the absorber within the feed mount assembly should reduce the effects of phase scanned back-scattered reflection side lobes.

In spite of the above-mentioned issues, the space feed is a good compromise between millimeter wave interconnection complexity and performance. It is instructive to compare our 4x4 space feed performance to that of other space feed systems that are described in the literature.   An illustrative example is the HAPDAR Space Fed Phased Array Radar [7]. The phased array for this system consists of an active dipole lens with a 41λ diameter, an f/d ratio of one, and is fed with a 5 horn monopole feed which has a 9 dB horn edge taper. Measured performance includes the following parameters: 39.5dBi gain, -28dB peak side lobe levels, and 2.4dB spillover and

mismatch losses. This compares favorably to the 3dB illumination spillover and reflection loss simulation of the 4x4 array.

2.6   Mutual Coupling

Most first order array analyses assume that each element ignores any effects that the elements have on each other within the array environment. Inter-element interaction, or mutual coupling, can result in reduced gain at large scan angles, or in extreme cases, scan blindness [8]. Analysis was performed to evaluate the mutual coupling experienced by the lens. HFSS was used with an infinite array assumption ("Master/Slave" boundary condition option), to evaluate the severity of mutual coupling over the scan volume. It is anticipated that the infinite array analysis is more stringent than the electrically small 4x4 array. It will however, indicate potential problems for the 4x4 array that can be used to determine the expected performance of a larger array. A plot of return loss versus scan angle in three planes can be seen in Figure 2.6-1. It can be seen that the scan tends to fall off at about 40 degrees in the E Plane (vertically) and about 55 degrees in the H Plane (horizontally). In the intercardinal plane, there is less sensitivity to mutual coupling.

A Wide Angle Impedance Matching Network (WAIM) can significantly improve the wide-angle scan performance of a phased array under the influence of mutual coupling. A WAIM typically consists of one or more sheets of dielectric that covers
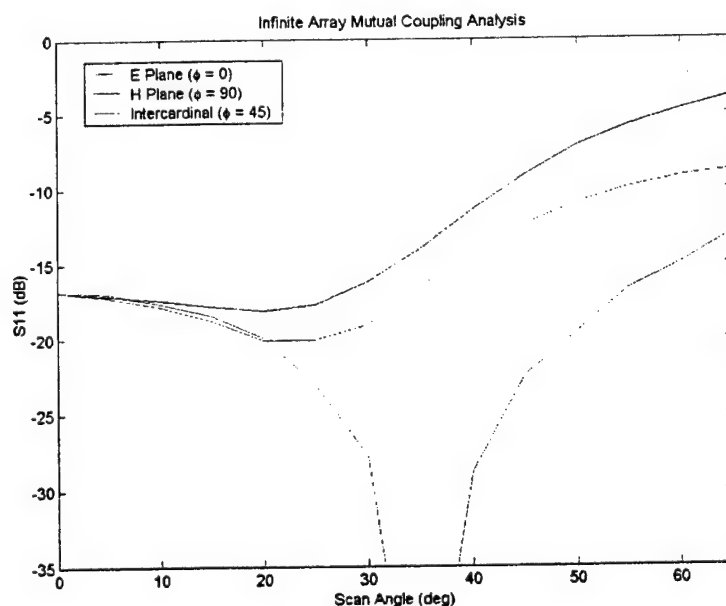
Figure 2.6-1. Mutual Coupling Return Loss Analysis.

one or both of the faces of the lens. It reactively loads the mutual coupling EM reactive near field region between the elements in a prescribed manner such that the array is able to scan out to much wider angles without significant element impedance mismatch [9]. It can also serve the dual purpose of a radome for environmental protection of the antenna.

3. Mechanical Design

From an interconnect perspective, the primary objective of the project was to create an array antenna having 16 active elements in a 4x4 configuration. Each element is to have EMXT devices on the sidewalls and a conductive (metal) "floor" and "ceiling". Each EMXT device requires a unique bias voltage plus a ground connection to realize the unique element phase shift control. Figure 3-1 illustrates the rectangular array grid of EMXT waveguide along with their respective bias/control circuits.
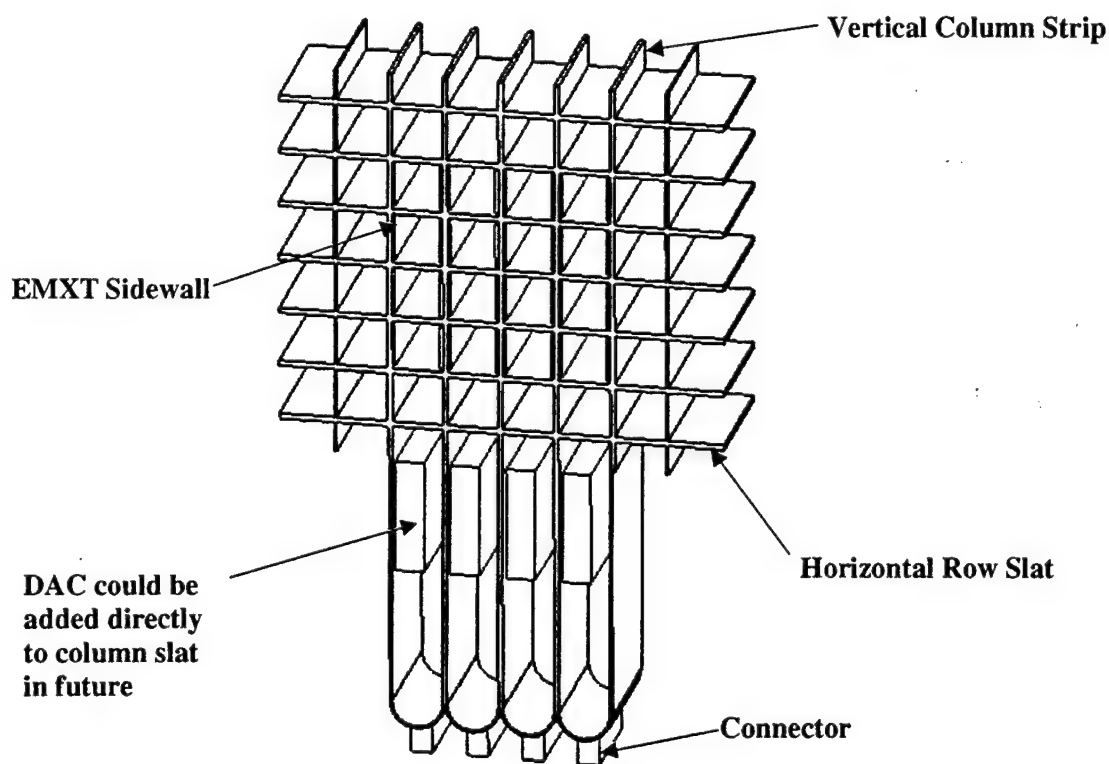
Figure 3-1. Sketch of a 4x4-size array antenna, indicating key elements of a packaging and interconnect approach scalable to larger array.

Figure 3-2 shows the array mounted in the antenna box. The antenna box held the feed horn and the lens in position, and provided electrical isolation from external interference. It was lined with absorptive foam to minimize multiple reflections between the horn and the lens. It also held the interconnect required to bias the EMXT sidewalls.
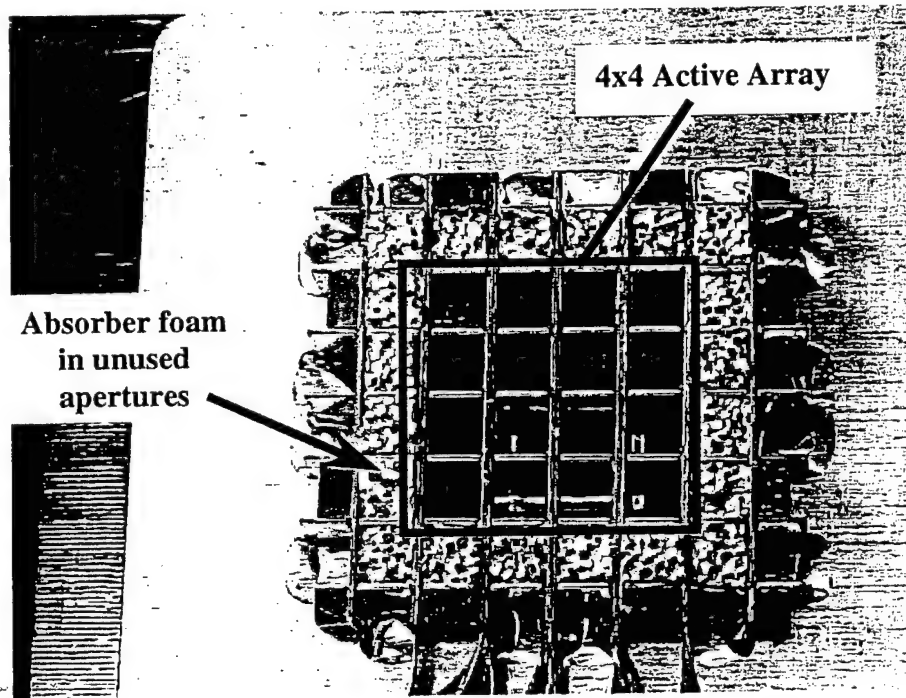
Figure 3-2. Close-up of a portion of the assembled test fixture showing the array antenna mounted in antenna box.

4.   Test Results

The antenna was tested in an anechoic chamber with a Hewlett-Packard 85301C network analyzer and F/R 959+ chamber control and data acquisition software. Antenna patterns were taken using standard methods [10]. The EMXT biases were controlled with a standard PC equipped with a DAC card and custom software.

Although theoretical curves for element phase versus applied bias voltage were available from EMXT measurement and simulation, several factors were present that necessitated additional calibration. Construction tolerances, EMXT electrical performance variations, and mutual coupling all contributed to a departure from theoretical performance. The calibration process yields curves for the approximate

element phase versus bias voltage. The theoretical phase is calculated for each element using standard phased array formulas [11], and then the appropriate voltage is extracted from the calibration curve table. This voltage is then applied to the element through the DAC card in the Beam Steering Computer (BSC). Because the calibration process is not exact, phase errors still exist which result in lower gain and higher sidelobes. However, with more accurate calibration, which is possible with a near field range, much better patterns can be achieved.
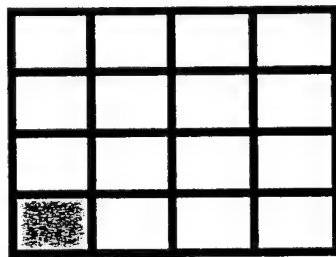
▧▧▧▧ **Dead element**

Figure 4-1. Initial Array Front Face with 'Dead' Element

The first 4x4 prototype had one DC-shorted element at initial turn on (See Figure 4-1). Possible causes are chip infant mortality, damage during lens construction, or Electro-Static Discharge (ESD). After manual calibration of the array, a boresight pattern was taken that showed 4dBi of gain (See Figure 4-2). This was better than the 2.5 dBi estimate from computer simulation. The probable cause for the discrepancy is the method that was used to simulate the EMXT in HFSS. This resulted in a more pessimistic estimate for the back-scattering from the EMXT than was actually realized in the laboratory.

Unfortunately, over the course of characterizing the prototype, 4 more elements became non-functional, and all subsequent data presented herein is for an array with only 11 working elements (See Figure 4-3). ESD is the suspected cause of this further degradation. After the loss of the additional array elements, the gain was reduced to approximately 2dBi at boresight.
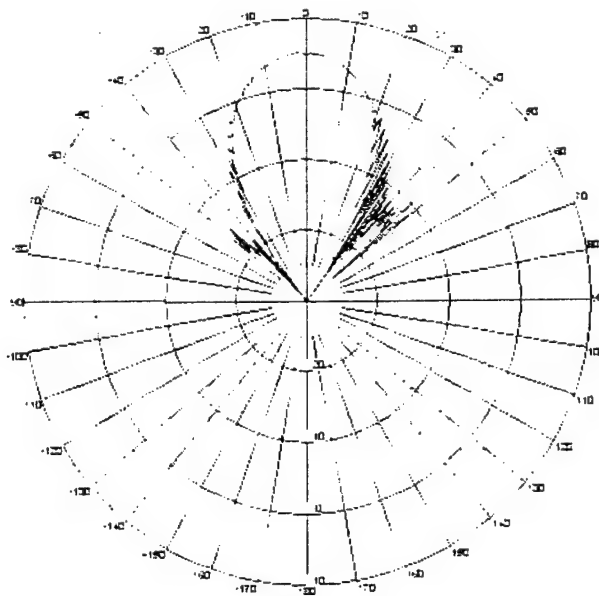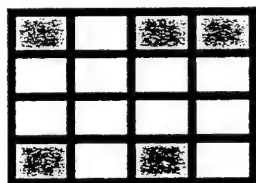
Figure 4-2. Boresight Pattern with 15 of 16 Elements Live

Dead elements

Figure 4-3. Array Front Face with 11 of 16 Elements Live

Patterns for the array were taken in the E Plane (vertical), H Plane (horizontal), and intercardinally (at –45° and +45° angles). Beam steering of ± 30° off boresight was demonstrated (See Figures 4-4 and 4-5 – *Note: Patterns shown are not all 30° scans*). Scan angles beyond 30°-40° tended to fall off in gain faster than the theoretical cos(θ) limit. This is most likely due to mutual coupling, inoperative elements, and non-optimum calibration. As can be seen, the sidelobes of the patterns tended to be higher than optimal, a direct result of the non-ideal calibration.
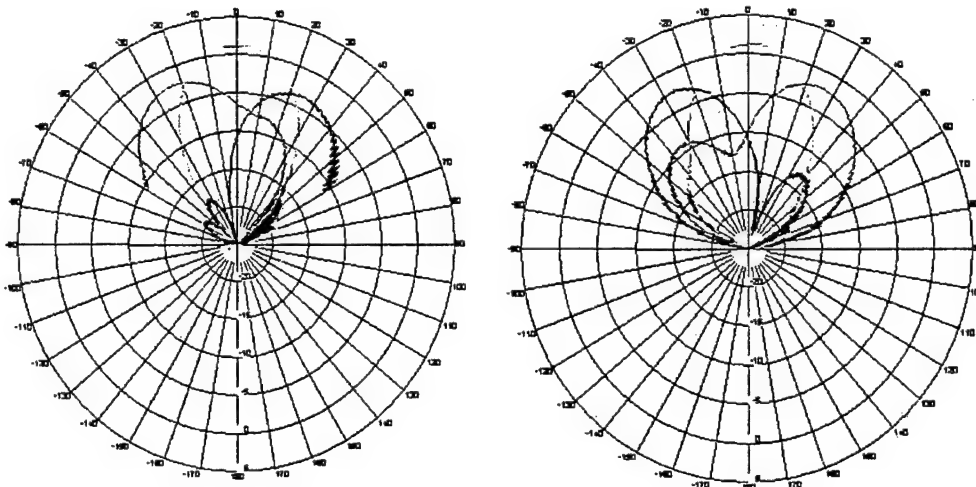
Figure 4-4. Antenna Patterns in E and H Planes (11 of 16 Elements Live)
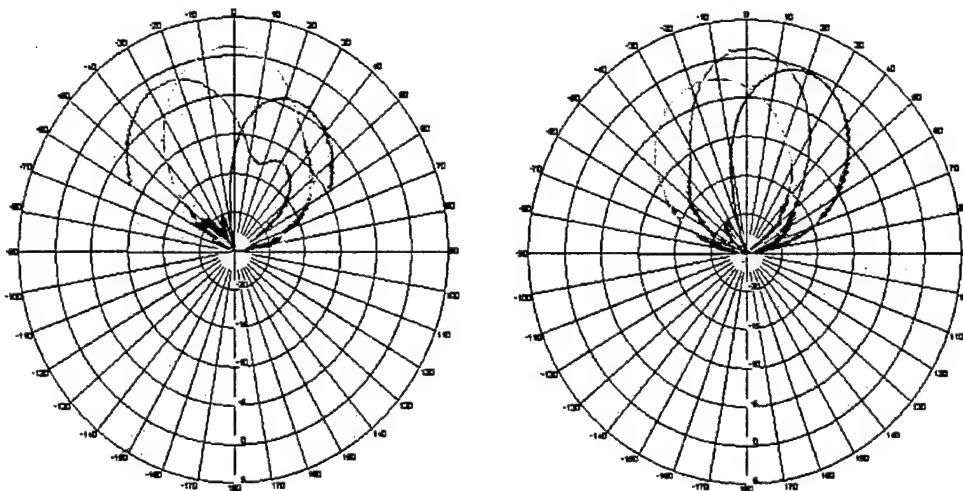
Figure 4-5. Antenna Patterns in Intercardinal Planes (11 of 16 Elements Live)

In addition to standard beam positions, several fan beam shapes were also attempted. These are shown in Figure 4-6 for both the E and H Planes. Because array pattern syntheses requires a rather high fidelity aperture control, the patterns suffered as a result of the small 4x4-aperture size and the 5 'dead' elements. However, phase-only beam-shaping capability was demonstrated.
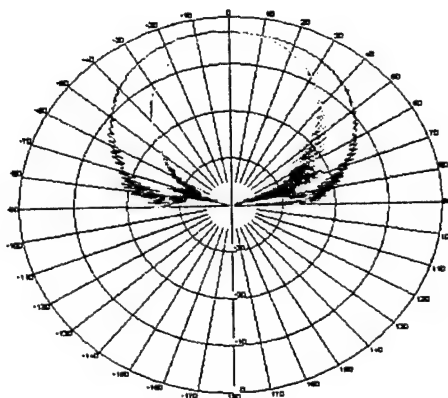
E plane Fan Beam:
E & H plane cuts
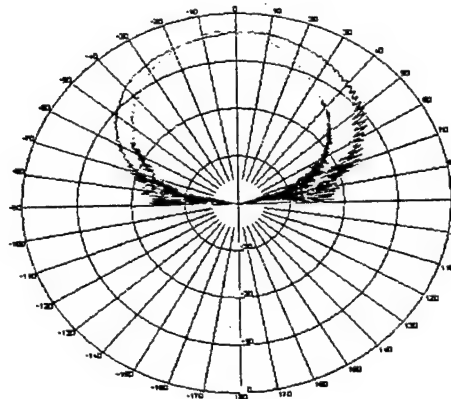
H plane Fan Beam:
E & H plane cuts

Figure 4-6. Fan Beam Patterns in E and H Planes (5 'Dead' Elements)

After the initial calibration was performed, a gradient optimizer was used to maximize the gain at the peak beam position. This approach was chosen due to schedule constraints and the lack of availability of a millimeter wave near field range. Because of the limitations in the original calibration scheme, we were subsequently able to further improve the gain of the pattern several dB at specific beam pointing angles (See Figure 4-7). This further supports that a more precise calibration method, such as a near field holography, would produce higher gain patterns than previously demonstrated.
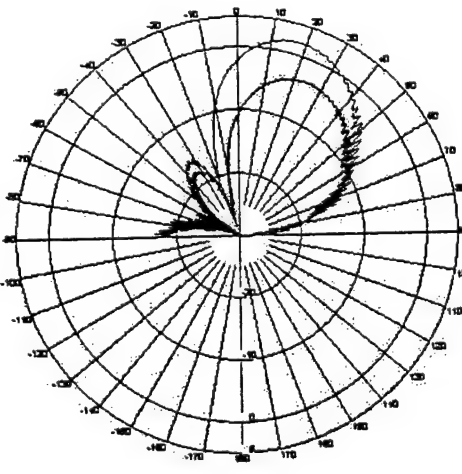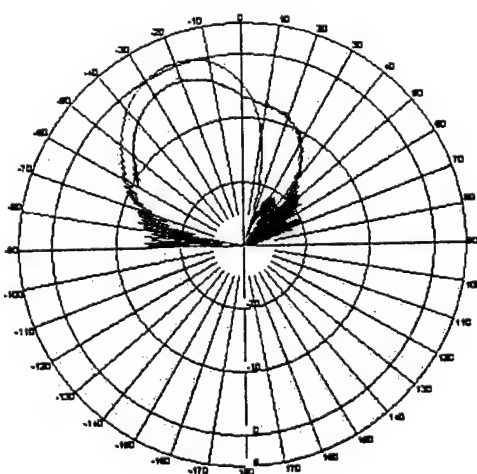
Figure 4-7. Optimized Patterns (Red) versus the Manually Calibrated Pattern (Blue) for 25° scan angles (dBi) (with 11 of 16 elements live)

5. Discussions and Future Work

The feasibility of a high performance 38 GHz waveguide lens utilizing analog 360° was verified in this work by means of a 4x4 proof-of-concept space fed lens demonstration. The following areas for future work to improve the performance of the array were identified in the course of this effort:

1. Mitigation of the effect of EMXT performance variations due to normal MMIC (Monolithic Microwave Integrated Circuit) integrated circuit process variations.
2. Improvement of the array calibration procedure
3. Reduction the parasitic resonance and resistive insertion losses in the next generation EMXT devices

5.1 EXMT Fabrication Tolerances

This is currently under investigation. The bias and calibration scheme used in this work assumed that every EMXT device within the array has identical surface impedance (Z_s) vs. DC voltage curves. This is not likely, due to EMXT device variations resulting from MMIC IC fabrication tolerances. Computer simulations of the performance of TEM waveguides with non-equal surface impedances are currently in process and test fixtures are under construction to experimentally verify the results of these studies. It is feasible, in the worst case scenario, to provide different control signals to each sidewall within a waveguide to optimize a single waveguide's performance. In addition, calibration schemes to account for waveguide-to-waveguide control voltages are also being considered. These results will be presented in future publications.

5.2 Improved Array Calibration

The quality of the array calibration scheme is readily improved with the use of a planar near field antenna metrology range with aperture holographic capability [12-14]. Aperture holography is an extremely powerful diagnostic and calibration tool since the aperture amplitude and phase excitation for any set of EMXT control voltages can be readily determined. Optimal calibration algorithms can be developed with this aperture information.

5.3 Improved EMXT Device Performance

The Schottky varactor diode not only has a variable capacitance C_V but also has a internal series resistance R_S. This resistance has been identified as the main factor

contributing to the loss in the initial InP varactor EMXTs developed by RSC. Reducing this resistance will significantly reduce the loss in the EMXT. Another effective but less obvious way to reduce the EMXT loss is to optimize all the components of the equivalent circuit such that the current flowing through the diode is minimized. This optimization process requires carefully selecting the substrate thickness, the strip width and gap, and the diode anode geometry and size in order to minimize loss.

Such EMXT performance improvements are currently being aggressively pursued by the Rockwell Scientific Company. The next generation EMXT devices will incorporate GaAs device technology with the use of Planar Air Bridge Schottky (PAS) Diodes. It is well known within the industry that these diodes are capable of providing low loss performance at millimeter wave frequencies. Initial data is given in the following section.

5.4   GaAs EMXT Insertion Loss and Phase Shift Simulation

The simulated effective impedance of the GaAs Schottky diode EMXT is used as sidewall boundary conditions in an HFSS model of a 10mm long waveguide with a 3x3mm aperture. Insertion loss and phase shift as function of the diode capacitance, (i.e. bias voltage), was simulated. With the current GaAs EMXT design, simulations show that a 360° phase shifter with insertion losses of 1.8, 2.0, 3.0, and 4.5 dB, can be achieved with a series resistance of 1.0, 1.5, 2.0, and 3.0 Ohms, respectively. Figure 5.4-1 plots the phase shift and insertion loss performance of the EMXT phase shifter with diode resistance of 1.0 Ohm.
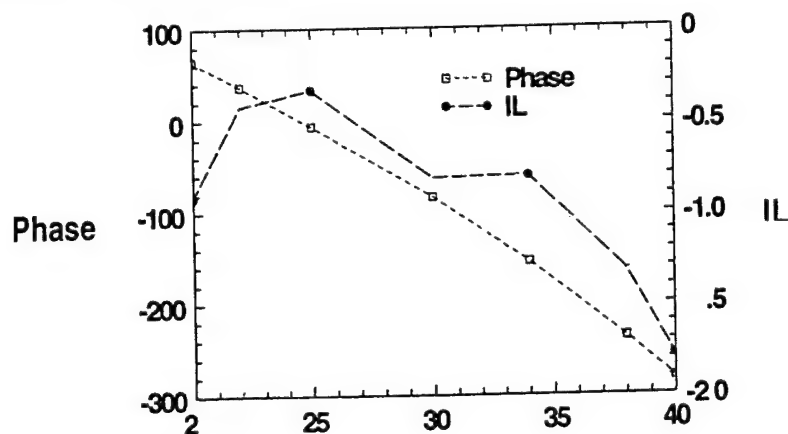

Figure 5.4-1. Simulated phase shift and insertion loss performance assuming a diode with 20-40 fF capacitance and 1.0 Ohm series resistance.

430

6. Acknowledgements

The authors would like to thank several personnel for their contributions. Joel Wichgers, Dan Houghkirk, and Bryan Hauck designed, built, and tested the BSC hardware and control software. Christina Conway contributed to the lens interconnect design. Mike Davidson and Russ Barta performed the antenna pattern and die level reflection tests. The contributions of these individuals are greatly appreciated.

7. References

[1] Sievenpiper, D., Zhang, L., Broas, R., Alexopolous, N., Yablonovitch, E., <u>High-Impedance Electromagnetic Surfaces with a Forbidden Frequency Band.</u> IEEE Transactions on Microwave Theory and Techniques. Vol. 47, No. 11, November 1999.

[2] Higgins, J.A., Xin, H., and Sailer, A., <u>Characteristics of Ka Band Waveguide using Electromagnetic Crystal Sidewalls,</u> IEEE 2002 International Symposium on Microwave Theory and Techniques, 99. 1071 – 1074.

[3] Pozar D.M., <u>Personal Computer Aided Antenna Design v. 4.03.</u> Antenna Design Associates, 1999.

[4] <u>High Frequency Structure Simulator, v. 8.0.25</u>, Ansoft Corporation, 2001.

[5] Brookner, E., <u>Practical Phased Array Systems</u>, Artech House, Norwood, MA, 1991.

[6] Skolnik, M., <u>Radar Handbook, 2nd Ed</u>, McGraw Hill, NY, NY, 1990, Chapter 7, Phased Array Antennas.

[7] Kahrilas, P.J., <u>HAPDAR - An Operational Phased Array Radar</u>, Proceedings of the IEEE, VOL. 56, NO. 11, November, 1968, pp. 1967 - 1975.

[8] Mailloux, R.J., <u>Phased Array Antenna Handbook</u>, Artech House, Norwood, MA, 1994.

[9] Lamberty, B.J., Geren, W.P., Goodman, S.H., Miller, G.E., Dallabetta, K.A., <u>Wide Angle Impedance Matching Surfaces for Circular Waveguide Phased Array Antennas with 70 Degree Scan Capability</u>, Proceedings of the 1992 Antenna Applications Symposium, University of Illinois, Robert Alerton Park, Sept. 1992.

[10] <u>IEEE Standard Test Procedures for Antennas</u>, IEEE Std. 149-1979, published by IEEE, Inc., 1979, distributed by Wiley-Interscience.

[11] Balanis, C.A., <u>Antenna Theory, Analysis, and Design</u>, John Wiley & Sons, New York, NY, 1997.

[12] Slater, Dan, <u>Near-Field Antenna Measurements,</u> Artech House, Norwood, MA, 1991.

[13] 1989 Antenna Measurements Techniques Society (AMTA) Workshop on Phased Array Antenna Testing.

[14] National Bureau of Standards (NBS), <u>Near Field Antenna Measurements, Short Course Notes</u>, Boulder, Colorado, 1989.

Miniature Controlled Receive Pattern
Antenna for GPS

Victor Sanchez, Eric Caswell, Ash Miller
Titan Systems Corporation – Aerospace Electronics Division

Dennis DeCarlo
Naval Air Systems Command
4.5.5 RF Sensors Division

Peter Rothenberg
EDO Corporation – Communications and Countermeasures
Systems Division (CCSD)

Abstract: A controlled receive pattern antenna array with reduced footprint has been developed for anti-jam GPS applications. The antenna consists of a stacked circular microstrip patch (reference channel) surrounded by eight dual-band monopole mode auxiliary elements in close proximity, resulting in a total array diameter of 4.6". The eight auxiliary elements are linearly combined, via a stripline hybrid feed network into two auxiliary port channels. A simple, two-channel closed-loop nulling electronics card is then used to operate the antenna in one of three modes: (1) a standard GPS mode with no nulling, (2) a ring-null mode where the pattern is squinted up off horizon at all azimuth angles and (3) a cardioid mode where a single null is placed on horizon and is steered in azimuth.

1. Introduction

The U.S. Navy and Marine Corps currently employ GPS navigation and targeting subsystems on a major fraction of their sea, air and land based weapon systems. The Navy realizes that the anti-jamming and anti-spoofing capabilities of military GPS user equipment are critical to successful mission completion in a battlefield environment and GPS-based navigation systems used on aircraft, ships, land vehicles and precision-guided munitions must be able to be protected from these threats. One of their approaches is to install nulling antennas and antenna electronics whenever feasible and cost effective. Due to the variety and sizes of Navy platforms one anti-jamming antenna system will not be adequate for all platforms. A National Research Council's Committee on the Future of the Global

Positioning System recommended that, "Research and development focused on reducing the size and cost of this hardware should actively be supported." It is very clearly stated in their reports that, "These future developments aimed at reducing the size and cost of antenna structures should be actively pursued."

The U.S. Navy primarily employs FRPA's, Fixed Reception Pattern Antennas, which do not offer spatial nulling capability. Some of the Navy platforms that require spatial nulling cannot support an increased footprint or significant increase in cost. In 1998 the Antenna Technology Group of the Naval Air Systems Command started a joint effort with Titan Aerospace Electronics Division (TAED) for the development of an antenna similar in size to a FRPA antenna that would provide anti-jamming capabilities. The Office of Naval Research Navigation Office was solicited for their support in funding this 6.2 development effort and has provided funding for the last three years.

In response to the Navy's need, Titan Aerospace Electronics Division has developed a small, anti-jam GPS antenna under the ONR NAVAIR Miniature Controlled Receive Antenna program (M-CRPA – Contract Number: N00421-00-C-0157). A diagram of this antenna array is shown below in Fig. 1. The M-CRPA
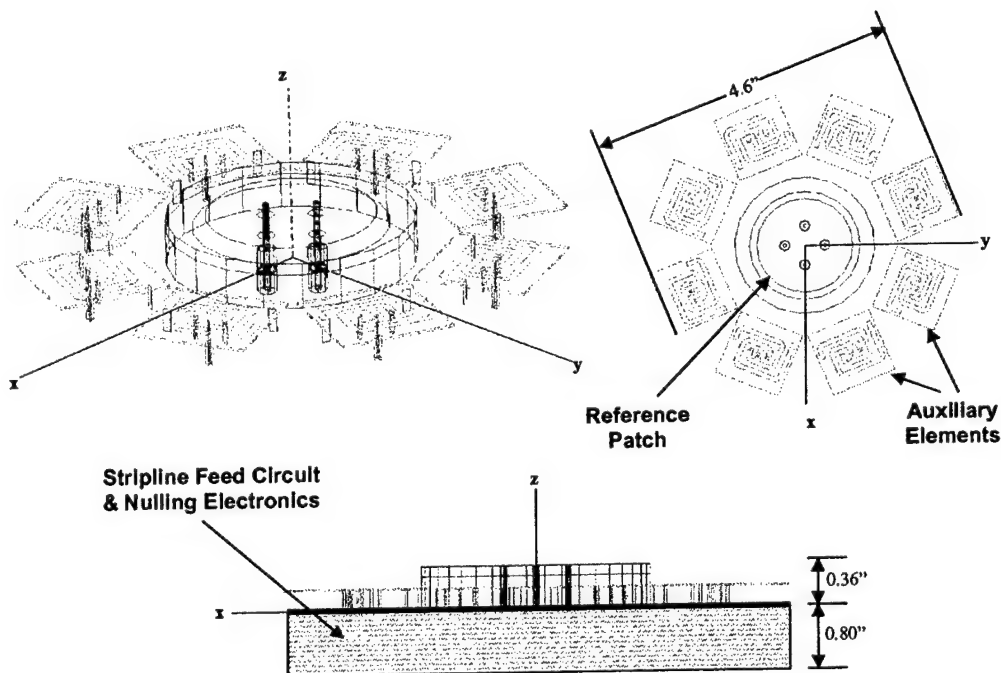

Figure 1. M-CRPA antenna geometry

array consists of a center, dual-band reference patch surrounded by eight dual-band monopole mode auxiliary elements. The monopoles are linearly combined into two auxiliary ports through a stripline feed card. The auxiliary port outputs of the feed card are combined with the center reference channel in a simple, two-channel nuller that is also realized in stripline. Both the feed card and the nuller were developed at EDO Corporation's Communications and Countermeasures Systems Division (CCSD). The antenna has a diameter of 4.6" and a height of 0.36". The feed and nulling electronics conform to the antenna diameter of 4.6" and adds a combined 0.8" to overall depth.

2. Antenna Operational Concept

The M-CRPA antenna is designed to operate in three different modes depending on the jamming scenario. Mode 1 is the standard GPS mode, which is used when no jammers are present for maximum GPS performance. Only the reference patch port is used for Mode 1. A basic stacked patch configuration is used for Mode 1 operation, as depicted in Fig. 2. The stacked patch has good hemispherical coverage and circular polarization, which is necessary for GPS operation.
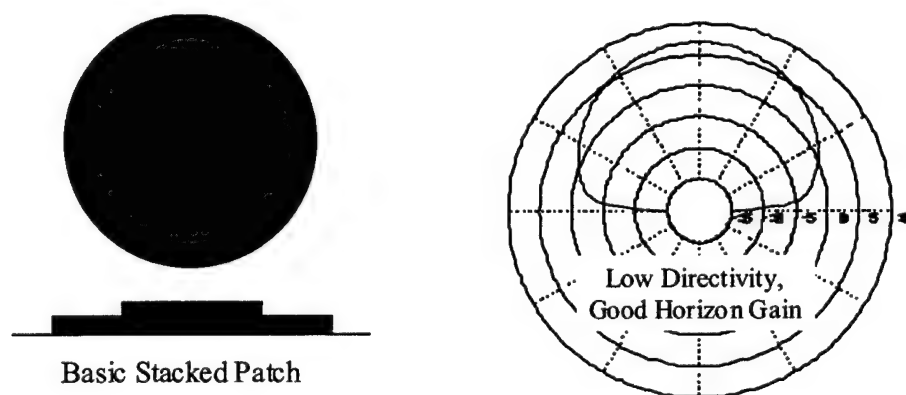

Basic Stacked Patch

Low Directivity, Good Horizon Gain

Figure 2. Mode 1 operation

When multiple jammers are present, Mode 2, or "skirt's up" mode, is used to form a ring null on the horizon in a manner similar to the LEAN antenna [1]. Fig. 3 shows the Mode 2 concept, which has the basic stacked patch surrounded by eight monopole mode auxiliary elements. Since the stacked patch has an intrinsic null in its horizontal polarization gain on horizon, only the vertical gain must be nulled by the auxiliary elements. Monopole mode auxiliary elements

were chosen because of their uniform horizon coverage for vertical polarization. Also, the zenith null in the monopole pattern minimizes the impact on the gain of the reference patch at zenith during nulling. The ring null is formed by sequentially exciting the auxiliary elements with a 45° phase shift yielding a pattern with uniform amplitude and a full 360° of phase shift in azimuth. This matches the amplitude and phase behavior of the circularly polarized stacked patch. The nulling electronics is then used to sum the aux element port and the stacked patch port with the appropriate complex weighting to create a null on the horizon at all azimuth angles. There is some horizontal degradation of performance (HDOP) necessarily associated with Mode 2 operation due to the elimination of satellite coverage near horizon. In a typical 24 hour period, one can expect an increase in HDOP of greater than 5 for only 5% of the total time. The nominal HDOP around the world is 2.5, per the GPS specification.

Basic Stacked Patch Plus
Eight 45° Sequentially
Phased Auxiliary Elements

Much Lower Gain on Horizon
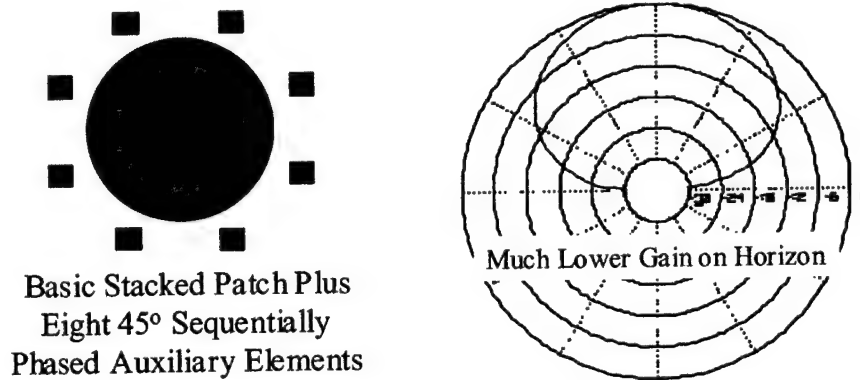
Figure 3. Mode 2 operation

Mode 3, or "Cardioid" mode, is used when only one jammer is present on the horizon. The concept is similar to Mode 2 operation but, in this case, all of the aux elements are fed in phase. This results in a single null on the horizon, as shown in Fig. 4, corresponding to the angle where the aux element port and stacked patch port are exactly out of phase. The nulling electronics automatically adjusts the complex weighting between reference patch and auxiliary port to form a null which tracks the jammer azimuth location. This mode is preferable to Mode 2 when a single jammer is present because its better antenna coverage, especially on horizon, results in less HDOP and thus better GPS performance.
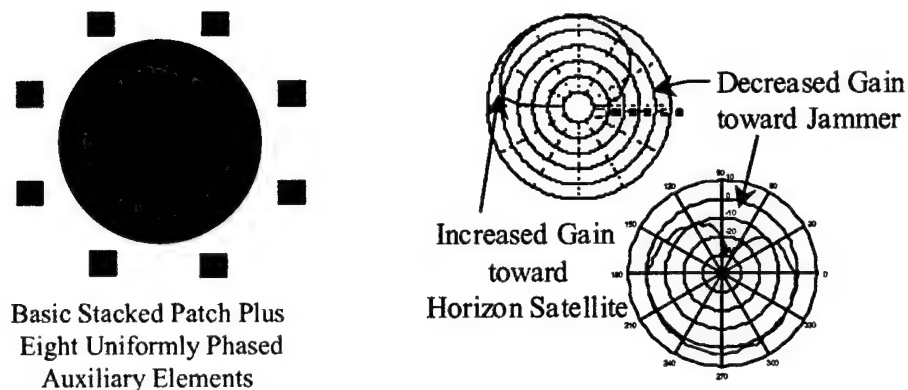
437

Basic Stacked Patch Plus
Eight Uniformly Phased
Auxiliary Elements

Decreased Gain
toward Jammer

Increased Gain
toward
Horizon Satellite

Figure 4. Mode 3 operation

The antenna and feed concept described above uses a simple two-channel nulling electronics card. The nulling card uses the a priori knowledge that a GPS jamming signal must be at least 30 dB stronger than the GPS signal itself to have an effect on the receiver performance. This information is used to suppress only the interfering signal at RF frequency between the antenna and the GPS receiver. By sampling the interfering signal in an independent RF path and applying a complex weight such that the net result is equal in amplitude and 180° out of phase, the interfering signal is suppressed while the GPS signal passes to the receiver. This result is shown graphically in Fig. 5. The cancellation electronics are connected in a closed loop that reacts in real time to the changes in the input signal and maintains the amplitude and phase correction [2,3]. Since this solution uses a mirror image of the jamming signal to create the null, all types of jammers (CW, swept, pulsed and broadband noise) will be suppressed. For broadband noise cancellation the time delay from each of the separate antennas through the electronics to the point of summation must be equal so that the noise is the same on both sides. Each jammer located at different locations generates a unique amplitude and phase solution at the point of summation. Therefore, classically for N jammers N+1 independent antennas and nulling electronics loops are required. The M-CRPA antenna is designed differently so that the auxiliary elements (in Mode 2) are summed to create a constant phase from jammers located near the horizon and using a single canceller loop will null all signals.
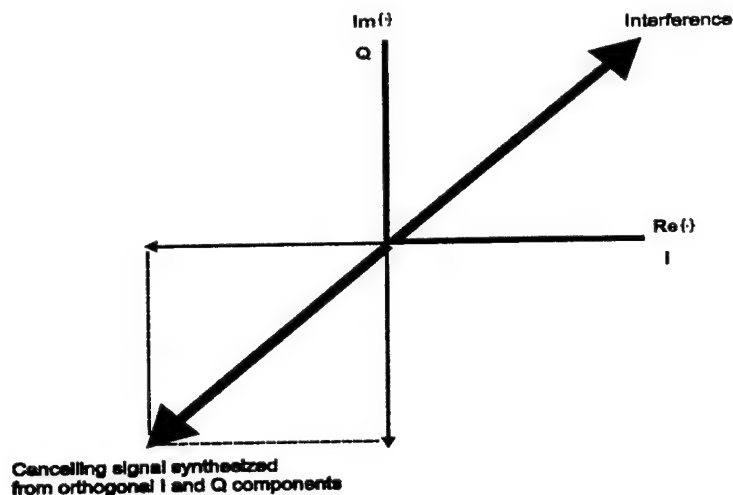
Figure 5. Cancellation vector equal and opposite to the interfering signal

3.0 Antenna Design and Simulation

The antenna concept outlined above was designed and simulated using Ansoft's HFSS. Both the center stacked patch and the auxiliary elements went through many iterations trading form factor, antenna pattern, and mutual coupling before the final design was set. Early nulling measurements indicated that phase and amplitude symmetry were critical to null depth, so a circular center patch and eight auxiliary elements were incorporated into the M-CRPA design. The symmetry was further improved by using four feed probes to excite the center, stacked patch. The center patch, also referred to as the reference patch or signal of interest, is shown in Fig. 6. The patch substrate is Rogers TMM 10 and the patch was simulated on a 10" square ground plane. The simulated return loss for the four feed probes is shown in Fig. 7. The patch is well matched at both L1 and L2 frequency bands.

439
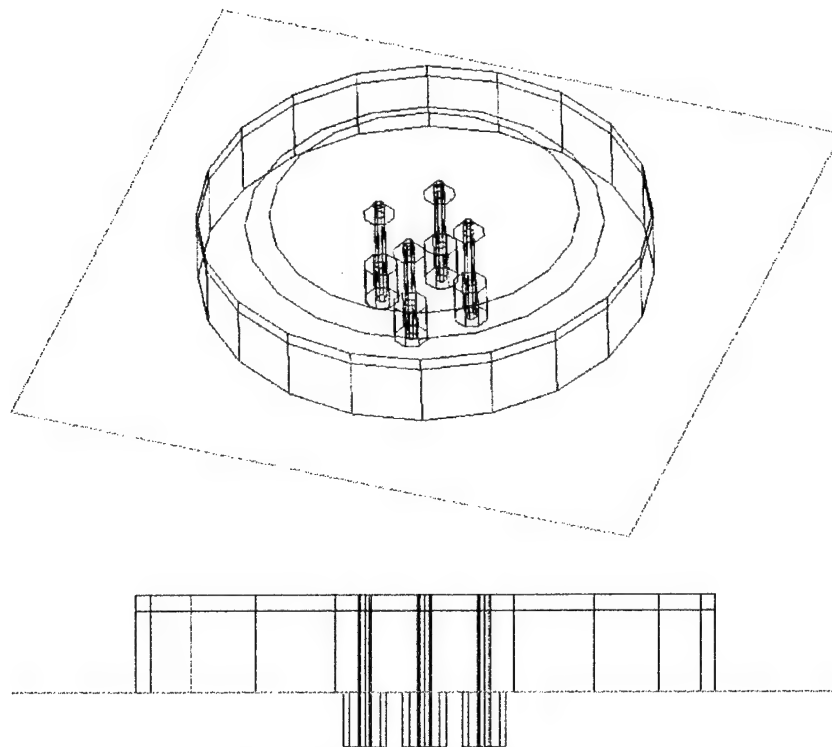
Figure 6. Center stacked patch
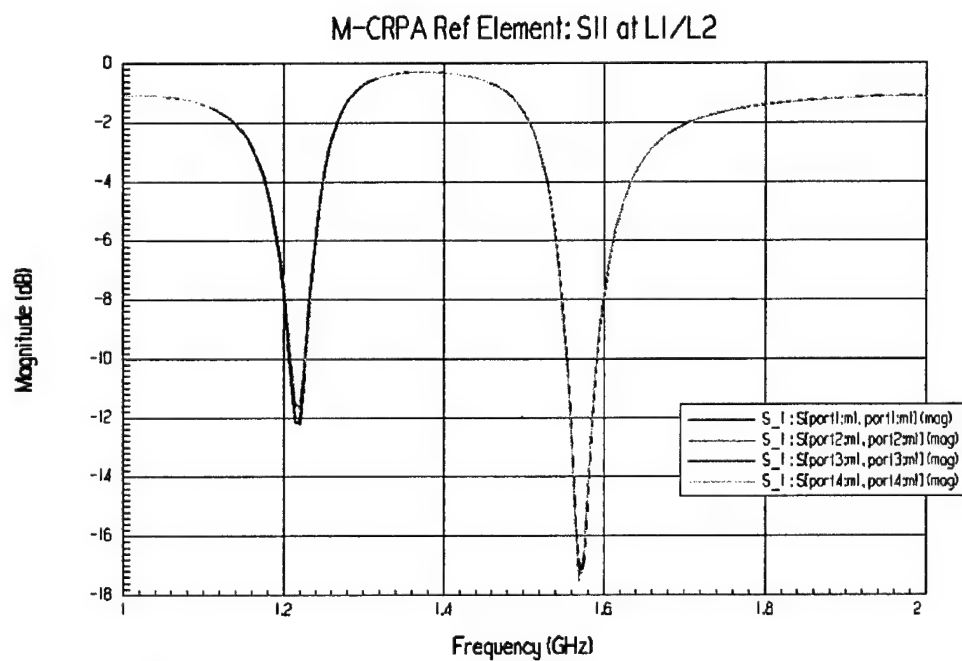
Figure 7. Simulated return loss of center stacked patch

Early designs of the M-CRPA array used single band monopole auxiliary elements. In order to reduce the height of the auxiliary elements a derivative of J. M. Boyer's DDRR-antenna (directional-discontinuity ring-radiator) was used [4]. The original DDRR element has a folded monopole with a ring resonator used to load and tune the antenna. The antenna was modified for dual band operation and the ring resonator was spiraled to reduce the antenna footprint, as shown in Fig. 8. Resistors were added to the ends of the spiral arms to dampen the high-Q response of the element and match the frequency response of the center patch. The associated loss in the auxiliary element gain is not critical to system performance since these elements are used for nulling only. Fig. 8 shows the simulated return loss of a single aux element. The aux element performs as desired and is very similar to the patch response shown in Fig. 7.
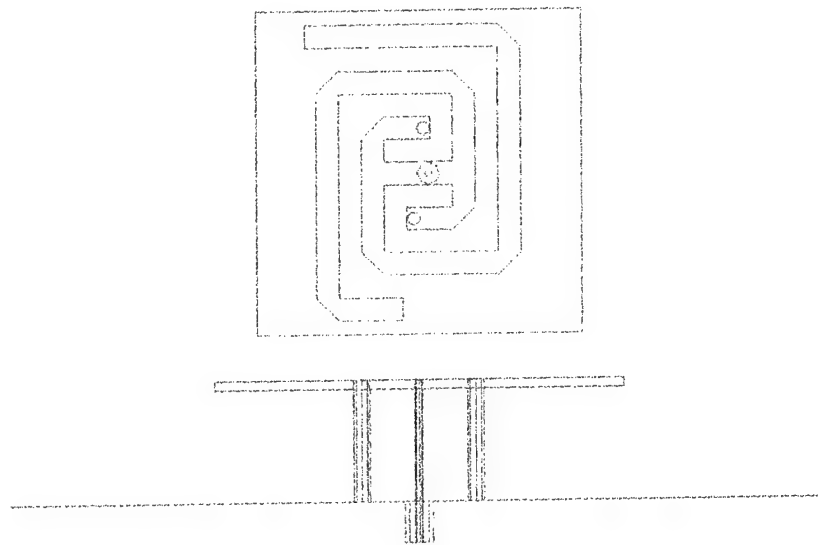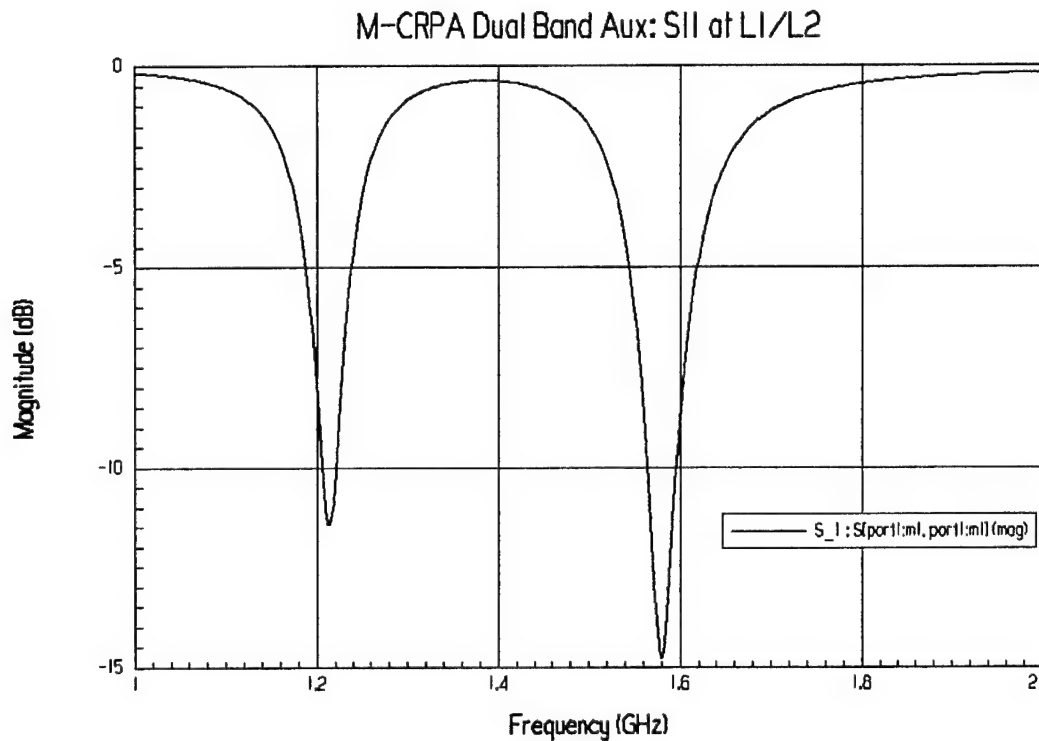
Figure 8. Final auxiliary element design

Figure 9. Simulated return loss of single auxiliary element

The final step in the M-CRPA design was to combine the center patch and aux elements in the array configuration shown in Fig. 10. The array spacing was optimized to provide satisfactory antenna operation and thus nulling performance while minimizing the array footprint and element coupling. In the final design, the aux elements are spaced every 45° in azimuth at a radial distance of 1.8" from the center of the patch. The simulated performance of each individual antenna port in the M-CRPA array environment is shown in Fig. 11. The four, center patch probes and the eight, aux elements are all well matched and tuned at L1 and L2.
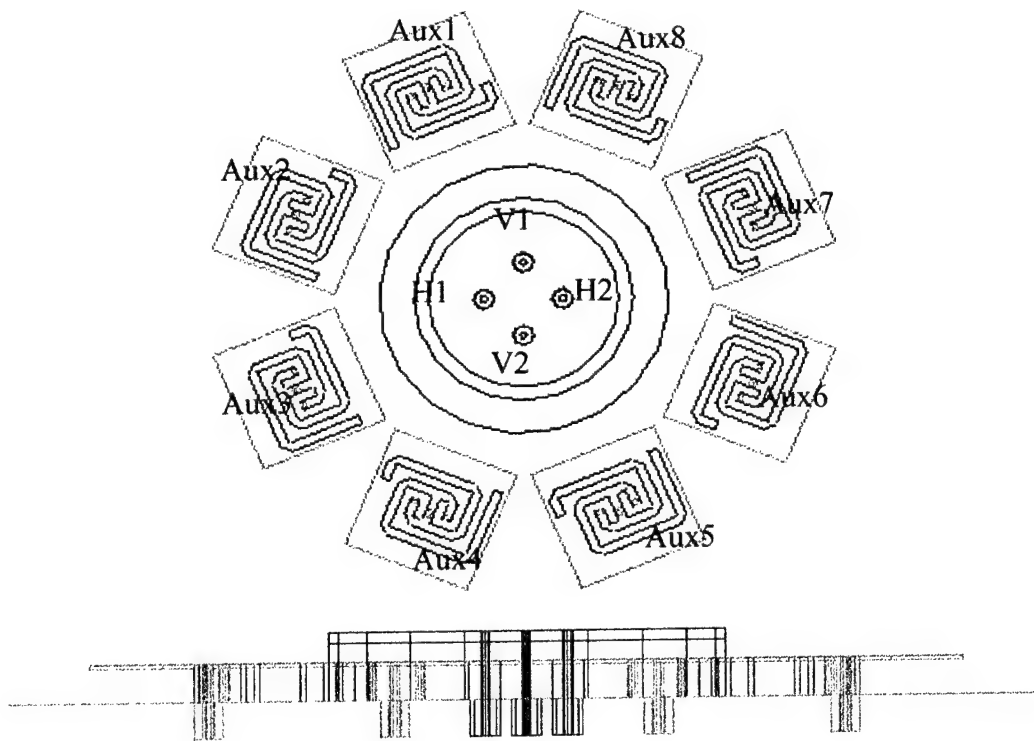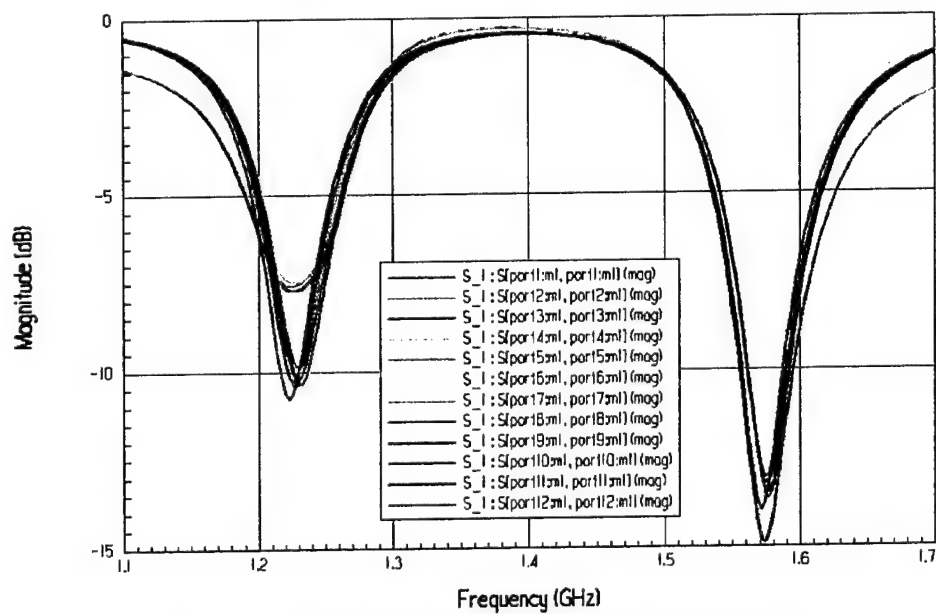
Figure 10. M-CRPA array configuration

Figure 11. Simulated return loss of M-CRPA array

443

4.0 Antenna Realization and Measured Results

Development and testing of the M-CRPA GPS antenna system was a joint effort between Titan AED, CCSD, and NAVAIR – RF Sensors Division. A prototype antenna element, shown in Fig. 12, was constructed and bench tested by Titan AED. The antenna has a diameter of 4.6" and a height of 0.36" above the ground plane. The center, dual-stacked patch reference element was tuned using fingers for both L1 and L2 operation. The eight dual-band auxiliary elements were similarly tuned by trimming the length of the spiral arms loading each auxiliary element. The measured return loss for the M-CRPA antenna is plotted in Fig. 13. In production, a more mechanically robust tuning method, such as turning screws, would be employed. The center patch and all eight auxiliary elements have very similar performance and are well matched over the L1 and L2 frequency bands.
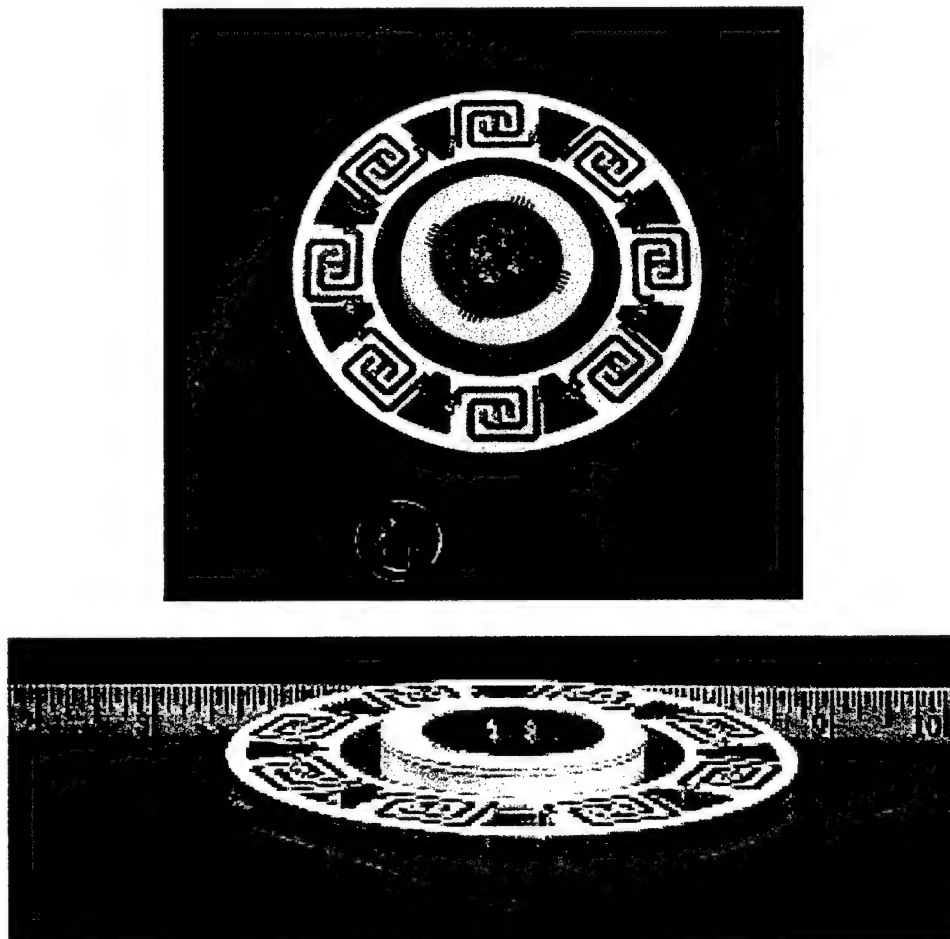

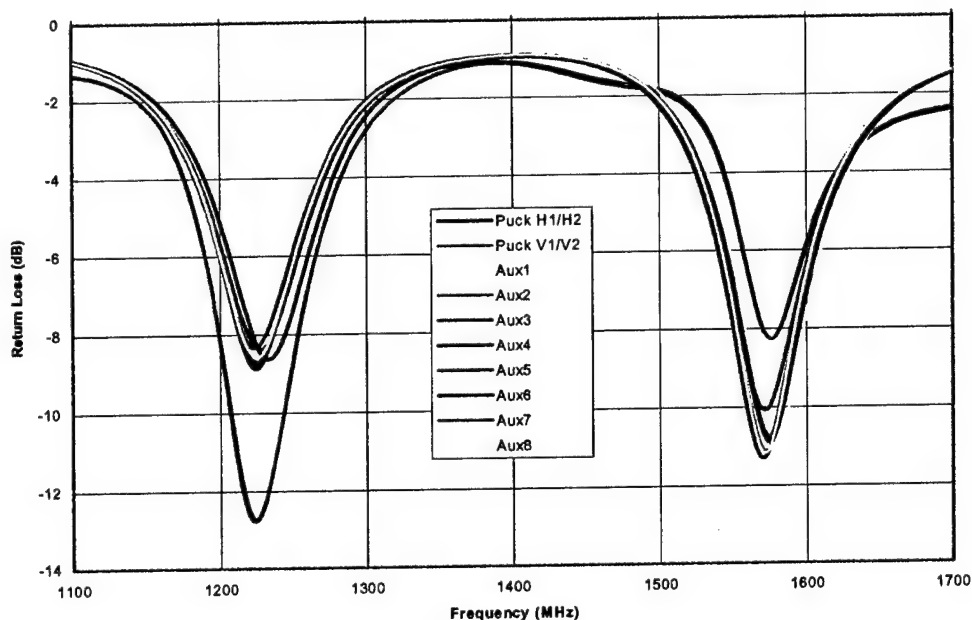**Figure 12.** M-CRPA antenna element

444

Figure 13. Measured return loss for M-CRPA antenna element

The antenna feed and nulling electronics were implemented by CCSD and consist of the coupler card, the canceller electronics and the solution hold test box. These elements are shown in Fig. 14 below. The four patch outputs are combined on the coupler card to create a single RHCP feed at L1 and L2. This port is referred to as the "Signal of Interest" (SOI) path. The eight auxiliary elements are combined in two different ways. Using a combination of 90° and 180° hybrids and 45° phase shifters the antenna elements are combined to create a constant phase sum relative to the phase of the SOI antenna. This is called the Mode 2 or the "Skirts up" mode port. In the second set of couplers the antenna elements are combined to create a continuous phase rotation which matches the phase rotation of the SOI antenna as the signal is moved 360 degrees around the antenna. This is Mode 3 or the "Cardioid" mode port. For the prototype, Mode 2 or 3 is manually selected. Mode 1 is the SOI signal only with the canceller electronics turned off. This mode is used only when there is no jamming signal present.
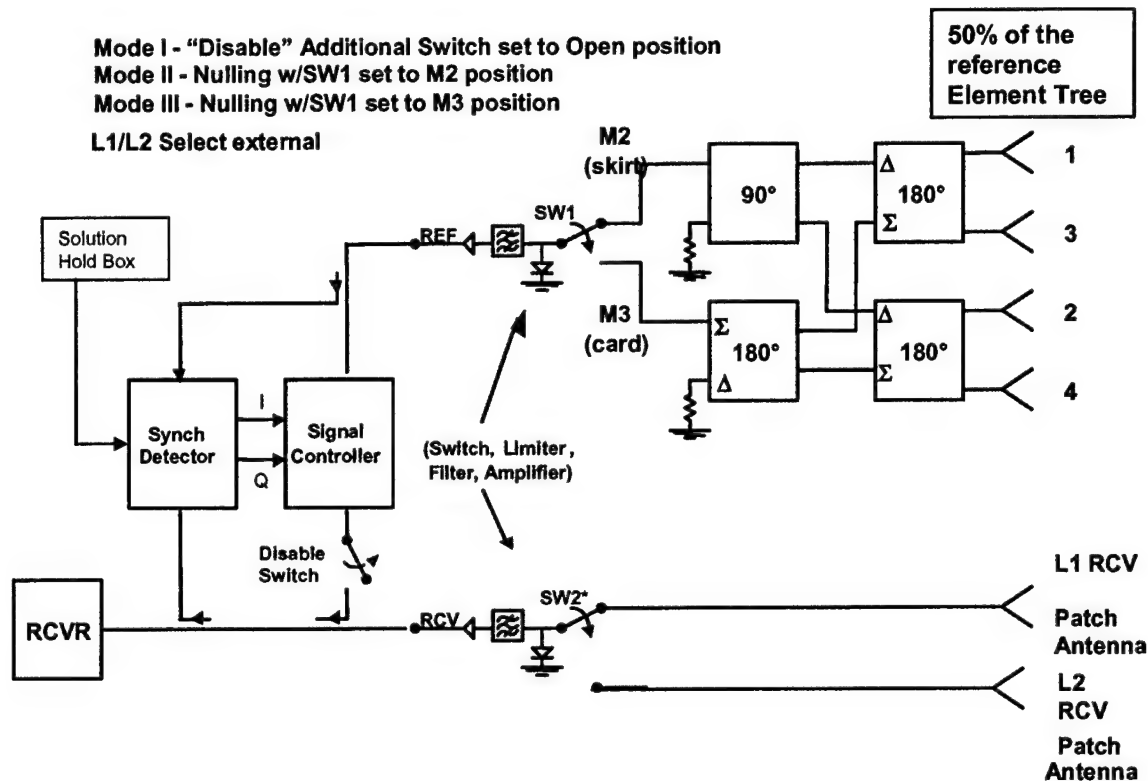
445

Figure 14. M-CRPA block diagram

The input RF signals at L1 and L2 are selected at SW2 and either/or is used for a cancellation solution. The GPS receiver makes the selection of the L1 or L2 jamming solution as it switches its input frequency. Simultaneous cancellation at L1 and L2 can be accomplished by adding a second cancellation loop. Each jammer at each frequency has its own unique solution vector. Typically GPS receivers can be programmed to operate in the either/or mode. The Mode 2 or Mode 3 outputs of the reference antenna array provide an all-in-view jammer reference signal (Mode 2) or a signal jammer reference (Mode 3). The jamming signal and the jamming content of the SOI signal are compared with a synchronous detector and amplitude and phase correction is generated. These two signals (I and Q) are then applied to a signal controller so that the resultant signal cancels the jamming signal in the SOI path. The point of cancellation is at the coupler below the disable switch. During antenna range testing, an external solution hold control circuit is applied to the synchronous detector so full 360° antenna patterns can be generated in the presence of jamming signals.

An RF coupler card, combining all of the antenna elements together, was designed using a combination of discrete 90° hybrids and stripline. The design is

446

shown in Fig. 15. The three connectors on the left are the SOI output to the canceller (bottom connector) along with the Mode 2 and Mode 3 coupler combination outputs. On the other side of the card is the 12 antenna element feed connections.
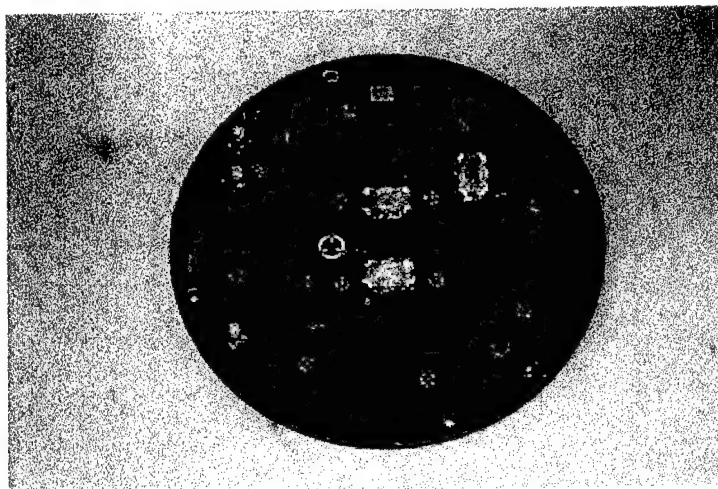

Figure 15. M-CRPA coupler card

The canceller electronics card is shown in Fig. 16. It is a dual sided 8-layer PC card with embedded RF stripline connections. Since it is a prototype, the time matching delays were added as coaxial cables on the top of the board. In production they would be realized in stripline form within the card. The covered areas are shielded sections that prevent leakage signals from interfering with the correct solution. Because of the high dynamic range of the card, internal leakage paths are reduced by up to 80 dB.
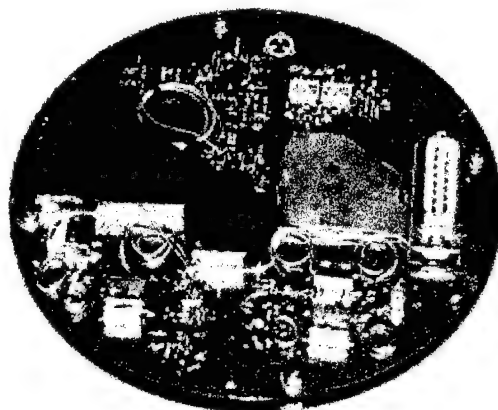

Figure 16. Canceller electronics card

The control box, shown in Fig. 17, controls the mode selection, frequency selection, and hold functions for operation of the M-CRPA system in a test environment. It has a programmable potentiometer for factory control of the internal calibration points of the system.
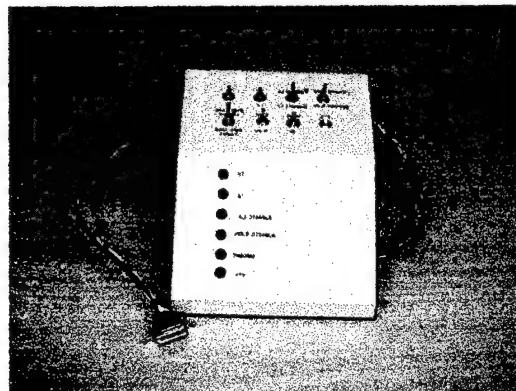

Figure 17. M-CRPA control box

Standalone measurements of the cancellation electronics are shown in Figs. 18 and 19 below. Fig. 18 shows the performance at L1 and Fig. 19 shows the performance at L2. The plots in the figures below show the cancellation depth for a combined CW and BB noise signal where the CW signal is 40 dB stronger than the noise signal. The divisions on the plots are 10 dB steps vertically and 2 MHz steps horizontally. The performance measured is greater than 60 dB for CW and 30 dB over the bandwidth of the P(Y) code.
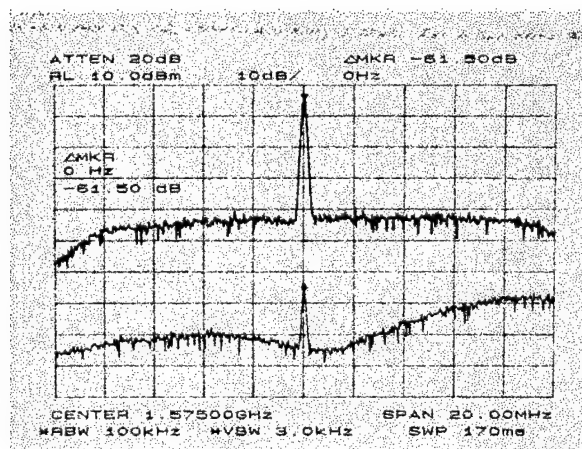

Figure 18. Canceller performance against CW and BB jamming at L1
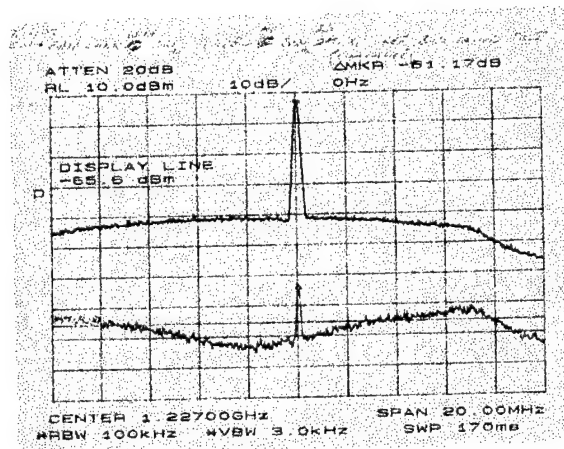
Figure 19. Canceller performance against CW and BB jamming at L2

The feed card shown in Fig. 15 was bench tested for insertion loss and phase error for each port. The results for the reference patch are shown in Table 1. The four ports of the reference patch have an average insertion loss of 2.8 dB and are phase matched to better than 2°. Each auxiliary element has an average insertion loss of 3.2 dB and phase error of 1.8° when excited in Mode 2 as seen in Table 2. In Mode 3, shown in Table 3, the average insertion loss of each aux element is 3.6 dB with a phase error of 3°. The insertion loss of the auxiliary ports for both Mode 2 and Mode 3 can be compensated by the amplitude control in the nulling electronics. Minimizing phase and amplitude ripple between auxiliary elements and the reference patch is critical to system performance because the nulling electronics methodology assumes that the antenna performance is symmetric. The insertion loss of the reference patch is also very important because it directly reduces system gain. Both issues will be improved in future implementations of the feed card.

Table 1. Measured feed performance at 1575 MHz for reference patch port

Reference Patch Port	Insertion Loss, [dB]	Relative Phase, [deg]
V1	2.3	0
H1	3.0	-90.9
V2	2.6	-178.8
H2	3.2	91.8

449

Table 2. Measured feed performance at 1575 MHz for M2 port

M2 Port (Skirt's Up)	Insertion Loss, [dB]	Relative Phase, [deg]
Aux 1	2.7	0
Aux 2	2.6	-47.0
Aux 3	3.8	-92.8
Aux 4	3.5	-135.6
Aux 5	3.1	179.5
Aux 6	2.8	131.0
Aux 7	3.6	92.5
Aux 8	3.4	46.7

Table 3. Measured feed performance at 1575 MHz for M3 port

M3 Port (Cardioid)	Insertion Loss, [dB]	Relative Phase, [deg]
Aux 1	3.7	0
Aux 2	3.8	-0.6
Aux 3	3.6	-2.2
Aux 4	3.7	3.6
Aux 5	3.3	-2.8
Aux 6	3.6	-2.2
Aux 7	3.3	7.8
Aux 8	3.4	4.8

The anti-jamming performance characteristics of the MCRPA array were evaluated in the Naval Air Systems Command's Facilities for Antenna and RCS Measurements (FARM) anechoic chamber. The FARM Rectangular Anechoic Chamber measures 100" x 40'x 40' with a 12ft cylindrical quiet zone and meets TEMPEST requirements. The chamber is used for the measurement of antenna characteristics (100 MHz to 18 GHz) including radar cross section (3 to 18 GHz). This facility is part of the GPS Joint Program Office antenna systems test infrastructure organization. The infrastructure is used for testing and evaluating future GPS antenna systems. The personnel and facility have been conducting GPS antenna characterization measurements for more than 15 years. Measurements are conducted on the antenna itself when mounted on a CRPA specification ground-plane. For the non-interference environment, measurements include single element voltage standing wave ratios (VSWR), gain pattern and axial ratio measurements. In an environment consisting of various jammer combinations, the gain pattern, the system convergence time, and power reduction are measured. From these measurements anti-jam system performance predictions can be calculated based on coverage improvement factors, jammer to signal ratios and receiver channel state values.

450

The M-CRPA GPS antenna system was mounted on a curved rectangular ground plane, which is similar to the size and shape of a typical airplane fuselage, as shown in Fig 20. A side view of the prototype M-CRPA antenna system is shown in Fig. 21. The coupler card and nulling electronics are mounted behind the ground plane shown in Fig. 20 and are connected to the antenna using short cables. Production units of the antenna system would have the coupler and nulling cards connected directly to the antenna and would only extend 0.8" behind the ground plane. Antenna pattern measurements were taken in 3 different modes. Mode 1 is the standard GPS mode that is used when no jammers are present. Elevation pattern cuts of the reference patch for various azimuth angles are plotted in Fig 22. The gain of the reference patch is about 0 dBiC, which includes an average feed card insertion loss of 2.8 dB for the four reference patch ports.
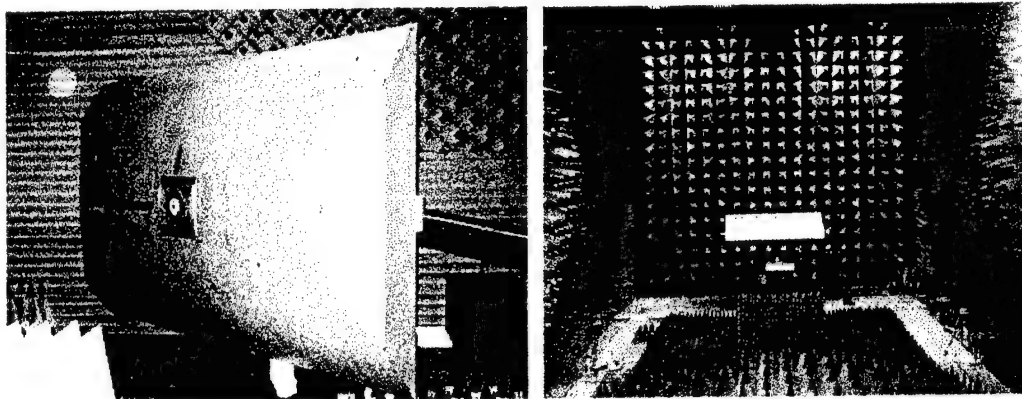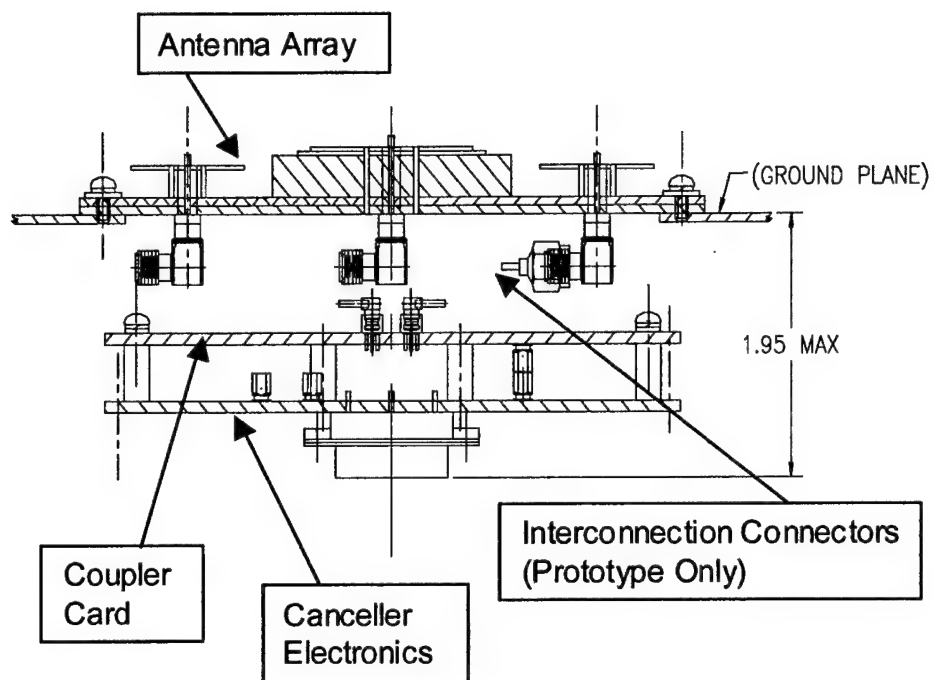

Figure 20. Measurement test facility

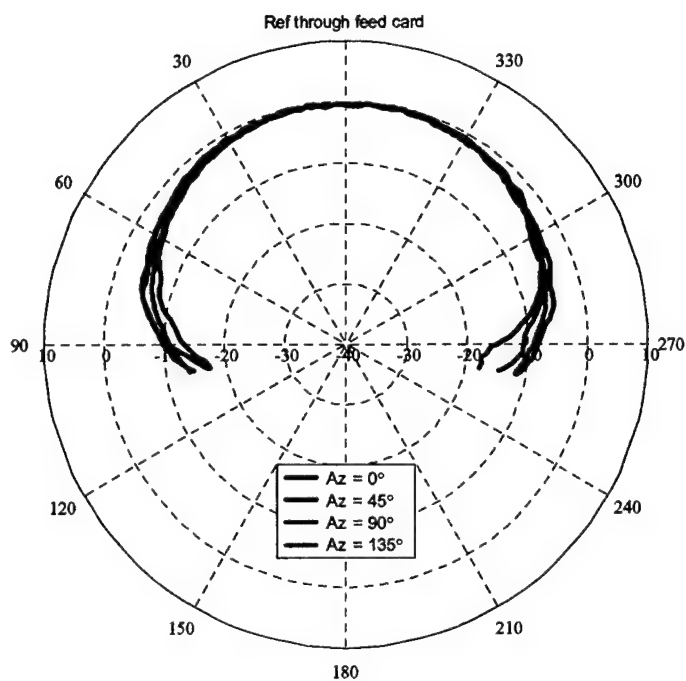**Figure 21.** Diagram of M-CRPA antenna system

Figure 22. Elevation cuts of reference element at various azimuth angles

When multiple jammers are present on the horizon, Mode 2 or "skirt's up" mode, is used to create a ring null on the horizon. Three jammers were placed in the anechoic chamber at azimuth angles of 240°, 270°, and 300° with elevation angles of 10°, 15°, and 10°, respectively. The nulling electronics were switched to Mode 2 with active nulling enabled, and then the hold was initiated. The three jammers were then removed from the chamber and the antenna pattern measurements were taken. The elevation cuts are shown in Fig. 23 for Mode 2 with 3 jammers present. The antenna gain for low elevation angles has been reduced at all azimuth angles as desired. An azimuth cut of the M-CRPA GPS antenna pattern at an elevation angle of 10° is shown in Fig. 24. The plot compares the antenna gain when no jammers are present versus the gain of the antenna in "skirt's up" mode. The arrows indicate the location of the jammers. In the direction of the jammers, the antenna gain has been reduced significantly. The plot also shows the expected nulling performance based on the measured reference patch and Mode 2 port antenna patterns.
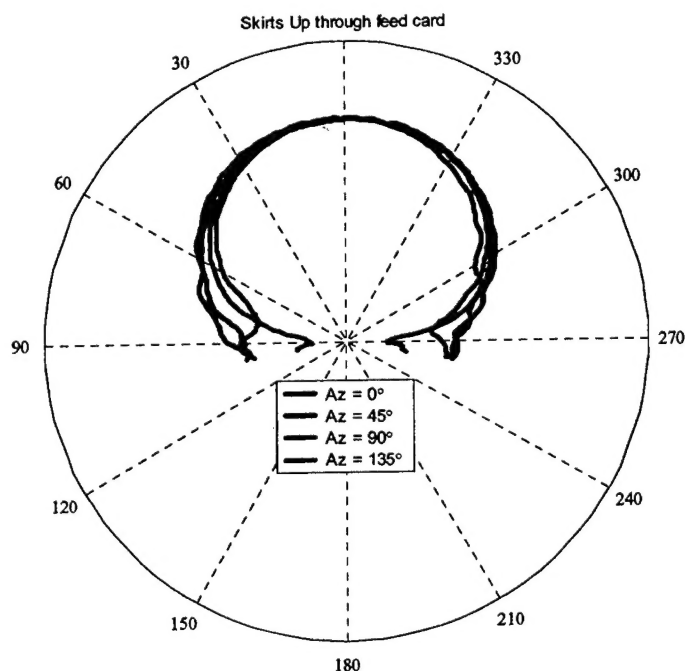

Figure 23. Elevation cuts of M-CRPA GPS antenna in M2 mode for 3 jammers

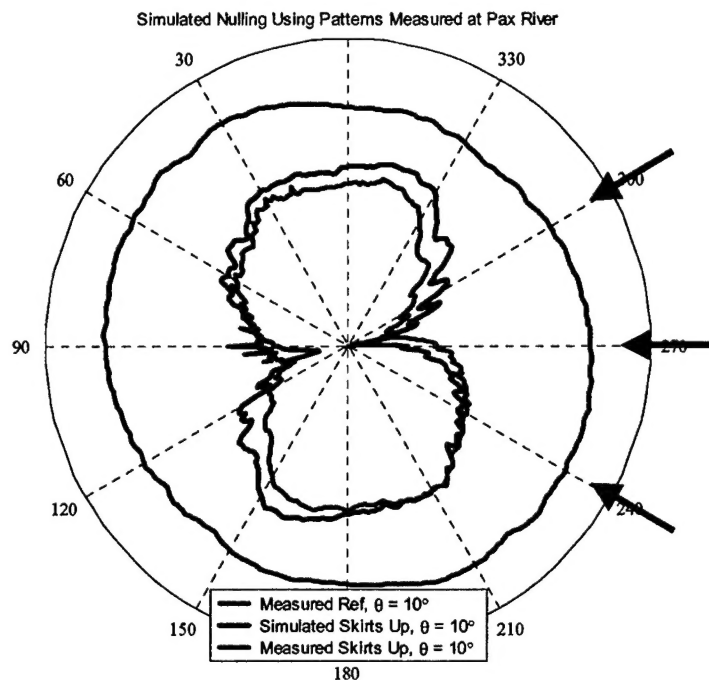**Simulated Nulling Using Patterns Measured at Pax River**

Figure 24. Comparison of azimuth cuts for M-CRPA GPS antenna in M2 mode with and without jammers present

When only one jammer is present Mode 3 or cardioid mode should be used to maintain antenna gain in all directions except towards the jammer. A similar process described for the "skirt's up" case is used to null the jammer and initiate a solution hold. Fig. 25 shows the elevation cuts and Fig. 26 shows an azimuth cut for the antenna when nulling in Mode 3. The jammer was located at an azimuth angle of 90° and an elevation angle of 10° from the horizon. In the direction of the jammer, the antenna gain was reduced to acceptable levels.
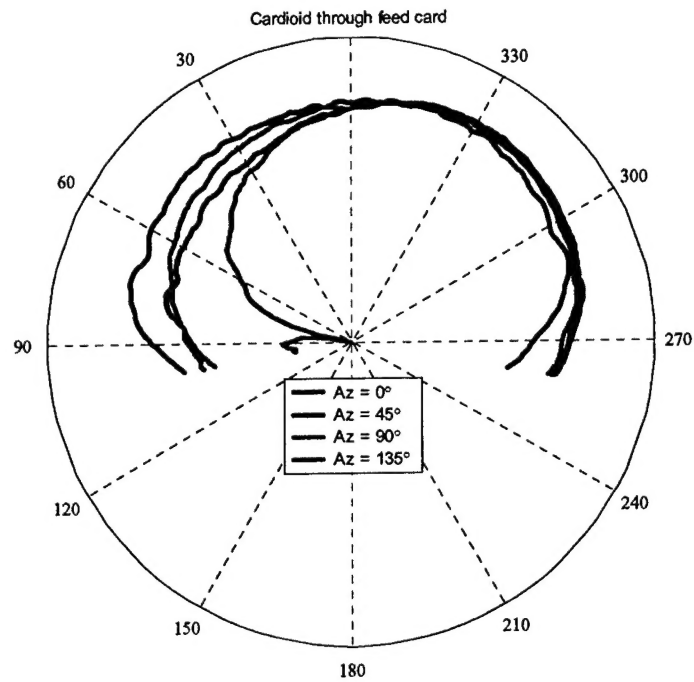
454

Figure 25. Elevation cuts of M-CRPA GPS antenna in M3 mode for 1 jammer
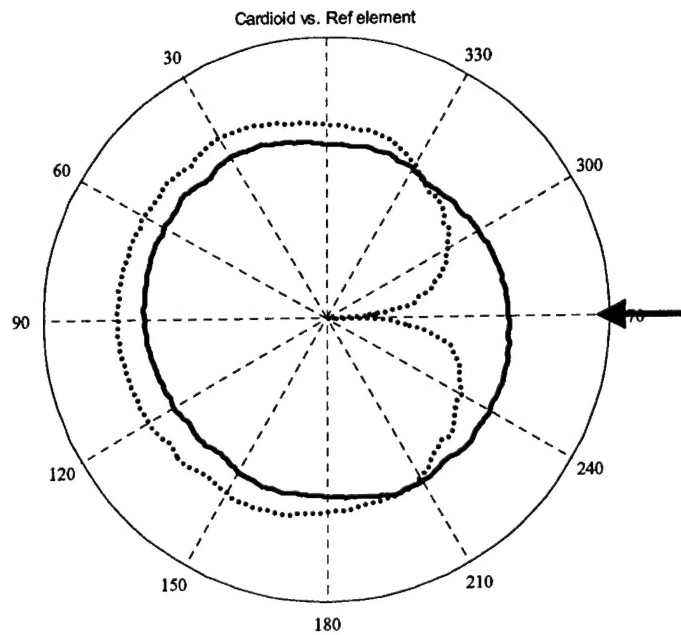

Figure 26. Comparison of azimuth cuts for M-CRPA GPS antenna in M3 mode
with and without jammer present

4.0 Conclusions

A small, 4.6" diameter, anti-jam GPS antenna array has been developed and tested. The M-CRPA array is capable of operating in standard GPS reception mode, "skirt's up" mode, or cardioid mode depending on the number of jammers present on the horizon. The primary advantage of the M-CRPA design, other than its small size, is its ability to provide multi-jammer performance without the N+1 antenna limitation for suppressing N jammers. It uses minimal electronics compared to classical CRPA systems providing the opportunity for smaller packaging and lower cost. In on going work, we are investigating installation effects and working on methods to reduce system losses and mitigate coupling effects to improve absolute gain levels.

5.0 References

[1] M.B May, B. R. Tanju, A.E. Zeger and B.S. Abrams, "Low Elevation Antenna Nuller," SPAWAR SBIR Technical Report, pp. 8-1 through 8-10, 1997.

[2] Rabindra N. Ghose, "Operation of an Adaptive Canceller", *Interference Mitigation, Theory and Application*, pp.78-86, IEEE Press, 1996.

[3] Ashok Talwar, "Interference Cancellation Improves GPS Receiver Performance," *Microwaves & RF Magazine*, April 1997.

[4] G.W. Horn, "The Half Wavelength DDRR Antenna," *CQ*, pp. 1313-17, 118-119, September 1967.